The influence of stellar birth environment on protoplanetary disc dispersal

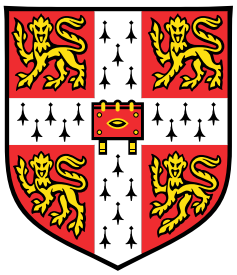

Andrew Winter

Supervisor: Prof. Cathie Clarke
Dr. Richard Booth

Institute of Astronomy
University of Cambridge

This dissertation is submitted for the degree of
Doctor of Philosophy

Darwin College May 2019

Declaration

I hereby declare that except where specific reference is made to the work of others, the contents of this dissertation are original and have not been submitted in whole or in part for consideration for any other degree or qualification in this, or any other university. This dissertation is my own work and contains nothing which is the outcome of work done in collaboration with others, except as specified in the text. This dissertation contains fewer than 60,000 words including appendices, footnotes, tables and equations and has fewer than 150 figures.

Andrew Winter
May 2019

Abstract

The influence of stellar birth environment on protoplanetary disc dispersal

Andrew Winter

Protoplanetary discs (PPDs) are the progenitors of planets and represent the material available for their formation. Recent surveys indicate that exoplanetary architectures are diverse and the processes that govern the evolution of PPDs contribute significantly to the properties of these architectures. Most studies of PPDs consider their secular evolution, disregarding the influence of environment on the evolution and eventual dispersal of the disc. However, a growing body of empirical studies have found evidence that they are in fact influenced by their stellar neighbours. In this dissertation I focus primarily on two mechanisms by which discs evolving in close proximity to other stars might be truncated and dispersed by their neighbours. These are tidal truncation by star-disc encounters and external photoevaporation due to irradiation by massive stars. I make the distinction between encounters that occur in multiple systems and those that occur between individual stars (type I and type II encounters). I model the specific case of HV and DO Tau, apparently isolated stellar systems connected by an extended dust 'bridge', as a historic type I encounter within a quadruple system. I then theoretically quantify the influence of type II tidal encounters on PPDs in the distant and close regimes. Coupling recent developments in the theory of photoevaporating discs with a viscous evolution model, I similarly quantify the dispersal timescale of PPDs due to irradiation by massive stars. Comparing these mechanisms in local environments, I find that external photoevaporation dominates over type II encounters as a dispersal mechanism in local star forming regions. Applying photoevaporation models to the OB association Cygnus OB2, I successfully reproduce the observed disc survival fractions, implying that external photoevaporation is having a significant influence on PPDs in that region. Finally, I link the dispersal timescales to star formation physics, illustrating that outside of the solar neighbourhood a much larger fraction of stars may be exposed to environments that disperse discs rapidly. Tentatively, this indicates that the sun may lie in a special region for planet formation, where the number of stars for which PPDs remain mostly uninfluenced by stellar neighbours is maximised.

Acknowledgements

I would not have been able to complete this dissertation without the influence of a huge number of people, both during my time in Cambridge and before.

First and foremost, I thank my parents, John and Wendy, for their endless support throughout my life.

The many people that I have met during the last three years have undoubtedly made my time what it was. Special mentions go to Pablo, Cameron and Aneesh at the Institute of Astronomy, whose shared interest in wine has proved an efficient tool for maintaining sanity during even the most challenging of periods. Further indulgence in vices has been kindly facilitated by Ollie Batey, without whom the last three and a half years would have been far less interesting.

I am extremely thankful for the enduring patience and thoughtful suggestions of Richard Booth throughout my Ph.D., but especially during the early stages. Having always made himself available for discussion and freely offered advice, he is in no small way responsible for many of the skills that I have learned during this time.

Finally, this work would clearly not have been achievable without the guidance of Cathie Clarke. I have been fortunate to have a supervisor whose advice has proven invaluable for every aspect of my academic life at Cambridge and I have no doubt will continue to be so in the future.

Table of contents

List of figures

List of tables

Chapter 1

Introduction

Charting exoplanet demographics is one of the most active fields in modern astronomy (Winn and Fabrycky, 2015). At the time of writing, the number of discovered exoplanets numbers nearly 4000, and the new *Transiting Exoplanet Survey Satellite* (*TESS*) mission has now began to contribute to this sample (Gandolfi *et al.*, 2018). *TESS* is expected to find 1000s of new planets over its lifetime, including 10s of approximately Earth-mass planets (Ricker *et al.*, 2015). Among several recent discoveries, a system of 7 such planets found orbiting around the cool M-dwarf, Trappist-1, has captured the imagination of both scientists and a broader audience (Gillon *et al.*, 2017). Additionally, high resolution spectroscopy can now be used to probe the astmospheres of discovered exoplanets (Charbonneau *et al.*, 2002; Snellen *et al.*, 2010; Brogi *et al.*, 2012; Sedaghati *et al.*, 2017; Nortmann *et al.*, 2018). The upcoming *James Webb Space Telescope* (JWST) will greatly improve such measurements due to its high sensitivity and broad wavelength coverage, providing a wealth of data on exoplanet properties using transit spectroscopy (Beichman *et al.*, 2014; Bean *et al.*, 2018). Such exciting developments offer insights into the Earth's formation within the context of the broad range of observed exoplanet architectures, and promise to answer questions pertaining to the frequency of life in the universe.

While discovering and characterising exoplanets is in itself of the utmost interest, understanding these observations requires studying their progenitors. Protoplanetary discs (PPDs) comprise dust and gas that orbits a young star ($\lesssim$ 3–10 Myr old – Haisch *et al.*, 2001b; Ribas *et al.*, 2014), which is the material available for planets to form from during these early stages of stellar evolution. Using the *Atacama Large Millimeter/submillimeter Array* (ALMA), a large number of PPDs have now been spatially resolved. Of particular interest have been the recent observations of rings or gaps in the circumstellar discs (ALMA Partnership *et al.*, 2015; Clarke *et al.*, 2018; Pérez *et al.*, 2018) that may be the result of young planets clearing material along their orbits (Lin and Papaloizou, 1979; Baruteau and

Papaloizou, 2013; Bae *et al.*, 2017; Kanagawa *et al.*, 2018; Fedele *et al.*, 2018). Alternative explanations are also possible, including (though not limited to): dust growth near snowlines (Zhang *et al.*, 2015; van der Marel *et al.*, 2018), magnetically-induced zonal flows (Flock *et al.*, 2015) and self-induced dust traps due to backreaction on the gas (Gonzalez *et al.*, 2017). Possibly the strongest evidence for planet induced gaps is the recent discovery by Clarke *et al.* (2018). They found gaps in ALMA observations of the PPD around CI Tau, which is the first disc known to host a hot Jupiter (inferred from radial velocity measurements – Johns-Krull *et al.*, 2016; Biddle *et al.*, 2018). In general, the aforementioned studies highlight that the processes which govern the evolution of dust and gas in PPDs are highly relevant for understanding the observed architectures and compositions of exoplanets.

Exoplanets and their progenitors are largely considered as secularly evolving systems, with properties independent of their environment. However, there is a growing body of work that indicates that this is not the case: the formation and evolution of planets is dependent on the host star's birth environment. Stars form in groups (Lada and Lada, 2003) and, depending on the number and density of neighbouring stars, a PPD can suffer the influence of external stellar feedback mechanisms. In particular, a disc can be depleted by tidal interaction with other stars if their passage is sufficiently close (Clarke and Pringle, 1993; Ostriker, 1994; Hall *et al.*, 1996; Pfalzner *et al.*, 2005b; Olczak *et al.*, 2006; Breslau *et al.*, 2014). Alternatively, a PPD irradiated by far ultraviolet (FUV) and extreme ultraviolet (EUV) photons from neighbouring massive stars can be heated sufficiently to lose mass at the outer edge in a process called 'external photoevaporation' (Johnstone *et al.*, 1998; Störzer and Hollenbach, 1999; Adams *et al.*, 2004; Facchini *et al.*, 2016; Haworth *et al.*, 2018a). If an environment is sufficiently dense or neighbours are massive enough then these mechanisms will disperse the PPD, reducing the time and mass available for planet formation. How this influences the resulting exoplanet population remains uncertain. Chemical signatures, for example the meteoritic abundance of the daughter products of short-lived isotope ^{60}Fe, which can only be produced during nucleosynthesis and dispersed by supernova events, may indicate external influences have been important for the formation of our own solar system (e.g. Cameron *et al.*, 1995; Williams and Gaidos, 2007, see also Adams 2010 and Busso 2018 for recent reviews). Additionally, the distribution of stellar birth environments is a function of position and time throughout the universe (e.g. Longmore *et al.*, 2014; Adamo *et al.*, 2015; Reina-Campos and Kruijssen, 2017). Therefore, quantifying the influence of environment has consequences for understanding planet formation outside of the solar neighbourhood.

In the remainder of this introduction I will outline the processes that govern PPD evolution. In Section 1.1 I briefly review the formation and evolution of PPDs in general, followed by a discussion of their dispersal in the case that they are not influenced by environment in

Section 1.2. In Section 1.3 I discuss how feedback by stellar neighbours can lead to faster disc dispersal, introducing the two dispersal mechanisms that will be the primary focus of this work. Finally, I lay out the goals and structure of the remaining chapters in Section 1.4.

1.1 Formation and viscous evolution of PPDs

PPDs ubiquitously form around young stars due to the conservation of angular momentum as the nascent stellar core undergoes gravitational collapse (Shu *et al.*, 1987). Stars form from overdensities in the interstellar medium (ISM); if a region has a sufficient density, it will collapse into one or many cores. As such a core collapses, outflows in the form of bipolar jets also carry material away, driven by radiation pressure from the central star and the centrifugal acceleration of gas along magnetic field lines (Konigl, 1982; Pudritz and Norman, 1983; Shu *et al.*, 1994; Carrasco-González *et al.*, 2010). This process continues until the surrounding envelope is depleted, and a young star with a circumstellar disc remains. The material orbiting the star at this stage is what is available for the eventual formation of planetary systems. Throughout this work I frequently refer to the viscous evolution of the PPD, which I will discuss in this section. For a more complete review of the processes governing disc evolution, see Williams and Cieza (2011).

An important process in a PPD is the radial transport of angular momentum. This process results in accretion onto the central star (such that the disc is depleted) and the spreading of material (such that the disc expands), as shown in Figure 1.1a. Observed accretion rates indicate that the timescale on which a disc viscously evolves is on the order of the disc lifetime (Hartmann *et al.*, 1998; Manara *et al.*, 2016). Additionally, Tazzari *et al.* (2017) find evidence for such spreading indicated by the fainter and more extended PPD population in Lupus with respect to younger regions. However, the physical mechanism and rate of such transport throughout the disc remains unclear. In general, for a thin disc undergoing Keplerian rotation (i.e. with angular velocity $\Omega = \Omega_{\rm K} = \sqrt{Gm_*/r^3}$) and where the hydrostatic vertical structure is decoupled from the radial evolution of the surface density $\Sigma(r,t)$ for radius, r, at time, t, then we have:

$$\frac{\partial \Sigma}{\partial t} = \frac{3}{r}\frac{\partial}{\partial r}\left[r^{1/2}\frac{\partial}{\partial r}\left(\nu r^{1/2}\Sigma\right)\right], \tag{1.1}$$

where $\nu(r)$ is the kinematic viscosity at r. Equation 1.1 is the result of conservation of mass and angular momentum for a viscous fluid, where the physics of angular momentum transport is contained within the ν parameter. I.e. the mechanism of viscous angular momentum transport could be molecular or turbulent, so long as it acts locally (Balbus and Papaloizou, 1999). Further quantifying the behaviour of a PPD over time requires a definition of ν.

In the limit of thin accretion discs, assuming that the viscosity is a power law in radius $\nu \propto r^{\gamma}$ means that equation 1.1 conveniently has a similarity solution of the form (Lynden-Bell and Pringle, 1974):

$$\Sigma \propto \frac{1}{3\pi\nu_1 R^{\gamma}} T^{-\frac{5/2-\gamma}{2-\gamma}} e^{\frac{R^{2-\gamma}}{T}}. \tag{1.2}$$

I have defined:

$$R \equiv \frac{r}{R_1}; \qquad \nu_1 = \nu(R_1); \qquad T \equiv 1 + \frac{t}{\tau_{\text{visc.}}}, \tag{1.3}$$

where R_1 is the disc scale radius and $\tau_{\text{visc.}}$ is the viscous timescale

$$\tau_{\text{visc.}} = \frac{1}{3(2-\gamma)^2} \frac{R_1^2}{\nu_1} \tag{1.4}$$

at R_1. Hartmann *et al.* (1998) discuss the advantages of choosing $\gamma = 1$: this is equivalent to a constant α-viscosity prescription (Shakura and Sunyaev, 1973) where the midplane temperature T_{mid} within the disc is $T_{\text{mid}} \propto r^{-q}$ where $q = 1/2$ (physically a range $1/2 \leq q \leq 3/4$ is reasonable – see Kenyon and Hartmann, 1987). The associated steady state surface density profile is then $\Sigma \propto r^{-1}$. With this choice, we can write the surface density evolving in isolation as a function of time and radius:

$$\Sigma = \frac{M_0}{2\pi R_1^2 R} \exp\left(-\frac{R}{T}\right) T^{-1.5} \tag{1.5}$$

where M_0 is the initial disc mass. We have obtained this result by following Shakura and Sunyaev (1973) in parameterising the kinematic viscosity $\nu = \alpha c_{\text{s}}^2 \Omega^{-1}$ for the sound speed c_{s} and angular velocity Ω, and α is assumed to be a constant. For a vertically isothermal disc with scale height $H(r)$, we have $H = c_{\text{s}}/\Omega$ and $c_{\text{s}} \propto T_{\text{mid}}^{1/2}$. Assuming a value of H/r at the scale radius, $H_1/R_1 = 0.05$, this allows us to write:

$$\alpha \approx 5.4 \times 10^{-3} \left(\frac{\tau_{\text{visc.}}}{1\,\text{Myr}}\right)^{-1} \left(\frac{R_1}{40\,\text{au}}\right)^{3/2} \left(\frac{m_*}{1\,M_\odot}\right)^{-1/2} \tag{1.6}$$

for a stellar host of mass m_*. The value of H/r is a weak function of r; the exact value for H_1/R_1 is here effectively absorbed into the value of α, which dictates the rate of angular momentum transport (and therefore accretion onto the central star).

In the following work I will refer the above prescription where viscosity becomes an important consideration for disc evolution. However, the choice of α and the physical mechanism(s) that induce viscous torques within the disc remain a topic of debate. Angular momentum transport due to molecular viscosity is too inefficient to explain observed mass accretion rates (e.g. Spitzer, 1962; Pringle, 1981). Turbulence represents a viable alternative

mechanism. In hot, ionised regions of a disc the magnetorotational instability (MRI – caused by the Lorentz force induced by the differential rotation of a magnetised fluid) can drive such turbulence (Velikhov, 1959; Chandrasekhar, 1960; Balbus and Hawley, 1991). However, in cooler parts of the disc, magnetohydrodynamic (MHD) effects are expected to weaken or suppress the turbulence induced by MRI (e.g. Bai and Stone, 2013, see also Turner *et al.* 2014 for a review). Some alternative candidates for inducing turbulence include self-gravity (Gammie, 2001), Rossby waves (Lovelace *et al.*, 1999) and the vertical shear instability (Urpin and Brandenburg, 1998), among others. Nonetheless, laboratory experiments suggest that hydrodynamic turbulence remains inefficient at transporting angular momentum in fluids under Keplerian rotation (Ji *et al.*, 2006), supporting the importance of magnetic fields in this context (see Section 1.2.2).

While the viscous accretion onto the central star depletes a disc, it is not the ultimate mechanism for disc dispersal. Under viscous evolution alone, with $\gamma = 1$ as above, the disc mass evolves as $M \propto t^{-1/2}$. For typical disc masses and accretion rates, we would then expect a PPD to be optically thick for ~ 100 Myr, and spend a similar period of time in a transition phase where the disc is optically thin. This is not supported by observations that indicate discs are dispersed rapidly at late times; I review some physical processes that can induce such rapid mass removal in isolated discs in Section 1.2.

1.2 Secular dispersal mechanisms

Observations indicate that PPDs generally persist around their stellar host for ~ 3 Myr (Haisch *et al.*, 2001b; Ribas *et al.*, 2014), although there is order of magnitude intrinsic scatter in this figure (Armitage *et al.*, 2003). The removal of gas from the disc sets a strict timescale on which gas giants can form, and likely influences the chemical composition of other planets (e.g. O'Brien *et al.*, 2018). The low frequency of so-called 'transition discs' (making up $\sim 10\%$ of all discs) that are optically thin in the infrared indicates that the timescale on which a disc is finally dispersed is much shorter than its overall lifetime (i.e. there are two timescales for disc depletion – Skrutskie *et al.*, 1990; Kenyon and Hartmann, 1995; Duvert *et al.*, 2000). Modelling infrared emission from PPDs suggests that discs are commonly depleted rapidly from inside-out during the later stages of disc evolution (Ercolano *et al.*, 2011; Koepferl *et al.*, 2013).

While the focus of this work is the influence of external mechanisms on disc dispersal, understanding the importance of environment requires comparing them with the secular dispersal of a PPD. Debate continues regarding the dominant process that disperses the gaseous component, however in this section I will introduce some relevant physical processes

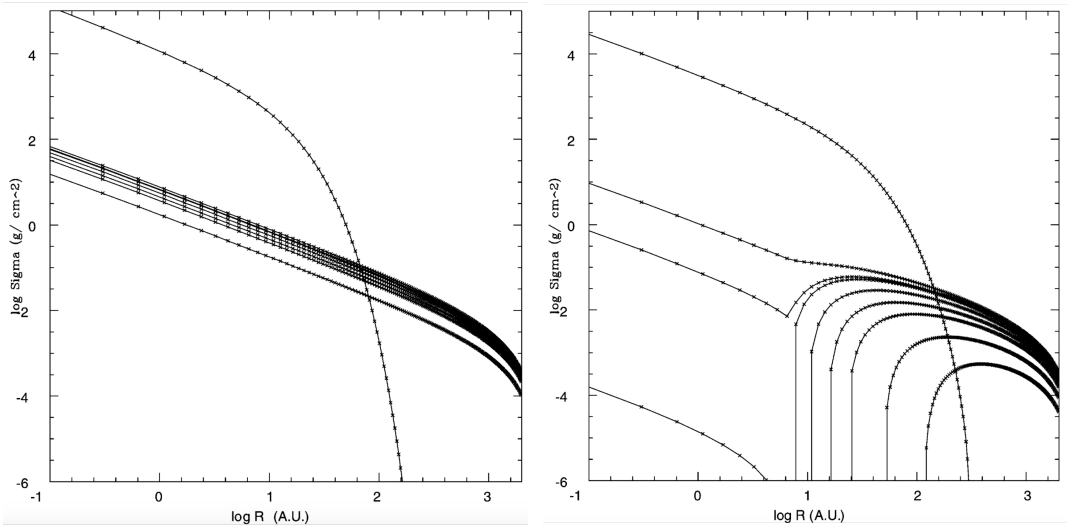

(a) Viscous evolution only (b) Internal photoevaporation

Fig. 1.1 Surface density evolution for a disc subject to viscous evolution as presented by Clarke *et al.* (2001). Each line represents a different time, increasing from top to bottom. The top line is the initial state of the PPD, while the other lines are chosen to be at the later stages of disc evolution. The total timescale shown is dependent on the PPD and host star properties (e.g. viscous timescales and photoevaporative mass loss rate – under reasonable assumptions ~ 10 Myr). In figure 1.1a the disc evolves under viscous torques only, and is not dispersed rapidly at late times. In figure 1.1b internal photoevaporation is considered. In this case, winds launched close to the critical radius r_g open up a gap in the disc. After this gap has opened, short viscous timescales inwards of this radius leads to rapid clearing of the inner part of the disc in ~ 0.1 Myr.

for a PPD evolving in isolation. These mechanisms are internal photoevaporation, MHD winds and giant planet formation. In general, these processes disperse the disc by creating an inner hole and suppressing the flow of material onto the star to some extent. This scenario is consistent with observations (Ercolano *et al.*, 2011), and additionally they can all give rise to the empirically supported rapid phase of dispersal at the end of the disc lifetime (Pollack *et al.*, 1996; Clarke *et al.*, 2001; Armitage *et al.*, 2013). Whether giant planet formation occurs in a PPD (or whether a disc is rapidly dispersed by internal or external processes) will also have an influence on the nature of the ultimate exoplanet architecture and chemistry.

1.2.1 Internal photoevaporation

One of the primary mechanisms responsible for disc depletion is photoevaporation. In this context, photoevaporation is the depletion of a PPD due to irradiation by FUV photons (with energies 6 eV$< h\nu <$ 13.6 eV), EUV photons (13 eV$< h\nu <$ 0.1 keV) and X-ray

(0.1 keV$< h\nu$). 'Internal' refers to the role of the host star in irradiating the disc. Models of photoevaporative winds have a long history, partly motivated to explain long-lived ultra compact HII regions around massive stars that are replenished by the photoevaporating disc material (Hollenbach *et al.*, 1994). Ionising radiation from the central star heats (and ionises) the surface layer of the disc such that outside some critical radius r_g this ionised layer becomes unbound. The sound speed equals the orbital velocity at:

$$r_g = \frac{Gm_*}{c_{\rm s}^2} \sim 7 \left(\frac{m_*}{1 M_\odot} \right) \text{ au}, \tag{1.7}$$

where the last approximation uses the temperature of photoionised gas ($\sim 10^4$ K, yielding $c_{\rm s} \sim 10$ km/s). Particles with velocities equal to the sound speed are unbound at radii $r > 2r_g$, while for $r \ll r_g$ the ionised atmosphere is approximately in hydrostatic equilibrium. Hollenbach *et al.* (1994) define a 'weak stellar wind' model, referring to stellar winds for which the associated ram pressure is less than the pressure from the disc atmosphere at the base of the ionised atmosphere at $r \sim r_g$. This regime is appropriate for stars of mass $m_* \lesssim 20 M_\odot$. In this case photoevaporation is dominated by the diffuse EUV photons emitted by recombination in the ionised atmosphere at $r \sim r_g$. The photoevaporative mass loss is:

$$\dot{M}_{\rm wind,int.} = 2 m_{\rm H} v \int_{r_g}^{\infty} 2\pi r n_0(r) \, {\rm d}r, \tag{1.8}$$

where $m_{\rm H}$ is the atomic mass of hydrogen, $v \approx c_{\rm s} \approx 10$ km/s is the velocity of the flow, and $n_0(r)$ is the number density of hydrogen at the base of the ionised atmosphere. In its most general form, the full self-consistent solution is achieved by solving the eigenvalue problem arising from the contribution of diffuse ionising fluxes from recombination to give n_0. In this way, Hollenbach *et al.* (1994) find that for a disc with an outer radius $r_{\rm d} > r_g$ (and an inner radius within r_g), the photoevaporative mass loss rate is:

$$\dot{M}_{\rm wind,int.} \approx 4.1 \times 10^{-10} \left(\frac{\Phi_{\rm i}}{10^{41} \, {\rm s}^{-1}} \right)^{1/2} \left(\frac{m_*}{1 M_\odot} \right)^{1/2} , M_\odot \, {\rm yr}^{-1}, \tag{1.9}$$

where $\Phi_{\rm i}$ is the EUV photon count from the host star. Later hydrodynamical simulations have been compared with the analytic models (Liffman, 2003; Font *et al.*, 2004), modifying the numerical value of r_g and the resultant mass loss rate by a factor of a few. However, the qualitative picture of internal photoevaporation remains similar.

Later models coupled the viscous evolution of the PPD to the influence of a photoevaporative wind driven by the central star (Clarke *et al.*, 2001; Armitage *et al.*, 2003; Ruden, 2004; Takeuchi *et al.*, 2005; Jones *et al.*, 2012; Rosotti *et al.*, 2017). Assuming a reasonable

ionising flux (photon counts of $\Phi_{\rm i} \sim 10^{41}$–$10^{44}$ s^{-1} – Alexander *et al.*, 2005), these models find that photoevaporation initially has a negligible influence on disc evolution. However, once a disc is sufficiently depleted, the accretion rate approaches the photoevaporative mass loss rate and a gap opens up close to r_g due to the thermal wind. This rapidly leads to the accretion of material inside of this radius which has a short viscous timescale and is no longer replenished by material from outer regions (inside-out clearing). The influence of internal photoevaporation compared to solely viscous evolution is illustrated in figure 1.1 (taken from Clarke *et al.*, 2001). As the inner disc clears, it becomes optically thin to Lyman continuum photons such that this mechanism can also explain the rapid clearing of outer parts of the disc (Alexander *et al.*, 2006a). The predicted lifetime and eventual rapid dispersal of the PPD in this model is broadly consistent with observations (Alexander *et al.*, 2006b).

I have so far neglected discussion regarding the type of radiation that dominates mass loss in photoevaporating PPDs since the qualitative behaviour is similar. However, the studies that I have discussed above consider the EUV photons as the dominant driver of photoevaporative mass loss (e.g. Hollenbach *et al.*, 1994). Subsequent studies considered X-ray (Ercolano *et al.*, 2008, 2009; Owen *et al.*, 2010) and FUV (Gorti and Hollenbach, 2009; Gorti *et al.*, 2009, 2015) induced photoevaporation. Since X-rays and FUV photons penetrate a much higher column density of neutral gas than EUV photons, they heat gas and drive winds at larger radii, causing photoevaporation at tens of au from the central star. Similarly, since higher mass loss rates ($\sim 10^{-8} M_\odot$ yr^{-1}) are expected when all X-rays and FUV photons are considered, this implies higher masses for transition discs. This is not supported by observations (Andrews and Williams, 2007; Cieza *et al.*, 2008, 2010) and this loss rate may therefore be an overestimate. Later studies have demonstrated that the photoevaporation rate is dependent on the spectrum of emitted photon energies as well as the disc metallicity (Ercolano and Clarke, 2010; Nakatani *et al.*, 2018a,b). Ultimately, the relative importance of photons of different energies is still under debate, and is likely to depend on the properties of the disc and its host star.

1.2.2 Magnetohydrodynamic winds

Magnetic fields are believed to play an important role in angular momentum transport and winds in accretion discs in a variety of astrophysical contexts. They represent a mechanism by which free energy can flow throughout a disc due to differential rotation, and can cause turbulent heating and outflows. Unravelling their evolution and influence is a hugely complicated problem, involving chemistry, ionisation physics and non-ideal MHD effects. Balbus (2011) presents a useful overview of the equations that describe the MHD fluid flows in the context of PPDs, and I review the fundamental concepts here. The velocity $\boldsymbol{v}_s$ of species s of

density ρ_s obeys mass conservation such that:

$$\frac{\partial \rho_s}{\partial t} + \boldsymbol{\nabla} \cdot \rho_s \boldsymbol{v}_s = 0. \tag{1.10}$$

For neutral particles (with subscripts dropped for convenience), the dynamical equation is

$$\rho \frac{\partial \boldsymbol{v}}{\partial t} + \rho \left(\boldsymbol{v} \cdot \boldsymbol{\nabla} \right) \boldsymbol{v} = -\boldsymbol{\nabla} P - \rho \boldsymbol{\nabla} \Phi - \boldsymbol{p}_{ni} - \boldsymbol{p}_{ne}, \tag{1.11}$$

where P is the pressure of the neutral particles, Φ is the gravitational potential and $\boldsymbol{p}_{ni}$, $\boldsymbol{p}_{ne}$ are the momentum exchanges between neutral particles and ions or electrons respectively. This momentum exchange is dependent on the density, cross section and relative velocities of particles. For example:

$$\boldsymbol{p}_{ni} = \rho \rho_i \gamma (\boldsymbol{v} - \boldsymbol{v}_i) \tag{1.12}$$

where

$$\gamma \equiv \frac{\langle w_{ni} \sigma_{ni} \rangle}{m_i + m_n} \tag{1.13}$$

is the drag coefficient, σ_{ni} is the effective cross section for neutral-ion collisions, and w_{ni} is the relative velocity between the two species. Typical values for $\langle w_{ni} \sigma_{ni} \rangle$ and $\langle w_{ne} \sigma_{ne} \rangle$ are calculated by Draine *et al.* (1983). In astrophysical contexts, $\gamma \approx 3 \times 10^{13}$ cm^3 s^{-1} is typical (the cross-section is inversely proportional to the relative particle velocity – see also Osterbrock, 1961). Rewriting a version of equation 1.11 for ions and electrons, and considering a weakly ionised gas where the density of charged species is low, then the Lorentz force and the momentum exchange between species dominates. Ignoring the rest of the terms, this yields:

$$\frac{\boldsymbol{J}}{c} \times \boldsymbol{B} = \boldsymbol{p}_{in} + \boldsymbol{p}_{en} \approx \boldsymbol{p}_{in} \tag{1.14}$$

where c is the speed of light, momentum exchange is conserved (i.e. $\boldsymbol{p}_{in} = -\boldsymbol{p}_{ni}$). The current density is

$$\boldsymbol{J} \equiv e n_e \left(\boldsymbol{v}_i - \boldsymbol{v}_e \right), \tag{1.15}$$

where e is the proton charge and J is the current density. Substituting equation 1.14 into equation 1.11, it is clear that collisional coupling means that the neutral particles are effectively subject to the magnetic Lorentz force in the same manner as charged particles. In fact, considering the equation of motion for electrons and invoking Ohm's law and Faraday's law, it can be shown that equation 1.11 becomes:

$$\rho \frac{\partial \boldsymbol{v}}{\partial t} + \rho \left(\boldsymbol{v} \cdot \boldsymbol{\nabla} \right) \boldsymbol{v} = -\boldsymbol{\nabla} P - \rho \boldsymbol{\nabla} \Phi + \frac{1}{4\pi} \left(\boldsymbol{\nabla} \times \boldsymbol{B} \right) \times \boldsymbol{B}. \tag{1.16}$$

Considering the force balance equation for electrons, the electric field $\boldsymbol{E}$ in the induction equation $\partial \boldsymbol{B}/\partial t = -\boldsymbol{\nabla} \times \boldsymbol{E}$ can be similarly decomposed. The contributions include magnetic induction, electron collisions (Ohmic resistivity), the influence of a transverse magnetic field (Hall effect) and neutral–ion collisions (ambipolar diffusion). The full induction equation is therefore:

$$\frac{\partial \boldsymbol{B}}{\partial t} = \boldsymbol{\nabla} \times \left(\underbrace{\boldsymbol{v} \times \boldsymbol{B}}_{\text{Induction}} + \underbrace{\frac{c\,(\boldsymbol{\nabla} \times \boldsymbol{B}) \times \boldsymbol{B}}{4\pi e n_e}}_{\text{Hall effect}} + \underbrace{\frac{[(\boldsymbol{\nabla} \times \boldsymbol{B}) \times \boldsymbol{B}] \times \boldsymbol{B}}{4\pi\gamma\rho\rho_i}}_{\text{Ambipolar diffusion}} - \underbrace{\eta_{\mathrm{O}} \boldsymbol{\nabla} \times \boldsymbol{B}}_{\text{Ohmic}} \right), \tag{1.17}$$

where (Spitzer, 1962; Krall and Trivelpiece, 1973; Jackson, 1975; Blaes and Balbus, 1994):

$$\eta_{\mathrm{O}} = \frac{c^2}{4\pi\sigma_{\mathrm{cond}}} \approx 234 \left(\frac{n}{n_e} \right) T^{1/2} \ \mathrm{cm}^2 \ \mathrm{s}^{-1} \tag{1.18}$$

is the resistivity for a given conductivity σ_{cond} at temperature T. Equations 1.10, 1.16 and 1.17 govern the evolution of a fluid under the influence of a magnetic field in a general sense.

Equation 1.17 highlights the complexity in understanding the evolution of astrophysical fluids when considering magnetic fields, and the necessity for simplification. The relative contributions of induction, the Hall effect, ambipolar diffusion and Ohmic resistivity are considered in detail by Balbus and Terquem (2001, see Balbus 2011 or Armitage 2011 for a review). Whether each is significant depends on the temperature, density, ionisation fraction and magnetic field strength. In the limit of a weak magnetic field strength and high density, equation 1.17 suggests that the contribution of the Hall effect and ambipolar diffusion is small. If the resistivity η_{O} is also small, then applying mass conservation (equation 1.10), then the induction equation 1.17 simplifies and it is straightforward to show that:

$$\frac{\partial \Phi_B}{\partial t} = \frac{\partial}{\partial t} \int_{\mathscr{S}} \boldsymbol{B} \cdot \mathrm{d}\boldsymbol{A} + \oint_{\mathscr{C}} \boldsymbol{B} \cdot \boldsymbol{v} \times \mathrm{d}\boldsymbol{l} = 0 \tag{1.19}$$

where Φ_B is the magnetic flux through surface $\mathscr{S}$, bounded by curve $\mathscr{C}$ (composed of infinitessimal elements $\mathrm{d}\boldsymbol{A}$ and $\mathrm{d}\boldsymbol{l}$ respectively). Equation 1.19 implies that the magnetic flux through an arbitrary surface moving in the fluid is constant, which corresponds to the 'freezing' of the magnetic field into the fluid element (this is the ideal MHD limit). In this case and under the assumption that

$$\frac{\mathrm{d}\Omega^2}{\mathrm{d}r} < 0, \tag{1.20}$$

(true for Keplerian discs) then a magnetic torque is present between annuli in a disc such that angular momentum is transported outwards and the torque in turn grows; this is the

magnetorotational instability (MRI – see Balbus and Hawley, 1998, for a review). The extent to which MRI influences cool, dense PPDs remains an unanswered question, since it is marginal whether the diffusive influence of non-ideal MHD effects dampen the growth of the instability. A 'dead zone' where MRI is suppressed is expected in the midplane, while MRI may be able to operate close to the central star (for radii $r \lesssim 0.1$ au) and in the surface layers where ionisation is sufficient (Gammie, 1996). However, depending on physical assumptions including the dust properties within a PPD, it is possible that MRI mediated angular momentum transport is insufficient to induce observed accretion rates; ambipolar diffusion can suppress the instability in the rarefied and ionised upper layers of the PPD (Bai and Stone, 2011; Mohanty *et al.*, 2013; Dzyurkevich *et al.*, 2013; Bai and Stone, 2013).

Magnetic fields can also induce accretion by MHD winds due to centrifugal acceleration of gas along magnetic field lines. The theoretical description of winds driven by MHD effects was put forward by Blandford and Payne (1982), who used the influence of magnetic fields primarily to explain angular momentum loss in accretion discs around black holes, as well as the drivers of extended radio jets observed around active galactic nuclei (see also Pudritz and Norman, 1983). This prescription has since been extended to various physical limits, geometries and scaling laws (e.g. Li *et al.*, 1992; Contopoulos and Lovelace, 1994; Sauty and Tsinganos, 1994), although the fundamental principles remain similar. Broadly, these studies consider physical quantities that are conserved along the poloidal field lines. These constants are derived from the continuity and induction equations, as well as the conservation of specific angular momentum and energy. The centrifugal force and the gradient in the toroidal magnetic field balance with the temperature gradient and gravity to dictate the acceleration of gas along the field lines.

To quantify this process in PPDs, Bai and Stone (2013) used stratified shearing box simulations to show that magnetic fields can launch winds from $\sim 2H$ above the midplane, resulting in accretion rates that match observations (a conclusion that is supported by later global simulations – e.g. Gressel *et al.*, 2015). Bai *et al.* (2016) subsequently developed a simplified 1D model (a generalisation of the earlier prescription of Weber and Davis, 1967) for the wind kinematics based on the local simulations that include microphysics. The authors highlight that magnetically driven winds are intrinsically dependent on the ionisation of surface layer gas induced by FUV photons from the central star. Thus, the interplay between photoevaporation and MHD effects is important for disc evolution and dispersal. Broadly, increasing the penetration of FUV photons into the disc surface increases the mass loss in the wind without altering the accretion rate, while increasing the poloidal magnetic field (which is related to the toroidal component – Kudoh and Shibata, 1997) increases the ratio of the accretion rate to the mass loss in the wind.

While further investigation into MHD within PPDs is required, particularly in linking theoretical predictions to observed disc properties, magnetic winds are expected to be a significant driver of their evolution. MHD effects can give rise to the two timescale behaviour characteristic of PPD evolution as in the case of photoevaporation if there is a transition to magnetic wind dominated angular momentum loss over the course of the disc lifetime (Armitage *et al.*, 2013; Bai, 2016). In this paradigm, the timescale for disc dispersal would crucially depend on the magnetic fields in the collapsing primordial gas and the subsequent flux transport throughout the disc, which is in turn related to disc microphysics (Bai and Stone, 2017). MHD winds have also been used to explain the high accretion rate onto HL Tau without invoking a degree of turbulence that would be difficult to reconcile with the observed dust settling (Hasegawa *et al.*, 2017). Fang *et al.* (2018) used observations of forbidden lines in PPDs to trace gas kinematics, which they find to be consistent with magnetic winds driven from disc radii $0.1\,\mathrm{au} \lesssim \mathrm{r} \lesssim 10\,\mathrm{au}$. Future studies may clarify how MHD effects couple with photoevaporation, and how observational signatures can distinguish their relative importance and interplay (Pascucci *et al.*, 2018).

1.2.3 Giant planet formation

The presence of giant planets significantly influences the architecture of planetary systems and allows molecules (particularly volatiles) to be distributed to terrestrial planets in the habitable zone (Chambers and Wetherill, 2001; Horner and Jones, 2012; Grazier, 2016; Agnew *et al.*, 2018). They also represent a significant portion of the total mass of the PPD from which they form, and hence wherever they are found they must have contributed to some degree to the dispersal of their progenitor. Since this work is concerned with the evolution of planet progenitors, I restrict attention here to this latter point. I briefly review the two main models for giant planet formation: core accretion and gravitational instability. We will see that the latter only acts on massive (young) discs, and is therefore not a dispersal mechanism *per se*; it is included here for completeness.

Core accretion

The growth of a giant planet by core accretion begins in the same manner as for terrestrial planets (Safronov and Zvjagina, 1969; Goldreich and Ward, 1973; Pollack *et al.*, 1996). In this scenario, dust grains gradually coagulate into larger particles, and settle towards the midplane as they reach centimetre sizes (see Testi *et al.*, 2014, for a review of dust evolution in PPDs). These particles then aggregate to form planetesimals of kilometre size scales. Early models for the growth of these planetesimals assumed accretion is dominated by pair-wise

collisions, a process that would require long timescales and low dynamical temperatures. In fact, the velocities of planetesimals are sufficiently high to induce significant scattering and orbital excitation such that growth rates are too low (Levison *et al.*, 2010). Instead, pebble (millimetre to centimetre) sized objects are accreted much more easily onto a planetesimal since gas drag reduces the relative velocity as the pebble passes (Johansen and Lacerda, 2010; Ormel and Klahr, 2010). Since a large amount of mass has been found in pebbles in PPDs (e.g. Testi *et al.*, 2003), this mechanism offers an attractive solution to the problems associated with pair-wise growth (e.g. Brauer *et al.*, 2007; Zsom *et al.*, 2010). Interaction between the dust/pebbles and the gas can also lead to instabilities (such as the streaming instability) that induce high concentrations solid material and promote rapid growth (e.g. Youdin and Goodman, 2005; Chiang and Youdin, 2010; Drążkowska and Dullemond, 2014; Squire and Hopkins, 2018).

Once a planet core has reached a sufficient mass, the escape velocity at the surface will be greater than the thermal energy of the surrounding gas and it can accrete an envelope around the solid core. Further accretion is initially regulated by the pressure effects of the existing envelope and the influence of perturbations. However, if a planet is born in proximity to a sufficient reservoir of material then eventually the pressure gradient will be overcome by gravity and the envelope will undergo collapse. In the case of giant planet formation, this leads to increased surface gravity and more accretion, thereby initiating a phase of runaway accretion where the planetary growth rate accelerates. This latter stage is rapid, and the total timescale for Jupiter analogs in the core accretion scenario is expected to be on the order of Myr (Lissauer, 1987), approximately coinciding with the timescale for disc evolution and dispersal.

Gravitational instability

Stars form by the gravitational collapse of material onto a core, and this gravitational instability (GI) has also been proposed as a viable scenario for the formation of giant planets in a sufficiently massive PPD (Kuiper, 1951; Cameron, 1978; Boss, 1997). In this case, planets quickly form on the orbital timescale $\tau_{\text{orb.}} = 2\pi/\Omega$ (~ 1000 yr for material close to the edge of the disc) directly from the collapse of the gaseous disc. The heavy elements in the core are then deposited as the cores accrete material (dust and/or planetesimals) over longer timescales. The threshold at which material in a self-gravitating disc undergoes collapse is

$$Q = \frac{c_{\text{s}}\kappa}{\pi G\Sigma} < 1, \tag{1.21}$$

where κ is the local epicyclic frequency. The value of the Toomre (1964) Q in equation 1.21 is the ratio of pressure and rotation support against collapse versus the influence of self-gravity (Safronov, 1960). For discs that are sufficiently cold (low c_s) or massive (high Σ) fragmentation and massive planet (or brown dwarf) formation proceeds rapidly. Otherwise, planet formation can only proceed by the slower bottom-up core accretion process. As an approximate guide, a PPD is likely to be GI either if it exhibits significant local density fluctuations or has a mass $M \gtrsim 0.1\,m_*$ (Boss, 2002).

Finding observational evidence for PPDs undergoing collapse is challenging both because the process is innately shortlived and because the spiral density waves induced in GI discs can also be explained by massive planets/companions (e.g. Meru *et al.*, 2017). Additionally, GI induced density waves transport angular momentum outwards and mass inwards (Lynden-Bell and Kalnajs, 1972; Durisen *et al.*, 1986). In general this leads to depleted, extended discs as for the viscous transport mechanisms discussed in Section 1.1, although whether an α formulation is appropriate is dependent on the host mass–disc mass ratio (Forgan *et al.*, 2011). For massive discs thats are unstable, variable accretion is expected (e.g. Zhu *et al.*, 2009, 2010; Vorobyov and Basu, 2010), and GI has been suggested as the driver of bursts of high accretion observed in many discs in events named after the first such case, FU Orionis (Herbig, 1977; Stamatellos *et al.*, 2011, 2012). This hypothesis is supported by the finding that FU Orionis discs are generally very massive, with $M \sim 0.05$–$0.5\,M_\odot$ (Cieza *et al.*, 2018). In this case, gravitational stability limits the mass of a PPD at early times, and is a viable mechanism for the formation of the most massive planets on short timescales. However, GI is not a mechanism for disc dispersal since it operates exclusively on massive discs. Therefore, if it is found to contribute significantly to the overall population of giant planets, then this would indicate a reduced importance of giant planet formation as a dispersal mechanism with respect to wind driven mass loss.

1.3 Environment and PPDs

I have so far limited discussion to processes which govern isolated disc evolution. However, stars do not in general form in isolation and spend their first few Myr (during the time they host PPDs) in gravitationally bound clusters or unbound associations (Lada and Lada, 2003; Kruijssen, 2012). In such regions of enhanced stellar density, it is possible that stellar neighbours interact with a PPD, influencing its evolution. Indeed, the outer radii of discs in the sample collected by de Juan Ovelar *et al.* (2012) are reduced at stellar surface densities $\Sigma_{\rm stars} \gtrsim 10^{3.5}$ stars/pc^2. If these interactions reduce the time and mass available for planet formation then exoplanet properties may be a function of the environment a star is born

into. Quantifying the stellar feedback on discs is therefore important in understanding planet formation in general. This is especially true since star formation conditions (and the resultant stellar birth environments) in the solar neighbourhood are not representative of the vast majority of star formation over the history of the universe. Therefore the considerations I outline in this section, and will continue to address throughout this thesis, are necessary if we want to generalise what we learn from local planet formation to the diverse range of observed star forming regions.

In the remainder of this section, I will first introduce two mechanisms by which stellar neighbours can influence disc evolution: tidal encounters (Section 1.3.1) and external photoevaporation (Section 1.3.2). In Section 1.3.3 I will review some relevant issues pertaining to the birth environment of the stellar hosts of PPDs.

1.3.1 Star-disc encounters

In regions of enhanced stellar density and multiplicity, one might expect some fraction of stars to experience a close encounter with their neighbours. If this happens while a PPD is present, then that disc is subject to the gravitational perturbations due to the passing star. This possibility has been considered by numerous investigations that have aimed to assess the degree to which encounters alter PPD evolution. Theoretical works have quantified how the resonances induced throughout a disc drive angular momentum loss and truncation (Goldreich and Tremaine, 1978; Lubow, 1981; Ostriker, 1994; Ogilvie, 2002). More recently, simulations have been applied to investigate the phenomenon. This has included parameter exploration of individual encounters using test particles (Clarke and Pringle, 1993; Hall *et al.*, 1996; Pfalzner *et al.*, 2005a,b; Lestrade *et al.*, 2011; Breslau *et al.*, 2014), statistical investigation of cluster dynamics combined with theoretical results (Olczak *et al.*, 2006; Vincke and Pfalzner, 2016), and hydrodynamical simulations of star cluster formation and disc interactions (Boffin *et al.*, 1998; Watkins *et al.*, 1998a,b; Bate, 2012). Some studies have even fully simulated the hydrodynamic evolution of PPDs evolving in a clustered environment for timescales long enough to investigate the influence of encounters (Rosotti *et al.*, 2014; Bate, 2018), however it is not presently practicable to use such computationally expensive simulations to perform parameter space exploration or even evolve a single simulation for ~ 10 Myr.

In general the influence of stellar encounters can be divided into two types: encounters within stellar multiple systems (including binaries) and encounters with neighbouring stars that are unbound. For convenience, I will label these type I and type II tidal encounters respectively. Type I can be interpreted as a process that contributes to global PPD initial conditions, since they primarily influence discs at the beginning of their lifetime. Additionally,

there remains limited evidence that stellar multiplicity is dependent on environment (Correia *et al.*, 2013, but see Duchêne and Kraus 2013 for a review). It follows that the influence of type I encounters on PPDs is practically independent of environment on spatial scales larger than the bound system. In contrast, type II encounters occur throughout the lifetime of the PPD (and indeed the host star) and can therefore be considered a dispersal mechanism. They are also clearly dependent on the environment a star is born into as the frequency of encounters increases with the density of stars and their relative velocities. I will review studies on disc evolution under the influence of each of these two encounter types below.

Type I: Encounters in stellar multiple systems

Around half of all stars are believed to form in stellar multiple systems (Raghavan *et al.*, 2010), implying that type I encounters should be frequent. This hypothesis is supported by simulations of star formation and disc evolution presented by Bate (2018), which indicate that early encounters do occur during the decay of higher order stellar multiplicity. However, finding direct observational evidence of a PPD influenced by type I perturbations is challenging since they occur on short $\sim$ 1000 yr timescales, and only the strongest (prograde and/or close) encounters leave clear signatures in the disc (e.g. Muñoz *et al.*, 2015; Cuello *et al.*, 2019). In addition, since stellar multiplicity (and by extension the influence of type I encounters) is nearly independent of environment, comparisons between different disc samples are not helpful in quantifying their influence. However, some individual examples of these encounters have been found in multiple systems. Observations by Cabrit *et al.* (2006) of the extended structure around RW Aurigae have been successfully modelled as spiral arms induced by a binary interaction (Dai *et al.*, 2015). Recently, similar features have been observed in the discs evolving in the triple systems AS 205 and HT Lup (Kurtovic *et al.*, 2018). We might further subdivide these type I encounters into those that occur regularly within a bound multiple system that is stable or quasi-stable, and those single encounters that occur during the chaotic decay of a higher order multiple. I will call these type Ia and Ib respectively. Evidence of the first observed encounter in a presently unbound or marginally bound system (indicating a type Ib or type II interaction) is presented in Chapter 2.

The decay of higher order systems is a chaotic process, thus it is difficult to make general statements about the degree of tidal truncation experienced in such a scenario (a type Ib encounter). Instead, the theoretical treatment of disc evolution in multiple systems is restricted to the case of binary systems (type Ia). Papaloizou and Pringle (1977) calculated the evolution of PPDs under the influence of a torque induced by a close binary companion and found that the perturbations shorten the disc lifetime to a degree, dependent on the viscous evolution of the disc. In this case, the maximum disc extent is always within the

Roche lobe (see also Paczynski, 1977; Armitage *et al.*, 1999). Daemgen *et al.* (2013) found lower accretion rates for tighter binary separations in Chamaeleon I, implying reduced disc masses. This indicates that binary interaction indeed shortens the PPD lifetime. Additionally, comparisons to discs around binaries in the Orion Nebula Cluster (ONC – Daemgen *et al.*, 2012) led the authors to conclude that the effect of binaries on PPD evolution is independent of environment. To fully quantify the influence of both binaries and chaotic higher order systems, a robust statistical understanding of primordial stellar multiplicity and star formation processes is required. Either further full hydrodynamic simulations of star formation in the style of Bate (2018) or physically motivated N-body initial conditions including multiples are likely to be necessary for this purpose.

Type II: Individual encounters

The influence of type II interactions is strongly dependent on the stellar environment, since the density of stars and the dispersion of velocities dictate the timescale on which stars encounter each other. Many studies have used N-body simulations to investigate how many type II encounters occur in a stellar cluster for given initial conditions. For example, Olczak *et al.* (2006) suggest that encounters have a significant influence on up to $\sim 15\%$ of PPDs in the core of the ONC. Other studies have investigated how sub-structure within a young cluster can enhance local densities and therefore encounter rates (e.g. Craig and Krumholz, 2013). In an environment with fixed properties the frequency of type II encounters can also be written analytically. I will refer to the differential encounter rate multiple times in the following chapters and I review relevant equations here. Following Ostriker (1994, see also Binney and Tremaine 1987), the differential encounter rate $\mathrm{d}\mathscr{E}$ can be expressed in terms of the impact parameter b. We consider a disc perturbed by a star with mass M_2 with relative velocity $\boldsymbol{v}_\infty$ in the limit of large separation (and $v_\infty \equiv |\boldsymbol{v}_\infty|$). The region is assumed to have some effective stellar density n_{eff}, a stellar initial mass function (IMF) ξ and the distribution of v_∞ of neighbours relative to a given star is $g(v_\infty)$. Then the differential encounter rate can be written:

$$\mathrm{d}\mathscr{E} = 2\pi b v_\infty n_{\mathrm{eff}} g(v_\infty) \xi(M_2)\, \mathrm{d}b\, \mathrm{d}v_\infty\, \mathrm{d}M_2 \tag{1.22}$$

The impact factor can in turn be related to the closest approach distance x_{min}:

$$b^2 = x_{\mathrm{min}}^2 \left(1 + \frac{2GM_{\mathrm{tot}}}{v_\infty^2 x_{\mathrm{min}}}\right), \tag{1.23}$$

where $M_{\mathrm{tot}} \equiv M_1 + M_2$ is the total mass of the two stars (M_1 is the mass of the host star). For simplicity, we consider a cluster with a Maxwellian velocity distribution, with one

dimensional velocity dispersion σ_v, which yields:

$$g(v_\infty) = \frac{4\pi v_\infty^2}{(4\pi\sigma_v^2)^{3/2}} \exp\left(-\frac{v_\infty^2}{4\sigma_v^2}\right). \tag{1.24}$$

We define $V^2 \equiv v_\infty^2/4\sigma_v^2$, then the differential encounter rate for a star of mass M_1 is

$$\mathrm{d}\mathscr{E} = \eta(x_{\min}, V^2, M_2; M_1)\,\mathrm{d}x_{\min}\,\mathrm{d}V^2\,\mathrm{d}M_2, \tag{1.25}$$

where

$$\eta \equiv \frac{2\sqrt{\pi}GM_{\rm tot}n_{\rm eff}}{\sigma_v}\left(1+\frac{4\sigma_v^2 x_{\min}V^2}{GM_{\rm tot}}\right)\exp(-V^2)\xi(M_2). \tag{1.26}$$

In the case that we are considering a cluster comprised of stars with a single mass $\bar{m}_*$, then the IMF becomes a Dirac delta-function $\xi(m_*) = \delta(m_* - \bar{m}_*)$.

A prescription for the influence of a given encounter is required to use equation 1.25 in quantifying the influence of type II encounters. Such a prescription has been approached analytically (Goldreich and Tremaine, 1979; Lubow, 1981; Ostriker *et al.*, 1992; Ostriker, 1994) and using *N*-body simulations to model close encounters (Clarke and Pringle, 1993; Hall *et al.*, 1996; Pfalzner *et al.*, 2005b,a; Breslau *et al.*, 2014). The problem with the analytic approach is that it is not possible to treat the closest (and most damaging) encounters with a linearised theory, and so far no adequate comparisons have been made with simulations (hydrodynamic or *N*-body – see Chapter 3). The computational approach suffers from a large parameter space that is necessary for the range of encounters experienced by stars evolving in clusters. While the numerical studies have yielded prescriptions for the truncation radius and/or mass loss, this is usually achieved by fixing some combination of the trajectory eccentricity, mass ratio of the stars and the disc orientation. In particular, studies that apply these prescriptions often assume that the encounter is always prograde and parabolic (e.g. Olczak *et al.*, 2006; Pfalzner *et al.*, 2006), which have the greatest tidal influence on a PPD (e.g. Clarke and Pringle, 1993; Ostriker, 1994). These issues are addressed in Chapter 4.

1.3.2 External photoevaporation

Similarly to internal photoevaporation, external photoevaporation is a process by which PPDs can become dispersed by high energy photons that heat the disc and drive thermal winds. The difference is the source of these photons, with external photoevaporation referring to heating sources that are neighbouring massive stars as opposed to the PPD host star. The first evidence that external photoevaporation occurs were the observations of 'proplyds'

close to θ^1 Ori C in the ONC, exposed to an FUV flux $F_{\rm FUV} \sim 5 \cdot 10^4\, G_0$[1] (O'Dell *et al.*, 1993; O'Dell and Wen, 1994). These proplyds are cometary-like structures that are strongly irradiated by an ionising source; the ionisation front in this context is what gives rise to their characteristic shape (see Johnstone *et al.*, 1998). More recently, proplyds have been found at much more moderate $F_{\rm FUV} \lesssim 3000\, G_0$ (Kim *et al.*, 2016). Additionally, the absence of a proplyd only indicates that the ionisation front (the location outside which Lyman continuum photons ionise the gas) is not visible, and does not imply mass loss is not being induced by the incident photons. Haworth *et al.* (2017) found that photoevaporative winds are driven by external irradiation in the extended ($\sim$ 900 au) disc around IM Lup, exposed to $F_{\rm FUV} \lesssim 4\, G_0$ (Cleeves *et al.*, 2016). Additionally, Guarcello *et al.* (2016) found that the fraction of stars with surviving PPDs in the massive Cygnus OB2 association decreases with increasing $F_{\rm FUV}$ in the range 10^3 – $10^4\, G_0$. Taken together, these observations strongly suggest that PPD evolution is significantly altered by massive neighbouring stars.

Mass loss due to external photoevaporation proceeds in the form of a thermal wind driven from the edge of the PPD, unlike in the case of internal photoevaporation where winds are launched close to r_g. In a sense this outside-in clearing might be expected to be inefficient at dispersing the disc, since when the disc is depleted down to small radii the potential from the central star is large and mass loss due to the thermal wind decreases. In the absence of viscous torques, this negative feedback influence would effectively limit photoevaporative mass loss at late times. However, disc viscosity speeds up PPD dispersal in two important ways. First of all, disc material at the outer edge (where it can be more effectively photoevaporated) is replenished by viscous expansion. Therefore, if the irradiating flux is sufficient, the outer radius is set by a balance of viscous expansion and photoevaporative mass loss. Secondly, external photoevaporation effectively cuts off the viscous redistribution of mass to the inner parts of the disc where angular momentum transport is rapid. This has the same influence on dispersal as internal photoevaporation, illustrated in figure 1.1, where the inner material is rapidly accreted once the mass reservoir of the outer disc is depleted. Thus, in the absence of a viscous disc evolution model, PPD dispersal timescales due to external photoevaporation will be overestimated.

Johnstone *et al.* (1998) quantified the influence of extreme FUV and EUV flux on an extended PPD (see also Störzer and Hollenbach, 1999). In the case of external photoevaporation, X-ray photons have to penetrate a large column density of neutral gas and will only dominate heating and dictate mass loss if they can dominate ionisation close to the disc edge. Tielens and Hollenbach (1985) calculate that this happens when the distance to the ionising

[1] $1\, G_0 \equiv 1.6 \times 10^{-3}$ erg cm^{-2} s^{-1} is the Habing (1968) unit, the average FUV flux in the solar neighbourhood.

source is:

$$d < 0.1 \sqrt{\frac{L_X}{10^{32}\,\mathrm{erg\,s^{-1}}}}\,\mathrm{pc}, \tag{1.27}$$

where L_X is the X-ray luminosity. In practice this is rarely the case (Lepp and McCray, 1983). Past studies have therefore focused on the contribution of FUV and EUV photons. The nature of the thermal wind depends on the energy of photons that predominantly drive it; I review the two cases below.

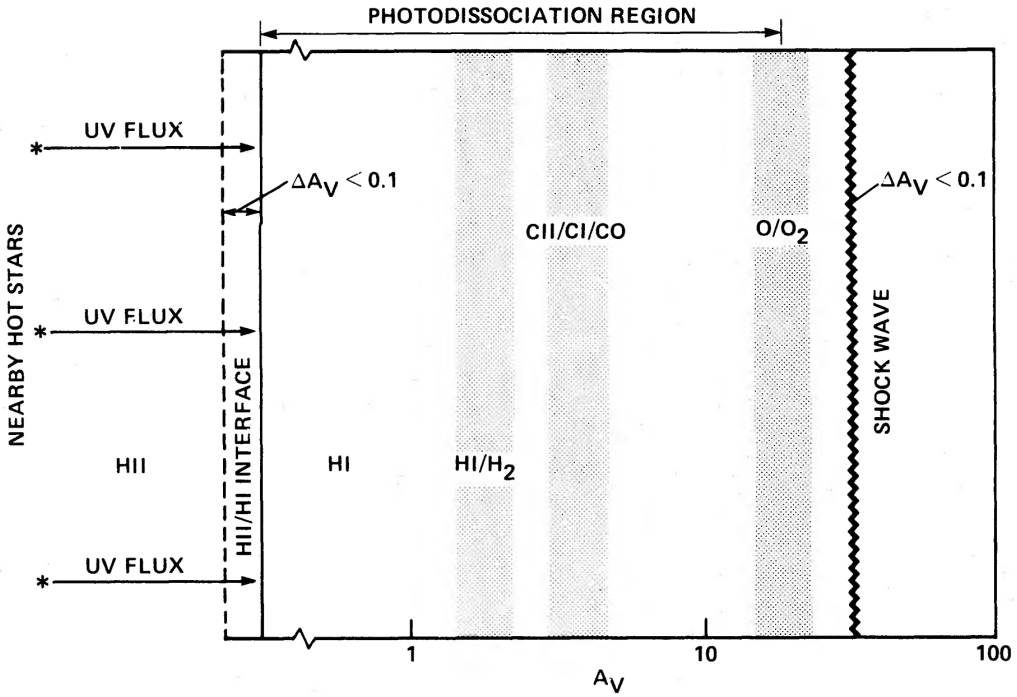

Fig. 1.2 Schematic diagram of a PDR for gas exposed to a strong FUV flux, taken from Tielens and Hollenbach (1985). At low visible extinction A_V, gas is entirely dissociated (atomic) with some singly ionised elements with ionisation energies below the Lyman limit. The PDR region stretches to the transition between O/O_2.

FUV dominated flow

For FUV dominated photoevaporation, the thermal pressure at the surface of the PPD is set by the heating due to FUV photons, which dissociate molecules and create a photodissociation region (PDR – see Tielens and Hollenbach, 1985; Hollenbach and Tielens, 1997). Figure 1.2 is a schematic diagram of a PDR from Tielens and Hollenbach (1985). At the surface of the PDR, temperatures reach up to $T \sim 1000$ K, but the gas remains largely neutral. At $A_V \sim 5$ ionised carbon transitions to atomic carbon and warm CO, while for $A_V \gtrsim 10$ oxygen is also in its molecular form. Many heating mechanisms raise the temperature of the gas throughout

the PDR. Broadly, these are: photoelectric heating via the dust, collisions between dust/gas and electronic (de-)excitation. Cooling is dictated by infrared atomic fine-structure lines and by low energy molecular rotational lines.

The distinct regions through which an FUV driven flow from a supercritical ($r_{\rm d} \gtrsim r_g$) disc passes are indicated schematically in figure 1.3a from Johnstone *et al.* (1998). At the base of the flow, pressure gradients drive winds at velocity v_0 and the density (which is n_0 at the base). The FUV irradiated PDR is effectively a contact discontinuity, hence if the density (velocity) of the flow inside and outside the ionisation front at radius $r_{\rm IF} \gg r_{\rm d}$ are $n_{\rm I}$ ($v_{\rm I}$) and $n_{\rm II}$ ($v_{\rm II}$) respectively, we have:

$$n_{\rm I} v_{\rm I} = n_{\rm II} v_{\rm II} \tag{1.28}$$

and

$$n_{\rm I}\left(v_{\rm I}^2 + c_{\rm s_I}^2\right) = n_{\rm II}\left(v_{\rm II}^2 + c_{\rm s_{II}}^2\right). \tag{1.29}$$

Since $v_{\rm II} \sim c_{\rm s_{II}}$ and the ionised gas ($r > r_{\rm IF}$) has a sound speed $c_{\rm s_{II}} > c_{\rm s_I}$, we have:

$$v_{\rm I} \approx \frac{c_{\rm s_I}^2}{2c_{\rm s_{II}}} < \frac{c_{\rm s_I}}{2}. \tag{1.30}$$

For strong FUV flux, the pressure gradient in the PDR is sufficient to drive supersonic flows from within the PDR. Then equation 1.30 implies that at some radius $r_{\rm s}$, the neutral wind hits a shock front. Inside this radius, the velocity of the flow remains approximately constant (pressure gradients are inefficient at accelerating transonic gas) and the density scales with r^{-2} to conserve mass flux. Outside of this radius, the velocity of the PDR flow scales with r^{-2} at constant density to once again conserve mass flux. At a radius $r_{\rm IF} > r_{\rm s}$ the wind meets an ionisation front, outside which the wind is exposed to Lyman continuum photons that do not penetrate the PDR. In this case, causality implies that FUV flux dictates the photoevaporative mass loss rate.

The mass loss rate $\dot{M}$ from the edge of the disc is dependent on the FUV field strength. Regardless of the mechanism (EUV or FUV), we have:

$$\dot{M}_{\rm wind,ext.} = 4\pi\mathscr{F} r_{\rm d}^2 \mu m_{\rm H} n_0 v_0 \tag{1.31}$$

where $r_{\rm d}$ is the outer radius of the disc, $m_{\rm H}$ is the hydrogen mass, and $\mathscr{F}$ is the fraction of the solid angle subtended by the disc edge. In the case of FUV driven winds, the value of v_0 is dependent on the temperature in the PDR, which is in turn dependent on the FUV flux $F_{\rm FUV}$. However, for $F_{\rm FUV} \gtrsim 10^4\ G_0$ the temperature of the PDR (and therefore the mass loss rate)

is relatively insensitive to $F_{\rm FUV}$, or equivalently the distance d to the FUV source (Tielens and Hollenbach, 1985).

The mass loss rate $\dot{M}_{\rm wind,ext.}$ is dependent on the density at the base of the flow n_0 (which is related to the disc mass), disc outer radius, the mass of the host star and the FUV field strength. Much of the physics of the problem is contained within v_0, the velocity at the base of the flow. Johnstone *et al.* (1998) assumed reasonable values based on the PDR temperature at in the limit of large $F_{\rm FUV} \gtrsim 10^4\,G_0$ and supercritical discs with $r_{\rm d} > r_g$. However, to find a more general solution, full PDR calculations must be coupled with the hydrodynamic properties of the disc. This was the approach of Adams *et al.* (2004), who used the PDR treatment by Kaufman *et al.* (1999) coupled with a solution to the steady-state momentum and continuity equations to calculate the mass loss rates with $r_{\rm d} < r_g$. In fact, that study found that considerable thermal winds are driven down to $r_{\rm d} \sim 0.15\,r_g$. This treatment was developed further by Facchini *et al.* (2016), who applied updated PDR calculations by Bisbas *et al.* (2012). By also calculating the location of r_g self-consistently they found significantly different mass loss rates and greatly expanded the parameter space to more moderate $F_{\rm FUV}$ and larger radii. Additionally, they found that the growth of dust grains within a PPD leads to much higher mass loss rates even down to $F_{\rm FUV} \sim 30\,G_0$ due to a smaller FUV opacity (and therefore greater penetration of FUV photons into the gas). This suggests that photoevaporation plays a much more important role in a wider range of environments than was previously thought. Recently Haworth *et al.* (2018a) presented a full grid of mass loss rates applying this method over a broad parameter space.

EUV dominated flow

Lyman continuum photons can dominate the flow in the limits of small and large distances from an ionising source. If the number of incident EUV photons is sufficiently large, the ionisation front lies close to the edge of the disc and the subsonic shell dominates the column density (McCullough *et al.*, 1995). In this case, the radius of the shock front $r_{\rm s}$ lies close to the edge of the disc, and in the limit $r_{\rm IF} \lesssim 2.5 r_{\rm d}$ the radius of the shock front would be $r_{\rm s} < r_{\rm d}$. Physically, this suppresses the shock; the wind is launched at a subsonic velocity and mass loss is dictated by the EUV photons that drive supersonic winds outside $r_{\rm IF}$. Similarly, if the FUV flux is low such that the PDR region is sufficiently thin, then the pressure gradient is small and the associated flow remains subsonic, while the gas is approximately constant density along the streamlines. Once again, the mass loss rate in this scenario is dictated by the supersonic wind at the ionisation front. Hence, EUV dominates the flow in the close and distant regimes. The exact range of distances is dependent on the stellar mass of that source, but in general EUV driven mass loss is expected for distances $d \ll 0.1$ pc from a massive star

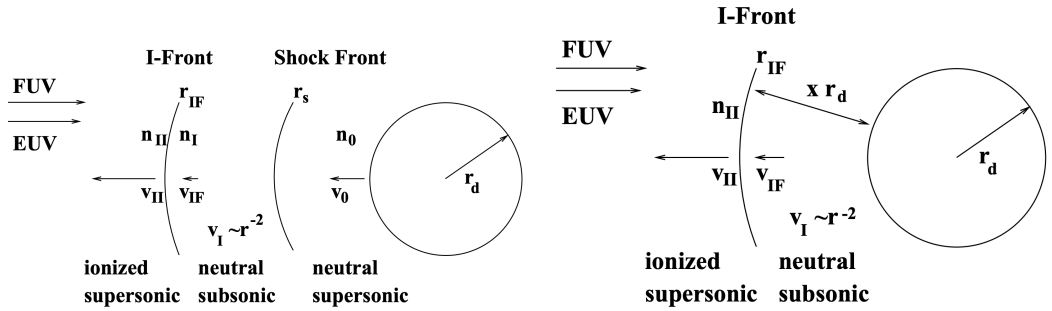

(a) FUV dominated flow (b) EUV dominated flow

Fig. 1.3 Schematic diagrams from Johnstone *et al.* (1998) showing the distinct regions passed through by FUV dominated (figure 1.3a) and EUV dominated (figure 1.3b) photoevaporative flows from the outer edge of an externally irradiated PPD in the supercritical regime.

(see Johnstone *et al.*, 1998, and Chapter 5). In both the distant and close regimes the flow is characterised by a neutral, subsonic wind from the edge of the disc, as shown in figure 1.3b.

1.3.3 Star formation environments

To understand the relative importance of the environment for disc evolution, not only must the influence of neighbours on a PPD be quantified, but also the range of stellar birth environments that physically exist. Scally and Clarke (2001) find that type II encounters are likely to be less efficient at dispersing PPDs than external photoevaporation in the case of the ONC. However, the literature presently lacks comparisons between type II encounters and photoevaporation in a general sense. Fatuzzo and Adams (2008) assumed a canonical density profile within stellar clusters and combined it with the observed distribution of the total number cluster members N_c in the solar neighbourhood (assuming $N_c < 10^5$, and using the cluster sample compiled by Lada and Lada, 2003) to estimate the influence of photoevaporation over all stars. However, specific star formation environments were not considered in that study; modelling individual young stellar populations is necessary to compare with observations and test the theory (see Chapter 5). Additionally, the expected environment distribution for PPDs has not yet been linked to star formation theory (see Chapter 7).

Star formation is a broad topic spanning galactic down to stellar spatial scales. It is governed by the evolution of self gravity, magnetic fields and turbulence in a primordial giant molecular cloud (GMC – see reviews by Shu *et al.*, 1987; McKee and Ostriker, 2007; Krumholz, 2014). The physics of this process is largely tangential to the evolution of PPDs; however, of interest here are the initial conditions of stars that result from the collapse of the

primordial gas. In particular, the local stellar density is important in quantifying the influence of tidal encounters, while the total mass of the cluster or association is indicative of the most massive neighbouring stars (and corresponding FUV luminosity). Finally, the period during which stars and gas coexist within a region (the embedded phase) is important since the gas contributes to the gravitational potential (increasing the overall density) and causes extinction (reducing the FUV flux). Ultimately, these properties are determined by the GMCs that are the progenitors of clusters and associations.

It is now understood that the properties of GMCs are variable depending on the galactic scale ISM properties (e.g. Longmore *et al.*, 2014; Adamo *et al.*, 2015; Reina-Campos and Kruijssen, 2017). Recent studies have found that the density threshold required for star formation to proceed is at least an order of magnitude higher in the central 250 pc in galactocentric radius (the central molecular zone, CMZ) than in the solar neighbourhood (Longmore *et al.*, 2013; Ginsburg *et al.*, 2018). Given that at higher densities, star-disc encounters are more frequent and FUV fields are stronger, we would expect PPD lifetimes to be reduced in the CMZ with respect to the Galactic disc. Indeed, preliminary studies into the PPD population towards the CMZ indicate low disc survival fractions in young stellar populations (Stolte *et al.*, 2010, 2015). Below I will briefly review some considerations in quantifying the environments of PPDs; I present a quantative approach in Chapter 7.

Density distribution

A density continuum well describes the distribution of primordial gas (Vazquez-Semadeni, 1994; Padoan and Nordlund, 2002; Hill *et al.*, 2012) and stars (Bressert *et al.*, 2010; Kruijssen, 2012). The distribution can be understood by considering a turbulent velocity field within a GMC that is supersonic beyond some length scale. The turbulence on these length scales can be understood as many independent interactions that operate to compress or rarify the local gas density. This naturally gives rise to a lognormal density distribution that is scale free above the minimum length-scale upon which turbulent velocities are supersonic (Vazquez-Semadeni, 1994; Passot and Vázquez-Semadeni, 1998). This principle is borne out by numerical simulations of turbulent star formation (Nordlund and Padoan, 1999; Klessen, 2000; Ostriker *et al.*, 2001; Li and Nakamura, 2004). The overall distribution of gas density is therefore quantifiable by understanding the mean density at the scale of interest. The corresponding stellar density is then dependent on the star formation efficiency (SFE), which is a function of the local gas overdensity (e.g. Krumholz and McKee, 2005; Kruijssen, 2012). Thus, the stellar density distribution can be related to the average primordial gas density on a given spatial scale.

Cluster mass distribution

The word 'cluster' in this context requires discussion, since it strictly refers to a gravitationally bound group of stars, while groups of stars that are unbound are referred to as 'associations'. However, since disc evolution occurs on relatively short timescales compared to the dynamical evolution of a stellar population (~ 100 Myr for typical open clusters), the distinction between bound and unbound groups in this context is of secondary importance. I will therefore generally refer to stellar clusters throughout this work, where this is understood to refer to the initial group of stellar objects irrespective of their dynamical state.

As discussed above, stars form over a continuum of densities such that any definition of a group of stars is to some extent arbitrary; however, there are physical limits on the sizes and masses of observed GMCs and it follows that there are also limits on the minimum and maximum number of local stellar members. Star formation physics governs the distribution of the number of associated members N_c (or cluster mass M_c). Reina-Campos and Kruijssen (2017) quantified the maximum M_c expected as a function of the galactic scale primordial gas properties by considering the maximum length on which that gas is unstable to perturbations (which is the Toomre, 1964, length). Recently, Trujillo-Gomez, Reina-Campos and Kruijssen (in prep.) have quantified the bottom of the cluster formation hierarchy by considering the limit at which high SFE leads to merging of lower mass stellar groups. Between these upper and lower limits, the initial cluster mass function (ICMF) is determined by the (scale-free) fractal collapse of molecular clouds, giving rise to a power law with an index $\beta \approx 2$ (Elmegreen and Falgarone, 1996; Guszejnov *et al.*, 2018). Thus, both the stellar density distribution and the ICMF can be quantified to understand the environmental conditions experienced by young stars and their PPDs.

Embedded phase

Since star formation across a cluster (or GMC) proceeds on a similar timescale to PPD evolution, it is necessary to consider the epoch during which primordial gas coexists with the stars, called the 'embedded phase'. The primordial gas in young clusters could influence disc evolution by increasing the gravitational potential (and stellar densities), causing extinction of photons (reducing incident EUV or FUV flux), and ram pressure stripping or accretion. The degree to which these mechanisms influence PPD populations is poorly constrained, since numerically calculating the evolution in a full hydrodynamic simulation is expensive (although see Bate, 2018).

The evolution of gas in a GMC during the star formation epoch remains a broad and challenging problem. During the embedded phase, where gas coexists with massive stars,

radiative feedback gives rise to HII regions that can expand and clear out large regions of gas. Some numerical studies have found this expulsion mechanism is efficient, and gas is lost in Myr timescales (e.g. Walch *et al.*, 2012; Colín *et al.*, 2013; Ali *et al.*, 2018). Others have found that accretion flows and high escape velocities can make the feedback less efficient (Matzner, 2002; Dale *et al.*, 2005; Dale and Bonnell, 2011). In the latter case, gas may persist until a supernova injects it with sufficient momentum to drive expulsion (Pelupessy and Portegies Zwart, 2012; Walch and Naab, 2015). Ultimately, the evolution of the embedded phase is likely to be sensitive to the properties of the primordial GMC.

1.4 Dissertation overview

In the following chapters, I will discuss issues pertaining to the role of external influences in the evolution of protoplanetary discs. I will begin in Chapter 2 by reviewing the evidence for the first example of a historic (type Ib) encounter between HV Tau C and DO Tau, which I suggest were initially part of a quadruple multiple system.

In Chapter 3, I build on the linearised theory of angular momentum loss in discs as a result of distant tidal encounters, additionally comparing the theory to N-body and SPH simulation results in two and three dimensions. I use these predictions to quantify the influence of many distant type II encounters in clustered environments.

I develop a complete prescription for the influence of close encounters on PPD radius in Chapter 4. This includes a parameter space exploration of the encounter eccentricity, ratio of stellar masses and closest approach distance. Subsequently, I implement this prescription into a *Monte Carlo* model and make further statistical arguments to draw conclusions regarding the environmental conditions where tidal encounters are significant.

Type II encounters are compared with the influence of external photoevaporation in Chapter 5. To achieve this, I quantify the destruction timescale of an externally irradiated, viscously evolving PPD as a function of FUV flux. By using the observed properties of young stellar clusters I calculate the density and flux throughout real regions. The timescales for PPD depletion by tidal encounters and external photoevaporation can then be compared across these regions.

Chapter 6 incorporates external photoevaporation into a full dynamical model for the specific case of the massive Cygnus OB2 association. I use the viscous disc model with FUV induced mass loss to calculate the evolution of the PPD population to reproduce the surviving disc fractions found by (Guarcello *et al.*, 2016). I apply my models to make predictions regarding signatures of photoevaporation in the region.

I illustrate how future studies may be able to relate the findings presented in the above chapters to a more general distribution of stellar birth environments as a function of galactic-scale star formation in Chapter 7. This provides context for the evidence I discuss throughout this work for externally induced disc dispersal locally, since regions where dispersal mechanisms are efficient are more frequent in certain spatial and temporal locations throughout the universe. I draw conclusions about the importance of understanding externally induced disc dispersal, and indicate how future studies may approach observationally testing and quantifying planet formation processes in light of these findings.

Chapter 2

A historic type Ib encounter: HV and DO Tau

This chapter is based on Winter *et al.* (2018a), for which I ran the simulations, performed the analysis and wrote the majority of the text.

2.1 Introduction

In Chapter 1, I introduce the distinction between type I star-disc encounters that occur during the evolution of multiple systems independently of the cluster environment, and type II encounters between individual stars that are dependent on the local stellar density. All previous studies that have found observational signatures of tidal disruption of a PPD have done so in stellar multiple systems (type I encounters – Dai *et al.*, 2015; Kurtovic *et al.*, 2018). A further distinction exists between encounters that occur frequently in a stable multiple system or binary (type Ia) and during the decay of a multiple system (type Ib). The latter is likely to be observed in a state where the stars are presently unbound, as for type II encounters. This chapter concerns the first evidence of a type Ib encounter, an historic close interaction between the apparently isolated systems HV and DO Tau.

The Taurus star forming region contains almost exclusively young stars of age $\lesssim 3$ Myr and is considered an archetype of low-mass star formation, with a low stellar density and long dynamical timescale (Ballesteros-Paredes *et al.*, 1999). Larson (1995) and Kraus and Hillenbrand (2008) find evidence for hierarchical structure in Taurus on large scales, but not on smaller scales ($\lesssim 0.04$ pc); these small distance scales may be associated with higher order multiplicity. It is hypothesised that structure has been erased by dynamical interactions in this regime. If this sub-structure in Taurus previously existed, then enhanced numbers of

type Ib early close encounters could leave evidence in the form of truncated discs or tidal tails (e.g. RW Aurigae, Cabrit *et al.*, 2006; Dai *et al.*, 2015). Conversely, the low stellar density in Taurus means that type II tidal encounters are extremely rare.

Photometric observations of HV and DO Tau, which have a present day separation of $90.8''$ (0.06 pc), by Howard *et al.* (2013) using the *Photodetector Array Camera and Spectrometer* (PACS) of the *Herschel Space Observatory* were made at 70 μm, 100 μm and 160 μm (figure 2.1). The extended emission from each component, HV and DO, is directed towards the other, with a common envelope or 'bridge' (i.e. emission connecting the two) visible at 160 μm. While imaged at low resolution, the observed structure is reminiscent of tidal tail structures found in simulations of close encounters between disc-hosting stars (Clarke and Pringle, 1993; Muñoz *et al.*, 2015; Cuello *et al.*, 2019).

The following is an investigation of the hypothesis that DO Tau plus the 3 stars comprising HV Tau were originally formed as a bound hierarchical multiple, such that the present morphology of the system results from a close, disc mediated encounter and subsequent ejection of DO Tau from the system (a type Ib encounter). We aim to replicate observations using hydrodynamical modelling to understand the nature of such an interaction including the disc geometry and stellar kinematics.

2.2 Observational constraints

2.2.1 Stellar components

HV Tau is a young triple system in Taurus. A tight, optically bright binary, HV-AB, has projected separation 10 au (Simon *et al.*, 1996), and shares common proper motion with a third star HV Tau C at approximately 550 au separation (Duchêne *et al.*, 2010). The tight binary has an estimated age 2 Myr and a combined mass of $\sim 0.6 M_{\odot}$ (White and Ghez, 2001). The separation of AB could be larger than 10 au due to orbital eccentricity or deprojection, as suggested by a comparatively long orbital period. A mass of $0.5 - 1 M_{\odot}$ is inferred from the CO maps of the edge on disc of HV Tau C (Duchêne *et al.*, 2010). It is observed to be exceptionally red, with a high accretion rate (Woitas and Leinert, 1998; Monin and Bouvier, 2000).

DO Tau is a G star located at a projected distance 1.26×10^4 au (90.8" at 140 pc) west of HV Tau, which has position angle 95.3° relative to DO. Mass and age estimates range between $0.3 M_{\odot}$, 0.16 Myr (Hartigan *et al.*, 1995) and $0.7 M_{\odot}$, 0.6 Myr (Beckwith *et al.*, 1990). The whole system is depicted schematically with the components labelled in figure 2.2.

2.2.2 Disc properties

Kwon *et al.* (2015) used CARMA observations and models to deduce properties of DO Tau. Their models found an outer disc radius of ~ 75 au and consistent values for mass $M_{\rm disc} \approx 0.013 M_{\odot}$, inclination $\sim -33^{\circ}$, and position angle $\sim 90^{\circ}$, following the convention as described by Piétu *et al.* (2007). There remains ambiguity as to which side of the disc is closer to the observer as the quoted negative inclination angle can produce two rotation senses with the same aspect ratio.

HV Tau A and B have no associated infrared excess and therefore do not host a substantial disc, while C has an edge on disc of radius 50 au and mass $\sim 2 \times 10^{-3} M_{\odot}$ (Woitas and Leinert, 1998; Stapelfeldt *et al.*, 2003). Monin and Bouvier (2000) find that the observed disc radius does not depend on wavelength. This suggests the disc has been truncated, as otherwise the grain size-dependent radial drift of dust particles leads to a wavelength-dependent disc extent. To the contrary they note that the ratio of disc size to projected separation between C and close binary AB is $R_{\rm disc}/x_{\rm min} \equiv R_{\rm tidal} \sim 0.1$, where $R_{\rm disc}$ ($= 50$ au) is the outer disc radius, and $x_{\rm min}$ is the closest approach distance. This makes truncation due to tertiary interaction at the current separation is unlikely as a ratio of $R_{\rm tidal} \approx 0.35$ is required if the masses of C and combined AB are equal (Armitage *et al.*, 1999). It remains possible that the orbit of AB is highly eccentric, and that the periastron distance is sufficiently small to cause tidally induced truncation. Alternatively, an historic encounter may have left the disc truncated.

In modelling the disc around HV Tau C, Duchêne *et al.* (2010) find an inclination $\theta_i \approx 80^{\circ}$ and PA of approximately 20°, corresponding to an orientation such that the blue shifted side of the disc is pointing east with the northern side closer to us. The coplanarity of the centre of mass of AB and the disc of C is unlikely as the nearly edge on angle would lead to a very large actual separation. Duchêne *et al.* (2010) also suggest that scattered light images might imply a disc size greater than 50 au, and gas emission alone suggests a radius up to 100 au. A model with temperature profile $T \propto R^{-q}$ is found to fit well with $0.4 < q < 0.6$ and a temperature at 50 au of 15-30 K.

2.2.3 *Herschel*/PACS data

The *Herschel*/PACS survey observations of HV/DO Tau are discussed by Howard *et al.* (2013), and we use that data to produce figure 2.1. At 160 μm the extended emission connects HV and DO in a common envelope. Of particular interest is the 'V-shaped' emission close to HV Tau and the tail to the North-East of DO Tau (see figure 2.2), seen clearly at 100 and 160 μm, which we aim to reproduce as the result of a disc-disc interaction producing two tidal tails.

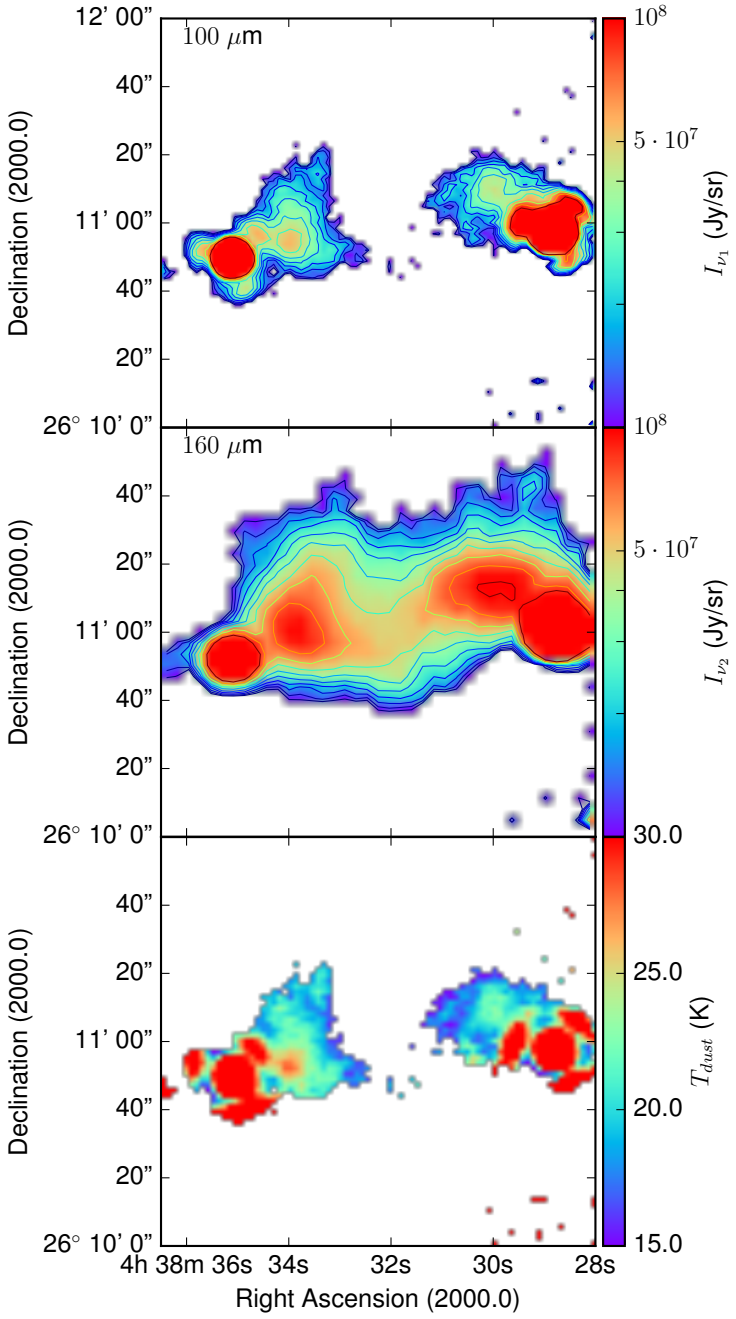

Fig. 2.1 *Herschel* observations of HV/DO Tau (data presented by Howard *et al.*, 2013). The top two panels are the specific intensity in the 100 μm, and 160 μm overlaid with logarithmic contours. Both stars appear to be associated with extended emission. The edge of the image is close to DO Tau (east), which results in excess noise. The bottom panel is the inferred dust temperature distribution assuming that the cloud is optically thin. The point spread function (PSF) in the 100 μm observations results in incorrect temperature estimates in these regions.

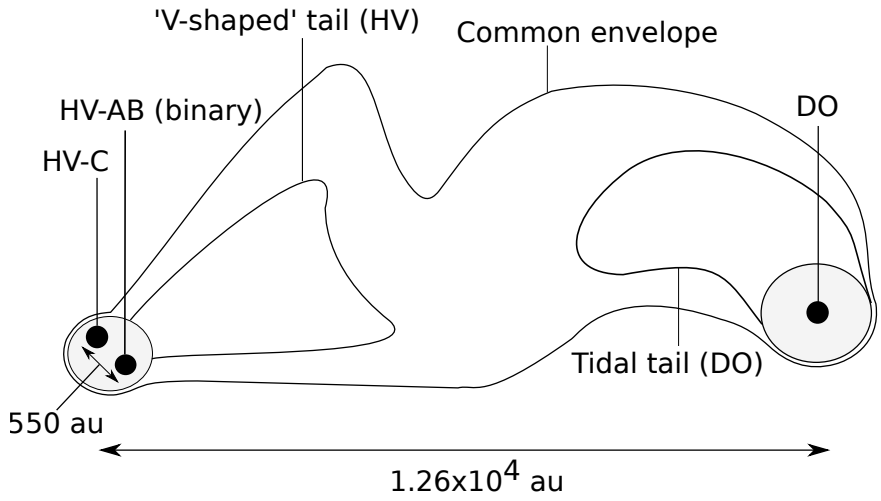

Fig. 2.2 Schematic diagram of the 160 μm dust emission structure visible in figure 2.1 with positions of the stellar components overlaid. The diagram is simplified to highlight the features which we aim to reproduce in our models. HV Tau is a system of three stars, the tight binary HV-AB shown here as one point has a projected separation of $\sim$ 10 au. HV-C has a PA of $\sim 45^\circ$ with respect to HV-AB, and HV has a PA of 95.3° with respect to DO.

Numerous studies have shown that two tails, or a 'bridge' structure, can be produced as a result of prograde or inclined encounters (Toomre and Toomre, 1972; Clarke and Pringle, 1993; Muñoz *et al.*, 2015). Observed morphology is dependent on viewing angle and interaction parameters. Angular momentum transfer between star and disc, and therefore the quantity of circumstellar material ejected during an encounter, is a strong function of the closest approach distance (see Chapter 3). As we will discuss in Section 2.2.4, a collision between the discs is required to produce the observed emission.

2.2.4 Cloud temperature and mass

To compare the mass in the envelope of our model to that of the observations, we reproduce the expected flux at 100 μm and 160 μm using the method outlined by Hildebrand (1983). The specific intensity of radiation at frequency ν across the envelope can be written:

$$I_\nu = \left(1 - e^{-\tau_\nu}\right) B_\nu(T_{\rm dust})$$

where $B_\nu(T_{\rm dust})$ is the Planck disribution at a given dust temperature $T_{\rm dust}$, and τ_ν is the optical depth of the dust. The latter can be rewritten $\tau_\nu = \kappa_\nu \Sigma_{\rm dust}$ if we assume that κ_ν is spatially uniform.

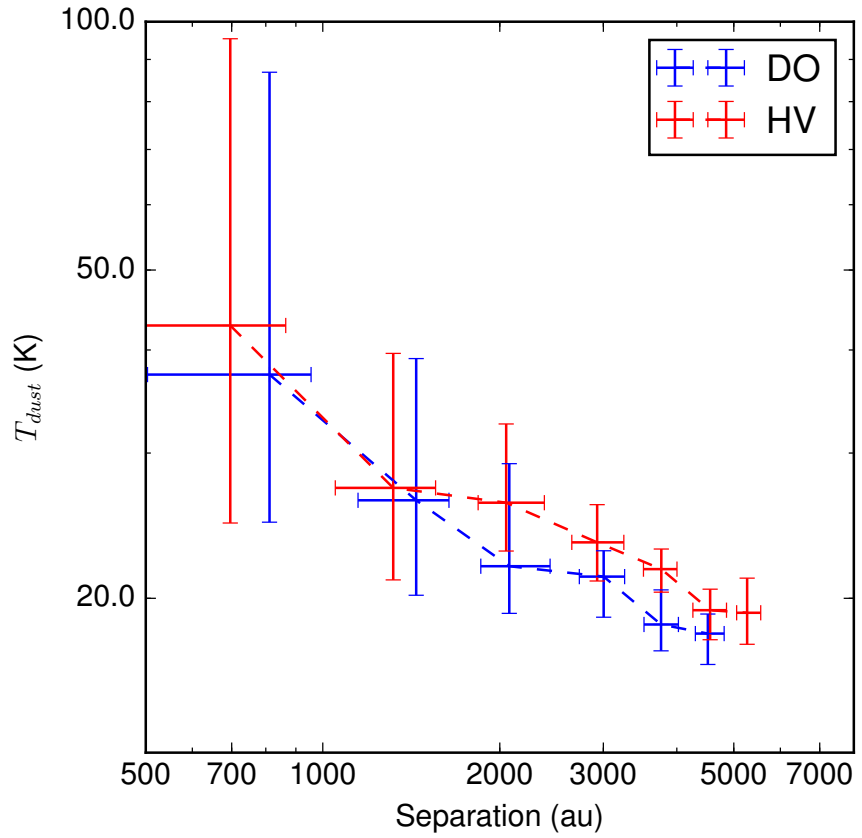

Fig. 2.3 Distribution of the dust temperature of each pixel in figure 2.1 as a function of separation from HV Tau (red) and DO Tau (blue). The error bars are the 1σ range in separation and temperature for a given bin of pixels. Close to the star the optical depth and the PSF result in considerable errors in the determination of temperature.

We estimate the dust mass and temperature by assuming that $\Sigma_{\rm dust}$ is sufficiently small such that the cloud is optically thin ($1-e^{-\tau_\nu} \approx \kappa_\nu \Sigma_{\rm dust}$). This approximation is useful away from the stars (a posteriori we find $\Sigma_{\rm dust} \sim 10^{-4}$ g cm^{-2} in this region), although it is likely to break down locally to HV and DO Tau where $\Sigma_{\rm dust}$ is large. When we come to presenting our models and final mass estimates (Section 2.3.2) we will produce an intensity map from the simulation data for comparison with observations. For the two frequencies $\nu_1 = c/100\ \mu$m, $\nu_2 = c/160\ \mu$m, we use the opacity of spherical dust grains with radius a following a power law distribution $n(a) \propto a^{-3}$ between $a_{\rm min} = 10$ nm and $a_{\rm max} = 1.023$ cm as computed by Tazzari *et al.* (2017).

We integrate the resulting surface brightness I_ν over the normalised transmission spectra for PACS $S_{\nu_{1,2}}$:

$$I_{\nu_{1,2}} = \frac{\int I_\nu(\nu) S_{\nu_{1,2}}(\nu)\,{\rm d}\nu}{\int S_{\nu_{1,2}}(\nu)\,{\rm d}\nu}$$

and hence

$$\frac{I_{\nu_1}}{I_{\nu_2}} \approx \frac{\int B_\nu(\nu;T_{\rm dust})\kappa_\nu(\nu)S_{\nu_1}(\nu)\,{\rm d}\nu}{\int B_\nu(\nu;T_{\rm dust})\kappa_\nu(\nu)S_{\nu_2}(\nu)\,{\rm d}\nu} \cdot \frac{\int S_{\nu_2}(\nu)\,{\rm d}\nu}{\int S_{\nu_1}(\nu)\,{\rm d}\nu}.$$

We invert this expression to estimate the temperature at each pixel, as shown in the bottom panel of figure 2.1. The point spread function (PSF) of the 100 μm observations combined with the greater optical depth result in considerable errors close to the stars. However, we find evidence for a temperature gradient within the cloud (figure 2.3).

Having obtained the temperature in each pixel we can determine the column density of dust that is required to match the observed emission map. We find a dust mass of $\sim 1-5\times10^{-4}\,M_\odot$, depending on assumed values of $T_{\rm dust}$ close to the stars (where the temperature is uncertain). For a dust to gas ratio $\Sigma_{\rm dust}/\Sigma_{\rm gas}=10^{-2}$ this yields an estimate of the total cloud mass of $M_{\rm cloud}\gtrsim 10^{-2}\,M_\odot$. This is greater than the total present day mass of the disc around DO Tau, and suggests that a large fraction of the circumstellar material has been ejected into the ISM (or possibly accreted onto the stellar components) during the hypothesised past encounter. However, if the material originates in discs, the dust to gas ratio could be enhanced (e.g. Ansdell *et al.*, 2016) and our derived cloud mass would be an overestimate.

Considering a distribution of grain sizes appropriate for the ISM lends support for the hypothesis that the cloud material originated in PPDs. We apply opacities calculated from an ISM dust grain distribution $n(a)\propto a^{-3.5}$, and a maximum grain size $a_{\rm max}=1$ μm (see Tazzari *et al.*, 2017). This yields lower temperatures ($\sim$ 10-20 K) throughout the cloud and a dust mass of $\gtrsim 5\times10^{-3}M_\odot$ (or a total cloud mass of $\gtrsim 0.5M_\odot$). This large mass is physically unlikely given the emission is associated with the stellar components of similar mass. Further, we estimate the Jean's mass:

$$M_{\rm J}\approx 2M_\odot\left(\frac{c_{\rm s}}{0.2\,{\rm km/s}}\right)^3\sqrt{\frac{10^3\,{\rm cm^{-3}}}{n_{\rm H}}}$$

where $n_{\rm H}$ is the number density of hydrogen, and the sound speed $c_{\rm s}\approx 0.5$ km/s for a gas with $T=15$ K. If the total mass is 0.5 $M_\odot$ and the volume is $\sim 10^4\times2\cdot10^3\times2\cdot10^3$ au^3 this yields $M_{\rm J}\sim 0.5\,M_\odot\sim M_{\rm cloud}$. The free-fall timescale in this case is $t_{\rm ff}\sim 0.03$ Myr, much smaller than the stellar ages. Such a cloud could be interpreted as residual material from an initial star forming core, however it is unclear whether such material could be supported against gravitational collapse on this timescale. In addition, this interpretation offers no clear mechanism for the formation of the apparently tidal morphology. We therefore focus on the hypothesis that the material between the two systems originated in the dics around HV-C and DO.

2.2.5 Kinematics

The proper motions DO Tau and the (unresolved) binary AB in HV Tau are recorded in *Gaia DR2* (Gaia Collaboration *et al.*, 2016, 2018; Lindegren *et al.*, 2018). DO Tau has a velocity in declination $v_{\delta,\mathrm{DO}} = -21.340 \pm 0.091$ mas/yr and in right ascension $v_{\alpha,\mathrm{DO}} = 6.128 \pm 0.126$ mas/yr. HV Tau AB has $v_{\delta,\mathrm{HV}} = -21.783 \pm 0.171$ mas/yr and in right ascension $v_{\alpha,\mathrm{HV}} = 4.888 \pm 0.126$ mas/yr. This yields $\Delta v_\delta = v_{\delta,\mathrm{DO}} - v_{\delta,\mathrm{HV}} = 0.29 \pm 0.17$ km/s and $\Delta v_\alpha = v_{\alpha,\mathrm{DO}} - v_{\alpha,\mathrm{HV}} = 0.82 \pm 0.24$ km/s. If the velocity vector was anti-parallel to the position vector (i.e. the systems were moving away from each other) we would expect $\Delta v_\delta \gtrsim 0$ and $\Delta v_\alpha < 0$. However, as mentioned the HV-A and -B are unresolved and multiplicity introduces uncertainties into the centre of mass velocity of HV, for which an upper bound is set by the relative velocity of the AB pair (~ 1.5 km/s; Duchêne *et al.*, 2010). Hence the kinematic constraints are consistent with common proper motion of the two systems. Based on the projected separation, the escape velocity is ~ 0.4 km/s, and it is possible that HV and DO Tau are marginally bound or unbound. The one dimensional velocity dispersion in the Taurus region is estimated to be $\sigma_v \sim 2$–4 km/s, although the value is uncertain due to difficulty in establishing membership (Bertout and Genova, 2006; Rivera *et al.*, 2015). The relative proper motion components of HV and DO, which are both considerably less than this, hint at a common origin.

No radial velocity measurement for either star is present in the *Gaia DR2*. DO Tau is estimated to have a radial velocity of 16.04 ± 0.17 km/s by Nguyen *et al.* (2012), however no such estimate exists for HV Tau. Therefore constraints cannot presently be placed on the geometry of the system using the radial velocity differential.

2.2.6 Summary of observational constraints

The following key criteria need to be considered in addressing the possibility of a previous tidal encounter.

- For any given parameters of a proposed fly-by, the time of the interaction should not be older than the age of the stars. Because our hypothesis requires that the stars are coeval, this immediately implies considerable error in the claimed ages. However, 0.16 Myr is the lowest age estimate for any of the stellar components, and so any interaction timescale smaller than this is feasible. Longer timescales may also be reasonable if the age of DO Tau is underestimated.

- Disc orientations should be approximately consistent with the observations, although modelling the evolution of a violent encounter over a long period of time introduces

considerable uncertainty in obtaining present day orientation. Broadly, the disc around HV Tau C is edge on, with the plane of the disc aligned with the extended emission, while the disc around DO Tau is face on.

- Solutions for the stellar kinematics should be consistent with the present size of the disc around HV Tau C. I.e. the tight binary HV Tau AB should not orbit C post-interaction such that $R_{\rm tidal} > 0.5$, where $R_{\rm tidal}$ is here the ratio of observed disc size (~ 50 au) to the closest approach distance. The closest separation between HV Tau C and DO should not be significantly less than twice the outer radius of the disc around DO Tau - i.e. 150 au. Although it is possible that the viscous spreading of this disc may have an impact on its present extent.

- When recovering a flux from the surface density distribution in a given model, the dust to gas ratio required to reproduce the same flux as in the 100 μm and 160 μm and initial total disc mass should be sensible, and consistent between wavelengths.

- The parameters of such an interaction should be capable of producing common envelope surrounding both stars with the structure seen in figure 2.1. Although it may not be possible to reproduce the structure precisely, especially if the binary HV-AB has a significant effect, the aim of the modelling process is to show that the observations can feasibly result from a disc-disc interaction.

2.3 Numerical method

The complexity of the HV/DO system is approached by dividing the problem into a kinematics study of the stellar components, and hydrodynamical modelling of star-disc and disc-disc interactions. For the hydrodynamics we apply a smoothed particle hydrodynamics (SPH) treatment of the gas particles. Its computationally expensive nature means that we cannot rely on Markov chain *Monte Carlo* (MCMC) or similar statistical techniques to constrain the parameters which yield the observed structure. We explore a large number (~ 500) of low resolution models with 10^4 particles to find promising configurations for which ejected material approximately traces the observed structure, allowing variation in disc orientations and surface density profiles (see Section 2.3.3). We then rerun promising models with a resolution of 10^6 particles and refining the disc properties and viewing angles to find a model that yields extended structure closest to observations.

2.3.1 Kinematic modelling

The first stage in obtaining a model is exploring the kinematic parameter space of a multiple encounter of a three star system (DO, HV-C and HV-AB, the latter we will consider as one star – see below) to find solutions which satisfy the dynamical conditions discussed in Section 2.2. As in the case of the hydrodynamics, we cannot use an MCMC exploration of the kinematic parameter space due to the chaotic nature of the three body problem. Instead, we search for a (non-exhaustive) library of kinematic solutions for further hydrodynamical modelling. We do this by uniformly varying parameters which describe the initial conditions of the three bodies and checking for consistency with observations. Viable solutions are initially bound, but we do not have further a priori constraints. We apply the following parameterisation of the problem (sampling uniformly over each within the defined range) as it allows us to minimise the size of the exploration space by choosing likely ranges, with the caveat that drawing statistical conclusions from our kinematic library is problematic. We simulate the trajectories of the three star particles by applying the N-body 4$^{\text{th}}$ order Hermite integrator (Makino and Aarseth, 1992) in the GANDALF code (which is also used for the SPH simulations described in Section 2.3.2, Hubber *et al.*, 2018).

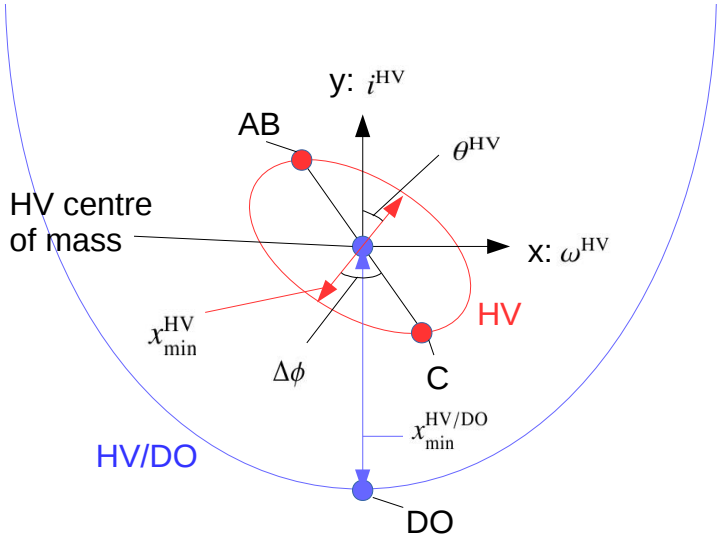

Fig. 2.4 Schematic diagram illustrating the parameters used to define the initial conditions for our 3-body simulations. The blue line traces the HV/DO trajectory, with coordinates centred on the centre of mass of the HV system. The red line traces the HV-AB/C trajectory. The circular markers represent the locations of the components of each orbit at the time of the closest approach between DO Tau and the centre of mass of HV (blue circles). The positions of HV-AB and -C are shown as red circles. The angles as discussed in the text are annotated.

	$x_{\rm min}^{\rm HV/DO}$/au	$e_0^{\rm HV/DO}$	$x_{\rm min}^{\rm HV}$/au	$e_0^{\rm HV}$	$\theta^{\rm HV}$ /°	$i^{\rm HV}$ /°	$\omega^{\rm HV}$ /°	$\Delta\phi$ /°
Range	0-2000	0-1	100-1500	0-1	0-360	0-360	0-180	0-360

Table 2.1 Parameter range searched for solutions to the present day arrangement of HV and DO Tau.

Our parameterisation is illustrated in figure 2.4. We are helped by the small separation of the binary AB, which we hereafter consider as a single star with the combined mass. With this approximation all stellar components now have the same mass within uncertainties: we assume $0.7\,M_{\odot}$. To parameterise the interaction of the three remaining stellar components, we consider two distinct orbital equations of the form

$$x = \frac{h^2}{\mu}\left(\frac{1}{1+e\cos(\phi-\theta)}\right) \tag{2.1}$$

for HV and for HV/DO, where HV is the orbit of HV-C and HV-AB, while HV/DO is the 'two-body' system of DO and the centre of mass of HV. In equation 2.1, x is the separation between bodies, ϕ is the phase, θ is the angle of the periastron in the plane (equivalent to rotation in the z-axis), h is the specific angular momentum and $\mu = G(m_1+m_2)$. For HV/DO we fix $\theta = 0°$. For HV, the orbit of C and AB is rotated in the y-axis by angle i and in the x-axis by angle ω. Finally, we define $\Delta\phi$, the difference in phases as HV/DO reaches periastron. This leaves 8 initial values fully parameterising the system: $e_0^{\rm HV/DO}$, $x_{\rm min}^{\rm HV/DO}$, $e_0^{\rm HV}$, $x_{\rm min}^{\rm HV}$, $\theta^{\rm HV}$, $i^{\rm HV}$, $\omega^{\rm HV}$, $\Delta\phi$.

The ranges for each parameter over which we search for successful kinematic solutions are summarised in table 2.1. We focus on the solutions for which DO is initially bound to HV ($e_0^{\rm HV/D0} < 1$) as they offer the most likely scenarios for a close encounter between stellar components. Further, highly hyperbolic encounters are physically unlikely. We apply one further restriction that configurations for which the energy of the HV initial orbit exceeds the energy of the DO trajectory are discounted. This is both because in this regime our orbital parameterisation does not make physical sense, and because our investigation finds that solutions for which the orbital energies are comparable are also relatively rare. We search uniformly over the remaining parameter space for successful solutions.

Our criteria for a 'successful' kinematic solution are as follows. A lower limit of 50 au is placed on all interactions as this is a conservative constraint, a distance below which either disc would be significantly over-truncated. Additionally an upper limit on the closest approach distance between HV Tau C and DO Tau is set at 300 au. This is motivated both by the present day disc outer radii and the study of Muñoz *et al.* (2015) and our own findings

that a close flyby is required to produce the observed extended structure in the tidal tails (see Section 2.4). After encounter, DO must either be unbound from the whole system, or reach a maximum separation $> 1.2 \times 10^4$ au. HV Tau C and AB must remain bound. Acceptable final maximum separation of the HV wide binary is between 400 and 1500 au, consistent with observed projected separation of 550 au. We impose a minimum periastron distance of 125 au to prevent over-truncation of the disc around HV Tau C.

2.3.2 Hydrodynamics model

We use the SPH code GANDALF (Hubber *et al.*, 2018) to simulate the discs. We adapt it to include a locally isothermal equation of state as a function of radial separation from the nearest star. Self-gravity is disregarded, the gravitational potential being dominated by the stellar component.

We employ artificial viscosity parameters as prescribed by Morris and Monaghan (1997) to minimise the effects of viscous diffusion in the tidal tails. However, inevitably at the required integration times on the order of 0.1 Myr, the effect of numerically accelerated viscous spreading and magnified inter-particle torques result in a loss of structure. This is especially the case where there is considerable mass loss from the disc, as during the violent interactions necessary to produce significant external structure.

2.3.3 Disc interaction initial conditions

Pfalzner *et al.* (2005b) showed that for discs in which there is significant mass transfer one cannot analogously extrapolate the structure of tidal tails from star-disc interactions (where one disc is excluded). Therefore both discs are required simultaneously for all models where closest approach distance is of order the disc radius. For disc-disc simulations, the work of Muñoz *et al.* (2015) offers initial constraints on the closest approach between HV Tau C and DO Tau, where extremely close interactions with $R_{\rm tidal} \sim 10.0$ both result in the near-destruction of the original discs and also in significant sapping of orbital energy and stellar capture (although a large disc mass approximately 10% of the star mass is used in this study). Conversely, encounters with a large closest approach distance such that $R_{\rm tidal} < 0.5$ do not produce significant external structure (i.e. angular momentum transfer is insufficient to unbind a large fraction of the disc mass).

Due to the uncertainty in the line of sight separation (and therefore the angle of orientation) of the present day system, the appropriate disc orientations are not immediately clear. For the initial conditions of the three star encounter, a snapshot is taken from an appropriate kinematic model at a time before close encounter. To ensure that discs are dynamically

settled prior to the encounter, this time is chosen to be five orbital periods at the radius of the outer disc before the closest approach between any two stellar components. The discs around HV Tau C and DO are added at an orientation that matches the present day orientation if the two stellar systems are in the plane of the sky. The simulation is then continued with SPH discs included to examine the hydrodynamic evolution of the multiple star interaction. Subsequently, disc orientations in promising models are modified to better match the extended structure.

The surface density profile of the discs is both important to the structure and quantity of ejected material, and hard to constrain given that it may be significantly altered in a close interaction. It is treated as a power law such that

$$\Sigma = \Sigma_0 \left(\frac{R}{R_0} \right)^{-p}$$

where both 'shallow' ($p = 0$) and 'steep' ($p = 1$) surface density gradients are tested.

We define the gas temperature by distance R to the nearest star:

$$T = \max \left\{ T_0 \left(\frac{R}{R_0} \right)^{-q}, 15 \text{ K} \right\},$$

with $q = 0.6$ and a temperature at 50 au of 20 K is adopted for HV Tau C, and the same profile assumed for DO Tau. Variations in temperature only have a modest effect on the observed structure as a result of star-disc interaction (Dai *et al.*, 2015). Our choice of temperature profile for the hydrodynamic simulations is based on those inferred by Duchêne *et al.* (2010), although results in a lower temperature than we found in Section 2.2.4 through the cloud. This discrepancy could be due to heating of the ejected material during the disc-disc encounter, which we do not model here as there are considerable uncertainties in the temperature estimates. The temperature in both the disc and the cloud are both empirically derived and therefore represent reasonable choices.

Outer radii of the discs prior to interaction are not well constrained, due to uncertainty in the extent of truncation by the initial fly-by. Further, the post-interaction relaxation of the disc, including viscous spreading and possible further dynamical binary interactions in the case of HV-C, is not well characterised. To eject sufficient material to produce observed structure, initial tests suggest that R_{out} such that $R_{\text{tidal}} \equiv R_{\text{disc}}/x_{\text{min}} \approx 0.8$ is reasonable. This is the initial estimate for a given kinematic model, and the outer radii are subsequently tuned to fit observations. The inner radius is defined to be $R_{\text{disc}}/20$. Choosing a conservative inner radius is necessary given that a significant proportion of the discs pass though each other. The smoothing lengths of the sink particles are chosen to be half of the inner radius of the

$x_{\rm min}^{\rm HV/DO}$	$e^{\rm HV/DO}$	$x_{\rm min}^{\rm HV}$	$e^{\rm HV}$	$\theta^{\rm HV}$	$i^{\rm HV}$	$\omega^{\rm HV}$	$\Delta\phi$
864 au	0.85	653 au	0.38	28°	158°	10°	94°

Table 2.2 Kinematic parameters of the best-fit model. Parameters are defined in Section 2.3.1.

disc with the smallest extent. The final parameter required to define the disc interactions is the relative masses of the two discs (i.e. how many SPH particles each contains), which we allow to vary.

2.4 Modelling results

We will refer to the model presented below as the 'best-fitting model'; this is in the sense that it best matches observations of all the models studied. The size of the parameter space involved and the computational expense of the simulations means that the number of models examined is not exhaustive, and that usual statistical parameter space exploration techniques were not practical.

2.4.1 Kinematic properties

The distribution of semi-major axes in the initial systems ($a_0^{\rm HV/DO}$ and $a_0^{\rm HV}$) are shown for successful kinematic solutions is shown in figure 2.5. As discussed in Section 2.3.1, it is not possible to draw statistical conclusions from this distribution. However, most solutions exist for $a_0^{\rm HV/DO} \gtrsim 10^4$ au, although the model which best reproduces the extended bridge structure (Section 2.4.3) has $a_0^{\rm HV/DO} \approx 5800$ au. The parameters of this model are presented in table 2.2. The orientation of the HV/DO angular momentum vector is approximately anti-parallel that of HV-AB/C. This reversal of the orbits appears surprising. However, if the forming stars were initially separated by $\sim 4 \cdot 10^4$ au (initial apastron) it is possible that local velocity fields in the collapsing gas of the primordial system lead to non-aligned orbits.

The important dynamical properties of the chosen kinematic model are summarised in table 2.3. By integrating backwards, all stellar components in this model are found to remain bound on timescales > 1 Myr. Initially HV-AB/C has an orbit with a semi-major axis $a_0^{\rm HV} \approx 10^3$ au, and eccentricity $e_0 \approx 0.37$. The encounter with DO removes angular momentum from the HV system, and results in DO being marginal bound, with a large semi-major axis $a_{\rm f}^{\rm HV/DO} \approx 1.5 \times 10^4$ au, sufficient to reach the observed present day projected separation.

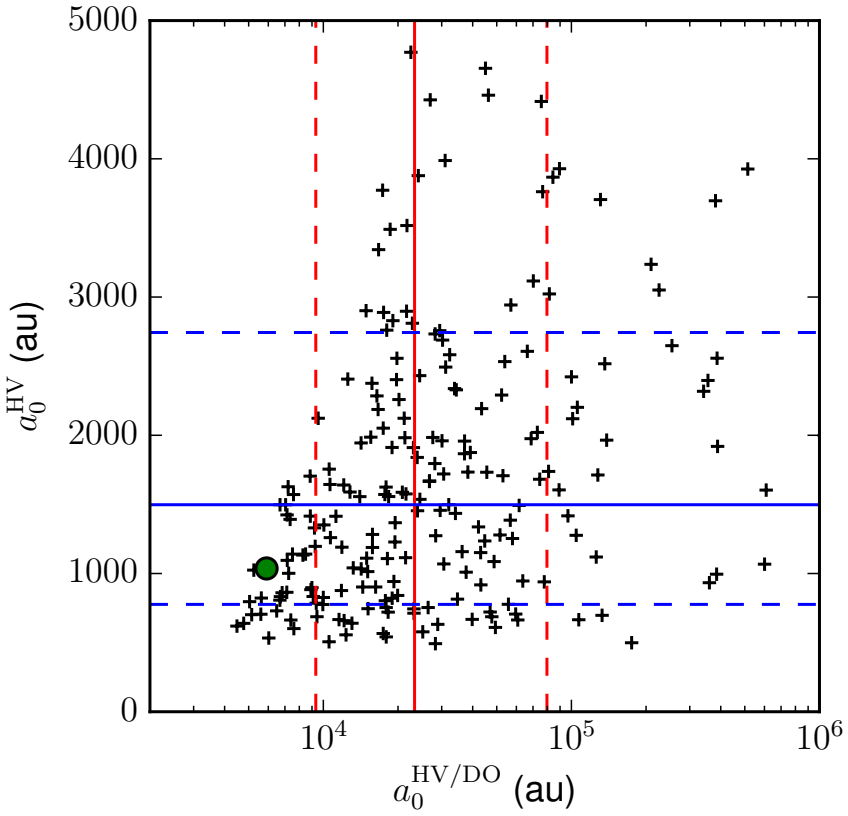

Fig. 2.5 The distribution of the initial semi-major axes of the HV ($a_0^{\rm HV}$) and HV/DO ($a_0^{\rm HV/DO}$) trajectories for successful solutions of our kinematic parameter space exploration. The solid lines (horizontal blue for $a_0^{\rm HV}$ and vertical red for $a_0^{\rm HV/DO}$) represent the median of the results. The associated dashed lines indicate the associated 16$^{\rm th}$ and 84$^{\rm th}$ percentile values. The green circle represents the location of our chosen 'best-fit' solution in reproducing the extended emission between the stellar systems (see Section 2.4.3).

The closest encounter between each stellar component is also consistent with observations. The single encounter between HV Tau C and DO Tau is the closest between any of the components at 285 au, and is close enough to truncate discs to $\sim$ 100 au. No interaction involving AB is close enough such that a $\sim$ 10 au binary would be disrupted and the closest approach distance between HV Tau C and AB is the final periastron distance.

Finally, the time since the closest encounter to reach the projected present day separation for our preferred system orientation is $\sim$ 0.1 Myr, which is consistent with even the lowest estimate for the age of any of the stellar components.

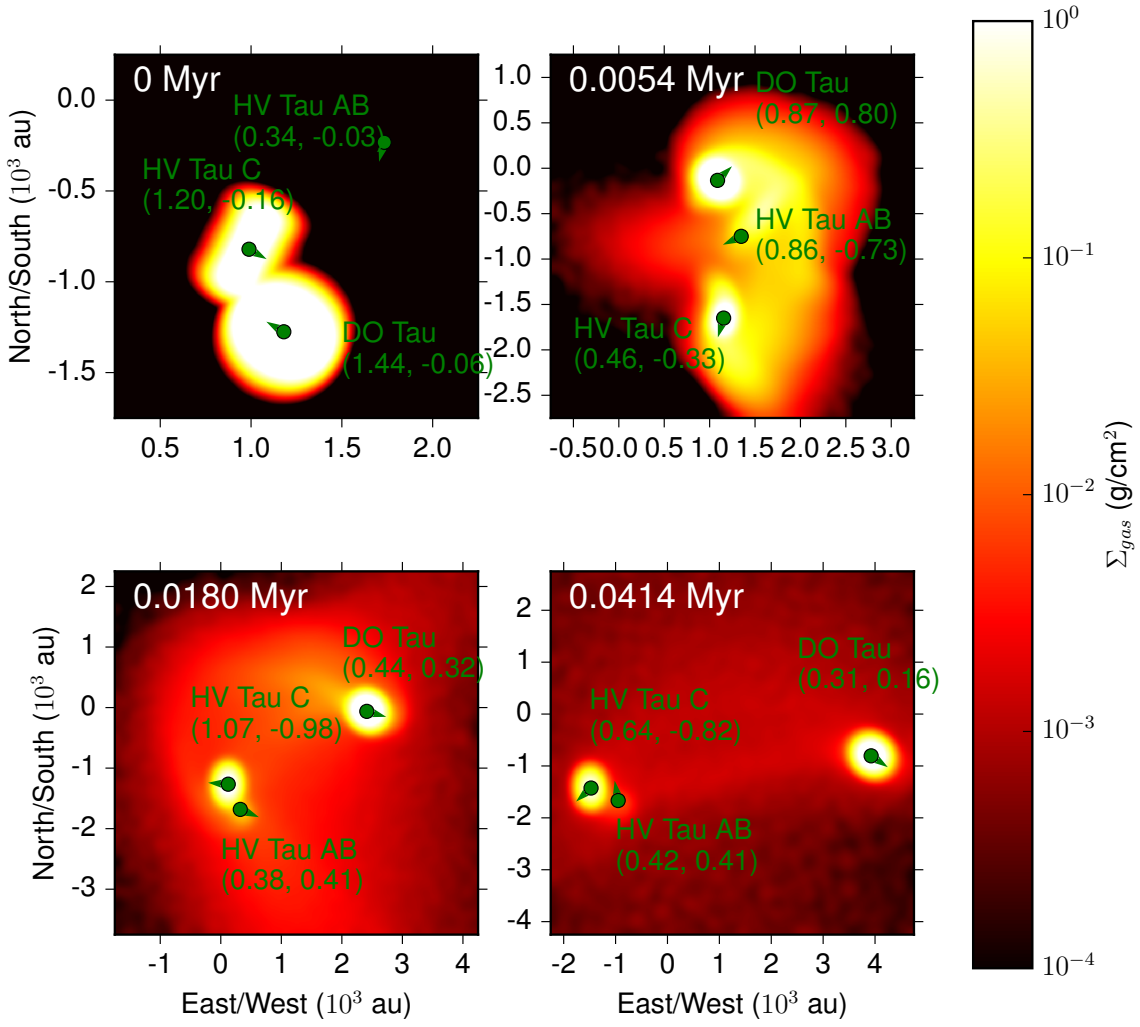

Fig. 2.6 Snapshots of our chosen model before and after the disc-disc interaction. The colour scale represents the gas surface density normalised to give the correct flux scale in figure 2.7, and the orientation is the same as in that figure. Stellar components are marked with green circles. The numbers in brackets are the magnitude of the proper motion and the radial velocity in km/s respectively, with the direction of proper motion indicated by an arrow. HV Tau AB is considered in our models to be a single sink particle, as discussed in the text.

	$x_{\rm min}$/au	a_0/au	e_0	$a_{\rm f}$/au	$e_{\rm f}$
HV-C/DO	285	-	-	-	-
HV-AB/DO	657	-	-	-	-
HV-AB/C	445	$1.05 \cdot 10^3$	0.37	859	0.48
HV/DO	-	$5.76 \cdot 10^3$	0.85	$1.48 \cdot 10^4$	0.95

Table 2.3 Dynamical properties of the stellar components of the best-fitting model, where $x_{\rm min}$ is the closest approach distance and a_0, $a_{\rm f}$, e_0, $e_{\rm f}$ are the initial and final semi-major axes and eccentricities of the binaries respectively.

	R_0/au	$x_{\rm min}$/au	$R_{\rm obs}$/au	$M_{\rm rel,0}$	$M_{\rm obs}/M_\odot$	p
HV-C	320	285	$\sim 50-100$	0.33	~ 0.002	0
DO	355	285	~ 75	1.0	0.013	0

Table 2.4 Disc properties of the best-fit model. The quantities are as follows: R_0 is the initial outer radius of the disc, $x_{\rm min}$ is the closest encounter with any stellar component, $M_{\rm rel,0}$ is the initial relative mass of each disc, $M_{\rm obs}$ is the observed total disc mass, p is the power law index for the surface density. The subscript 0 pertains to initial values in the model and 'obs' the observed (present-day) values.

2.4.2 Disc properties

The properties of the circumstellar discs found by tuning to best match the *Herschel* observations in figure 2.1 are shown in table 2.4, and the snapshots of the gas surface density distribution during the encounter are shown in figure 2.6. The initial radii for HV Tau C and DO Tau discs are 320 au and 355 au respectively, which means that the stellar components penetrate the discs at the closest approach distance of 285 au. We find that both a smaller mass and outer radius are required for the disc around HV-C with respect to DO. The present day observed disc mass ratio is $M_{\rm disc}^{\rm HV-C}/M_{\rm disc}^{\rm DO} \approx 0.15$, while our chosen model has an initial mass ratio of 0.33. At the time of our chosen snapshot this ratio in the simulation becomes ~ 0.13, with the disc around HV Tau C losing a greater fraction of the initial mass.

In our model the orientation is such that the disc around HV Tau C is approximately edge on with the plane along the direction of the 'V'-shaped emission, as suggested by observations (see figure 2.6). The disc around DO Tau is also approximately face-on, and thus the geometry of the system is compatible with the observed extended structure discussed below. These disc orientations lead to a collision in which the discs collide approximately perpendicular in a strongly penetrating encounter. This violent interaction induces significant pressure gradients and justifies the need for hydrodynamic simulations.

2.4.3 External structure

To reproduce the extended structure between HV and DO, we have introduced a moderate temperature gradient with respect to the projected distance d from each stellar component:

$$T_{\rm dust} = 35\,{\rm K}\left(\frac{d}{950\,{\rm au}}\right)^{-0.32}$$

with a maximum temperature of 35 K, which is consistent with the temperature profile found in Section 2.2.4. The resulting surface brightness of the extended structure at 100 μm and 160 μm in our model is shown in figure 2.7. To obtain this flux distribution we have had to assume a large initial total gas mass of $M_{\rm tot,0} = 0.18\,M_\odot$ (with $\Sigma_{\rm dust}/\Sigma_{\rm gas} = 10^{-2}$). This is on the order of the mass we would expect if the interaction occurred at an early evolutionary stage. Approximately 50% of the mass is accreted in our simulations at the time of the snapshot, which leaves $0.09\,M_\odot$ total mass, of which $\sim 0.027\,M_\odot$ is retained in the disc around DO Tau and $3.5\times10^{-3}\,M_\odot$ in that of HV Tau C. The remaining mass occupies the external structure. These disc masses are a factor ~ 2 greater than the present day, and indeed the mass of the total system is an overestimate due both observational and numerical factors as follows. Firstly, we find resolution-dependent diffusion of SPH particles into the ISM (away from what we consider the 'bridge' between HV and DO). As we increase the resolution, for simulations run at a resolution lower than 10^6 particles, a smaller fraction of SPH particles are lost to the ISM. Therefore we expect that increasing the resolution further would decrease the required total initial mass of the system. Additionally, increasing the initial radii of the discs has a similar effect of increasing the mass of the bridge while preserving the observed structure; however this additionally enhances accretion rates and therefore compounds resolution issues at late times. Alternatively, the dust-to-gas ratio in the original discs may be enhanced (Ansdell *et al.*, 2016), which would mean we overestimate the gas mass.

We have chosen a snapshot at a separation between HV and DO of $\sim 5\times10^3$ au, half of the observed present day separation. This is because, as discussed in Section 2.3.2, resolution effects mean that the structure diffuses as the model is integrated in time. Integrating further to the present day results in a numerical loss of structure due to low resolution in the region between the stellar components. Contrary to the diffusive numerical effects described above, this means that additional initial mass would be required to produce sufficient surface density at the present day separation.

Overall, the main features seen in the 100 μm and 160 μm observations are well produced in our model, namely the V-shaped emission close to HV Tau and the tidal tail close to DO Tau. The broad envelope shape is less well reflected in our models, however these regions

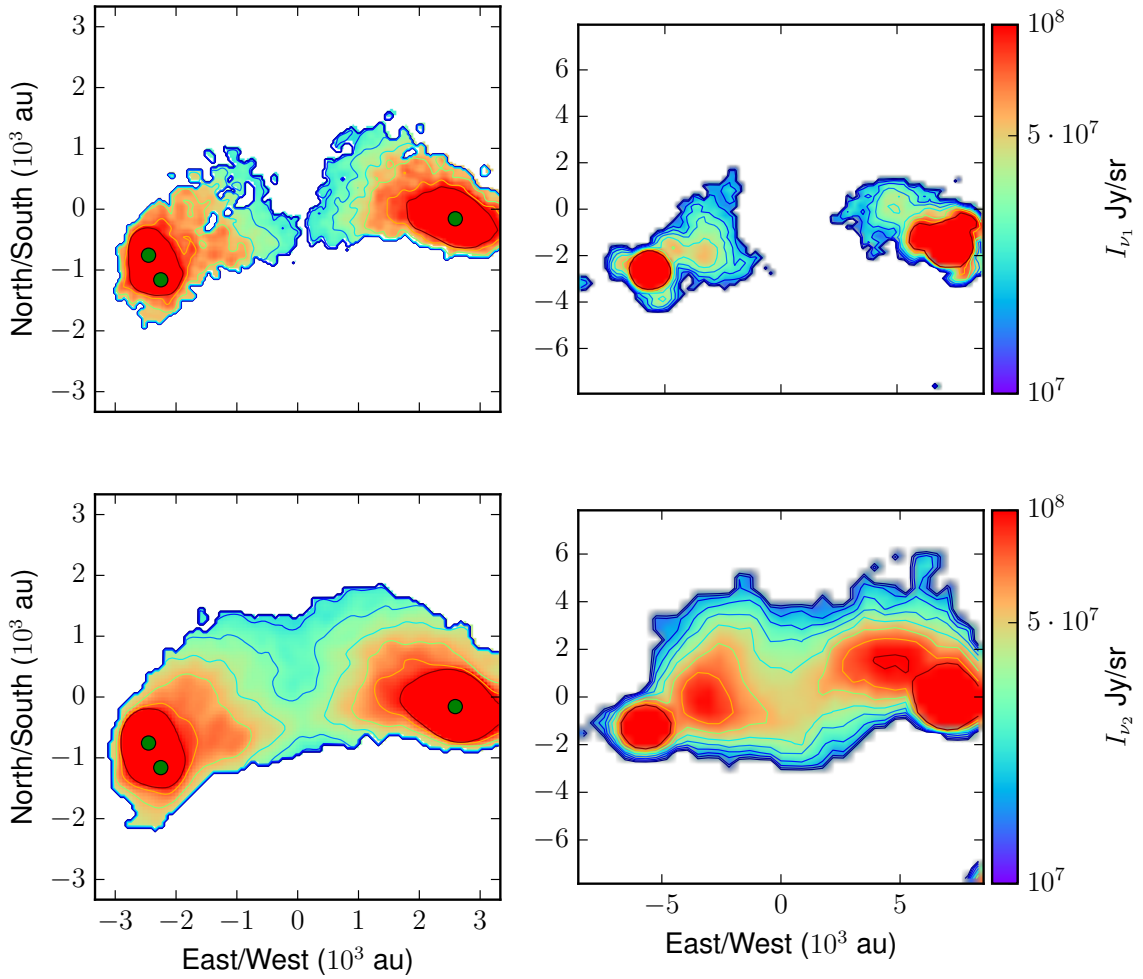

Fig. 2.7 Surface flux distribution of our chosen model (left) next to the observations (right) at 100 μm (top) and 160 μm (bottom). All fluxes are truncated at the 3σ background noise level in the respective wavelength observations. The model snapshots are at $\sim 4 \times 10^4$ years after the disc-disc encounter between HV-C and DO. This is a shorter than the time required to reach the present-day separation, and is chosen due to numerical limitations (see text for details).

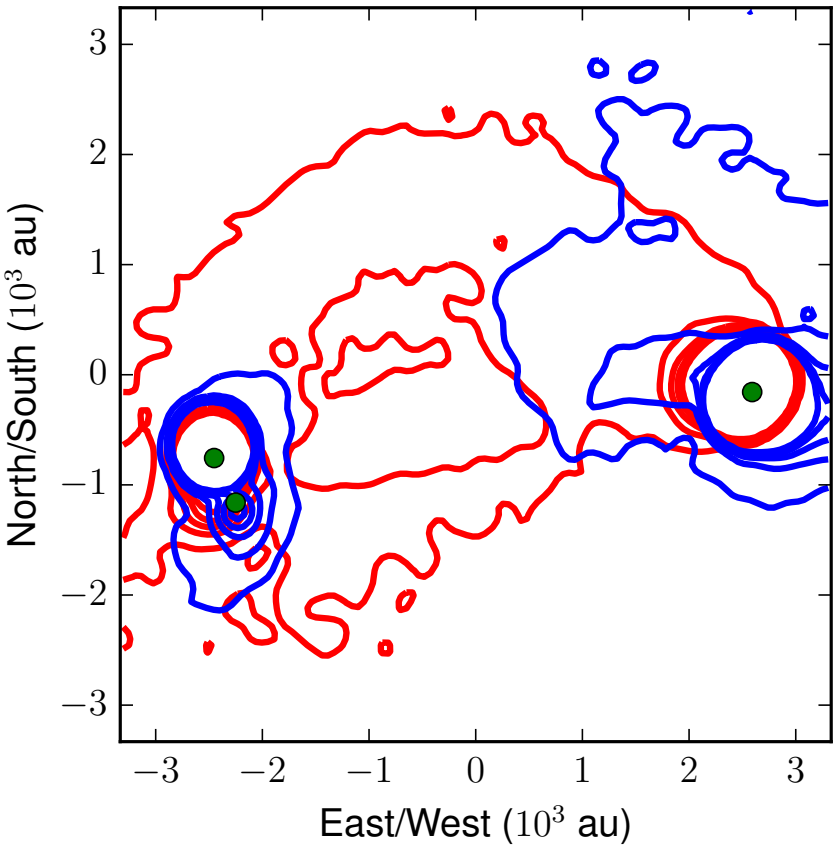

Fig. 2.8 Simulated variation in surface density $\Sigma_{\delta v_z} = \int \rho_{\delta v_z} dz$ of material, where $\rho_{\delta v_z}$ is the mass density of particles with relative line of sight velocity $\delta v_z = v_z - \langle v_z \rangle$ with respect mean line of sight velocity $\langle v_z \rangle$. The blue contours are for SPH particles with 0 km/s $< \delta v_z <$ 1 km/s , while the red contours are for -1 km/s $< \delta v_z <$ 0 km/s. Contours are linearly spaced over a factor 5 in surface density in arbitrary units.

have a low resolution of SPH particles which can result in a loss of structure. Additionally, uncertainties in the temperature profile discussed in Section 2.2.4, particularly at the outer edge and centre of the envelope where we only have detections at 160 μm, mean that we are unable to accurately map the surface density to an intensity distribution. However, the agreement between our model and the observations is sufficient to suggest that a disc-disc interaction ~ 0.1 Myr ago is a viable mechanism by which the extended structure between HV and DO Tau has been produced.

2.4.4 Gas velocity

In figure 2.8 we demonstrate that we expect to find some sub-structure in the line of sight gas velocities. The standard deviation in line of sight velocity of the SPH particles v_z for the best

fit model is $\sigma_{v_z} \approx 1.3$ km/s. We divide the deviation from the mean gas velocity $\delta v_z = v_z - \langle v_z \rangle$ into two bins, red shifted (-1 km/s$< \delta v_z < 0$ km/s) and blue shifted (0 km/s$< \delta v_z < 1$ km/s). The results in figure 2.8 illustrate both the large scale velocity structure of the whole system, and the line of sight motion of the wide binary HV Tau C and AB.

Although, as previously discussed, the present day system is at approximately double the separation of the snapshot, figure 2.8 is indicative of the velocity field we would expect to obtain from observations if a past encounter produced the observed extended emission. Future observations of the gas in the region can be compared with our results to establish the likeliness of the scenario we suggest here.

2.5 Conclusions

We have used hydrodynamic modelling to support the conclusion that the three stars making up HV Tau and the apparently unrelated star, DO Tau, had a past encounter ~ 0.1 Myr ago. While it is difficult to make hard conclusions regarding the dynamical history of the system and subsequent disc evolution, our modelling suggests the following scenario:

- HV Tau A, B and C initially formed a quadruple system with DO Tau $\gtrsim 0.1$ Myr ago, with a spatial scale of ~ 5000 au (and an orbital period of ~ 0.3 Myr).
- The highly eccentric orbit of DO Tau led to a close encounter with HV Tau C 0.1 Myr ago. During this type Ib encounter, the disc around HV Tau C interacted strongly with the disc around DO Tau, leading to rapid accretion and truncation of the discs. This was likely the first encounter and therefore we expect the age of the original system to be $\lesssim 0.4$ Myr.
- After this encounter the DO Tau trajectory became either marginally bound or marginally unbound to reach a separation $> 10^4$ au.
- The tidal tails of this event can be observed in the 160 μm dust emission to the present day.

Our findings support the hypothesis that there previously existed sub-structure in Taurus down to smaller spatial scales which has now been dynamically erased (Kraus and Hillenbrand, 2008). Given the improbability of a close encounter producing tidal tails that can be observed for timescales ~ 1 Myr, there may have been many more type Ib interactions in the region.

Chapter 3

Linearised theory of distant type II star-disc encounters

Winter *et al.* (2018b) is the source text for this chapter. I performed the analytic calculations, ran the simulations and I am the main contributor to the text.

3.1 Introduction

This chapter concerns the influence of distant type II encounters on the evolution of a PPD. Distant encounters have a less damaging effect on the disc with respect to close encounters, however they are also far more frequent during the evolution of a stellar cluster. It is therefore important to understand the influence of such interactions to quantify their relative significance. Historically, the theory of the tidal effects in this context has largely been divided into the influence of dynamical interactions between an existing binary and a perturbing star (e.g. Press and Teukolsky, 1977; Heggie and Hut, 1993; Heggie and Rasio, 1996), and between a perturber and a single star with surrounding PPD (e.g. Goldreich and Tremaine, 1978; Lubow, 1981; Ostriker, 1994; Ogilvie, 2002). The implicit focus for a particular study in each case has either been on angular momentum transfer to the perturbing star (e.g. Press and Teukolsky, 1977) or to the unperturbed system (be it PPD or binary – e.g. Lubow, 1981), or both (e.g. Ostriker, 1994), depending on whether the authors are considering mechanisms for stellar capture, tightening of a binary or induced accretion. In each case the relevant physical phenomena are similar, and require the contributions of various resonances between the natural frequencies of the unperturbed system and the trajectory of the perturber.

The most relevant study to this chapter is that of Rosotti *et al.* (2014), who found evidence that there is a significant range of encounter distances which, while not causing mass loss from the disc, extract significant angular momentum from the outer disc and thus influence the growth of disc size. In our exploration of this effect, the re-analysis of the numerical data of Rosotti *et al.* (2014) revealed no detectable effect of the wider cluster environment on disc size (Rosotti *et al.*, 2018). It is nevertheless possible that effects that would not be measurable over the duration of the simulation might prove to be important for real discs in clusters of sufficiently high density. Given the interest in this possibility that has been spurred by the Rosotti *et al.* (2014) study, we here subject the suggested effect to detailed scrutiny.

The only detailed hydrodynamical study that has considered angular momentum transfer in non-penetrating disc encounters is that of Muñoz *et al.* (2015), which concentrated on the evolution of the stellar components during a disc-disc interaction. In that work the aim was not a comparison with the theoretical predictions for angular momentum transfer. It differs from this work in that both stellar components hosted a massive disc, which complicates interpretation of angular momentum exchange, especially as many of the models involved strong disc-disc interactions. Our goal here is a robust, general expression for encounter induced angular momentum loss within the disc in the linear, low disc mass regime as a function of orientation, stellar mass ratio and closest approach distance.

We adopt the following approach in addressing angular momentum transfer in non-penetrating star-disc encounters. First, we develop the relevant linearised equations for a ring of particles around a star undergoing a parabolic encounter. Our approach bears similarities to that of Ostriker (1994) but we have re-derived relevant expressions for several reasons. Most importantly, that study was concerned with the case of young massive discs which might be relevant to the formation of binary stars by capture. We, by contrast, are concerned with the progressive influence of multiple encounters throughout the pre-main sequence period and therefore need to treat the case that the disc mass is small compared with the mass of the stars. As we shall see, some of the expressions from Ostriker (1994) should clearly not be applied to the case of low disc mass since they predict an infinite change in specific energy and angular momentum in the test particle limit. Further, Ostriker does not present explicit expressions for arbitrary stellar mass ratios and relative phase between pericentre and the line of nodes of the disc and stellar orbits, nor for the dependence of the angular momentum transfer on disc surface density profile.

We test the linearised expressions we derive by comparison with numerical integration of the response of a ring of test particles to a parabolic perturber. We then use smoothed particle hydrodynamic (SPH) simulations to reproduce this calculation for a disc including

pressure and viscosity forces, which we compare to a disc reconstructed with an appropriate surface density profile from the test particle ring results. We find excellent agreement between the linearised expressions, the test particle calculations and the SPH simulation results, thus validating the use of SPH to model star-disc encounters in the linear regime. We will nevertheless find that the asymptotic fall-off of the angular momentum transfer with pericentre radius implies that the cumulative effect of distant encounters is small.

The rest of this chapter is organised into the following sections. Section 3.2 reviews the relevant equations and our modelling techniques. Our numerical results are laid out in Section 3.3, and these are discussed in the context of a stellar cluster in Section 3.4. Our conclusions are summarised in Section 3.5.

3.2 Theory and method

3.2.1 Linearised equations

To compare theoretical angular momentum transport in discs to our models, we modify the relevant equations derived by Ostriker (1994). These results are a first order approximation for the change in the magnitude of angular momentum in a PPD with original angular momentum vector $L_z\hat{\boldsymbol{e}}_z$ during an encounter for which the minimal separation between stellar components $|\boldsymbol{x}(t)|_{\min} = x_{\min}$ occurs at $t = 0$. In this case, for $\Delta L \ll L$, it is easy to show that

$$\frac{\Delta L}{L} = \frac{|\boldsymbol{L}|_{t\to+\infty} - |\boldsymbol{L}|_{t\to-\infty}}{|\boldsymbol{L}|_{t\to-\infty}} = \frac{\Delta L_z}{L_z} + \mathscr{O}(\Delta L_\perp^2/L_z^2) \tag{3.1}$$

where $L_\perp$ is the change of angular momentum perpendicular to $\boldsymbol{e}_z$. Hence the linearised equations are concerned with the change parallel to the original angular momentum vector of the disc.

The way that Ostriker (1994) calculates this is by first decomposing $\boldsymbol{f}_{\rm ext}$, the external force exerted by the star per fluid element in the disc, into spherical harmonics. Angular momentum change per unit time per fluid element is the $\hat{\boldsymbol{e}}_z$ projection of the cross product of $\boldsymbol{f}_{\rm ext}$ with the position vector of the fluid element relative to the central star. The angular momentum change of the fluid element is then obtained by integrating the torque over time. For a fluid element that remained on a circular orbit throughout the interaction, the total angular momentum change associated with the interaction would be zero, as discussed by Heggie and Rasio (1996) in the context of perturbations to a non-eccentric binary. Angular momentum transfer is associated with the torque acting on the fluid element's *perturbed* trajectory. This is evaluated by considering the temporal Fourier decomposition

of the element's perturbations and the interaction between each Fourier component and the corresponding Fourier component of the external force. For each fluid element, disturbances are excited at frequencies which correspond to resonances with the forcing frequency of the perturbing star (Goldreich and Tremaine, 1978). For a central potential Φ_0, the natural frequencies within the disc are the circular, epicyclic and vertical angular frequencies, which, at radius r_0 in an unperturbed disc, are:

$$\Omega_0^2 \equiv \frac{1}{r_0}\frac{\partial \Phi_0}{\partial r_0}; \quad \kappa_0^2 \equiv \frac{1}{r_0^3}\frac{\partial \left(r_0^4 \Omega_0^2\right)}{\partial r_0}; \quad \chi_0^2 \equiv \left.\frac{\partial^2 \Phi_0}{\partial z^2}\right|_{r_0; z=0}$$

respectively. For a disc of negligible mass, this means that

$$\Omega_0^2 = \kappa_0^2 = \chi_0^2 = \frac{GM_1}{r_0^3}$$

where M_1 is the mass of the disc hosting star. These frequencies are associated with corotation, Lindblad and vertical resonances respectively. For a given azimuthal wavenumber m, the equations

$$m\Omega_0 - \omega = 0; \quad m\Omega_0 - \omega = \pm\kappa_0; \quad m\Omega_0 - \omega = \pm\chi_0$$

can be solved for a corresponding radius r_0 (we henceforth drop the subscript) at each forcing frequency ω. The positive and negative Lindblad or vertical frequencies correspond to inner and outer resonances respectively. Angular momentum transfer within the disc is associated exclusively with radii in resonance with the forcing frequency ω. However, $\boldsymbol{f}_{\text{ext}}$ is Fourier decomposed such that every location in the disc is always in resonance with some component of the forcing potential since it has a continuum spectrum.

The evaluation of the angular momentum transfer from these resonances is discussed more fully in Appendix A.1. Ostriker (1994) found an inner vertical resonance (IVR) term dominates at large radii, which does not in fact contribute to angular momentum transfer to first order (see Appendix A.1 and Lubow, 1981). This means that the dominant resonances are the inner Lindblad resonances (ILRs), resulting in a steeper asymptotic power law of $x_{\min}/r$ than if the IVR contributed to first order. Additionally, the focus of Ostriker (1994) was the regime of high (order unity) disc to star mass ratio and hence was developed to address this limit. This formulation is clearly not to be used in the limit of low disc mass since it predicts an infinite change in *specific* energy and angular momentum in the test particle limit (cf. equation 2.48 in Ostriker, 1994). Instead, our calculation leads to an expression, equation A.4, equivalent to the test particle result quoted (but not employed) in equation 2.50 of that study.

For all values of $x_{\rm min}/r$ there are just two dominant contributions to angular momentum loss in the disc. They are the $m = 2$ ILR for close encounters ($x_{\rm min}/r \lesssim 6$ for equal mass stellar components) or the $m = 1$ ILR for larger $x_{\rm min}/r$, where the latter corresponds to the limit of small forcing frequency $\omega = 0$, as discussed in Appendix A.1. These contributions are evaluated in equations A.6 and A.4 respectively.

3.2.2 Ring of test particles

To assess the effect of a stellar encounter at a single radius within a disc, we apply a test particle calculation. We use the general Bulirsch-Stoer algorithm of the MERCURY orbital integrator for solar-system dynamics (Chambers, 1999).

We set up a ring of 200 test particles at $r = 1$ au from a central star with mass $M_1 = 1\,M_\odot$. A second star of mass M_2 is placed on a parabolic trajectory at a time 200 test particle orbits prior to the closest approach, and integrated for the same time after that approach. The system is further defined by two angles: the angle between the direction of pericentre and the line of intersection of the disc and the orbital plane, α, and the angle between the angular momentum vector of the disc and that of the orbit, β. The system is scale-free in that the only pertinent quantities are the ratio of the closest approach to test particle ring radius $x_{\rm min}/r$ and the mass ratio between the stellar components M_2/M_1.

The specific angular momentum for each particle is then compared to the corresponding particle in a ring which remains unperturbed over the same period, and the average angular momentum loss over all the particles represents the total loss for the ring. During encounters for which $x_{\rm min}/r \lesssim 2$, some particles become unbound from the initial star. For an unbound particle (i.e. one with a post-encounter eccentricity $e > 1$) we remove the angular momentum of that particle from the disc. This choice does not influence the majority of results, especially in the distant regime of interest. If we chose to ignore unbound particles and average only over those remaining, then at $x_{\rm min}/r = 2$ this only changes the recorded angular momentum loss by $\sim 10\%$ for prograde encounters, and less when $\beta \neq 0^\circ$ for which encounters are less destructive.

3.2.3 Hydrodynamic modelling

Numerical method

We use the SPH code GANDALF (Hubber *et al.*, 2018) to simulate a star-disc interaction including hydrodynamic forces. The encounters under consideration are non-penetrative, and therefore we do not expect strong shocks. For this reason we apply the α-viscosity

formulation of Monaghan (1997) to model the viscous redistribution of angular momentum throughout the disc with a lower value of $\alpha_{\rm AV} = 0.1$ so that viscous evolution is slow. Particles are integrated using the leapfrog kick-drift-kick integration method with a cubic spline kernel. We do not include the self gravity of the SPH particles, or the gravitational effects of the discs on the stars. However, any accreted particles contribute to the mass of the associated sink particle. The smoothing length for both sink particles is defined to be half the inner radius of the disc, $R_{\rm in}/2$.

To investigate the influence of the finite height of the disc, we compare our 3D calculations with equivalent 2D SPH calculations for prograde and retrograde (co-planar) encounters. The resolution at 3D is fixed at 10^6 particles. To reproduce the calculations in 2D, the variable smoothing length h_i for particles at the same radius r_i in the disc needs to be equivalent:

$$h_i = \eta \left(\frac{m_{\rm 3D}}{\rho_i} \right)^{1/3} = \eta \left(\frac{m_{\rm 2D_i}}{\Sigma_{\rm 2D}(r_i)} \right)^{1/2},$$

where $m_{\rm 3D}$ is the (constant) mass of each particle in 3D, and $m_{\rm 2D_i}$ is the position dependent mass of the equivalent particle in 2D. The surface density in 2D $\Sigma_{\rm 2D}$ for a given particle at radius r_i must also be equal to the surface density in 3D such that

$$\Sigma_{\rm 2D}(r) = \Sigma_{\rm 3D}(r) = \Sigma(r)$$

for a prescribed surface density profile Σ. Hence, the mass m_i of a particle at a given radius r_i is

$$m_{\rm 2D_i} = \left\{ \sqrt{2\pi\Sigma(r_i)} H(r_i) m_{\rm 3D} \right\}^{2/3}$$

where $H(r)$ is the scale height of the disc, which is defined in Section 3.2.3, along with our chosen surface density profile. For our physical parameters we find a corresponding 2D resolution of $\sim 10^5$ particles to compare with the 3D version with 10^6 particles.

Initial conditions

We choose disc parameters consistent with those of Rosotti *et al.* (2014), in which hydrodynamic disc evolution is studied in a stellar cluster of 100 stars, so that a comparison can be drawn with their results. These conditions are described as follows.

The surface density follows a truncated power law

$$\Sigma(r) = \Sigma_0 \left(\frac{r}{r_0} \right)^{-p} \tag{3.2}$$

for $p = 3/2$, where r_0 and Σ_0 are the scale radius and surface density scale respectively, and are such that the total mass of the disc is $0.05M_\odot$, although as discussed in Section 3.2.3, this does not modify the overall gravitational potential. Rosotti *et al.* (2014) choose a range of disc radii, but here we choose the model referred to as R10 in that study. This model has an outer disc radius $R_{\rm out} = 10$ au and inner radius of $R_{\rm in} = 2$ au around a star of mass $1M_\odot$.

We choose a locally isothermal equation of state, such that the temperature is

$$T(r) = \max\left[T_0\left(\frac{r}{r_0}\right)^{-q}, 20\text{K}\right]$$

where $q = 3/2$. The height of the disc $H = c_s/\Omega$, where c_s is the sound speed and Ω is the Keplerian frequency, is chosen so that H/r is 0.05 at the inner radius. This implies that $T_0 = 20$ K for $r_0 = 14$ au.

The disc is evolved for ~ 12 orbits at the (viscously evolving) outer radius before and after the stars reach the closest approach distance. This is sufficient for the disc to 'relax' prior to the closest approach but short enough so that the viscous evolution has not significantly altered the surface density profile. As has been found in previous studies (e.g Hall *et al.*, 1996) we find that angular momentum transfer occurs when the phase of the perturbing star is close to pericentre, and for all our SPH results this corresponds to a time span which is $\lesssim [\Omega(R_{\rm out})]^{-1}$, the orbital period at the outer edge of the disc.

3.3 Numerical results

3.3.1 Perturbed ring

The sum of the contributions to $\Delta L/L$ from the numerical integrations in equations A.6 ($m = 2$ ILR, exponential term) and A.4 ($m = 1$ $\omega = 0$ ILR, power law contribution) and the results for a ring of test particles are plotted in figure 3.1 for various orientations. For nearly all regions of the parameter space these results are within order unity of the theoretical counterparts; certainly this is the case for all results for which $|\Delta L/L| > 10^{-5}$. There is some deviation in the results for which the trajectory is highly inclined, in particular for the $\beta \approx 60^\circ, 120^\circ$ results. This is likely to be because the linear estimate for $\Delta L/L$ is made assuming the change in angular momentum is dominated by the change in the initial direction of $\boldsymbol{L}$, which is ΔL_z (see Appendix A.1), whereas this is not strictly true for encounters with a periastron close to perpendicular to the disc plane. However, the regions of parameter space for which the results deviate significantly are those for which angular momentum loss is negligible. This is still true when the mass ratio between the perturbing and central

star M_2/M_1 is increased, as shown in figure 3.2. For this reason we do not investigate the deviation further in this study.

In the limit of large closest approach distances $x_{\rm min}$, the angular momentum loss for a ring at radius r scales as $(x_{\rm min}/r)^{-5}$, which corresponds to the contribution of the $m = 1$, $\omega = 0$ ILR, as approximated by equation A.4. At closer periastron distances, the exponential component from the exact resonances in equation A.6 dominate for prograde and inclined trajectories.

The eccentricity perturbations induced by the tidal disruption are shown in figure 3.3. As angular momentum is proportional to $\sqrt{1-e^2}$, then $\Delta L \propto \Delta e^2$ for $\Delta e \ll 1$ as the particles are initially on a circular ($e = 0$) orbit. Indeed, the change in eccentricity scales with $(x_{\rm min}/r)^{-5/2}$ in the limit of distant encounters, which is in agreement with the results of Heggie and Rasio (1996) for an initially non-eccentric binary. A quantitative comparison with the results of Ostriker (1994) is made in the following Section 3.3.2.

The ratio of the mass of the perturbing star M_2 to that of the host star M_1 also influences the angular momentum loss. From equation A.4 we expect the asymptotic dependence $x_{\rm min} \gg r$ to be $\Delta L/L \propto M_2/M_1$ for $M_2 \gg M_1$. In the close encounter regime however, the exponential component (equation A.6) dominates out to greater $x_{\rm min}/r$. This is shown in figure 3.2 for both test particle and theoretical calculations with $M_2/M_1 = 10$. The loss at $x_{\rm min}/r \sim 6$ is found to be more than two order of magnitudes larger in this case than for $M_2/M_1 = 1$.

3.3.2 Perturbed disc

Ring integration results

To draw useful conclusions regarding cluster dynamics, we present angle-averaged results. The angle averaging is simply the integral over the solid angles such that

$$\left\langle \frac{\Delta L_{\rm r}}{L_{\rm r}} \right\rangle = \frac{1}{4\pi} \int_0^{2\pi} {\rm d}\alpha \int_0^{\pi} {\rm d}\beta \, \sin\beta \frac{\Delta L_{\rm r}}{L_{\rm r}}(\alpha, \beta)$$

evaluated at any given $x_{\rm min}/r$.

We also present, for comparison with Ostriker (1994), the results applied to a synthetic disc that is composed of a suitably weighted ensemble of particle rings which correspond to the same surface density profiles. The fractional change of angular momentum is

$$\left. \frac{\Delta L_{\rm d}}{L_{\rm d}} \right|_{x_{\rm min}} = \frac{\int_{R_{\rm in}}^{R_{\rm out}} {\rm d}r \, r\Sigma(r) \left\langle \Delta L_{\rm r}\left(x_{\rm min}/r\right) \right\rangle}{\int_{R_{\rm in}}^{R_{\rm out}} {\rm d}r \, r\Sigma(r) L_{\rm r}(r)} \tag{3.3}$$

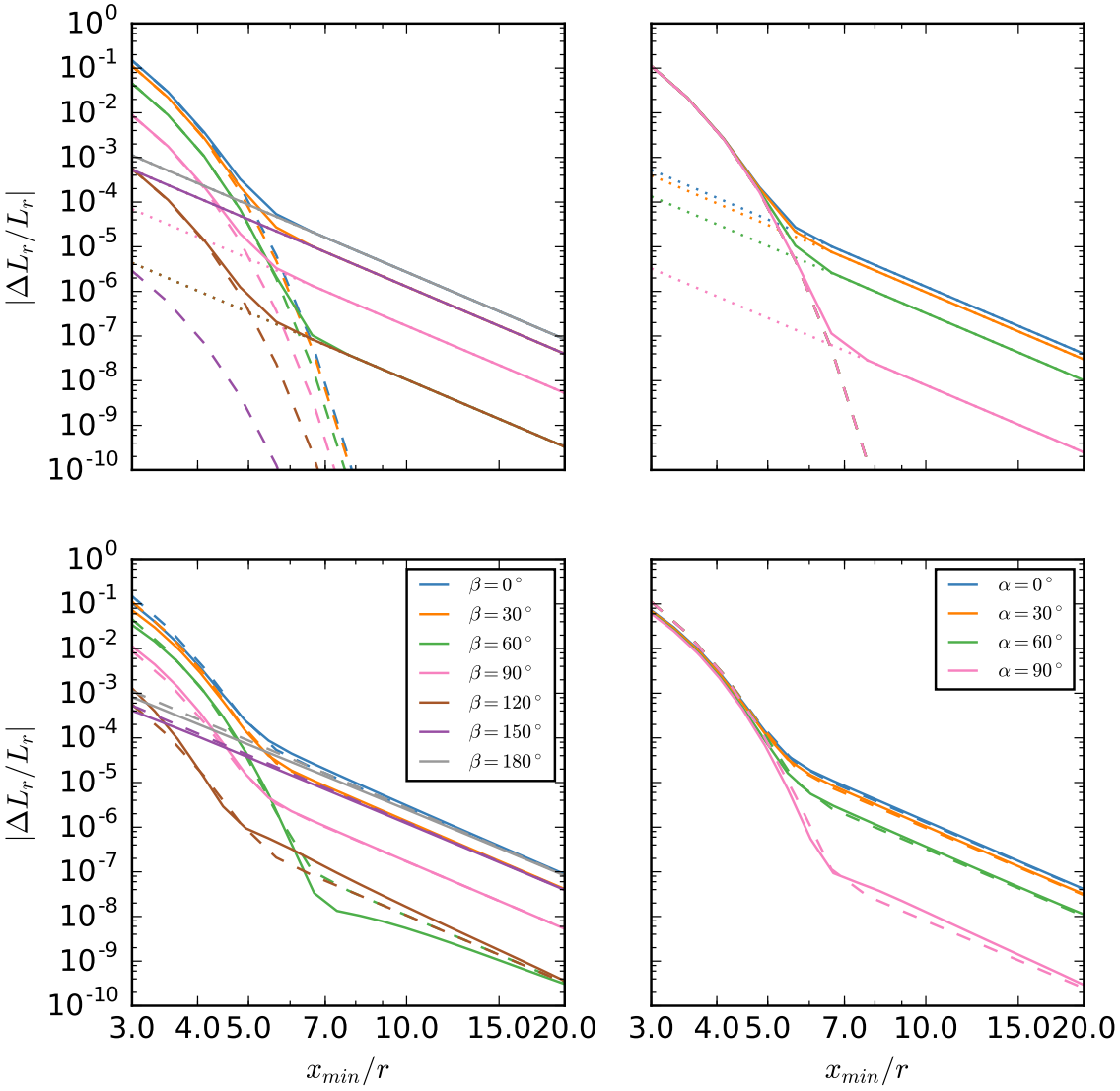

Fig. 3.1 Change of angular momentum for a ring around a central star due to a parabolic encounter between stars of equal mass. The results on the left are for $\alpha = 0°$ and various β values, while those on the right are for $\beta = 30°$ and varying α. In the top panels are the results of evaluating equations A.4 (dotted lines) and A.6 (dashed lines) for the linear approximation of the fractional angular momentum change, with the solid line showing the sum of the two components. In the bottom plots, the dashed lines are the theoretical results, while the solid lines are the results for a ring of test particles.

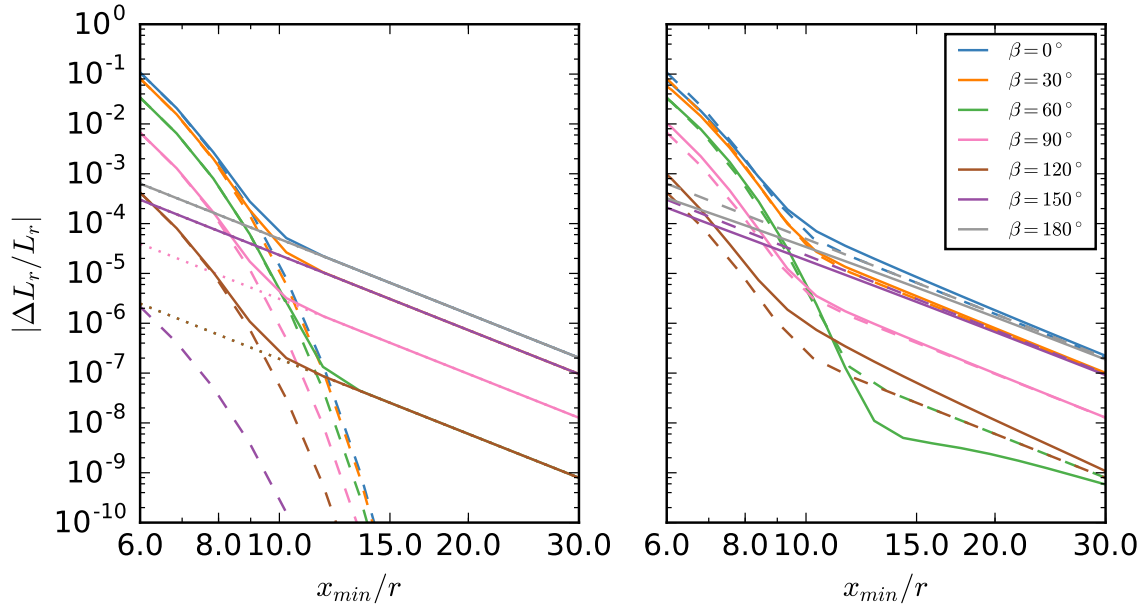

Fig. 3.2 Fractional angular momentum loss for a massless ring around a central star of mass M_1 when perturbed by a star of mass M_2 such that $M_2/M_1 = 10$. Results are shown for $\alpha = 0°$ and varying β. In the left panel, the evaluation of equations A.4 and A.6 are shown in dotted and dashed lines respectively, while the sum is shown as a solid line. In the right panel the solid lines are for a ring of test particles, with the dashed lines being the theoretical counterparts.

for a disc with an arbitrary surface density profile Σ. For a low mass disc composed of test particles, orbits are Keplerian such that $L_\mathrm{r} \propto r^{1/2}$.

The angle averaged results for a ring of particles, and discs as described in equation 3.3 applied to power law surface densities (equation 3.2) are presented in figure 3.4 for various values of p, truncated at a given outer radius R_out. Practically, because we do not have numerical test particle results for $x_\mathrm{min}/r \to \infty$, contributions have to be truncated for small radial extents r within the disc, and we choose $R_\mathrm{out}/R_\mathrm{in} = 5$. The inner disc contributions would be negligible, and the results in figure 3.4 are dominated by the surface density at the outer radius due to the strong dependence on x_min/r.

Our results agree with those of Ostriker (1994, see figure 5 therein) in the exponential ILR regime described by equation A.6, as expected. The asymptotic slope differs slightly however, as in that study the vertical resonance was considered dominant, such that $\Delta L_\mathrm{d} \propto (x_\mathrm{min}/r)^{-4.5}$. By contrast, we find a power law index of -5 as predicted in equation A.4. Quantitatively our results are an order of magnitude lower at $x_\mathrm{min}/R_\mathrm{out} = 5$ and a factor ~ 30 lower at $x_\mathrm{min}/R_\mathrm{out} = 10$. However, since $\Delta L/L$ is small in this region, these differences are not of practical significance.

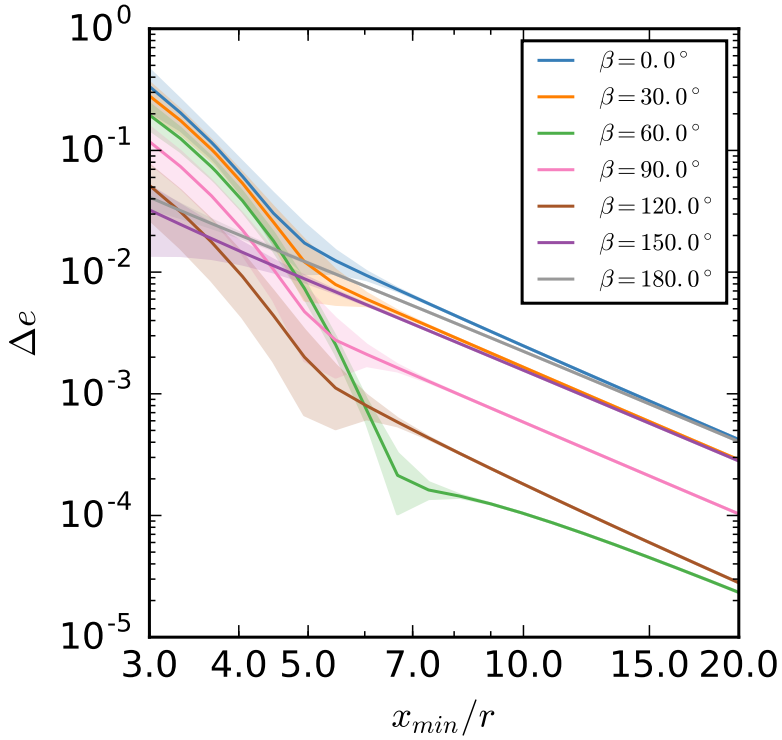

Fig. 3.3 Change in eccentricity Δe of a ring of initially non-eccentric test particles at radius r induced by a parabolic stellar encounter with closest approach $x_{\rm min}$ in which both stellar components have equal mass. The shaded region around each line indicates the standard deviation of the induced particle eccentricities around each result.

SPH disc results

In our comparisons between the hydrodynamic results and the particle ring ensemble (figure 3.5) the fractional angular momentum in both cases is plotted as a function of the ratio of $x_{\rm min}$ to the disc half-mass radius $R_{1/2}$. This radius is defined at the time of pericentre for an equivalent disc evolving viscously in isolation, although in practice there is little difference between this and the initial value of $R_{1/2}$. We make this choice of radius here for direct comparison with the results of Rosotti *et al.* (2014), and because it is not in general possible to clearly define an outer radius for a viscously evolving disc. The calculations become noise dominated for $|\Delta L/L| \lesssim 10^{-3}$. We see good agreement for $x_{\rm min}/R_{1/2} \gtrsim 4$, and results within a factor of order unity for closer encounters. For our chosen definition of radius (the half-mass radius $R_{1/2}$) with outer radius to inner disc radius ratio $R_{\rm out}/R_{\rm in} = 5$ and $p = 3/2$, we have $R_{\rm out} \approx 1.91 R_{1/2}$, which puts the closest encounters at $x_{\rm min}/R_{\rm out} \approx 1.57$.

The non-zero height of the disc in the 3D case has not significantly altered the results in comparison to the 2D case shown in figure 3.6. The majority of results are dominated

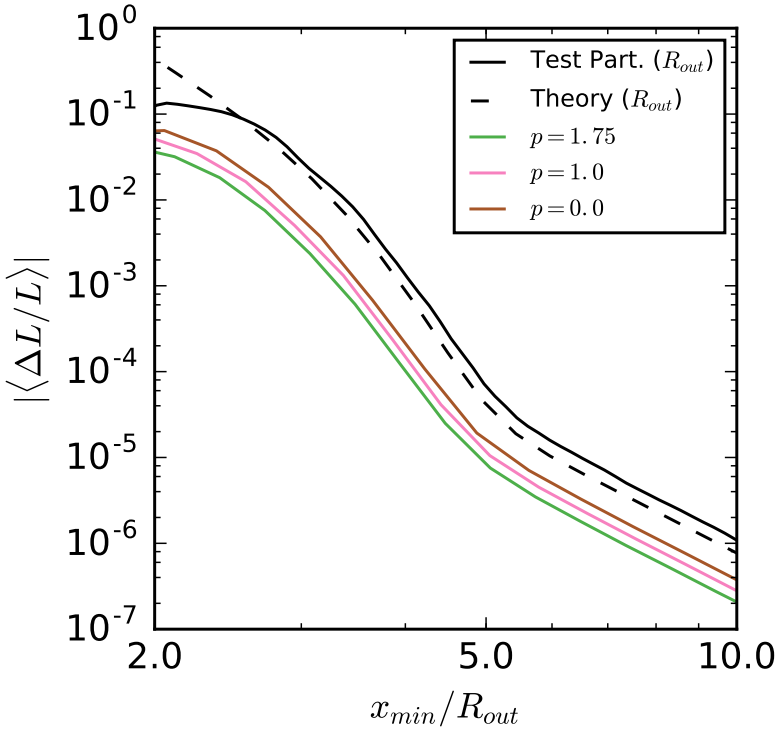

Fig. 3.4 Angle averaged angular momentum transfer due to an equal mass perturber for discs constructed from test particle rings with surface densities following various powerlaws $\propto r^{-p}$ and $R_{\rm out}/R_{\rm in} = 5$. The $p = 1.75$ and $p = 1$ results are comparable to the results in figure 5 of Ostriker (1994). The dashed line represents the theoretical angular momentum loss for a ring with radius $R_{\rm out}$, and this is compared with the ring of test particle case (solid black line).

by the exponential component, with the exception of the almost retrograde encounters $\beta = 150^\circ, 180^\circ$ where the $m = 1$, $\omega = 0$ ILR dominates for all $x_{\rm min}/r$. In figure 3.6 we have compared the SPH results with the equivalent disc reconstructed out of rings using the results in Section 3.3.2 which do not include viscous and pressure forces. For this comparison we used both the analytic surface density profile and one taken directly from an unperturbed SPH disc at the time of closest approach, but find no significant difference between them. The case shown in figure 3.6 is for the analytic surface density profile. The resolution and convergence of these results is demonstrated in Appendix A.2 for which no difference is found using 10^6 particles in 2D above the noise limit. The minor differences compared to the N-body results only play a significant role in strong interactions, where $x_{\rm min}/R_{1/2} \lesssim 5$ for a prograde encounter (and angular momentum transfer is non-linear). As these differences are not numerical in origin, they are indicative of hydrodynamical effects not present in the N-body calculations.

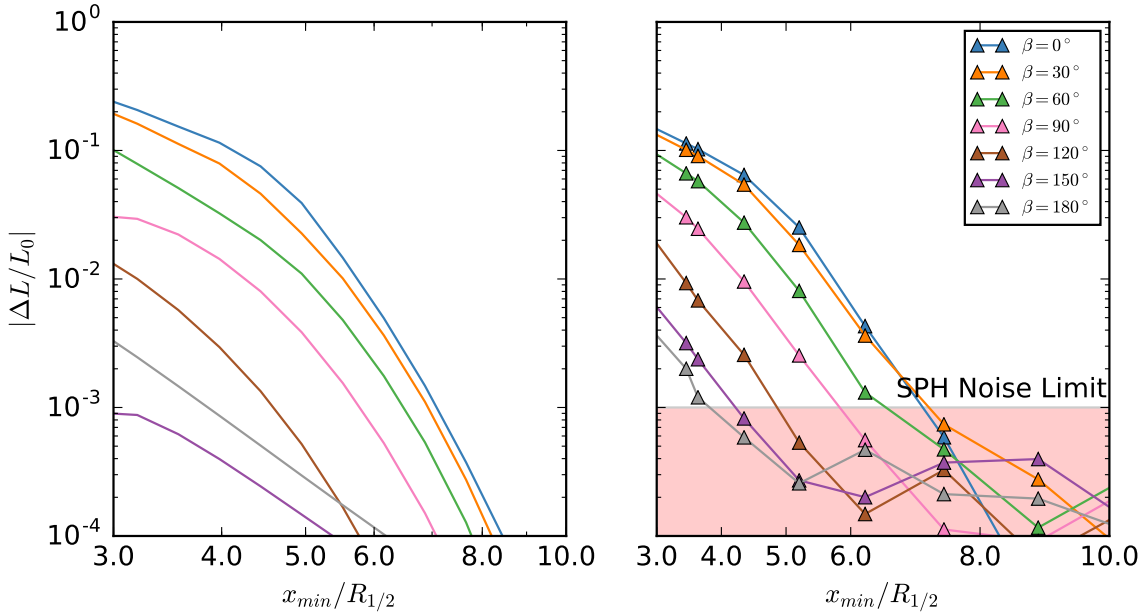

Fig. 3.5 Angular momentum transfer for a disc of half mass radius $R_{1/2}$ around a star of mass $1M_{\odot}$, perturbed by a star of equal mass for various closest approach distances $x_{\rm min}$. The angular momentum vectors between the disc and perturber are offset by various angles β, while $\alpha = 0°$. The left panel is for a disc of test particles, reconstructed from annuli results for analytic power law surface density distribution with $p = 1.5$. On the right is the same result for a 3D SPH simulation, with triangle markers representing data points. The region below the empirical noise limit is highlighted in red.

In summary, we have found good agreement across all of our results. The linear calculations detailed in Appendix A.1 match well with our integration of rings of test particles, and these results in turn agree with full hydrodynamical simulations for interactions such that $|\Delta L/L| > 10^{-3}$. Unfortunately the noise limit of the SPH simulations leaves us unable to test the power law dependence of the angular momentum transfer on $x_{\rm min}/r$ for distant encounters ($x_{\rm min}/r \gtrsim 6$). However these encounters are of little physical significance given their negligible effect on the disc. We conclude that our results for the tidal influence of a gravitationally focused encounter are robust.

3.4 Discussion

We show the angle averaged results for the fractional angular momentum change per encounter as a function of $x_{\rm min}$ and M_2/M_1 in figure 3.7. The black contour represents the point at which the fractional angular momentum loss per encounter is 0.1 and which we use as the demarcation between linear and non-linear encounters (corresponding to a reduction

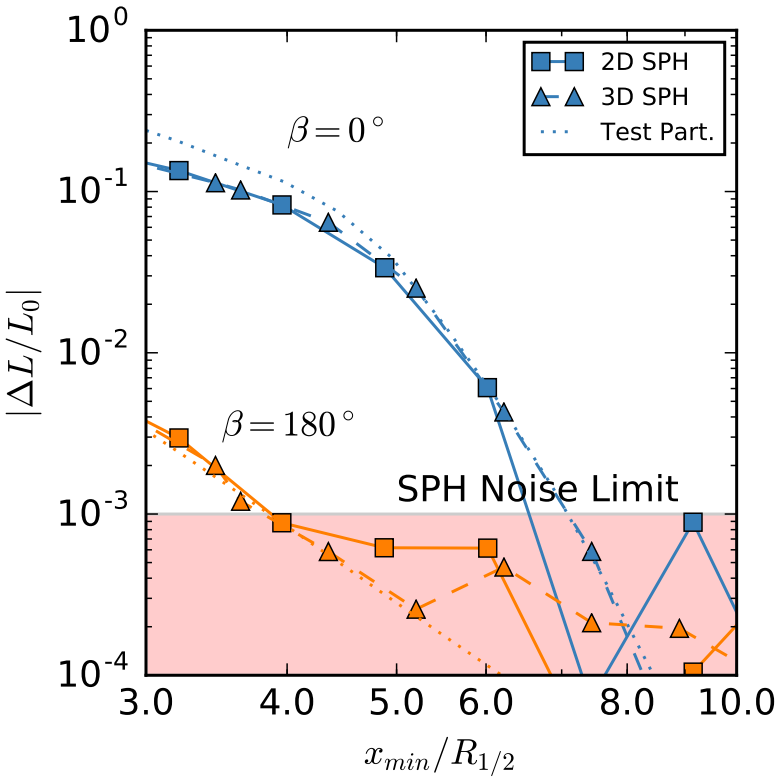

Fig. 3.6 The solid lines (square markers) show the angular momentum transfer for a disc of SPH particles due to a perturber as in figure 3.5 in two dimensions, hence with prograde and retrograde trajectories only. The same results are shown for the 3D case (dashed lines, triangle markers) and for a disc reconstructed from rings of test particles using the results of the MERCURY code calculations (dotted lines). The region in which the SPH calculations become noisy is shaded.

of the outer disc radius of around 20%). The value of $x_{\rm min}$ for which $\Delta L_{\rm r}/L_{\rm r} = 0.1$ we denote $x_{\rm lin}$, which is a function of the mass ratio M_2/M_1. For closer encounters (i.e. for $x_{\rm min} < x_{\rm lin}$) fractional angular momentum loss is of order unity. Figure 3.7 illustrates that, while more massive perturbers enter the non-linear regime at larger radius, the decline in angular momentum loss in the linear regime is steep for all perturber masses and relates to the exponential decline (equation A.6).

We illustrate the minor role of encounters in the linear regime by considering the integrated effect of encounters in a stellar population. As discussed in Chapter 1 (see equation 1.25 and 1.26) the differential encounter rate scales as

$$\mathrm{d}\mathscr{E}(x_{\rm min}) \propto \left(GM_{\rm tot} + 4\sigma_v^2 x_{\rm min}\right)\,\mathrm{d}x_{\rm min} \tag{3.4}$$

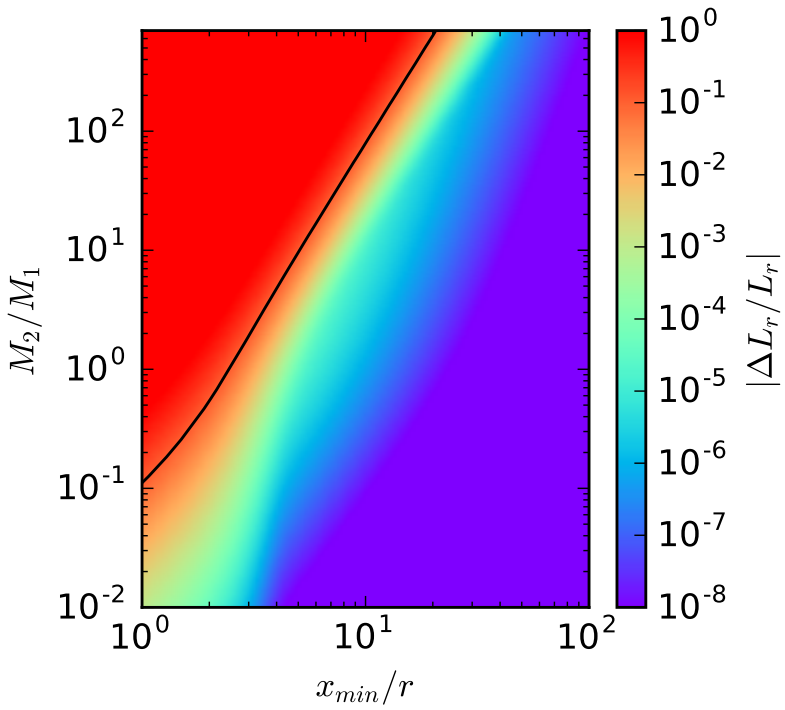

Fig. 3.7 Theoretical angle-averaged parameter space exploration for the fractional angular momentum loss induced for a ring of particles, surrounding a star of mass M_1, by a parabolic encounter with a star of mass M_2. The contour follows the line at which $\Delta L_\mathrm{r}/L_\mathrm{r} = 0.1$, where the linearised equations A.4 and A.6 evaluated here are no longer appropriate.

for a one dimensional velocity dispersion σ_v, and total mass M_tot. We can therefore compute, in a given time τ, the expected fractional change in angular momentum from encounters in a unit interval of x_min by combining equation 3.4 with the angle averaged change in angular momentum per encounter $\langle \Delta L_\mathrm{r}/L_\mathrm{r} \rangle$:

$$\frac{\partial(\Delta L_\mathrm{r}/L_\mathrm{r})}{\partial x_\mathrm{min}} = \int_0^\tau \left\langle \frac{\Delta L_\mathrm{r}}{L_\mathrm{r}} \right\rangle \frac{\partial \mathscr{E}(x_\mathrm{min})}{\partial x_\mathrm{min}} \mathrm{d}t. \tag{3.5}$$

We have assumed in equation 3.4 that encounters are uncorrelated and make no attempt to include the physical properties of a cluster, such as internal sub-structure (e.g. Craig and Krumholz, 2013), since here we are only interested in the influence of distant encounters relative to close ones, not the absolute effect of encounters on disc evolution.

In figure 3.8 we depict $\partial(\Delta L_\mathrm{r}/L_\mathrm{r})/\partial x_\mathrm{min}$ (equation 3.5) over a time interval such that the expected number of encounters with $x_\mathrm{min} < x_\mathrm{lin}$ over this time is unity. We see that the angular momentum change due to the cumulative effect of encounters decreases rapidly with x_min. Moreover, integration of $\partial(\Delta L_\mathrm{r}/L_\mathrm{r})/\partial x_\mathrm{min}$ over x_min outwards of x_lin shows that the

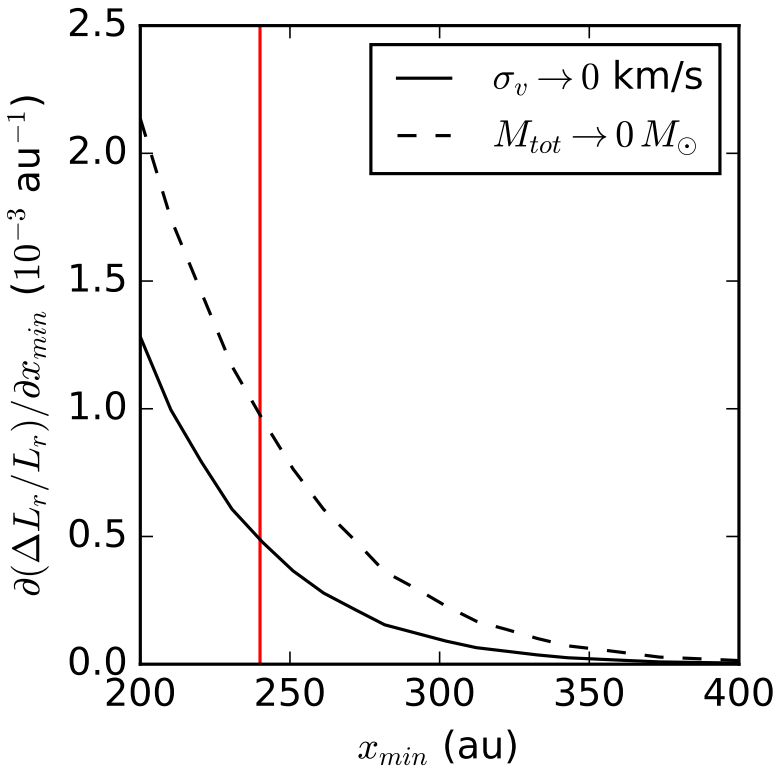

Fig. 3.8 Estimated differential total angular momentum loss for a ring of particles at $R_{\rm out} = 100$ au from the host star. Results are shown over a time period such that expected number of encounters such that $x_{\rm min} < x_{\rm lin} \approx 2.4 R_{\rm out}$ for each star is unity (see text for details). The value of $x_{\rm lin}$ is indicated by the vertical red line. This limit can be generalised for arbitrary mass ratio M_2/M_1 by applying the appropriate angular momentum loss threshold, as shown by the black contour in figure 3.7. The two most extreme cases for a cluster are shown: the solid line is the limit in which the stellar velocity dispersion is small, and the dashed line is in the limit of an energetic cluster (equation 3.4).

total fractional angular momentum loss due to encounters in the linear regime over this time interval is 1.7% in the limit of a cold cluster ($\sigma_v \to 0$), and 4% when the encounter rate (equation 3.4) is dominated by high velocity encounters. Since the time interval has been chosen so that each star is expected to have experienced one encounter inward of $x_{\rm lin}$ over this period, and since such encounters within $x_{\rm lin}$ cause an angular momentum reduction of order unity, it follows that the additional effect of encounters outside $x_{\rm lin}$ is negligible by comparison. This time period is dependent on the local physical conditions in the cluster, and may be greater or less than the age of a given stellar population. Although figure 3.8 illustrates the situation for equal mass encounters, the exponential fall-off in angular

momentum transfer in the linear regime at all masses (figure 3.7) means that this minor role for encounters in the linear regime persists for all M_2/M_1.

Finally, figure 3.7 shows the region of parameter space for which encounters are at all important, from which a 'close-regime' (i.e. a spatial region in which significant angular momentum loss from the disc occurs) can be defined for an arbitrary pair of stellar masses. This spatial scale is approximately proportional to $(M_2/M_1)^{1/3}$, consistent with the empirical findings of Breslau *et al.* (2014) for coplanar, prograde encounters. To obtain a general prescription for the effect of close encounters, a full study of the parameter space in this regime is required. Further complication arises since the encounters at large separations for large M_2 are frequently hyperbolic, particularly in hot, high density environments. These issues are addressed in Chapter 4.

3.5 Conclusions

We have presented a robust analysis of the angular momentum loss for PPDs during a gravitationally focused encounter. Good agreement is found between the theoretical prescription adapted from Ostriker (1994), the test particle case explored through N-body simulations, and hydrodynamic simulations for regions of parameter space for which ΔL is greater than the numerical noise limit.

The angular momentum transfer between disc and perturbing star is dominated by two resonances for non-retrograde encounters; the $m = 2$ ILR at small $x_{\rm min}/r$ ($\lesssim 6$ for $M_1 = M_2$) and the $m = 1$, $\omega = 0$ ILR for a secular perturbation at larger encounter distances. For close to retrograde encounters, $150^\circ \lesssim \beta \lesssim 210^\circ$ the $m = 2$ ILR contribution is negligible, and hence transfer is dominated everywhere by the $m = 1$ ILR.

We contextualise these results by plotting the angle averaged fractional change in angular momentum per encounter in figure 3.7 as a function of perturber mass and closest approach distance. Figure 3.7 demonstrates the steep fall off in efficiency of angular momentum transfer in the linear regime for all perturber masses. We show that the total angular momentum loss is always dominated by encounters in the non-linear regime (close encounters at separations less than the black contour shown in figure 3.7) and that the angular momentum transfer instead associated with the linear regime is a small fraction ($< 4\%$) of this value.

In the context of PPD evolution within a stellar cluster, this allows us to conclude that the influence of distant encounters on the disc is negligible, where 'distant' is here defined to be any encounter for which the fractional angular momentum loss at the outer edge is $|\Delta L/L| < 0.1$. If a cluster is composed of single mass stars this conclusion is equivalent

to the statement that encounters with $x_{\min}/R_{\text{out}} > 2.4$ can be ignored, despite the increased probability of such an encounter occurring.

Our theoretical prescription can also be applied to find the upper limit of the closest approach distance at which a disc is significantly truncated for a given mass ratio M_2/M_1. Influential encounters in the large M_2 regime can occur at comparatively large $x_{\min}/R_{\text{out}}$ and are therefore more likely to be considerably hyperbolic. We will consider the influence of hyperbolic non-linear encounters and their role in stellar clusters in the following chapter.

Chapter 4

Tidally truncated PPD radii in clusters

This chapter is based on Winter *et al.* (2018c), which I have divided between this and Chapter 5. I have performed all the simulations and analysis presented here and written the majority of the text.

4.1 Introduction

Having illustrated in Chapter 3 that the influence of frequent distant type II encounters has a negligible influence on a PPD with respect to a single close encounter, this chapter addresses the latter regime. This involves numerically quantifying the influence of all encounters on the outer radius of a disc in a given stellar cluster environment. We perform numerical simulations to establish a more general prescription for the tidal truncation radius than is currently available in the literature. Subsequently, we apply this prescription with theoretical stellar encounter rates to quantify disc outer radius evolution assuming this is driven by type II tidal interactions.

Previous works have made parameterisations of the truncation radius due to star-disc encounter, for example Breslau *et al.* (2014) find an empirical relation for the truncation radius of a disc of test particles for a range of perturber to host mass ratios M_2/M_1. However, as with the previous investigation of Hall *et al.* (1996), this calculation was not performed over an exhaustive range of disc orientations such that angle averaged results could be obtained. Nor were hyperbolic trajectories considered. Clearly a prescription for the former is necessary to apply to general encounters in a cluster. It also turns out that many encounters that occur in a cluster with a realistic distribution of stellar masses are highly hyperbolic (e.g. Vincke and Pfalzner, 2016), therefore an evaluation of the influence of hyperbolic encounters on a disc is also required.

Bhandare *et al.* (2016) attempted to expand on the Breslau *et al.* (2014) study by angle averaging over disc truncation radii. However the fitted prescription for the post-encounter disc radius is not scale-free since it would imply that the ratio of post-encounter radius to pericentre distance depends on the absolute value of the latter. Hence, while we expand on the parameter space by considering different eccentricity encounters, here we use a fresh approach for finding the mass dependence for angle-averaged tidal truncation radii.

For disc evolution we consider the case both of a solar mass star, and smaller stars at the hydrogen burning limit. We take a canonical initial outer disc radius of 100 au and apply statistical arguments to follow the radius evolution over 3 Myr of evolution for a range of cluster densities and velocity dispersions. Observational evidence suggests discs around brown dwarves are more compact than around solar mass stars (Alves de Oliveira *et al.*, 2013; Testi *et al.*, 2016; Tazzari *et al.*, 2017; Tripathi *et al.*, 2017). We aim to establish whether close encounters are a plausible mechanism for this difference.

4.2 Numerical method

We follow the same numerical method as discussed in Chapter 3 to evaluate the effect of a stellar encounter on a ring of test particles around a host star, which we review briefly here. The general Bulirsch-Stoer algorithm of the MERCURY orbital integrator for solar-system dynamics is used (Chambers, 1999).

We have modelled each ring with $N = 200$ particles, being a compromise between computational expense and accuracy (this choice is discussed in Appendix B.1). A ring of N particles is then fixed at some distance r from a central star of mass M_1. A second star of mass M_2 is placed on a trajectory at a time 50 test particle orbits prior to the closest approach, and integrated for the same time after that approach. Although for different r this does not physically correspond to the same phase difference the results are found to be insensitive to the initial location of the perturber.

We define two angles of orientation: the angle between the direction of pericentre and the line of intersection of the disc and the orbital plane, α, and the angle between the angular momentum vector of the disc and that of the orbit, β (as in Chapter 3). We angle-average all our results (Section 4.4), therefore the precise definition of the disc orientation is not important.

4.3 Outer radius definition

To establish the outer disc radius after an encounter $R'_{\rm out}$, previous studies have based definitions of this radius on some limit on the surface density of a disc (e.g. Breslau *et al.*, 2014). We define $R'_{\rm out}$ by the post-encounter circularisation radius of particles that remain bound after the encounter (i.e. considering the test particle to be a fluid element, for which pressure forces would damp eccentricity over time). Assuming Keplerian motion, angular momentum for a particle is $L \propto r^{1/2}$, therefore the fractional change in radius for a particle i:

$$\frac{\Delta r_i}{r} = \left(\frac{\Delta L_i}{L}\right)^2 + \frac{2\Delta L_i}{L}$$

We average the circularisation radii for all particles in the ring that remain bound and define the disc outer radius to be the maximum value of r' for all the rings in the disc. Rings where $< 90\%$ of the particles remain bound after the encounter are excluded in the determination of the new disc outer radius. Otherwise, the trajectories of a small number of particles introduce significant noise into the outer radius determination. The new outer radius of the disc is thus defined:

$$R'_{\rm out} = \max\left\{r + \Delta r : r < R_{\rm out} \text{ and } N'/N > 0.9\right\}$$

and the change in outer radius is $\Delta R_{\rm out} = R_{\rm out} - R'_{\rm out}$. In the case of close, coplanar, prograde and parabolic encounters, this definition yields the same truncation radius as in the literature $R'_{\rm out} \approx 0.28(M_2/M_1)^{1/3} x_{\rm min}$ (e.g. Hall *et al.*, 1996; Breslau *et al.*, 2014).

4.4 Angle-averaged model

To make our results applicable to general encounters, we produce a set of equations to define the post-encounter outer radius $R'_{\rm out}$ as a function of the encounter parameters: the closest approach distance $x_{\rm min}$, the eccentricity $e_{\rm pert}$ and the ratio of the perturbing to host mass M_2/M_1. The orientation of the disc with respect to the orbit of the perturbing star is also important for the truncation radius; to simplify the models we consider the angle-averaged results. These are given by

$$\left\langle \frac{\Delta R_{\rm out}}{R_{\rm out}} \right\rangle = \frac{1}{4\pi} \int_0^{2\pi} {\rm d}\alpha \int_0^{\pi} {\rm d}\beta \, \sin\beta \, \frac{\Delta R_{\rm out}}{R_{\rm out}}(\alpha, \beta)$$

where α and β parameterise the disc orientation as described in Section 4.2. The angle-averaging is in fact the sum over trapezia using the outer radius results at intervals of 30° so that calculations over the required range of angles are computationally practicable.

We now consider the nature of the fitting formulae that we apply to the numerical results for disc truncation radii. It turns out that an appropriate general form for a model is complicated by the non-trivial dependence on M_2/M_1, $e_{\rm pert}$ and $x_{\rm min}/R_{\rm out}$ for the contribution to the fractional change in angular momentum $\Delta L/L$ from various resonances. The dominant resonance in a given region of parameter space defines how the truncation radius scales locally with these variables. Creating a complete fitting function for each resonance would be both numerically challenging and of limited use for application to cluster models. Fortunately, considering the angle-averaged results, most regions of parameter space for which encounters are expected to be important can be modelled simplistically such that the the resulting fitting formula is an accurate description of the numerical results to within $\sim 10\%$.

We identify three distinct regions in $x_{\rm min}/R_{\rm out}$ space. It is more convenient to work in reciprocal space; we denote $R_{\rm out}/x_{\rm min} \equiv R_x$, with the associated post-encounter fractional radius $R'_{\rm out}/x_{\rm min} \equiv R'_x$. In Chapter 3 we show that the distant encounters have a negligible influence on the disc, and we are therefore free to assume that for R_x smaller than some limit, $R'_x \approx R_x$ (the 'distant regime').

The 'close regime' is the opposite limit for which R_x is large. Here R'_x is independent of R_x, constant for fixed M_2/M_1, $e_{\rm pert}$ (i.e. the final disc radius is independent of the disc's initial outer radius). The angular momentum loss increases with M_2/M_1 and decreases with increasing $e_{\rm pert}$ for close encounters, and the opposite for R'_x. Empirically, the dependence of this truncation radius on $e_{\rm pert}$ decreases as M_2/M_1 increases.

At this stage, we identify a useful quantity to generalise results for unit mass ratio to arbitrary M_2/M_1. In Chapter 3 we indicate the limiting distance for a closest approach above which linearised equations are applicable: $1/R_x > X^*_{M_2/M_1}$, which is a function of the ratio of the perturbing to host masses. This is defined by the value of R_x for which $\Delta L/L = 0.1$ at the outer edge of the disc. This is approximately

$$X^*_{M_2/M_1} \approx 2.4(M_2/M_1)^{1/3}, \tag{4.1}$$

consistent with the findings of Vincke and Pfalzner (2016). Equation 4.1 is plotted against the theoretical value obtained directly from the linearised equations in figure 4.1. This quantity defines the ratio of $x_{\rm min}$ to $R_{\rm out}$ within which encounters are significant and therefore provides an approximate mapping between results for the $M_2/M_1 = 1$ case and a general perturbing mass ratio. We define

$$f \equiv X^*_1/X^*_{M_2/M_1} \approx (M_2/M_1)^{-1/3} \tag{4.2}$$

such that an encounter with closest approach $x_{\min}$ in the case that $M_2/M_1 \neq 1$ is approximately dynamically equivalent to an encounter with closest approach $f x_{\min}$ in the case that $M_2 = M_1$.

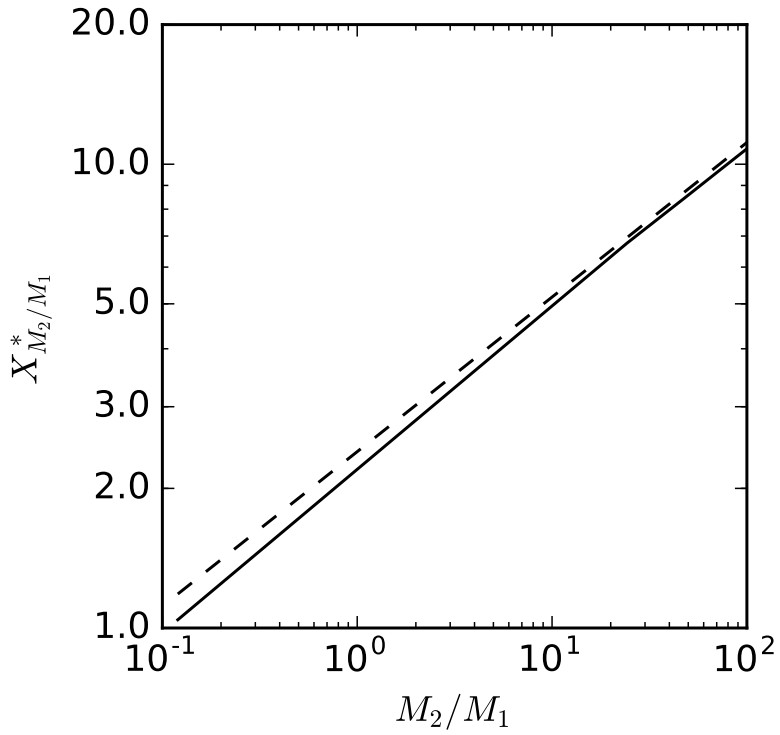

Fig. 4.1 The lower limit of the fractional closest approach distance $1/R_x$ for which the linearised equations apply, defined to be where $\Delta L/L = 0.1$ at the outer edge of the disc. The dashed line is the approximate value from equation 4.1, while the solid line is the value obtained directly from the linearised equations (Chapter 3).

With these definitions, we define the functional form of the model in the close-regime to be

$$R'_{x_{\text{close}}} \equiv \phi_1 {e_{\text{pert}}}^{f\phi_2} \cdot f \left(\frac{M_2}{M_1}\right)^{\phi_3} \tag{4.3}$$

where ϕ_i are fitting constants, $\phi_{1,2} > 0$. The quantity ϕ_1 represents the limiting value of R_x for unit mass ratio and a parabolic orbit, and therefore for a parabolic orbit of arbitrary mass ratio we would expect $R'_x = f\phi_1$ according to the argument set out above. However, we have included an additional correction factor dependent on M_2/M_1. This is because our unmodified scale factor f is based on the mass dependence of the $m = 2$ ILR, which is not the dominant resonance excited in the disc for extremely close encounters. While this in some respects makes our definition of f redundant, we expect this correction factor to be small ($|\phi_3| \ll 1$), and f is still meaningful in relating the scaling of our composite solutions.

Parameter	ϕ_1	ϕ_2	ϕ_3	ψ_1	ψ_2	ψ_3
Value	0.629	0.112	0.133	0.301	0.936	0.320

Table 4.1 Values for the fitting parameters for our general model for post-encounter disc radius.

Our model is simplified by making assumptions about how the dependence on eccentricity is related to the mass ratio, scaling ϕ_2 by f.

The functional form of the 'intermediate region' (between the region of negligible truncation and tidal truncation to a fixed fraction of the closest approach) is extremely complex. However, we find a much simplified linear prescription for the new outer radius to be acceptable:

$$R'_{x_{\text{inter.}}} \equiv (1 - \psi_1 e_{\text{pert}}^{-\psi_2}) R_x + f \psi_1 \psi_3 e_{\text{pert}}^{-\psi_2} \tag{4.4}$$

where $\psi_i > 0$ are fitting constants, and $\psi_1 < 1$. Our full model for the post-encounter radius is then

$$R'_x = \min \left\{ R_x, R'_{x_{\text{inter.}}}, R'_{x_{\text{close}}} \right\} \tag{4.5}$$

fully defined by the six fitting parameters $\phi_{i=1,2,3}, \psi_{i=1,2,3}$.

4.5 Post-encounter disc radius

Our model, the form of which is described by equations 4.2 through 4.5, is fitted with the parameters summarised in table 4.1. Figure 4.2 shows the results in the $M_2/M_1 = 1$ case. The model agrees with the simulation results within 10% except in the limit of large e_{pert} and $R_{\text{out}}/x_{\text{min}}$ (penetrating, hyperbolic encounters). Encounters in this region of parameter space are both unlikely and expected to yield capture scenarios and complete PPD destruction. Nonetheless, caution should be used when applying our results for arbitrary masses and eccentricities. Due to the divergence from the model in the highly hyperbolic limit, we exclude the $e_{\text{pert}} = 40$ results during our fitting procedure.

To obtain the final fitting parameter ϕ_3, we choose the value which best fits the simulation results for $M_2/M_1 = 10$, shown in figure 4.3. The form of the fitting function ensures that R'_{out} is less dependent on e_{pert} for large M_2/M_1. This assumption proves partially true. In fact, the relationship between these parameters is more complex, and in the $M_2/M_1 = 10$ case we find that $R'_{\text{out}}/x_{\text{min}}$ does not vary monotonically with e_{pert}. Our prescription is only out by more than 20% in the extremely hyperbolic case $e_{\text{pert}} = 40$, and for all the rest of the results the model is accurate within 10%.

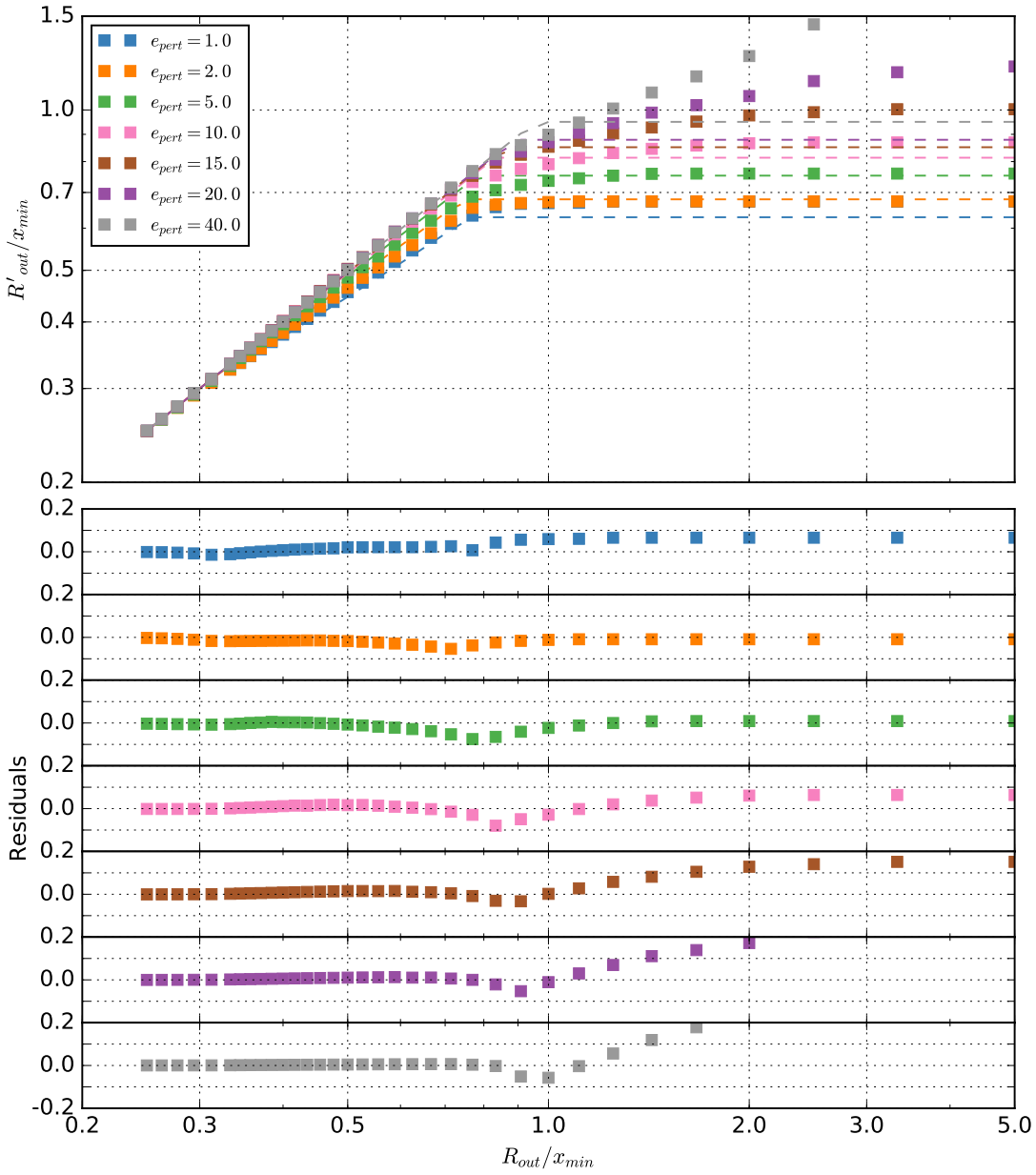

Fig. 4.2 The angle-averaged post-encounter radius $R'_{\rm out}$ of a disc with initial radius $R_{\rm out}$ as a fraction of the closest approach distance of an encounter $x_{\rm min}$ where stellar components are of equal mass $M_2/M_1 = 1$. Simulation data points are shown as squares. The model, which is fitted to the data points where the perturber eccentricity $e_{\rm pert} \leq 20$, is shown by the dashed lines (see the text for details). The residuals are shown in the bottom panel.

We further test our model for $M_2/M_1 = 100$, where the dependence of the truncation radius on $e_{\rm pert}$ is more complex and difficult to model accurately than at lower mass ratios. Despite this, the majority of our numerical results remain within $\sim 20\%$ of the model predictions. Since penetrating hyperbolic encounters with a mass ratio $M_2/M_1 \sim 100$ occur with low probability (given the form of the IMF and typical velocity dispersions in clusters), we do not address a more sophisticated treatment of this region of parameter space here.

A comparison between the simulation results and the model is shown for $M_2/M_1 = 0.5$ in figure 4.4. No further adjustment to the model parameters is applied in this case. Results are once again within 10% of the model for $e_{\rm pert} < 10$, and the discrepancies largely occur in regions which are both unlikely (highly hyperbolic and close encounters) and prone to inducing binaries or disc destruction.

Additionally, we investigate the effect of varying the particle number threshold for N'/N, and find that reducing it only influences the results for low probability (i.e. highly hyperbolic, penetrating) encounters. Our model remains in agreement with the simulation results within 10% in the regions of parameter space that are of interest.

4.6 Encounter rate

To generate appropriate cluster models, we must first establish the encounter rate for varying environments. The usual approach is to ask some variation on the question 'what is the probability that a disc experiences an encounter closer than some separation $x_{\rm min}$?' (e.g. Binney and Tremaine, 1987; Ostriker, 1994, and discussion in Chapter 1). However, this question crucially depends on the effective number density of the stellar population $n_{\rm eff}$ which is dependent both on sub-structure evolution and spatial location within the cluster (Craig and Krumholz, 2013). Instead of trying to model the global evolution of a stellar population with a spatially dependent number density distribution, we consider local conditions for simplicity. On the issue of sub-structure, Craig and Krumholz (2013) found that for a modest fractal dimension, D, the *overall* number of close encounters during the lifetime of the cluster can become enhanced by a factor of a few, even though the sub-structure is eliminated over a crossing time. Therefore this should be considered if we want an accurate estimate of the degree to which stellar encounters are important.

From Craig and Krumholz (2013) the effective number density is linked to the fractal dimension by

$$n_{\rm eff} = n_{\rm c} \cdot 2^{(3-D)(g-1)}$$

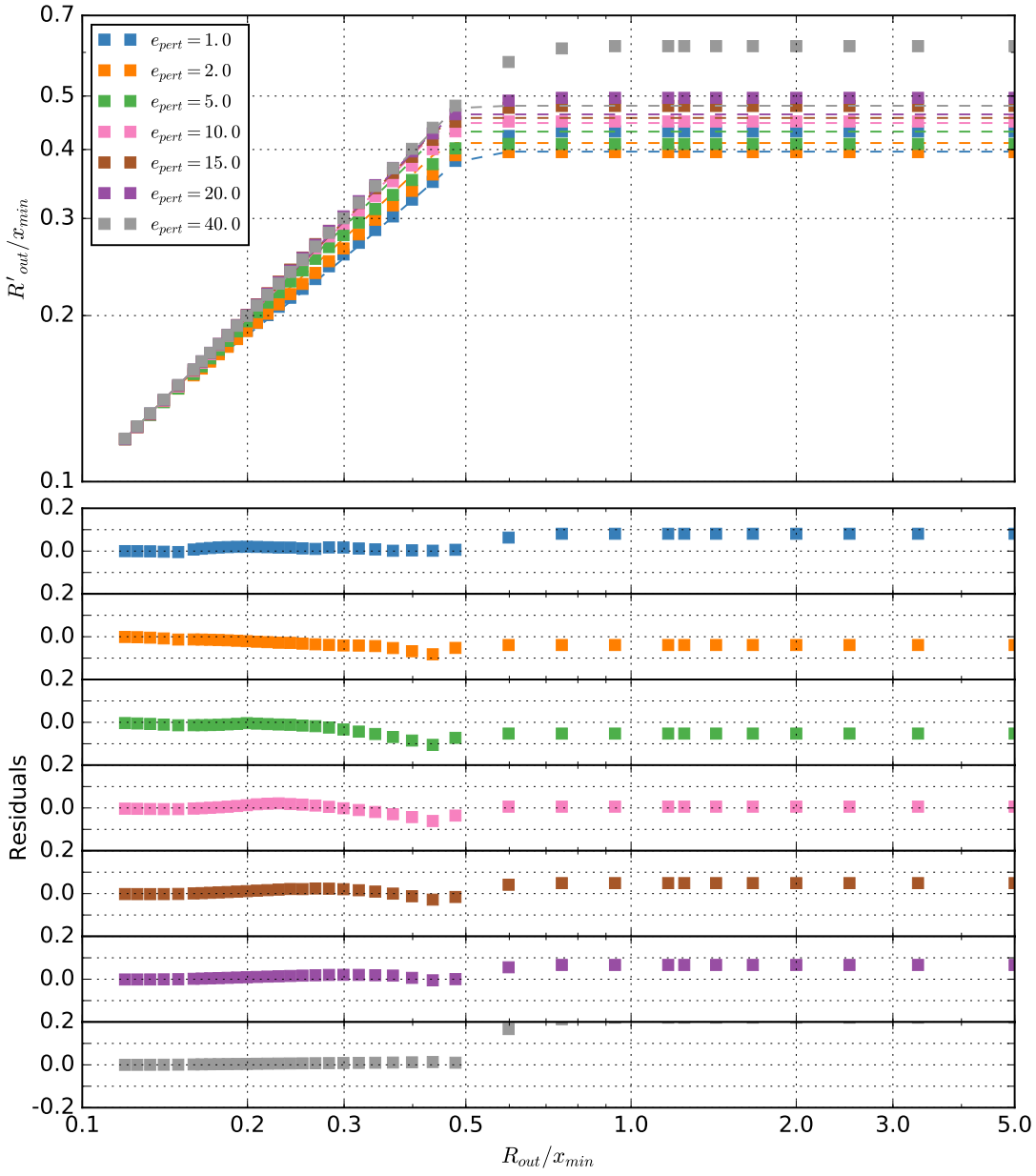

Fig. 4.3 As in figure 4.2 except the ratio of the perturber to host stellar mass is $M_2/M_1 = 10$. The model values (dashed lines) are fitted only to the simulation data of the $M_2/M_1 = 1$ case except in the asymptotic limit $R_{\rm out}/x_{\rm min} \gg 1$, where an additional mass dependent parameter is fitted (ϕ_3 – see text for details).

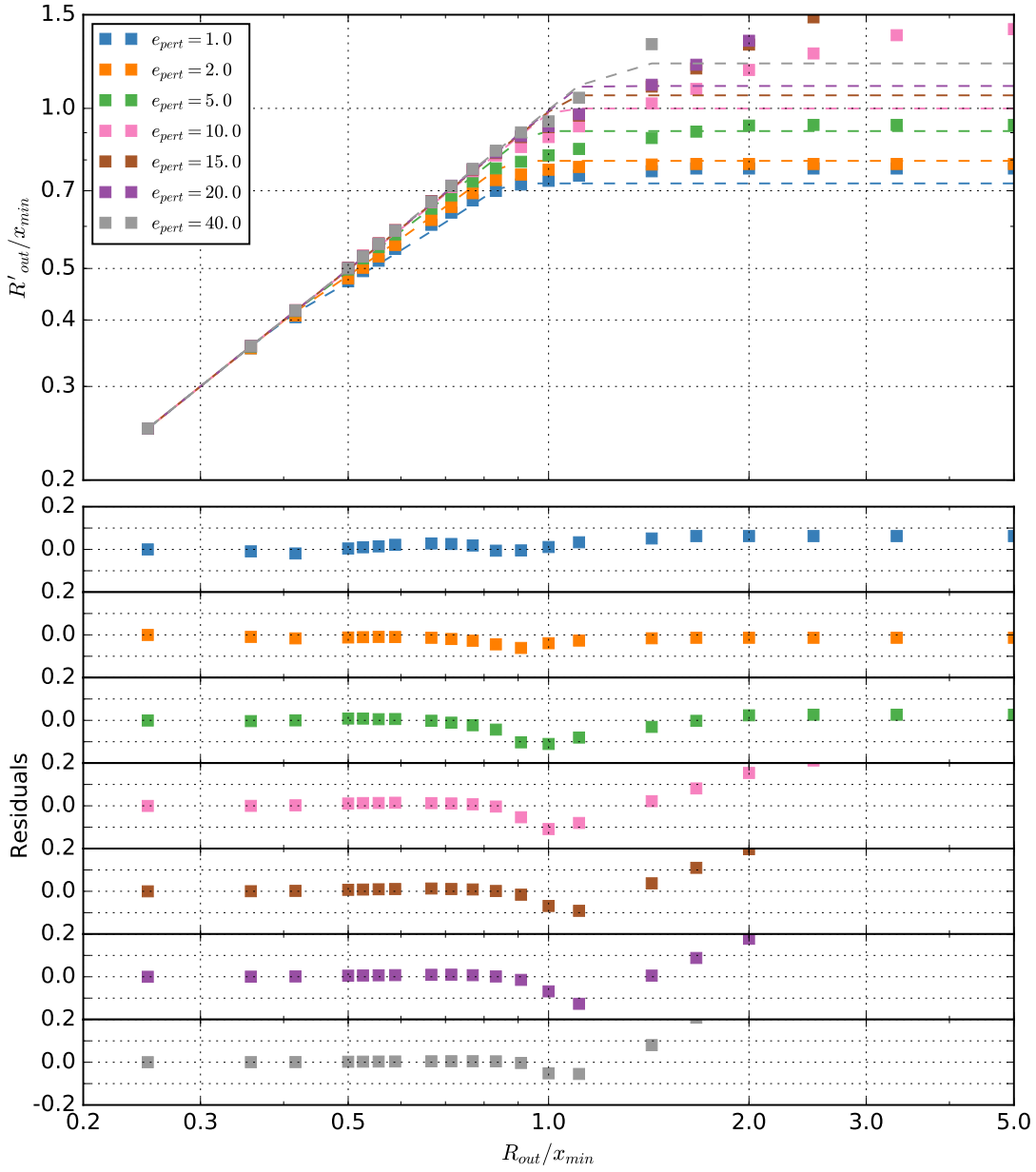

Fig. 4.4 Angle-averaged outer radius of a disc due to an encounter with a star with varying closest approach distance $x_{\rm min}$ and trajectory eccentricity $e_{\rm pert}$. Model (dashed lines) and simulation results (squares) for the case where $M_2/M_1 = 0.5$.

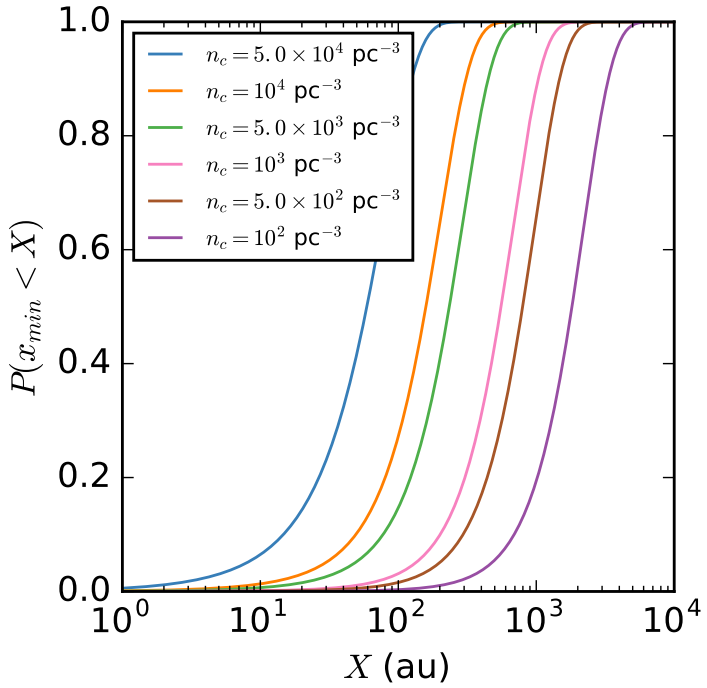

Fig. 4.5 The probability of a star having an encounter for which $x_{\rm min} < X$ in different stellar densities after 3 Myr. The cluster is assumed to have uniform density and be composed of stars with mass $1\,M_\odot$, with one dimensional velocity dispersion $\sigma_v = 4$ km/s.

where g is the number of fractal generations and $n_{\rm c}$ is the local stellar number density where there is no sub-structure ($D = 3$). The number of fractal generations is estimated to be

$$g = \frac{\ln(2N_{\rm c})}{\ln(8)} + 1 + s_2(D)$$

where $N_{\rm c}$ is the number of stars in the cluster and $s_2(D)$ is only non-zero for $D < 2$, in which case it is 1. We assume that the value of D decays over a crossing time, $\tau_{\rm cross}$, such that:

$$D(t) = 3 + (D_0 - 3)e^{-t/\tau_{\rm cross}},$$

at a time, t, since the star formation time. Apart from D_0, $n_{\rm c}$, σ_v and ξ, one further parameter needs to be assumed to link $\tau_{\rm cross}$, $n_{\rm c}$ and g. We choose to fix the total number of stars in the cluster $N_{\rm c}$. Given this, the crossing time is

$$\tau_{\rm cross} = \frac{2}{\sigma_v}\left(\frac{4\pi N_{\rm c}}{3n_{\rm c}}\right)^{1/3}.$$

The full theoretical encounter rate is defined in the Chapter 1 (equation 1.25), and is dependent on the IMF, the stellar number density n_c , the velocity dispersion σ_v and sub-structure as defined above. With the definition of η given in equation 1.26, the differential encounter rate (equation 1.25) is:

$$\mathrm{d}\mathscr{E} = \eta\,(x_{\min}, V^2, M_2; M_1)\,\mathrm{d}x_{\min}\,\mathrm{d}V^2\,\mathrm{d}M_2$$

where $V^2 \equiv v_\infty^2/4\sigma_v^2$ for relative velocity v_∞ between two stars at infinite separation (see Chapter 1 for discussion). In the most general form we aim to estimate the probability that an encounter occurs in a small region of parameter space: its closest approach in a spatial range $\delta x_{\min}$ around $x_{\min}$, a perturbing mass range δM_2 around M_2, a range of dimensionless square relative velocity at infinity δV^2 and a time range δt. For convenience, we label such a box A, its volume $\delta A = \delta x_{\min}\,\delta V^2\,\delta M_2\,\delta t$ and a coordinate in parameter space a. Assuming that encounters are uncorrelated, they can be modelled as a Poisson process and thus the probability that an encounter will occur in A is approximately

$$P(a \in A) \approx 1 - \exp\left(-\eta\,\delta A\right) \tag{4.6}$$

where η is evaluated at some point in A. In the limit $\delta A \to 0$ the term in the exponent can be integrated such that the probability of an encounter in any given range can be calculated.

Given this general encounter rate, we identify six distinct cluster models to investigate. For the most simplifying conditions, a cluster is composed of equal mass stars without any sub-structure. Two additional models are required to examine the effect of a realistic IMF and time-dependent sub-structure. In each case a 'high-density' and 'low-density' model give a sense of the dependence of disc evolution on n_c. Practically, the theoretical encounter rates give an immediate intuition for what high- and low-density regions are of interest. Equation 4.6 is evaluated as an integral over 3 Myr for a cluster comprised of solar mass stars and without sub-structure in figure 4.5. We choose a high-density model with $n_c = 5 \times 10^4$ pc^{-3} for which a significant fraction undergo an encounter such that $x_{\min} \lesssim 100$ au.

For a 'low-density' model we choose $n_c = 10^4$ pc^{-3}. This is not low-density in that it is higher than typical densities suggested by local observations, although theoretically making statistical predictions on such properties is strongly dependent on the galactic scale formation environment (see Chapter 7 and Kruijssen, 2012). Bressert *et al.* (2010) found that the stellar surface density distribution in the local 500 pc varies up to $\sim 10^3$ pc^{-2}, with a peak (by population) at ~ 22 pc^{-2}. However, we choose this as the low density case because the majority of stars in a region with $n_c = 10^4$ pc^{-3} have closest encounters such that 100 au $< x_{\min} < 10^3$ au. Therefore this represents an intermediate environment,

approximately the lowest density where we expect a population of PPDs to undergo any significant tidal truncation.

We additionally need to define a 1D velocity dispersion σ_v. In many cases, interpreting real cluster properties is not straightforward. For example, many clusters appear to be super-virial, and it is possible that this is because velocity dispersions are overestimated due to binaries (Gieles *et al.*, 2010). Incompleteness and uncertainties in establishing cluster membership also contribute to uncertainties in local stellar densities. For more detailed discussion see Stolte *et al.* (2010). For a review of the properties of young massive clusters see Portegies Zwart *et al.* (2010). A velocity dispersion of $\sim 1-5$ km/s is usual in most clusters (e.g. Hillenbrand and Hartmann, 1998; Clark *et al.*, 2005; Rochau *et al.*, 2010; Clarkson *et al.*, 2012), although in some environments a larger σ_v is observed, for example in OB associations (e.g. Cygnus OB2, see discussion in Chapter 6 and Wright *et al.*, 2016). In our models we initially assume $\sigma_v = 4$ km/s, then examine the effect of varying this value.

For the cluster models including a range of stellar masses, we apply a Kroupa *et al.* (1993) IMF:

$$\xi(m) \propto \begin{cases} m^{-1.3} & \text{for} 0.08\,M_\odot \leq m < 0.5\,M_\odot \\ m^{-2.2} & \text{for} 0.5\,M_\odot \leq m < 1.0\,M_\odot \\ m^{-2.7} & \text{for} 1.0\,M_\odot \leq m < 100\,M_\odot \\ 0 & \text{else} \end{cases} \tag{4.7}$$

such that ξ is normalised and continuous. In models for a single stellar mass, all stars are assumed to have $m = 1\,M_\odot$. All the cluster models are summarised in table 4.2. These models are not intended to be a realistic representation of an overall cluster. During the dynamic evolution of a real cluster the stellar density and mass distribution is likely to be spatially (and temporally) variable. These models are instead intended to reproduce local conditions and apply to a disc which has spent its life in a fixed stellar environment.

4.7 Numerical method

We adopt a *Monte Carlo* approach in quantifying the stochastic evolution of the outer radius of a disc embedded in a stellar cluster. For each model in table 4.2, 10^3 disc evolutions are calculated. In the case that an IMF is included (Models E and F), the mass of the host star is drawn from the distribution defined by ξ in equation 4.7.

For each disc, the parameter space (over time, mass of perturbing star and spatial separation) is divided into grid cells, each of size δA as defined in Section 4.6. Each grid cell is assigned a random number $u \in [0,1)$. If $u < P(a \in A)$, as defined in equation 4.6, then an

Model	n_c (pc^{-3})	D_0	σ_v (km/s)	N_c	IMF
A	10^4	3.0	4.0	-	-
B	5×10^4	3.0	4.0	-	-
C	10^4	2.0	4.0	10^3	-
D	5×10^4	2.0	4.0	10^3	-
E	10^4	3.0	4.0	-	ξ
F	5×10^4	3.0	4.0	-	ξ

Table 4.2 Summary of cluster model parameters. In cases where the fractal dimension $D_0 = 3.0$ (no sub-structure) the number of stars in the cluster is irrelevant. Where the IMF is not listed all stars are assumed to be of solar mass.

encounter is logged. The point in parameter space is then drawn at random (uniformly) from within the grid cell A.

Some consideration as to the maximum size of each grid cell δA is required. The size of a partition for each variable a_i should be limited such that $\delta a_i \ll \eta / |\nabla_{a_i}\eta|$ (i.e. η does not vary greatly across a grid cell). For the time dimension the size of δt is important only in cases where sub-structure is included, when it is necessary that $\delta t \ll \tau_{\rm cross}$, the crossing time of the cluster. Finally, the probability of two encounters occurring in the same grid cell A should be small. We define a maximum probability that two events occur in the same cell as 1%, this means that $P(a \in A) < 0.1$. From equation 4.6, this gives

$$\delta A < \frac{-\ln(0.9)}{\eta}$$

These conditions effectively define a maximum size for the grid cells, and we vary the cell partitions depending on the model parameters.

In this manner a series of encounters are assigned to a set of points $\{a\}$ in parameter space. The encounters are then applied to the disc under consideration in chronological order, such that the disc response is appropriate for each sequential encounter. The initial outer radius is defined to be 100 au regardless of host mass, and the outer radius of the disc responds to subsequent encounters as described in Section 4.5.

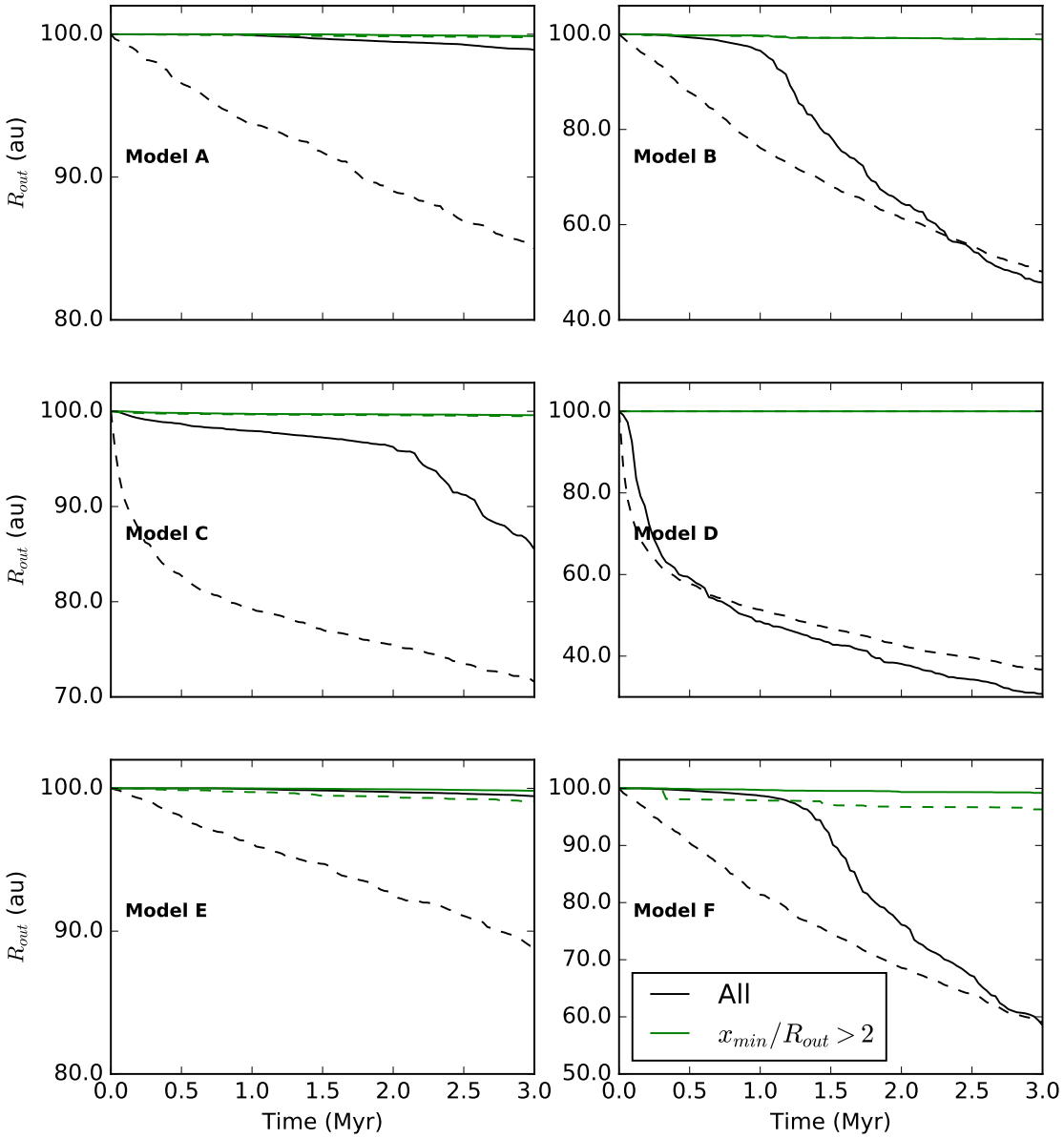

Fig. 4.6 Median (solid lines) and mean (dashed lines) outer disc radius evolution for each cluster model. The black lines are results for all discs, the green lines are for discs which did not have any encounters such that $x_{\rm min}/R_{\rm out} < 2$. The parameters for each of the models are shown in table 4.2.

Model	A	B	C	D	E	F
No close enc.	32%	0.8%	11%	0%	40%	1.4%

Table 4.3 The fraction of discs, out of a sample of 10^3, which did not undergo a close encounter ($x_{\rm min}/R_{\rm out} < 2$) over 3 Myr in each model.

4.8 Cluster evolution results

4.8.1 Uniform density cluster

The outer radius evolution results for all the models are shown in figure 4.6, where the uniform density clusters composed of $1M_{\odot}$ stars are top left and top right, which are the low- and high-density cases respectively. To interpret these results, we have categorised the discs according to the closest encounter distance of the disc in question. The threshold $x_{\rm min}/R_{\rm out} < 2$ is commonly taken as a criterion for significant disc truncation (e.g. Hall *et al.*, 1996). We show in green the subset of discs that are only influenced by encounters such that $x_{\rm min}/R_{\rm out} > 2$. The results including all discs are shown in black.

Clearly Model A yields no significant truncation, with the mean and median radii being little affected by encounters even when stars undergoing close encounters are included. The truncation extent is much greater in the high-density Model B, producing significantly reduced disc radii (~ 50 au). More distant encounters still have little effect on the disc evolution, in agreement with the results of Chapter 3. Further, the fractions of discs that do not experience a close encounter are shown in table 4.3; we find that for such a high density cluster very few discs have only distant encounters over 3 Myr.

4.8.2 Structured cluster

For a cluster with sub-structure we expect to see a rapid evolution of disc outer radii at early times due to the effective stellar density enhancement (and therefore the cluster encounter rate), which is reduced over a crossing time $\tau_{\rm cross}$, as the cluster relaxes. This is confirmed in figure 4.6. In the cases that the cluster initially has sub-structure (Models C and D), $R_{\rm out}$ initially drops more rapidly. As the cluster ages however, the rate of change $\mathrm{d}R_{\rm out}/\mathrm{d}t$ decreases so that after 3 Myr the average outer radii do not differ greatly from the unstructured case.

The extent of the difference between structured and unstructured models is dependent on the crossing time $\tau_{\rm cross}$, and therefore the number of local cluster members $N_{\rm c}$ for a given local stellar density. As we have fixed $N_{\rm c} = 10^3$ in both of our sub-structured models, the

cluster relaxes faster in the higher density Model D as opposed to the lower density Model C (see Section 4.6). It is possible to increase the length of time for which the number density is enhanced by structure, but this pushes into regions of parameter space which are physically unlikely, requiring dense and large stellar populations. Similarly, a smaller $\tau_{\rm cross}$ would reduce the time-scale over which density is enhanced.

4.8.3 Cluster with stellar mass distribution

A realistic IMF is implemented in Models E and F, which are shown in the right and left bottom panels of figure 4.6 respectively. The evolution of the disc radii for the global population is not significantly altered from Models A and B, without an IMF implementation. Some slight truncation for discs that only underwent distant encounters is observed in Model F due to the influence of high mass perturbers such that $M_2/M_1 \gg 1$. However, the fraction of discs that escape close encounters in this high density environment remains low at 1.4%.

While the overall statistical properties of the disc radii in the cluster similar regardless of whether we consider an IMF, doing so means that we can draw comparisons between discs around stars of different mass within a given environment. We discuss the mass dependence of the truncation radii below.

4.9 Mass dependent truncation

Given that a larger ratio M_2/M_1 yields greater angular momentum transfer, we expect the final outer radius of a disc to positively correlate with host mass M_1. In figure 4.7 we divide the samples for Model E and F into two even subsets by a mass threshold ($0.23\,M_\odot$) and plot the cumulative fraction of the outer radius distribution. Differences between the high- and low-mass sets are clear, and yield two-tail KS test p-values $\ll 0.05$ for our samples of 1000 stars in both Models E and F, and they are still $\lesssim 0.05$ when the same analysis is considered for a random subset of 100 stars. In the case that tidal truncation is the dominant truncation mechanism within a cluster, in principle it might be possible to find differences between the outer radius distributions in real observations. However, putting constraints on disc radii to within $\sim 10\%$ for such a large sample of discs is challenging.

4.10 Probability averaging

To produce a more thorough exploration of the effect of changing σ_v and $n_{\rm c}$, and given that final disc radii are largely determined by the 'strongest' encounter, the average outer radius

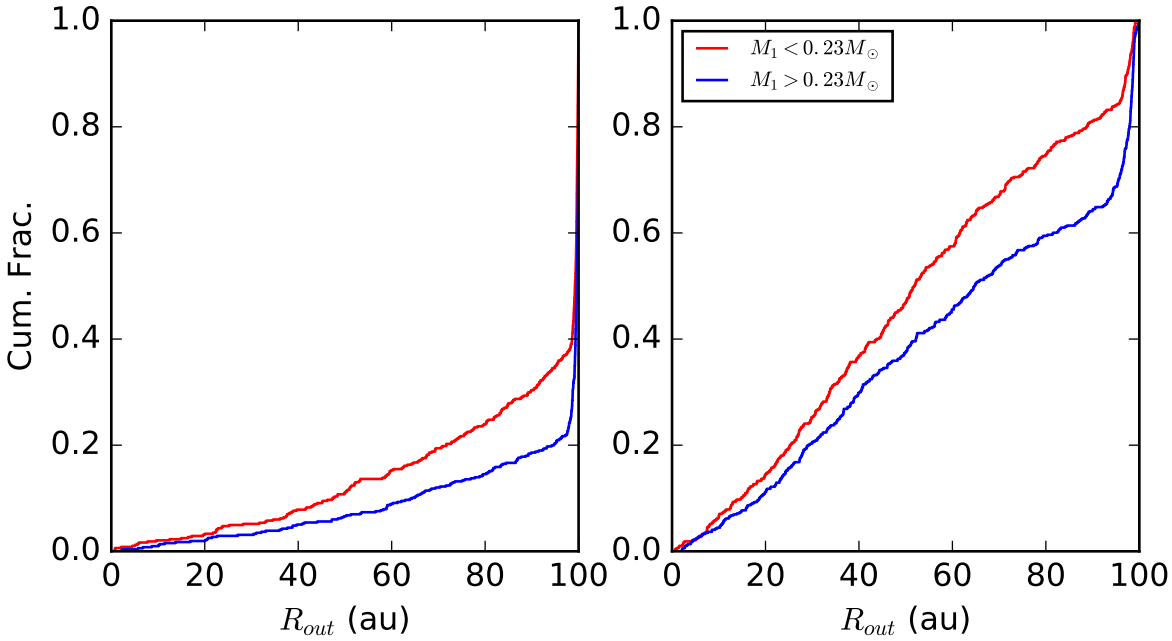

Fig. 4.7 Cumulative fraction of the outer radius distribution $R_{\rm out}$ of discs evolving in a cluster wherein stellar masses are drawn from the IMF ξ in equation 4.7 for Model E (left) and F (right). Samples of 1000 stars are divided into two approximately even samples by the host mass M_1 using the limit $0.23\,M_\odot$.

for a given stellar mass can be approximated by direct calculation in the following way. We choose two comparison masses, $M^* = 0.08 M_\odot$ and $1\,M_\odot$, and for each M^* sort the regions of encounter parameter space $\{A_i\}_{M^*}$ by the truncation radius of a 100 au disc, giving us a corresponding set of outer radii $\{R_{{\rm out},i}\}_{M^*}$, ordered from smallest to largest. The cumulative probability C_i over this set is:

$$C_{i+1} = C_i + P(a \in A_{i+1}) \cdot (1 - C_i),$$

where $C_0 = 0$. Each C_i is the probability that a stronger encounter than A_{i+1} has occurred over the relevant time period. Hence, the probability that A_i is the strongest encounter is $P(a \in A_i) \cdot (1 - C_{i-1})$. Then for a given host mass M^*, the mean outer radius can be approximated

$$\bar{R}_{\rm out}(M^*) = \sum_{i=1} R_{\rm out}(A_i; M^*) P(a \in A_i; M^*) \cdot (1 - C_{i-1})$$

where $R_{\rm out}(A_i; M^*)$ is the post-encounter outer radius of a 100 au disc hosted by a star of mass M^* due to an encounter in the parameter range A_i.

Applying this in varying cluster conditions yields the results in figure 4.8. These results are particularly interesting in the context of the outer radius dependence on the velocity

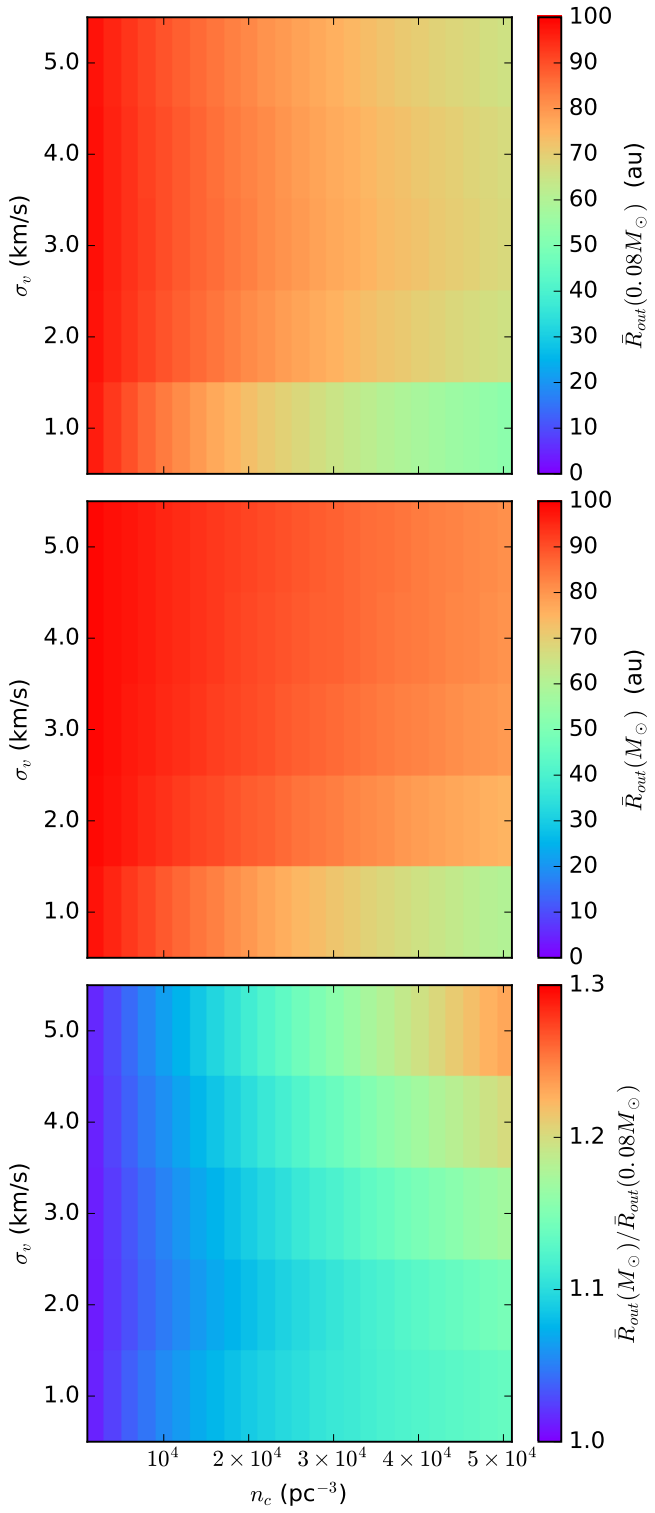

Fig. 4.8 Top: mean outer radius of a disc hosted by a star of mass $0.08\,M_\odot$ as a function of cluster properties, velocity dispersion σ_v and number density n_c. Middle: Mean outer radius for a disc around a $1\,M_\odot$ star. Bottom: Ratio between the average disc outer radius of a disc hosted by a $1\,M_\odot$ and $0.08\,M_\odot$ star.

dispersion within the cluster. Although overall encounter rates increase monotonically with σ_v, the likelihood of an encounter being hyperbolic also increases. In the case where $M_2/M_1 \lesssim 1$ the final outer radius of the disc is highly dependent on the eccentricity of the encounter. Therefore, particularly in the case of a relatively high mass star, tidal truncation is enhanced when the velocity dispersion within the cluster is small, even though there are fewer close encounters. Hence, a prescription for the dependence of truncation extent on eccentricity is an important addition to the theory of star-disc encounters. The most significant tidal truncation for all stellar masses occurs in regions with $\sigma_v \lesssim 1$ km/s and $n_c \gtrsim 2 \times 10^4$ pc^{-3}.

4.11 Conclusions

In this chapter, we have presented a full investigation of PPD radius distributions driven by tidal encounters in local environments with varying stellar density and velocity dispersion. Our main conclusions are as follows:

- The expected (mean) outer disc radius $\bar{R}_{\rm out}$ (from an initial outer radius of 100 au) in a given environment is dependent on the local stellar number density n_c, velocity dispersion σ_v and host mass M_1. The value of $\bar{R}_{\rm out}$ is minimised for large n_c, small σ_v and small host mass M_1.

- No environments for $n_c < 10^4$ pc^{-3} yield $\bar{R}_{\rm out} < 80$ au within 3 Myr regardless of σ_v and M_1. In most cases $\bar{R}_{\rm out}$ is larger than this, almost unchanged from the initial value. At higher local number densities $n_c \sim 5 \times 10^4$ pc^{-3} tidal encounters can significantly truncate PPDs below 100 au. A fiducial density threshold above which tidal truncation becomes significant in PPD evolution is therefore $n_c > 10^4$ pc^{-3}.

- The differential effect of host mass M_1 on the outer radius distribution is a rather weak effect. Unlike the degree of absolute truncation, the difference in outer radii between low- and high-mass host stars is maximised for large σ_v (and large n_c). Even in the extreme case of $n_c = 5 \times 10^4$ pc^{-3} and $\sigma_v = 5$ km/s the difference in $\bar{R}_{\rm out}$ between a brown dwarf and solar mass star is only $\sim 25\%$. A large sample of well-constrained PPD radii in such an environment would be required to detect any statistically significant differences between high- and low-mass stellar populations.

- Sub-structure can enhance encounter rates and therefore reduce disc radii within a stellar population in the short term. This is simply the statement that enhanced stellar densities result in increased truncation, and the canonical stellar density limit

of 10^4 pc^{-3} should be seen as a threshold on the effective local stellar density (i.e. incorporating the role of sub-structure) in the context of observed environments.

The relevance of these conclusions depends on whether there exist any environments in which star-disc encounters are the dominant truncation mechanism within a cluster. A comparison with photoevaporation rates in the densest cluster environments is presented in the following chapter.

Chapter 5

Type II encounters vs. external photoevaporation in star forming regions

The remainder of Winter *et al.* (2018c) not already included in the previous chapter is the source material for the following study. I compiled the observed samples, performed the analysis and wrote the majority of the paper. The viscous evolution code applied here was initially designed by Prof. Cathie Clarke, and the PPD mass loss rates induced by FUV photons are taken from Facchini *et al.* (2016).

5.1 Introduction

This chapter is a comparative study of the roles of type II tidal truncation and photoevaporation in setting the distribution of PPD radii in clustered stellar environments. This is achieved through first compiling a census of well studied star forming regions and depicting them in the plane of ultraviolet field strength versus stellar density. These two quantities are the main parameters that determine the importance of photoevaporative effects and dynamical truncation. This work bears closest similarity to that of Adams *et al.* (2006), who focused on the early stages of dynamical cluster evolution on young planetary systems. In that work both close encounters and FUV flux were considered. However, the intention was more on quantifying the dynamical evolution of young clusters, and less on estimating the resulting disc properties. In this chapter I will instead take observed environments as 'snapshots' in which I quantify the influence of PPD truncation mechanisms. Adams *et al.* (2006) only considered small clusters of $100-1000$ members, which are unlikely to host massive stars (with the greatest FUV luminosities). The mass function for young clusters is not steep below $\sim 10^5 - 10^6\,M_\odot$ (Schechter, 1976; Gieles *et al.*, 2006; Bastian, 2008; Portegies Zwart *et al.*,

2010) so that many stars spend their early phases in much more populated environments. Fatuzzo and Adams (2008) also investigated the influence of FUV fields over the observed local distribution of cluster masses. However, that study did not make a comparison between photoevaporation and encounters, nor did it quantify the density and field strengths in specific young clusters. The latter is a necessary step in targeting regions for observations of PPDs to test models for disc depletion. This chapter addresses the properties of observed clusters in the higher mass limit, and additionally contributes to the quantification of the role of photoevaporation in disc dispersal.

The externally photoevaporating disc evolution calculations presented in this chapter differ from previous works in that they consider a wider range of ultraviolet field fluxes (cf. Clarke, 2007; Anderson *et al.*, 2013) and take into account the influence of viscous torques (cf. Johnstone *et al.*, 1998; Adams *et al.*, 2004). They bear closest resemblance to those of the study of photoevaporation of discs in very low mass stars by Haworth *et al.* (2018b). Here however our focus is on the $\sim 1\,M_{\odot}$ stellar regime and in particular we focus on disc radius distributions to compare with the results of dynamical truncation presented in Chapter 4. Comparisons between the two truncation mechanisms are drawn in Section 5.4. Concluding remarks are made in Section 5.5.

5.2 Cluster environments

Our first stage in producing comparisons between truncation mechanisms is to assess the conditions within observed local star forming regions. We aim to produce a distribution of the far ultraviolet (FUV) flux for real stellar cluster members (Fatuzzo and Adams, 2008), and the corresponding local stellar number densities such that an estimation of the outer radius evolution can be made. To that end, we discuss the FUV luminosity as a function of stellar mass, and modelling assumptions below.

5.2.1 Properties of stellar clusters

We adopt the following approach in modelling real clusters, which are chosen such that there exist consistent measurements of the stellar surface density. To construct a cluster we fit the stellar positions with the Elson *et al.* (1987) surface density profile:

$$\Sigma(d_{\rm c}) = \Sigma_0 \left(1 + \frac{d_{\rm c}^2}{a^2}\right)^{-\frac{\gamma}{2}} \tag{5.1}$$

Cluster	ρ_0 ($M_\odot$ pc^{-3})	$r_{\rm core}$ (pc)	$r_{\rm eff}$ (pc)	$r_{\rm t}$ (pc)	γ	$M_{\rm clust}$ ($M_\odot$)	$m_{\rm max}^{-\sigma}$ ($M_\odot$)	$m_{\rm max}^{\rm obs}$ ($M_\odot$)
NGC 3603	$1.05 \cdot 10^5$	0.15	0.7	3.41	2.00	$1.3 \cdot 10^4$	67	-
Trumpler 14	$1.25 \cdot 10^5$	0.14	0.5	1.92	2.00	10^4	58	
ONC	$1.03 \cdot 10^4$	0.2	2.0	20.18	2.00	$4.5 \cdot 10^3$	37	~ 37
Arches	$1.30 \cdot 10^5$	0.2	0.4	-	3.27	$2.00 \cdot 10^4$	87	-
Quintuplet	523	1.0	2.0	-	3.27	10^4	58	-
Wd 1[a]	$9.52 \cdot 10^4$	0.28	0.86	-	4.00	$3.2 \cdot 10^4$	114	-
Cygnus OB2	21.9	3.9	5.1	-	5.80	$1.7 \cdot 10^4$	78	~ 100
Serpens A	743	0.16	-	0.25	4.00	17	-	5.1
Serpens B	495	0.14	-	0.21	4.00	6.8	-	5.1[b]
σ Ori	542	0.17	0.41	3.00	1.30	146	5.1	17
λ Ori	106	0.33	2.96	14.00	1.80	214	6.4	26.8
NGC 2024	$2.16 \cdot 10^3$	0.16	0.24	0.90	4.01	132	4.8	$15 - 25$

Table 5.1 Table of cluster and association properties used to generate a model cluster environments. Above the line are those for which properties are taken directly from Portegies Zwart *et al.* (2010). Below the line properties are found in independent sources (see Appendix C.1).

[a] Although numbers are recorded in Portegies Zwart *et al.* (2010), the reported values for $r_{\rm core}$, $r_{\rm eff}$ and γ are inconsistent. I therefore use $r_{\rm eff}$ from Mengel and Tacconi-Garman (2007), and fit an appropriate core radius.

[b] This is the maximum mass found throughout Serpens, placed at the centre of Serpens A. Therefore this represents the truncation value of the IMF, not the maximum mass in Serpens B.

as a function of the projected distance d_c from the apparent cluster centre, where a is a scale parameter such that r_{core} is the distance at which the *surface* density drops to half of its central value:

$$r_{core} = a\sqrt{(2^{2/\gamma} - 1)}$$

The associated volume density profile is

$$\rho(r_c) = \rho_0 \left(1 + \frac{r_c^2}{a^2}\right)^{-\frac{(\gamma+1)}{2}} \tag{5.2}$$

where

$$\rho_0 = \int_0^\infty y\Sigma(y)\,dy \Big/ \int_0^\infty 2z^2 \left(1 + \frac{z^2}{a^2}\right)^{-\frac{(\gamma+1)}{2}} dz.$$

Where it is not defined in the literature, the value of γ is obtained by fitting to r_{core} and the effective or half-light radius r_{eff}:

$$\int_0^{r_{eff}} y \left(1 + \frac{y^2}{a^2}\right)^{-\gamma/2} dy = \frac{M_{clust}}{4\pi\Sigma_0}.$$

In cases where $\gamma \leq 2$, we introduce a truncation radius r_t such as to give r_{eff} consistent with observations:

$$\int_0^{r_t} y \left(1 + \frac{y^2}{a}\right)^{-\gamma/2} dy = 2\int_0^{r_{eff}} y \left(1 + \frac{y^2}{a}\right)^{-\gamma/2} dy.$$

Hence we obtain a volume density profile ρ as a function of radius within the cluster r_c. Introducing a truncation radius means that the 2D profile deviates only slightly from the fitted profile for large r_c when truncating the 3D profile.

To obtain a number density at radius r_c the mass density is divided by the average stellar mass obtained from the IMF (equation 4.7; although a slightly different IMF is used in the case of Cygnus OB2, see Appendix C.1.1). However, as the FUV flux is sensitive to the mass of the most massive star in the cluster, the IMF must be truncated above the chosen m_{max}. Maschberger and Clarke (2008) find that m_{max} is consistent with random drawing for clusters with a given number of stellar components N_{clust}. We therefore draw the m_{max} distribution from the IMF, equation 4.7, the results of which are shown in figure 5.1. Our stellar atmosphere models are limited to stellar masses $< 100 M_\odot$ (Section 5.2.2), which is therefore our upper limit on m_{max}. A posteriori, evidence suggests photoevaporation dominates over tidal truncation. To confirm this result as unambiguously as possible, we seek to underestimate the influence of the FUV flux on a PPD population where there exists uncertainty in the correct prescription. For this reason, where there is no observational data for

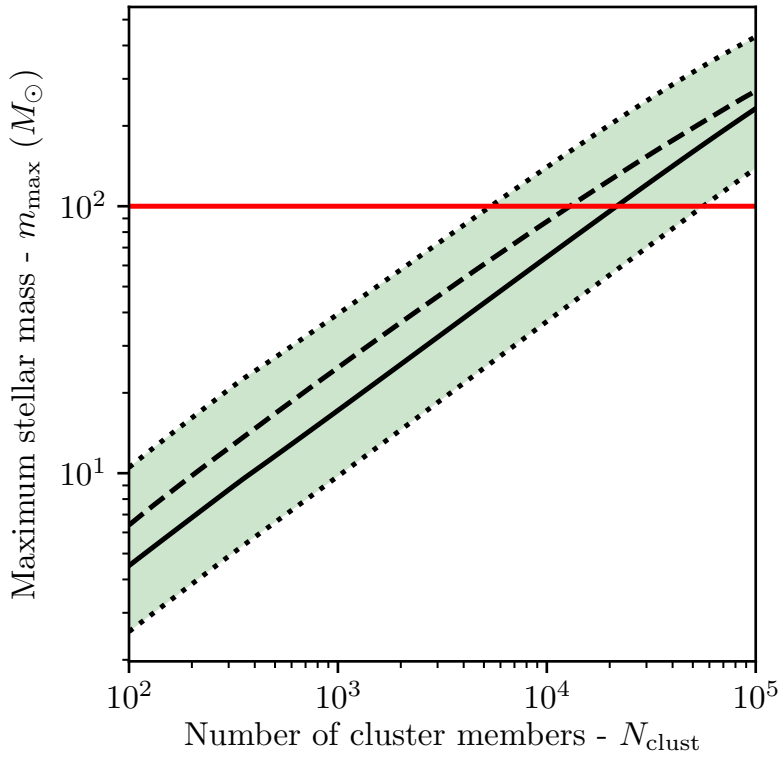

Fig. 5.1 The mass of the most massive cluster member $m_{\rm max}$ as a function of the number of members of that cluster $N_{\rm clust}$. The solid line is the median $m_{1/2}$ and the dashed line is the mean $\bar{m}_{\rm max}$. The dotted lines represent the 1-σ range, which is shaded. The horizontal red line at $100\,M_\odot$ is the greatest mass for which our stellar atmosphere models apply, and therefore an effective upper limit on the $m_{\rm max}$.

the most massive star in a cluster, we choose the value for $m_{\rm max}$ one standard deviation below the median (which we denote $m_{\rm max}^{-\sigma}$) to give an underestimate of the photoevaporation rate. For example, in the case of the ONC, the most massive star is a component of a binary, θ^1 Orionis C, with mass $\sim 37\,M_\odot$ (Kraus *et al.*, 2009) which is our adopted $m_{\rm max} = m_{\rm max}^{\rm obs} = 37\,M_\odot$. In the case of NGC 3603 the observed maximum stellar mass is poorly constrained, and therefore we adopt the conservative estimate $m_{\rm max} = m_{\rm max}^{-\sigma} = 67\,M_\odot$. The adopted properties for clusters are summarised in table 5.1. The first six regions come directly from Portegies Zwart *et al.* (2010). Other specific environments, for which data is obtained from other sources, are discussed in Appendix C.1.

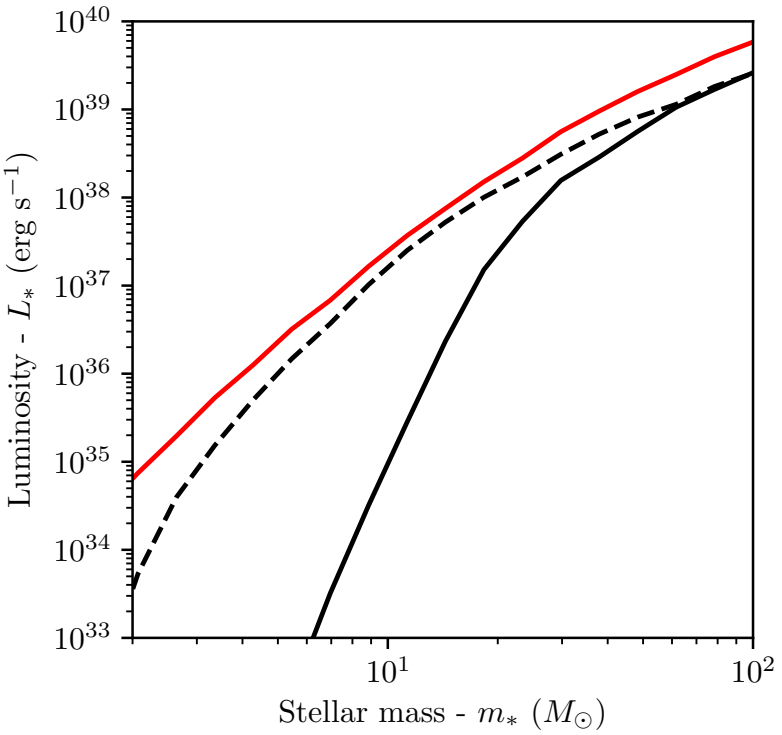

Fig. 5.2 Stellar luminosity as a function of mass based on the models of Schaller *et al.* (1992) and Castelli and Kurucz (2004), which can be compared with the results of Armitage (2000). The red line indicates the total luminosity, while the black dashed and solid lines represent the FUV and EUV luminosities respectively.

5.2.2 UV luminosity and stellar mass

To calculate the UV flux for a star of a given mass we follow Armitage (2000) for stars with a mass in the range $1-100\,M_\odot$. The total luminosities and effective temperatures $T_{\rm eff}$ are taken from the stellar model grids of Schaller *et al.* (1992), using the results for $Z = 0.02$ and the output closest to the time 1 Myr. These are combined with the stellar atmosphere models by Castelli and Kurucz (2004) to give the wavelength dependent luminosity (updated from the models applied by Armitage, 2000).

FUV photons have energies in the range 6 eV$< h\nu <$ 13.6 eV, while photons with energies higher than 13.6 eV are considered extreme ultraviolet (EUV). The results shown in figure 5.2, which are in agreement with those of Armitage (2000), despite our use of the more recent atmosphere models.

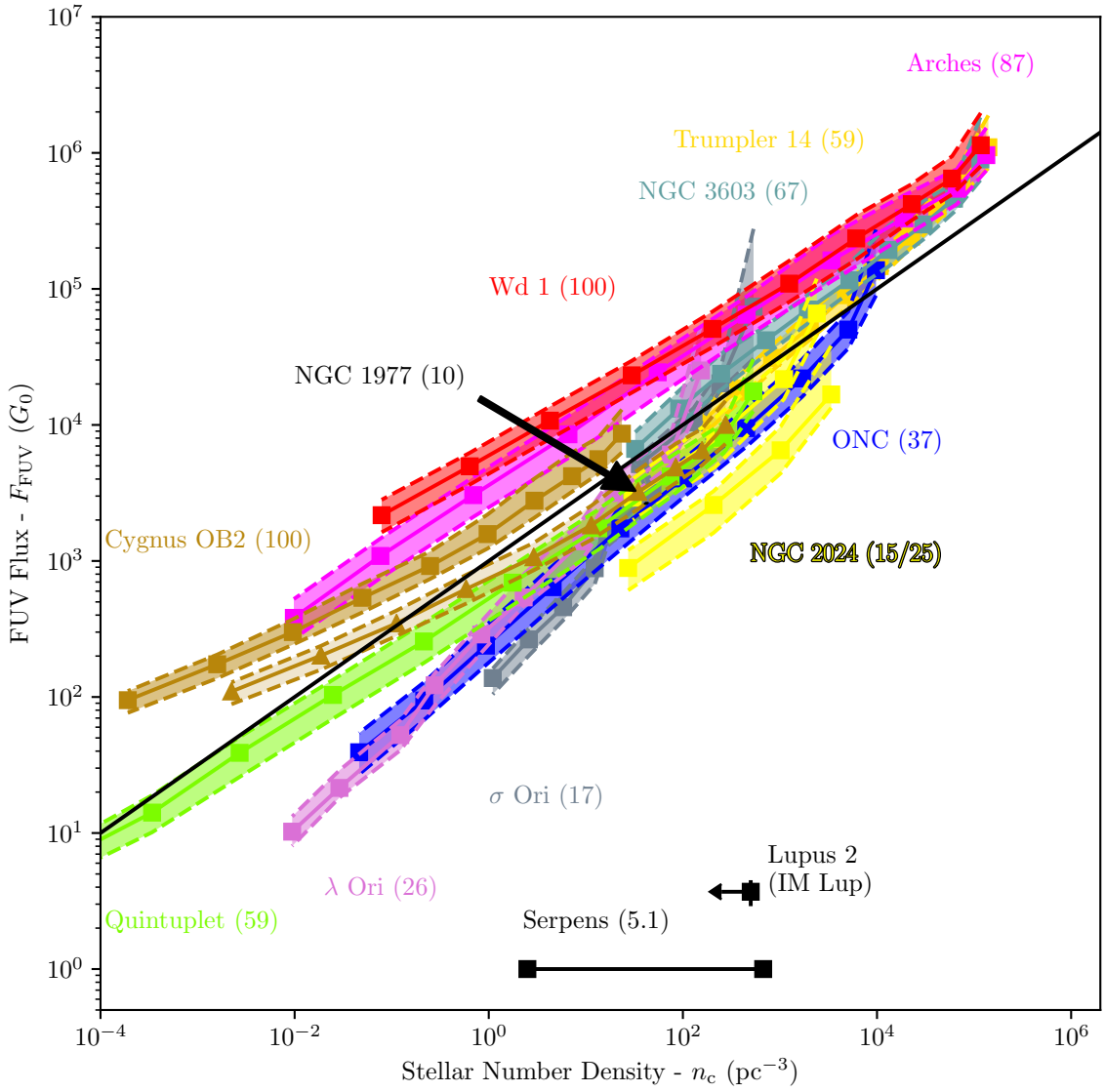

Fig. 5.3 Contours follow the local number density and FUV flux within each cluster. All clusters are divided into radial bins and the mean flux and number density in that bin are represented by the square markers, except in the case of a contour for Cygnus OB2 marked by triangles which are the results when sub-structure is considered. The shaded regions represent the standard deviation ($\pm 1\sigma$) of the flux in each radial bin. The numbers in brackets represent the assumed maximum stellar mass in solar masses for each cluster. The solid black line follows $F_{\rm FUV} = 10^3 (n_{\rm c}/{\rm pc}^{-3})^{1/2}\, G_0$.

5.2.3 Local environment distribution

In figure 5.3 the results of our cluster modelling are shown. The contours follow the density profile of the cluster, where stars are binned by radius. This yields a mapping between number density and FUV flux (assuming each cluster model is spherically symmetric). In some cases we do not directly model the environment (Lupus, Serpens, and NGC 1977 - see Appendix C.1 for details). Additionally, the Cygnus OB2 contour altered to match the density and flux distribution found by Guarcello *et al.* (2016) are shown with triangular markers in figure 5.3.

We find that for relatively massive clusters, $M_{\rm clust} \gtrsim 10^3\,M_\odot$, there is comparatively little dispersion in FUV flux for a given local number density. The relationship

$$F_{\rm FUV} = 1000 \left(\frac{n_{\rm c}}{\rm pc^{-3}} \right)^{1/2} G_0 \tag{5.3}$$

is shown as a solid black line in figure 5.3. It describes the contours for the massive clusters within a factor ~ 3, irrespective of $m_{\rm max}$, although we do not investigate cases for which $m_{\rm max} > 100\,M_\odot$ here. Since the contribution to local FUV flux peaks sharply for stars at ~ 40–$60\,M_\odot$ (with FUV luminosities $\sim 10^{39}$ erg s^{-1} – see Fatuzzo and Adams, 2008), the relative contribution to the local number density of stars which dominate $F_{\rm FUV}$ is only $\lesssim 10^{-3}$. The gradient of the individual cluster contours in $n_{\rm c} - F_{\rm FUV}$ space is therefore dependent on the radial profile of the stellar density. In regions where $n_{\rm c}$ falls steeply with radius, the flux increases less rapidly with $n_{\rm c}$. This is expected given the reduced distance of the stars at a low $n_{\rm c}$ from the centre of the cluster for steep density profiles.

The fact that most clusters follow this relationship is a different realisation of the results of Armitage (2000), in which the total FUV flux contribution as a function of stellar mass (convolved with relative number of stars at that mass), becomes much shallower above $m \gtrsim 40\,M_\odot$. In the case of EUV flux, which also has a truncating influence on PPDs, this is not true since the luminosity dependence on stellar mass remains steep up to $\sim 100\,M_\odot$. We discuss the consequences of figure 5.3 in the context of PPD dispersal in Section 5.4. Appendix C.2 contains some discussion about the assumptions made in producing the contours for specific clusters for which there were modelling complications.

5.3 Photoevaporation

We consider the evolution of the outer radius evolution of a disc that spends 3 Myr in environments of a given $F_{\rm FUV}$. Modelling disc evolution in this way requires knowledge of

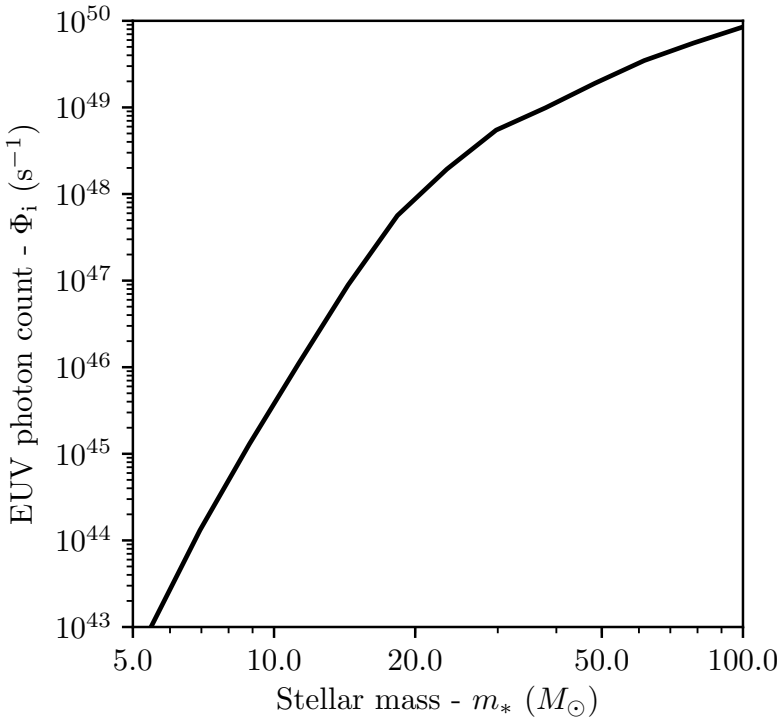

Fig. 5.4 Number of EUV photons $\Phi_{\rm i}$ emitted from a star as a function of stellar mass, based on the stellar atmosphere models by Castelli and Kurucz (2004).

mass loss rates over a range of disc radii and $F_{\rm FUV}$ values. The mass of the host star and disc also influences the photoevaporation rates, but this is addressed in detail by Haworth *et al.* (2018b) and in Chapter 7. Here we consider a $0.1\,M_\odot$ disc around $1\,M_\odot$ star. Mass loss rates are greater for lower mass stars, therefore the loss rates quoted here represent a lower limit for the majority of a given stellar population.

5.3.1 EUV vs. FUV induced mass loss

The mechanisms for EUV and FUV induced mass loss in PPDs are discussed qualitatively in Chapter 1. While we focus on the mass loss rates induced by FUV photons, some quantification of the ionising influence of the EUV photons is helpful. For regions FUV photons dominate mass loss, we use the results of Facchini *et al.* (2016) to obtain expressions for the mass loss rate as a function of $R_{\rm out}$ for a range of $F_{\rm FUV}$ values $30\,G_0 < F_{\rm FUV} < 3000\,G_0$. Outflows in the thin PDR limit are driven predominantly by the EUV photons. In this regime

Johnstone *et al.* (1998) find an expression for the mass loss:

$$\dot{M}_{\rm EUV} = 5.8 \times 10^{-9} \left(\frac{x}{1\,\rm pc}\right)^{-1} \left(\frac{f_r \Phi_{\rm i}}{10^{49}\,\rm s^{-1}}\right)^{1/2} \left(\frac{R_{\rm out}}{100\,\rm au}\right)^{3/2} M_\odot\,\rm yr^{-1} \tag{5.4}$$

where $\Phi_{\rm i}$ is the EUV photon luminosity of the ionizing source (shown as a function of stellar mass in figure 5.4), x is the distance to the same source, and f_r is the fraction of EUV photons that are not attenuated by the ISM, which we assume hereafter to be unity.

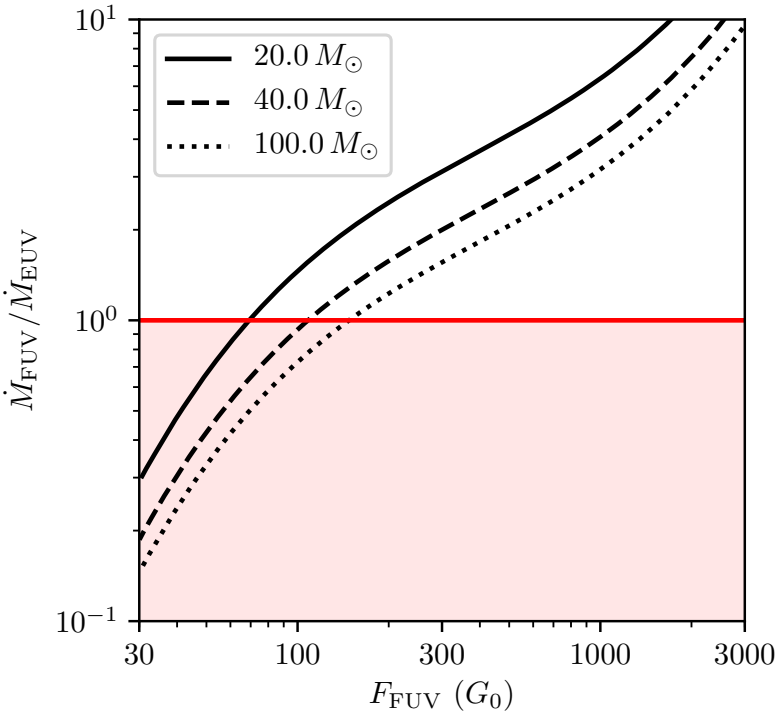

Fig. 5.5 Ratio of the initial mass loss rates in a $0.1\,M_\odot$ disc with $R_{\rm out} = 100$ au around a $1\,M_\odot$ induced by FUV versus EUV radiation. The region in which EUV photons induce greater mass loss ($\dot{M}_{\rm FUV}/\dot{M}_{\rm EUV} < 1$) is shaded red. The cases for radiating sources of mass $20\,M_\odot$, $40\,M_\odot$ and $100\,M_\odot$ are shown.

The ratio of the FUV to EUV loss rates are shown in figure 5.5. For the range of $F_{\rm FUV}$ values for which I have mass loss rates, the FUV dominates down to $F_{\rm FUV} \sim 100$. There exists a second region close to the star ($\lesssim 0.1$ pc, $F_{\rm FUV} \gtrsim 10^5\,G_0$) in which the EUV again dominates, although our models do not cover this regime. This can be understood in that the EUV mass loss rate varies inversely with distance (equation 5.4) while the FUV mass loss rate plateaus at high $F_{\rm FUV} \gtrsim 10^4\,G_0$ and then falls more steeply with declining $F_{\rm FUV}$ for $F_{\rm FUV} \lesssim 10^3\,G_0$. These $F_{\rm FUV}$ thresholds are lower than those found, for example, by Störzer and Hollenbach (1999) because the region where FUV is dominant is dependent on disc

radius, and our 100 au initial condition is larger than the disc radius considered in that study. In addition, the FUV induced mass loss rates found by Facchini *et al.* (2016) made a number of improvements to the theory discussed in Chapter 1. While we hereafter focus on the radius evolution of PPDs due to FUV radiation only, this is effectively a lower limit on the rate of photoevaporation for regions where EUV photons may dominate. This is sufficient for our purposes of comparing photoevaporation to tidal truncation in different regions.

5.3.2 Viscous disc evolution model

To calculate the disc evolution we follow the viscous model outlined in Chapter 1 and the numerical approach of Clarke (2007, see also Anderson *et al.* 2013), incorporating photoevaporative mass loss from the outer edge. In brief, the viscous evolution is modelled with a parameterised viscosity that scales linearly with radius (corresponding to constant Shakura and Sunyaev α and a temperature scaling as $R^{-1/2}$) and the evolution is defined over a one-dimensional grid equispaced in $R^{1/2}$. A zero torque inner boundary condition is applied. The cell that is deemed to be the instantaneous outer edge cell is subject to both viscous outflow from the inwardly lying cell and a sink term for mass leaving in the wind. If the resultant of these leads to mass accumulation in the edge cell, the edge cell is advanced outwards. In the case that the edge cell is subject to net mass loss, a threshold criterion determines whether the outer cell moves inwards. Provided the threshold value is sufficiently low, the evolution is insensitive to its exact implementation.

We apply this disc evolution calculation to a solar mass star, as this is the mass for which the largest datasets of PPD radii will be available, and they can be compared to the corresponding calculations in Section 4.10. To obtain an upper limit on the photoevaporation timescale we choose the maximum initial disc mass that is compatible with gravitational stability ($\sim 0.1\,M_\odot$ – see Chapter 1). The viscous α-parameter is chosen so that the initial accretion rate onto the star is $7\times10^{-8}\,M_\odot$ yr^{-1}, consistent with the upper end of the accretion rate distribution for solar mass stars (Manara *et al.*, 2016).

5.3.3 PPD destruction timescale

We apply our treatment of the disc radius evolution to a $0.1\,M_\odot$ disc around a $1\,M_\odot$ host star in figure 5.6. The disc shrinks throughout its evolution for $F_{\rm FUV}\sim 3000\,G_0$ but initially expands outwards for $F_{\rm FUV}\lesssim 300\,G_0$ until the mass loss rate (which increases with $R_{\rm out}$) balances the viscous expansion. The PPD then eventually shrinks once the disc has been significantly drained by both photoevaporation and accretion. As discussed in Chapter 1, photoevaporation accelerates disc destruction even when the disc is very compact because it

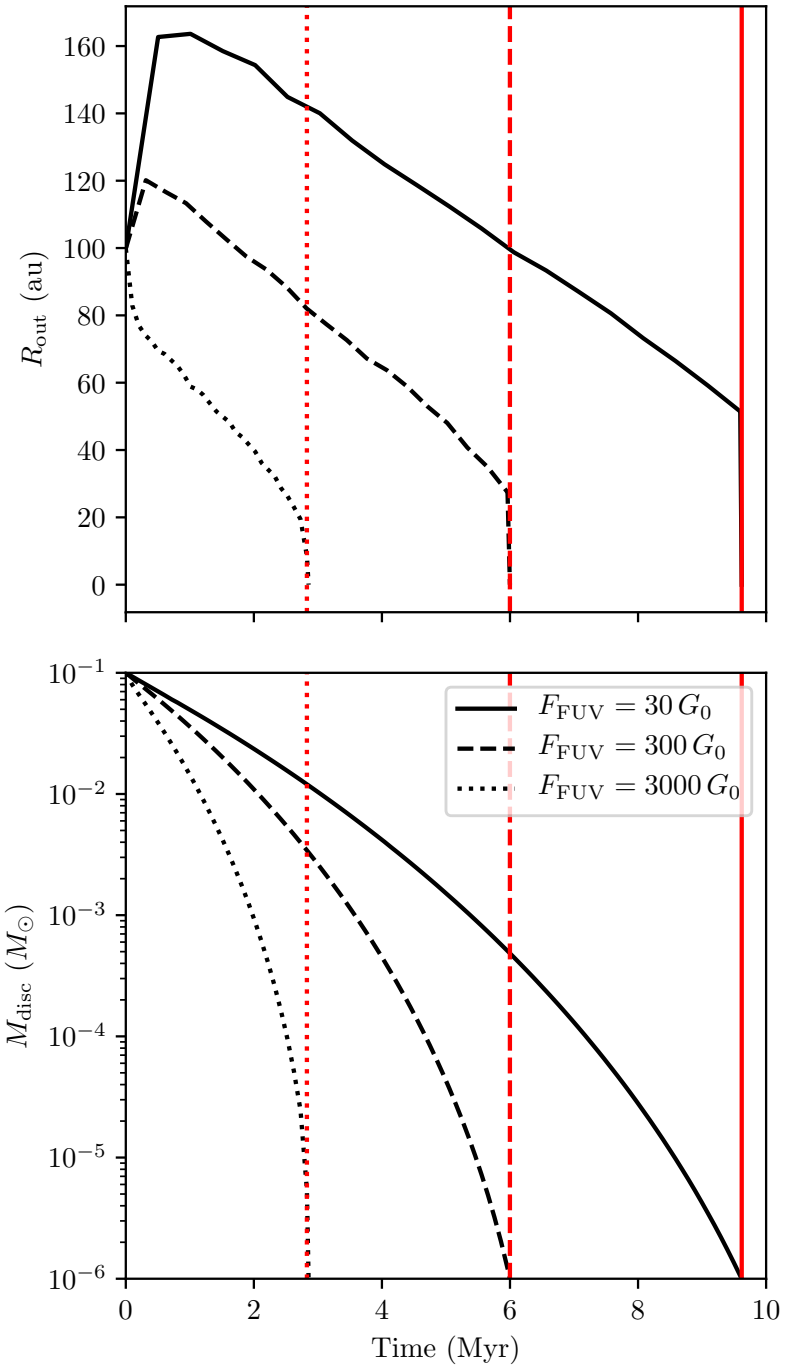

Fig. 5.6 Outer radius (top) and mass (bottom) evolution of a $0.1\,M_\odot$ PPD around a $1\,M_\odot$ star for $F_{\rm FUV} = 30$ (solid), 300 (dashed) and $3000\,G_0$ (dotted). We have marked our definition of the photoevaporation induced disc destruction timescale $\tau_{\rm phot.}(F_{\rm FUV})$ as a vertical red line in each case.

prevents the disc from viscously re-expanding by removing the material at the outer edge, thereby suppressing the evolution timescale.

The timescale $\tau_{\text{phot.}}$ over which the FUV flux destroys a PPD is defined to be the time at which the disc is depleted such that $R_{\text{out}} < 10$ au or the mass falls below $10^{-6} M_{\odot}$ (in practice the disc lifetime is usually dictated by the latter). Such a definition is appropriate both because it represents a reasonable lower bound of the detectability of PPDs and because the disc does not persist long at low masses/radii as shown in figure 5.6. The value $\tau_{\text{phot.}}$ is shown as a contour in figure 5.7, varying between $3 - 10$ Myr for $3000\,G_0 > F_{\text{FUV}} > 30\,G_0$.

Our definition of $\tau_{\text{phot.}}$ is conservative (i.e. the timescale over which photoevaporation completely destroys the disc). This is because our aim is to compare regions of dominance of the two truncation mechanisms (tidal encounters and photoevaporation) that act in different ways upon a disc population. Encounters are stochastic, and therefore cause a distribution of outer radii. In contrast, assuming all discs have the same initial conditions, the effect of FUV flux has a consistent effect on all discs in the same environment. Therefore, to estimate the timescale over which tidal encounters are irrelevant to the evolution of the PPD population as a whole, we choose $\tau_{\text{phot.}}$ to be the period over which the disc is completely dispersed.

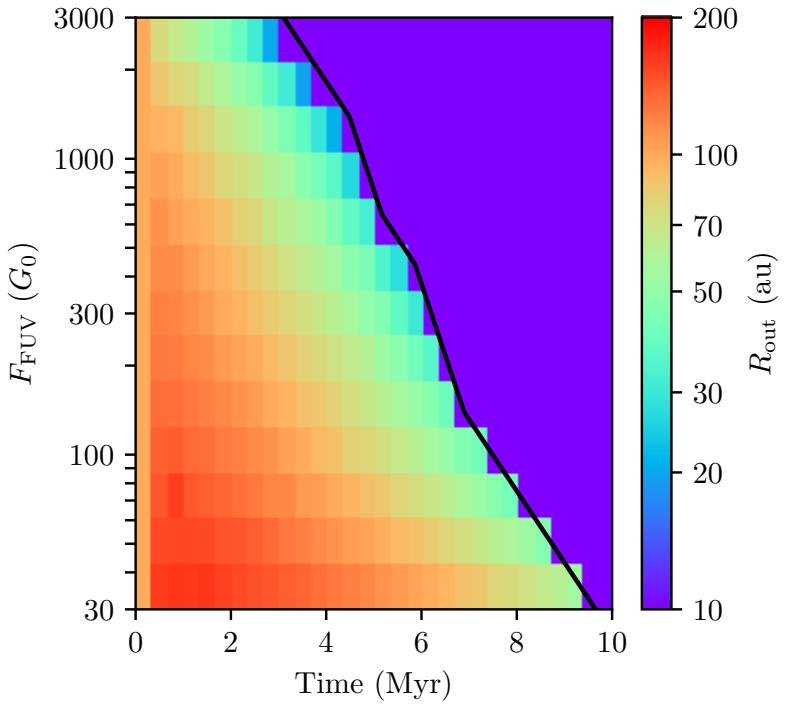

Fig. 5.7 The evolution of the outer radius of a $0.1\,M_{\odot}$ PPD around a $1\,M_{\odot}$ star in different (constant) FUV flux environments. The contour follows the time at which the disc is considered to be 'destroyed', where $R_{\text{out}} < 10$ au or $M_{\text{disc}} < 10^{-6}\,M_{\odot}$.

5.4 Type II tidal truncation vs. photoevaporation

In figure 5.8 we have marked the flux limit for which a $0.1\,M_{\odot}$ PPD around a $1\,M_{\odot}$ star survives for 3 Myr. We have also indicated the lower number density limit required to see significant tidal truncation in a disc population over the same period ($\sim 10^4$ pc^{-3} – see Chapter 4). As discussed in Section 4.10 this limit is moderately dependent on the local velocity dispersion, and some fraction of a population with $n_{\rm c} < 10^4$ pc^{-3} will experience type I or serendipitous type II encounters.

We find that in all regions where significant tidal truncation occurs within 3 Myr ($\tau_{\rm tidal} \lesssim 3$ Myr) also correspond to regions in which the FUV flux is sufficient to destroy the disc over this timescale ($\tau_{\rm phot.} < 3$ Myr). I.e. no clusters or associations which contain environments occupying the bottom right of figure 5.8 exist in the sample we present here. There is no evidence supporting tidal truncation as a dominant mechanism influencing PPD evolution in real clusters. However, some caveats and possibilities are due discussion:

- The cluster sample we have presented is not complete. It is possible that there exist clusters with a low $m_{\rm max}$ and enhanced stellar densities in which tidal encounters are important for disc evolution. Given that there is little variation in the flux-density profiles of the most massive clusters (figure 5.8), this likely can only be the case in clusters with $M_{\rm clust} \ll 10^3\,M_{\odot}$. We have found no such examples.

- In present cluster environments past sub-structure might have enhanced number densities, and thus the encounter rate. However, figure 5.8 indicates number densities must be increased by more than two orders of magnitude to make tidal truncation. Equally, an enhancement in number density also increase the local FUV flux to some degree. Sub-structure is also short-lived and exists during the highly embedded phase of star formation which is less well quantified than the (few Myr old) environments shown in figures 5.3 and 5.8. We emphasise that type I dynamical interactions taking place within small dense multiple systems would be considered as providing disc initial conditions, and not a mechanism for dispersal.

- Extinction within young clusters can reduce the effective $F_{\rm FUV}$ experienced by PPDs. Based on figure 5.8 the FUV flux would have to be reduced by a factor $\gtrsim 50$ to leave regions in a regime of tidally induced truncation. Cardelli *et al.* (1989) parameterise extinction as a function of wavelength, and in the FUV it is estimated at $A_{\rm FUV}/A_V \approx 2.7$. The column density of hydrogen, N_H, required for 1 magnitude extinction is $N_H/A_V \approx 1.8 \times 10^{21}$ cm^{-2} mag^{-1} (Predehl and Schmitt, 1995). For a factor 50 reduction in FUV flux, this corresponds to ~ 10 magnitudes, or $A_V \approx 3.6^m$ and $N_H \approx 6.5 \times 10^{21}$ cm^{-2}. If

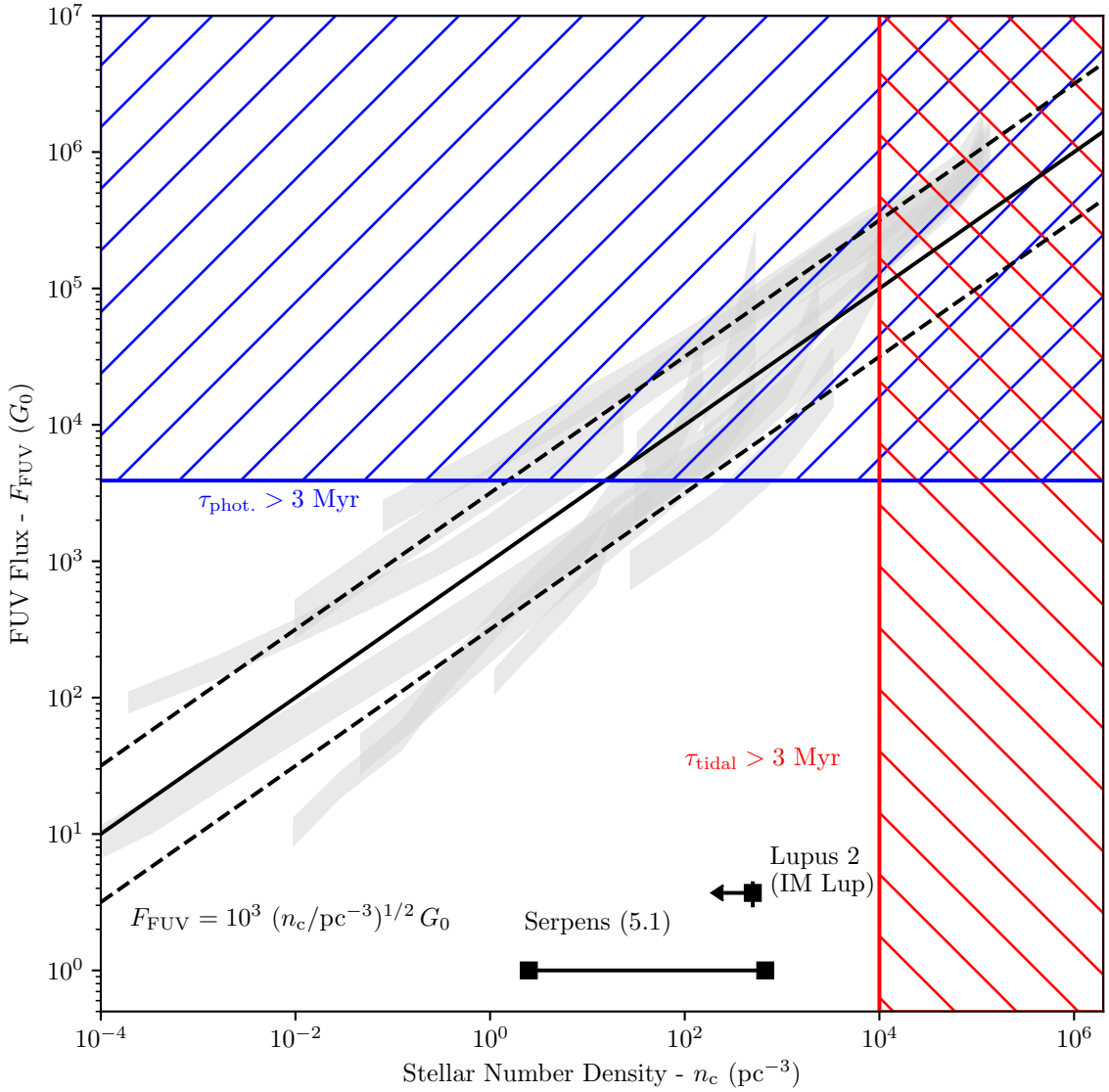

Fig. 5.8 Cluster contours in $n_{\rm c} - F_{\rm FUV}$ space as in figure 5.3 are shown here in grey. The horizontal blue line shows the minimum $F_{\rm FUV}$ such that the $0.1\,M_\odot$ disc around a $1\,M_\odot$ star will be completely destroyed by photoevaporation within 3 Myr. The vertical red line delineates the approximate regimes in which the number density is sufficient to produce significant tidal truncation for a 100 au disc within 3 Myr. The solid black line follows $F_{\rm FUV} = 10^3 (n_{\rm c}/{\rm pc}^{-3})^{1/2}\, G_0$, with dashed lines showing 1 dex around this value. The number in brackets next to the cluster name represents the assumed maximum mass in the cluster $m_{\rm max}$, which may be observed or predicted (see text for details).

the gas distribution is uniform over 2 pc this requires a volume density $n_H \sim 10^3$ cm^{-3}, which is high for a GMC (Solomon *et al.*, 1987). Such extinction is observed, for example toward Cygnus OB2 where $A_V \sim 4^m - 7^m$ is found, although this is likely due to foreground as well as internal gas (Wright *et al.*, 2010; Guarcello *et al.*, 2012). The influence of primordial gas is further discussed in Chapters 6 and 7.

- For the region in the top right of figure 5.8 (where both $\tau_{\rm phot.} \lesssim 3$ and $\tau_{\rm tidal} \lesssim 3$ Myr) type II encounters are still unlikely to shape the outer radius distribution for three reasons. Firstly, the definition of $\tau_{\rm phot.}$ is such that the discs are completely destroyed by external photoevaporation, while $\tau_{\rm tidal}$ is the timescale on which a PPD population might experience only mild tidally induced truncation. Secondly, the regions where both occur are spatially small, only existing in the very core ~ 0.1 pc of massive clusters and containing a small fraction of the overall stellar population. Thirdly, in these core regions with $F_{\rm FUV} \gtrsim 10^5\, G_0$ the EUV will play the dominant role in mass loss, shortening the disc lifetime even for the extremely massive PPDs ($0.1\, M_\odot$) studied here.

- Finally, the analysis in Chapter 4 of the effect of tidal truncation is based on the angle-averaged approach to individual encounters. In reality an additional scatter in outer radii of PPDs is expected (greater than that obtained using the *Monte Carlo* approach discussed in Section 4.7). The fraction of discs that experience close encounters however, will remain unchanged. As our focus has been the effect of truncation mechanisms on a whole population of discs, this scatter will not alter our conclusions. Additionally, because of the choice of $\tau_{\rm phot.}$ as discussed in Section 5.3.3, and the order of magnitude limit on $n_{\rm c}$ so that $\bar{R}_{\rm out}$ is only mildly truncated by encounters (see figure 4.8), the complete destruction of discs by photoevaporation renders the dispersion in encounter orientation irrelevant.

Ultimately, none of the environments studied in this chapter are even particularly close to the region in which tidal encounters to play a significant role. This does not preclude individual PPDs, or even small fractions of the PPD populations, from experiencing truncating encounters, particularly if they are type I. However as a physical mechanism for disc truncation and dispersal, photoevaporation is found to be far more efficient in real environments.

5.5 Conclusions

During this chapter we have quantified the influence of photoevaporation of a massive PPD and mapped out the density and FUV flux distribution in local star forming regions. This has allowed us to compare the influence of type II encounters and external photoevaporation on disc evolution. Our main findings from this comparison are as follows:

- In all the cluster environments discussed, regions for which the local number density is sufficient to yield significant truncation in a population of PPDs ($n_{\rm c} \gtrsim 10^4$ pc^{-3}) are also exposed to a strong FUV flux which causes complete destruction of even a massive disc within 3 Myr ($F_{\rm FUV} \gtrsim 3000\,G_0$). We find no environments in which type II tidal truncation shapes the distribution of outer radii.

- For massive clusters, the dispersion of FUV flux for a given local number density $n_{\rm c}$ is relatively small ($\lesssim 1$ dex). In particular, for $M_{\rm clust} \gtrsim 10^3\,M_\odot$ the FUV flux follows:

$$F_{\rm FUV} = 1000 \left(\frac{n_c}{\rm pc^{-3}} \right)^{1/2} G_0$$

  (equation 5.3). Deviation from this relationship can occur due to very steep or shallow density profiles with radius within the cluster, or the presence of sub-structure.

- In the less massive cluster regime $M_{\rm clust} \ll 10^3$, where the high-mass end of the IMF is not well sampled, the FUV flux is not defined by local number density. There exist examples of low-mass clusters for which the FUV flux is much less than the number density would suggest according to equation 5.3. However, even in these cases, the stellar densities are insufficient to induce significant tidal truncation of PPDs within 3 Myr.

In summary, type II star-disc interactions are a secondary truncation mechanism compared to external photoevaporation. As greater samples of PPD properties are measured with *ALMA*, more complete disc radius and mass distributions as a function of distance from massive stars and local number density will become available to test these conclusions.

Chapter 6

External photoevaporation of PPDs in Cygnus OB2

This chapter is based on Winter *et al.* (2019); I performed the simulations and analysis, the viscous disc evolution code was based on the original by Prof. Cathie Clarke. I am the main contributor to the text.

6.1 Introduction

Chapter 5 demonstrates the importance of external photoevaporation for dispersing PPDs in many local environments. In this chapter we consider some signatures that might be found by observing disc populations in the regions that experience strong FUV flux. The properties of young massive stellar clusters/associations and the giant molecular clouds (GMCs) from which they form are diverse, and the link between them is not well characterised (see Longmore *et al.*, 2014, for a review). During formation, the early cluster may undergo cold collapse (Tobin *et al.*, 2009; Kuznetsova *et al.*, 2018), or after the expulsion of gas the stellar population may become supervirial (Goodwin, 2009; Pfalzner and Kaczmarek, 2013), dependent on the density and velocity dispersion of the primordial GMC. This in turn influences the evolution of mass segregation (e.g. Bonnell and Davies, 1998) and substructure (e.g Goodwin and Whitworth, 2004) within the cluster. Because the environment of a star has an influence on the associated PPD, the dynamical history of a cluster is closely linked with the properties of its disc population.

While many authors have attempted to account for the local environment in considering PPD evolution (e.g. Scally and Clarke, 2001; Cleeves *et al.*, 2016; Guarcello *et al.*, 2016),

none have inverted this method and used observed disc populations to put constraints on the dynamical history of a star forming environment. This work is partly motivated by this goal.

Cygnus OB2 (Cyg OB2) is a young massive OB association in the Cygnus X region, and has been used as an empirical test of feedback mechanisms on PPD evolution. It contains many massive stars up to $\sim 100 M_{\odot}$ (e.g. Massey and Thompson, 1991; Wright *et al.*, 2015) which contribute to strong FUV radiation fields. Guarcello *et al.* (2016) analysed the disc fraction within Cygnus OB2 as a function of FUV flux, and found that surviving discs were less common at small projected separations from massive stars. Other authors, such as Wright *et al.* (2016), have made observations which indicate a complex dynamical sub-structure within the association. Collating this evidence, we here aim to apply N-body simulations and those combining viscous disc evolution and photoevaporation to replicate observations of Cyg OB2. We will reproduce the present day stellar kinematics and a dynamical history consistent with the observed disc fraction distribution. In this way we can shed light on both the history and the likely future of the PPD population and the stellar components.

In the remainder of this chapter we first review the observational constraints on the properties of Cyg OB2 in Section 6.2. We describe our numerical method and models in Section 6.3. In Section 6.4 we compare our models with the observational data. We draw conclusions in Section 6.5.

6.2 Properties of Cygnus OB2

6.2.1 Stellar population

Cyg OB2 is a young association at a distance ~ 1.33 kpc from the sun (Kiminki *et al.*, 2015). The majority of members formed $3-5$ Myr ago (Wright *et al.*, 2010), although some stars have ages as young as ~ 2 Myr (Hanson, 2003) and as old as ~ 7 Myr (Drew *et al.*, 2008). Estimates of the total stellar mass of Cyg OB2 have varied between $2\text{–}10 \times 10^4 M_{\odot}$ (Knödlseder, 2000; Hanson, 2003; Drew *et al.*, 2008; Wright *et al.*, 2010), although Wright *et al.* (2015) find a slightly lower mass of $\sim 1.6 \times 10^4 M_{\odot}$ within a radius of 13 pc of the apparent centre. This includes a population of ~ 169 OB stars, the most massive of which is $\sim 100 M_{\odot}$ with an age of ~ 2 Myr. Cyg OB2 does not exhibit evidence of mass segregation, whereby the most massive stars occupy regions with the greatest gravitational potential (Wright *et al.*, 2014a).

The initial mass function (IMF) at the high mass end is not agreed upon in the literature, with many authors arriving at different conclusions (Massey and Thompson, 1991; Massey *et al.*, 1995; Knödlseder, 2000; Kiminki *et al.*, 2007; Wright *et al.*, 2010; Comerón and

Pasquali, 2012). Wright *et al.* (2015) take into account massive stars which have evolved to their end state. In this way they find that the observed stellar masses follow an IMF $\zeta(m) \propto m^{-2.39\pm0.19}$ at high masses, which is approximately consistent with the 'universal' IMF of Kroupa (2001) (or indeed a Salpeter, 1955, IMF). However, inferring the high mass IMF is problematic since the occurance of supernovae in Cyg OB2 remains a point of debate (see Butt *et al.* 2003 and discussion in Wright *et al.* 2015).

Wright *et al.* (2016) describe the spatial density distribution in Cyg OB2 with an Elson, Fall and Freeman profile (EFF profile hereafter – Elson *et al.*, 1987):

$$\rho = \rho_0 \left(1 + \frac{r^2}{a_{\rm stars}^2}\right)^{-\frac{\gamma+1}{2}} \tag{6.1}$$

where $a_{\rm stars} = 7.5$ pc and $\gamma = 5.8$. Normalising for the total mass of the cluster this makes the central mass density $\rho_0 \approx 22 M_\odot$ pc^{-3}. However, this profile was derived for a small central region of ~ 8 pc$\times 8$ pc, which does not enclose the estimated core radius. Hence, when we consider the distribution of the stellar mass in our models (see Section 6.4.3) we will focus on reproducing the mass enclosed within a projected radius of 13 pc (Wright *et al.*, 2015).

6.2.2 Velocity dispersion

Wright *et al.* (2016) presented a high-precision proper motion study of the X-ray sources in Cyg OB2. They found that the region is gravitationally unbound and exhibits an anisotropic velocity dispersion with proper motion components $\sigma_\alpha = 13.0^{+0.8}_{-0.7}$ km s^{-1} and $\sigma_\delta = 9.1^{+0.5}_{-0.5}$ km s^{-1}. The radial velocity dispersion has also been measured to be $\sigma_r \sim 10$ km s^{-1}, although systematic overestimates due to the binary fraction introduce uncertainties (Kiminki *et al.*, 2007, 2008).

Interestingly Wright *et al.* (2016) found little evidence for expansion (or contraction) in the velocity field when considering the large scale variations of the proper motion distribution. This finding is independent of the definition of the centre of the association, and was argued by dividing proper motions into radial and azimuthal components. The ratio of kinetic energy between the radial and azimuthal directions was found to be approximately 60 : 40. In the radial (projected) velocities, no bias is found towards or away from the centre. In the azimuthal direction there is some preference for motions in the direction of negative PA, with a ratio in kinetic energy of 66 : 34. Because Cyg OB2 is not bound, this is interpreted by Wright *et al.* (2016) as a remnant of the angular momentum of the primordial GMC.

6.2.3 Sub-structure

Interpretation of the internal sub-structure in Cyg OB2 is not straightforward. Knödlseder (2000) concluded that it is a spherically symmetric region with a diameter of $\sim 2^\circ$ (46 pc). Since then, a number of authors have suggested a more complex morphology:

- Bica *et al.* (2003) suggested that Cyg OB2 is home to two open clusters which can be seen towards the centre. However, Guarcello *et al.* (2013) note that the two apparent clusters are divided by a bright nebula. This makes it unclear if the two are physically separate or merely appear so due to the higher extinction in the intervening region.

- Wright *et al.* (2010) found evidence of populations within Cyg OB2 with distinct ages, $3.5^{+0.8}_{-1.0}$ Myr and $5.25^{+1.5}_{-1.0}$ Myr for central and northwestern regions respectively. Ostensibly, this suggests multiple star forming events. However, the ages in physically separated regions exhibited a wide spread such that they are almost consistent with being coeval. Further the authors acknowledge a number of sources of uncertainty, including variability in pre-MS stars (Herbst *et al.*, 1994); binarity (Preibisch and Zinnecker, 1999); variable accretion (Baraffe *et al.*, 2009); or non-uniform extinction (Guarcello *et al.*, 2012).

- A large number of A stars were identified south of the apparent centre by Drew *et al.* (2008). This population appears distinct spatially and non-coeval with the OB population (although the estimated ages $\sim$ 5–7 Myr are nearly consistent with coevality within uncertainties). As the authors note, it is also possible that these stars are actually behind Cyg OB2 along the line-of-sight and wrongly associated due to projection (Schneider *et al.*, 2006).

- Guarcello *et al.* (2013) used a critical side length criterion in the minimum spanning tree of the disc-bearing population to suggest that Cyg OB2 has a clumpy sub-structure. However, as stated by the authors, the definitions of these clumps are dependent on the definition of the critical side length. Additionally, the non-uniform extinction due to foreground gas complicates this argument as in the case of the two open clusters identified by Bica *et al.* (2003).

- Perhaps the best evidence for underlying structure in Cyg OB2 has been the proper motion study of Wright *et al.* (2016). On small scales they found evidence for kinematic sub-structure, which is the correlation of proper motion vectors with position. Applying a Moran's I statistic (Moran, 1950) they found correlation with a significance of 9.7σ and 12.5σ in RA and Dec velocity components respectively.

6.2.4 PPD population

Guarcello *et al.* (2016) studied the correlation between the fraction of surviving PPDs as a function of the local FUV and EUV intensity. They use a sample of 7924 X-ray sources (Wright *et al.*, 2014b), for which the presence (absence) of a PPD is inferred by the presence (absence) of an infrared excess in the photometric data compiled from numerous surveys (see Guarcello *et al.*, 2013). Subsequently they estimate the local flux as a function of projected separation from each O star (see Guarcello *et al.*, 2007). The disc fractions as a function of $F_{\rm FUV}$ are divided into 6 bins between $\sim 10^3\,G_0$ and $\sim 5\times10^4\,G_0$. Over this space the disc fraction drops monotonically from $\sim 40\%$ to 18% with FUV intensity (see figure 3 in Guarcello *et al.*, 2016). These observations are discussed in the context of modelling in Section 6.4.2.

6.2.5 Observational summary & modelling challenges

Cyg OB2 is a well studied young association, and as such a large number of physical characteristics serve as constraints and measures for the success of any modelling attempts. Some such metrics are as follows:

- Wright *et al.* (2016) find that the velocity dispersion in Cyg OB2 is anisotropic. This suggests that the stars share the systematic large-scale velocity field of the primordial GMC. We will find that such observations cannot be reproduced by simple models without underlying sub-structure.
- Cyg OB2 presently has a central mass of $\sim 1.6\times10^4\,M_\odot$ within 13 pc of the centre. Any dynamical model should match this central density after evolving for the age of the association ($\sim 3-5$ Myr).
- Although Cyg OB2 is gravitationally unbound with a large velocity dispersion, there is no bias (inwards or outwards) in the radial component of kinetic energy. This apparently suggests a lack of recent rapid expansion, despite the high velocities. When we consider our final N-body model, we will explore what expansion metric we would 'observe' (Section 6.4.3).
- Statistical measures of the proper motion distribution suggest kinematic sub-structure which is probably indicative of stars travelling together as small virialised groups (Wright *et al.*, 2016).
- The disc fraction as a function of (projected) FUV field strength (Guarcello *et al.*, 2016) provides a constraint on the length of time for which external photoevaporation

has been an efficient mechanism in Cyg OB2. This allows us to put constraints on the gas expulsion timescale. We perform these calculations to constrain the appropriate N-body model in Section 6.4.2, then revisit the PPD properties obtained from our final model in Section 6.4.4.

All these metrics except the last are considered for our model in Section 6.4.3.

6.3 Numerical Method

The goal of our models is to reproduce the observed dynamical properties of the stellar population and the observed fractions of surviving discs. The latter is achieved by tracking the FUV flux experienced by PPDs evolving within a given N-body model. In this section we discuss the modelling procedure applied to both the stellar dynamics (Section 6.3.1) and the disc evolution (Section 6.3.2).

6.3.1 Kinematic modelling

The dynamical evolution of the stellar population is calculated using NBODY6++GPU (Wang *et al.*, 2015). This is an MPI/GPU accelerated version of NBODY6 (Spurzem, 1999; Aarseth, 2003), and has built-in routines to deal with the evolution of a stellar cluster within a (gas) potential. As the stellar components of Cyg OB2 are presently highly supervirial, the latter feature is necessary for an initially virialised state.

Gas potential

The complex nature of Cyg OB2 means that some simplifying assumptions are required for dynamical modelling. We first assume that the cluster was initially in virial equilibrium due to the contribution to the gravitational potential of the gas in the primordial association. This is achieved by invoking a Plummer potential (for numerical convenience) corresponding to a gas density profile:

$$\rho_{\rm gas} = \frac{3M_{\rm gas}}{4\pi a_{\rm gas}} \left(1 + \frac{r^2}{a_{\rm gas}^2}\right)^{-5/2}$$

where $M_{\rm gas}$ is the total gas mass, r is the radial distance from the centre of the association, and $a_{\rm gas}$ is the scale parameter. During initial tests, we have varied $a_{\rm gas}$ (and the stellar scale parameter $a_{\rm stars}$), and although it has a mild effect on the kinematic properties of our models, the exact value (within order unity) is not crucially important. This is particularly true in the stochastically defined initial conditions of sub-structured models (see Section

6.3.1 below), where kinematics are more dependent on the specific realisation. Physically we expect $a_{\rm gas} \gtrsim a_{\rm star}$, and we fix $a_{\rm star} = 7$ pc (as there is no clear evidence of past expansion) and $a_{\rm gas} = 10$ pc.

For a Plummer density profile the specific gravitational potential is:

$$\phi(r) = -\frac{GM_{\rm gas}}{a_{\rm gas}} \left(1 + \frac{r^2}{a_{\rm gas}^2}\right)^{-1/2}. \tag{6.2}$$

The total potential in a given cluster make up of N stars of mass m_i initially at distance r_i from the centre and r_{ij} from a star of mass m_j is:

$$U_{\rm tot} = \sum_i^N m_i \left(\phi(r_i) + \sum_{j \neq i}^N \frac{Gm_j}{2r_{ij}}\right). \tag{6.3}$$

Then using equations 6.2 and 6.3 we require that initially

$$Q_{\rm vir,0} \equiv \frac{\sum_i^N m_i v_i^2}{2U_{\rm tot}} = 0.5$$

where v_i is the magnitude of the initial velocity of the $i^{\rm th}$ star. The total gas mass is chosen to maintain initial virial equilibrium for a cluster with a given velocity dispersion.

Our prescription of gas removal introduces an expulsion timescale $\tau_{\rm exp}$ over which time the potential is removed. The gas mass is reduced linearly such that $\dot{M}_{\rm gas} = M_{\rm gas,0}/\tau_{\rm exp}$. We vary $\tau_{\rm exp}$ to investigate how this affects the disc population due to extinction (see Section 6.4.2). We fix the time at which gas expulsion is initiated to be $\tau_{\rm delay} = 1$ Myr, consistent with the age of the most massive stars in Cyg OB2 (~ 2 Myr) if the cluster age is 3 Myr (the period for which we evolve the whole system). We further define $\tau_{\rm gas} \equiv \tau_{\rm delay} + \tau_{\rm exp}$. For a discussion of the influence of gas expulsion on the dynamical state of a young cluster, see Baumgardt and Kroupa (2007).

Clearly, while computationally necessary here, a Plummer potential is not a realistic reflection of the physical conditions of the primordial gas distribution during the embedded phase. Initially, gas density distributions would trace the stellar density (since the stars form from the gas). Subsequently, we would expect gas expulsion to occur as expanding bubbles from the most massive stars in the region (e.g. Dale and Bonnell, 2011; Dale *et al.*, 2014; Ali *et al.*, 2018). We therefore expect intra-clump or -filament potential to reduce faster than inter-clump potential. The influence of a geometrically complex potential on the evolution of the stellar population is certainly of interest for accurately reproducing observed kinematics and spatial distributions. However, we assume that the Plummer potential imposed here is

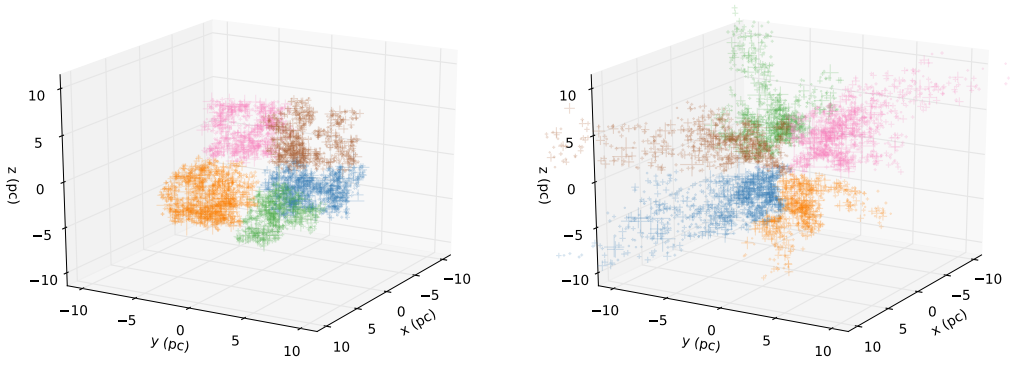

(a) FRAC (b) FILA

Fig. 6.1 Example of an initial spatial distribution of stars in FRAC and FILA models (figures 6.1a and 6.1b respectively). In the FRAC model, stellar positions are distributed with a 'clumpy' morphology, whereas the FILA model exhibits extended filaments. A subset of 5000 stars within a cube of side length 10 pc are shown, where the coordinate system is defined by the gas potential (see text for details). Both models have a stellar mass of $10^4 M_\odot$ and the same half mass as an EFF profile with $a_{\rm stars} = 7$ pc, $\gamma = 5.8$; the FILA model also follows the same radial density profile (equation 6.1 with the aforementioned parameters). The scatter points are coloured by the largest scale subgroup with which they are associated and scaled linearly by the mass of the star.

sufficient for reproducing the global distribution of stellar positions and velocities. This is justified since we are primarily interested in preventing the rapid escape of the high velocity stars from the central regions of Cyg OB2. This is achieved by our spherically symmetric potential.

Stellar initial conditions

We define three different types of stellar initial condition, which we label uniform (UNIF), fractal (FRAC), and filamentary (FILA). A uniform cluster exhibits no underlying sub-structure, while fractal and filamentary clusters have enhanced local number densities, and stellar positions are correlated with velocities. While the surface density of FRAC model is 'clumpy', and individual clumps can be spatially isolated, a FILA model is defined such that the (radially binned) surface density follows an EFF profile. A filamentary model captures the morphology seen in both observations and simulations of star forming regions (e.g. Bonnell *et al.*, 2008; Molinari *et al.*, 2010; André *et al.*, 2014), however we include both FRAC and FILA models in this work to compare their properties by the metrics of interest. We discuss the generation of each set of initial conditions below.

The simplest initial conditions are `UNIF` models for which stellar positions are simply drawn from an EFF profile (equation 6.1, Elson *et al.*, 1987). We fix $\gamma = 5.8$, consistent with the present day value, and fix $a_{\rm stars} = 7$ pc. The magnitude of the velocities are then chosen from a Maxwell-Boltzmann distribution

$$f(v) \propto v^2 \exp(-v^2) \tag{6.4}$$

with a random direction, then normalised as discussed in Section 6.3.1. Drawing from this distribution will produce a significant number of unbound stars (particularly at the high velocity dispersions we require – see Section 6.4.3). It is possible that this distribution is truncated at large velocities, and indeed star formation models suggest stars might have a smaller velocity dispersion than the primordial gas (Offner *et al.*, 2009, see Section 6.4.3).

A `FRAC` model is generated using the recipe fully described by Goodwin and Whitworth (2004) which we briefly review here (see also Scally and Clarke, 2002; Craig and Krumholz, 2013). First we define a cube with side length 2 (in arbitrary units) centred at the origin. We then divide it up into $(2P_0)^3$ sub-cubes, where P_0 is an integer (initially chosen to be unity) which dictates the number of the largest scale sub-clusters. The centre of each of these represent the potential positions for the first generation of stars, $g = 1$. All positions are offset by a vector with magnitude uniformly drawn between 0 and $2^{-(g+1)}/P_0$, and random (isotropically drawn) direction. 'Parent' positions $\boldsymbol{r}_g$ have 8 possible sites for 'child' positions $\boldsymbol{r}_{g+1}$ which are placed with a probability 2^{D_0-3}, where $D_0 \leq 3$ is the fractal dimension (which we fix at 2.5). Only existing children can parent future generations. We repeat this process until the number of positions greatly exceeds the number of stars in the model, at which point the members are randomly allocated to positions. The side length of the original cube is then redefined such that the initial half-mass radius matches that of an equivalent `UNIF` model with parameters $a_{\rm stars} = 7$ pc, $\gamma = 5.8$.

The velocities for each generation of stars $g = 1$ is chosen in the same way as for the `UNIF` model. Velocities for subsequent generations $\boldsymbol{v}_{g+1}$ are correlated to the velocity of the parent star $\boldsymbol{v}_g$:

$$\boldsymbol{v}_{g+1} = \boldsymbol{v}_g + \delta\boldsymbol{v}_{g+1}$$

where $\delta\boldsymbol{v}_g$ is a velocity with a random direction and magnitude δv_g. The latter is drawn from the modified Maxwell-Boltzmann distribution

$$f(\delta v) \propto \delta v^2 \exp\left(-2^g \delta v^2\right)$$

such that child stars have velocities correlated to their parents.

A FILA model is a hybrid between FRAC and UNIF. To construct the initial conditions we first produce a FRAC model and then force the stellar positions into an EFF profile. This is achieved by dividing the radial positions into bins, with the $j^{\rm th}$ bin containing $N_{{\rm c},j}$ stars approximately at radius $r_{{\rm c},j}$, and rescaling the size of each bin ($\Delta r_{{\rm c},j}$) from inside out to produce the appropriate number density with respect to imposed EFF profile:

$$\frac{N_{{\rm c},j}}{4\pi r_{{\rm c},j}^2 \Delta r_{{\rm c},j}} = \frac{\rho(r_{{\rm c},j})}{\langle m_{\rm star}\rangle}$$

where $\langle m_{\rm star}\rangle$ is the average stellar mass and $\rho(r)$ is defined in equation 6.1.

The results of this process are filament-like structures, as shown in figure 6.1, in which FRAC and FILA models are compared. In a FRAC model the density profile has hard edges and a clump-like sub-structure (as in figure 6.1a), while in the FILA model stellar density drops off smoothly with radius and produces filament-like sub-structure (as in figure 6.1b). This is because the initial clumps from which the stellar density is composed become 'stretched' radially when we impose the EFF profile, to produce several elongated distributions of stars. Both types of model demonstrate spatial and kinematic asymmetry with respect to the gas potential.

We draw stellar masses from a Kroupa (2001) IMF:

$$\xi(m) \propto \begin{cases} m^{-1.3} & \text{for} 0.08\,M_\odot \leq m < 0.5\,M_\odot \\ m^{-2.3} & \text{for} 0.5\,M_\odot \leq m < 1.0\,M_\odot \\ m^{-2.4} & \text{for} 1.0\,M_\odot \leq m < 100\,M_\odot \\ 0 & \text{else} \end{cases} \tag{6.5}$$

where at high mass end $> 1\,M_\odot$ we use the observed mass function in Cyg OB2 (Wright *et al.*, 2015). In our models stars are not primordially mass segregated.

Reproducing observations requires estimating an appropriate field of view, which is in turn dependent on the definition of the cluster centre. Observationally some discrepancy exists in this definition between different works, although authors generally agree within a few pc (see Wright *et al.*, 2016, for a discussion). For our purposes an approximate estimate of this centre is sufficient since we find that all the metrics we consider are only weakly dependent on our choice. For UNIF models, the cluster centre remains the centre of mass of the original set up. For FILA and FRAC models, where considerable anistropy exists in the stellar kinematic distribution, it is necessary to estimate the centre of mass for each snapshot in time. We choose an efficient (approximate) algorithm, in which we find the point which maximises the mass within a given projected radius (chosen to be $R_{\rm cent} = 10$ pc) by sampling

recursively over a grid of points. Providing the grid is sufficiently highly resolved, the centre we obtain is insensitive to the exact value of $R_{\rm cent}$ and number of iterations. All subsequent results should be understood in this context.

6.3.2 Disc evolution model

In this section we discuss the prescription we apply to calculate PPD evolution. Each disc is exposed to an FUV flux resulting from tracking the contributions from the stellar components within a given N-body model.

FUV flux and mass loss rate

As in the Chapter 5 we will consider mass loss in discs induced by FUV photons only. EUV photons dominate mass loss when external photoevaporation is already inducing very rapid or slow dispersal. Since we are interested on survival rates on a timescale of Myr, we are free to consider only the FUV induced contribution. We calculate the FUV flux experienced by each star in the same way as in Chapter 5, although in this context we also track the flux experienced by a given star over the course of our N-body simulations. For the FUV induced mass loss rates $\dot{M}_{\rm wind}$ we use the recent grid of models calculated by Haworth *et al.* (2018a). The grid covers a wide range of parameter space in outer disc radius (1 – 400 au), disc masses ($\sim 10^{-8}$ – $0.1\,M_{\odot}$), FUV field strengths (10 – 10^4 G_0) and stellar masses (0.05 – $1.9\,M_{\odot}$). These mass loss rates are interpolated linearly and applied to a viscously evolving disc to establish the expected disc properties in a given cluster environment.

Disc model and initial conditions

To calculate the state of PPDs evolving within the cluster we must take into account viscous expansion as well as the photoevaporative mass loss. The theoretical framework of this approach is discussed in Chapter 1 and the numerical method is outlined in Chapter 5 (see also Clarke, 2007). Under this model, we can write the accretion rate at the inner edge of the disc initially

$$\dot{M}_{\rm acc,0} = \frac{3\alpha M_{\rm disc,0} H_1^2 \Omega_1}{2R_1^2} \tag{6.6}$$

where $M_{\rm disc,0}$ is the initial disc mass, H_1 and Ω_1 are the scale height and Keplerian frequency at the disc scale radius R_1 (see Hartmann *et al.*, 1998). We truncate discs outside the initial outer radius $R_{\rm disc,0} = 2.5R_1$, such that the integral of equation 1.5 over the disc area yields

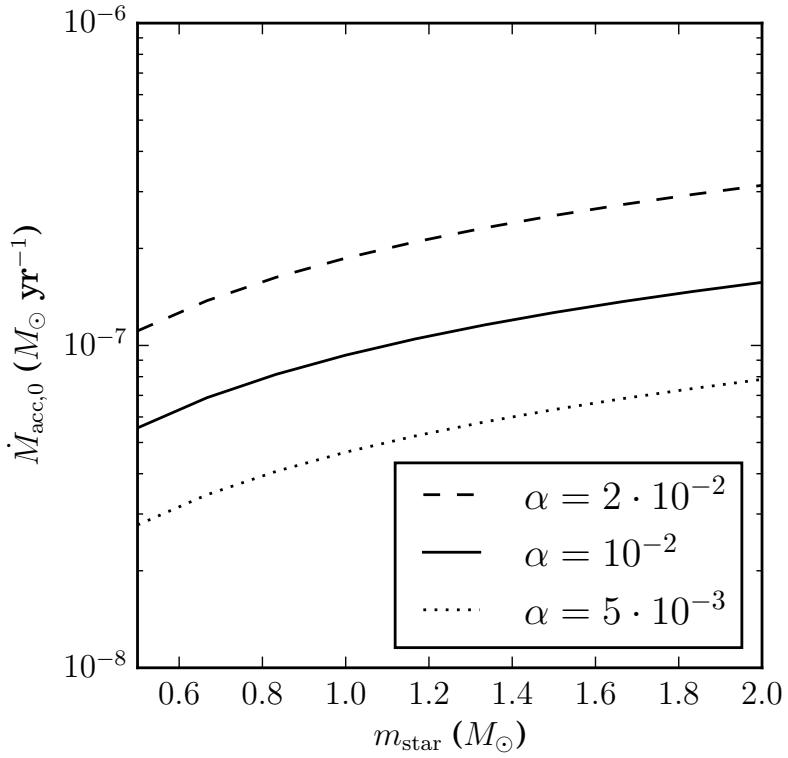

Fig. 6.2 Assumed initial viscous accretion rate (equation 6.6) as a function of stellar mass for $M_{\rm disc,0} = 0.1\,m_{\rm star}$ and a range of Shakura and Sunyaev α-viscosity parameters. The initial disc conditions are described in Section 6.3.2. The range of stellar masses we consider (0.5–2 $M_\odot$) is discussed in Section 6.4.2.

92% of $M_{\rm disc,0}$. We take the scale radius to be

$$R_1 = 40 \left(\frac{m_{\rm star}}{1\,M_\odot} \right)^{1/2} \text{au}. \tag{6.7}$$

Unless otherwise stated we will assume that $M_{\rm disc,0}$ is uniformly distributed between 0.01 – 0.1 $m_{\rm star}$ (Andrews *et al.*, 2013); then equation 6.7 means that the distribution of initial surface densities at R_1 remains independent of stellar host mass. The scale height H is proportional to the radius throughout the disc, and we choose $H_1/R_1 = 0.05$. The maximum initial accretion rate (equation 6.6) as a function of stellar mass is indicated in figure 6.2. The associated viscous timescale is $\tau_{\rm visc} \approx 0.5$ Myr for a solar mass star with $\alpha = 10^{-2}$, $R_1 = 40$ au (see equation 1.6). Combining equation 1.6 with equation 6.7 we have $\tau_{\rm visc} \propto m_{\rm star}^{1/4}$.

During this chapter we will explore the effect of altering disc initial conditions on their final properties, however we always consider a distribution of initial disc masses. Allowing a range of initial disc masses accounts for the observed range of stellar ages (since internal

processes deplete the disc over time) and variable disc initial conditions. Additionally, for a given FUV flux environment some fraction of discs survive, and the findings of Guarcello *et al.* (2016) indicate that this survival fraction reduces monotonically with increasing $F_{\rm FUV}$. We find that, depending on initial disc properties, dynamical mixing between regions of different FUV flux and the range of $F_{\rm FUV}$ within a single bin alone are insufficient to produce the observed survival fractions (i.e. observed survival fractions between $F_{\rm FUV}$ bins do not jump rapidly from $\sim 0\%$ to $\sim 100\%$ at a certain threshold). The chosen initial conditions and the variation between discs are therefore important in reproducing observations. Whether this dispersion is inherited from a tight correlation between stellar mass and PPD initial conditions is explored by considering host mass independent disc initial conditions in Section 6.4.4.

6.4 Results and discussion

6.4.1 Modelling approach

We aim to produce an N-body model, including initial gas potential, with a self-consistent treatment for the photoevaporation of the PPD population. We simplify the modelling procedure by the following approach:

1. First we estimate the gas expulsion timescale $\tau_{\rm gas} \equiv \tau_{\rm delay} + \tau_{\rm exp}$ by considering the observed surviving disc fractions as a function of FUV field strength (Section 6.4.2). The presence of primordial gas influences the models in two ways: it imposes a gravitational potential on the stellar population, and suppresses photoevaporation by extincting FUV photons. Using the latter effect we can calibrate the period of efficient exposure to the observed survival rate of PPDs. There exists a degeneracy in this calculation with the assumed disc viscosity, and we explore the influence of varying both parameters (see Section 6.4.2).

2. Having established the rate of gas expulsion, we apply the appropriate time-dependent potential to establish the dynamical evolution of the stellar population consistent with kinematic and spatial data. In Section 6.4.3 we deduce the initial conditions required to reproduce the observed anistropic velocity dispersion. In Section 6.4.3 we vary the initial stellar mass required to reproduce the observed central density (within 13 pc of the apparent centre).

3. Finally, we combine our findings into a 'best-fitting' model, and explore the evolution of PPDs over time in Section 6.4.4. This allows us both to test whether external

photoevaporation is a viable mechanism for disc depletion in Cyg OB2 and to make predictions regarding the disc properties for future observations.

6.4.2 Disc fractions and gas expulsion

We first estimate the influence of the timescale for gas expulsion on the PPD population survival fractions. A number of physical effects must be taken into account when considering the statistical distribution of disc fractions. Most obviously, projection effects can lead to a distribution of physical distances between stars for every apparent (projected) separation, and therefore a range of $F_{\rm FUV}$. Binarity and the initial PPD properties will also influence the total disc fraction. However, to first order, the steepness of the drop-off of the disc fraction with $F_{\rm FUV}$ indicates the length of time for which external photoevaporation has been an efficient mechanism for disc destruction in a given environment. Initial tests suggest that a massive gas mass ($\gtrsim 10^6 M_{\odot}$) is required to maintain virial equilibrium in the primordial Cyg OB2. Due to extinction of FUV photons, this gas mass is sufficient to dramatically reduce photoevaporation efficiency.

The current PPD population therefore allows us to constrain when the gas component of Cyg OB2 was expelled. The relatively short period of expulsion ($\lesssim 2$ Myr) means that we are free to consider the influence of FUV photons on disc evolution from the time $\tau_{\rm gas}$ at which gas is completely removed. Practically this means that we can apply a simplified `UNIF` model with the present day mass and 'switch on' photoevaporation at different times. We then compare the disc fractions as a function of FUV flux after 3 Myr of evolution, and thus estimate the gas expulsion timescale. The FUV flux in those bins is calculated in the same way as in Guarcello *et al.* (2016), using the projected distance between stars – this we call 'projected' $F_{\rm FUV}$ (as opposed to 'real' $F_{\rm FUV}$, as experienced by a given disc). As an estimate of the influence of dynamical mixing between projected FUV flux bins, we start with a stellar velocity dispersion 17 km/s and hold the stars in virial equilibrium with an external potential.

The rate at which irradiated discs are destroyed is also dependent on the α-viscosity parameter (Section 6.3.2). The chosen α dictates the rate at which a disc viscously expands into a region where photoevaporation rates are high, as well as dictating mass loss through accretion. This adds a degeneracy to our approach which, given uncertainties in α, introduces similar uncertainties in $\tau_{\rm gas}$. We investigate this degeneracy by calculating surviving PPD fractions for a number of different values for $\tau_{\rm gas}$ (1, 2, 2.5 and 2.75 Myr) and α (5×10^{-3}, 10^{-2}, 2×10^{-2}).

We calculate disc evolution for a subset of discs with host stars in the mass range 0.5 – 2 $M_{\odot}$. Stars less massive than this are not present in the sample used by Guarcello *et al.* (2016), while the disc mass loss rates calculated by Haworth *et al.* (2018a) do not apply

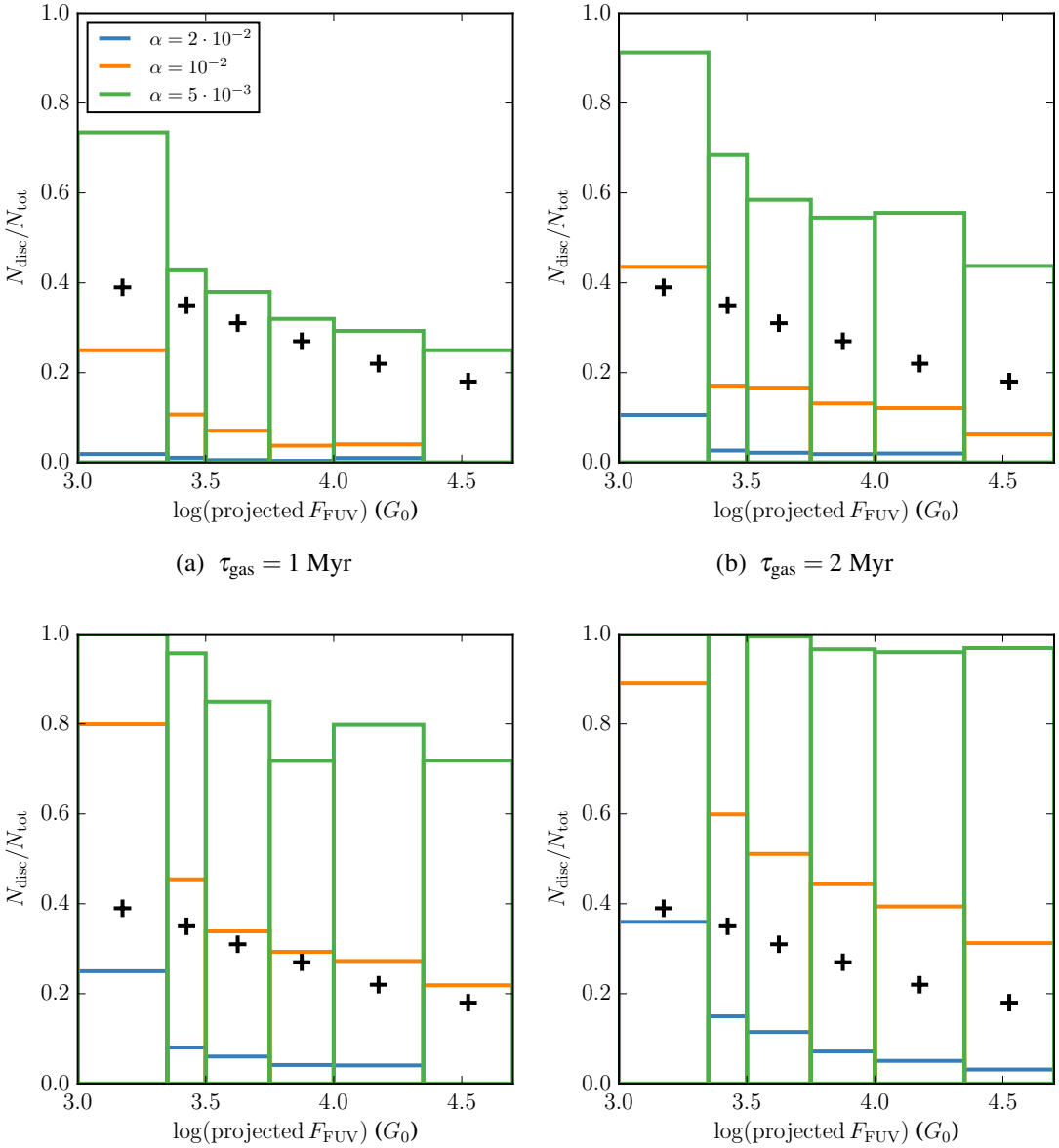

(a) $\tau_{\rm gas} = 1$ Myr

(b) $\tau_{\rm gas} = 2$ Myr

(c) $\tau_{\rm gas} = 2.5$ Myr

(d) $\tau_{\rm gas} = 2.75$ Myr

Fig. 6.3 Disc fractions versus projected FUV flux in a virialised cluster evolved for 3 Myr when external photevaporation is 'switched on' after a period $\tau_{\rm gas}$. Results are shown for a range of Shakura and Sunyaev α-viscosity values. The black crosses represent the observational values found by Guarcello *et al.* (2016). These results are used to calibrate the timescale for gas expulsion and the corresponding disc viscosity required to reproduce the observed disc fractions. We find that $\tau_{\rm gas} = 2.5$ Myr with $\alpha = 10^{-2}$ matches observed disc fraction. This value for α is effectively an upper limit since we assume that extinction efficiently shuts off photoevaporation before all gas is expelled.

for higher mass stars. A disc is considered destroyed if it has a mass $< 10^{-5} M_{\odot}$, which is estimated by Guarcello *et al.* (2013) as a limit below which SEDs are more difficult to interpret. In fact discs of such low mass ($\sim 10^{-5} M_{\odot}$) are destroyed quickly in regions of strong FUV fields, so our results are insensitive to the exact value of this threshold.

The results of this preliminary modelling procedure compared with the observational findings of Guarcello *et al.* (2016) are summarised in figure 6.3. We expect disc fractions at lower $F_{\rm FUV}$ are overestimated as we do not consider other disc dispersal processes (such as internal photoevaporation, see Section 6.4.4). We therefore focus on matching disc fractions in regions of higher $F_{\rm FUV}$. We find that $\tau_{\rm gas} = 2.5$ Myr and $\alpha = 10^{-2}$ give a good fit to the data for projected $F_{\rm FUV} \gtrsim 3000\,G_0$. Since we have assumed 100% extinction of FUV photons before gas is completely expelled, this α is an upper limit. As discussed above, reducing the expulsion timescale to $\tau_{\rm gas} = 1$ Myr while decreasing the viscosity such that $\alpha = 5 \times 10^{-3}$ also yields the correct disc fractions. However, if gas ejection was initiated at the time of formation of the most massive stars (~ 2 Myr) this would suggest instantaneous expulsion, which is not physical. In this case early supernovae may be responsible for driving gas mass loss (see discussion in Section 6.2.1). However, for short $\tau_{\rm gas}$ Cyg OB2 must have had a extremely large initial stellar mass to maintain the present day central density ($\gg 10^5 M_{\odot}$, see Section 6.4.3 and figure 6.7), which is neither supported by observations nor computationally practicable for the range of models we wish to explore.

While the simplified model presented in this section is not an accurate representation of the dynamical conditions in the region, it represents a first-order approximation on which we can base our choice of kinematic parameters in Section 6.4.3. We will again consider the disc fractions for a more realistic model in Section 6.4.4.

6.4.3 Stellar population properties

In this section we consider the initial conditions for our *N*-body models of the stellar population of Cyg OB2. We proceed by first aiming to reproduce the observed velocity dispersion in the region by varying the initial velocity distribution and sub-structure (Section 6.4.3). Subsequently, we match the observed central density by varying the initial stellar mass (Section 6.4.3).

Velocity dispersion, anisotropy and sub-structure

The first observable quantity we aim to reproduce is the central velocity dispersion and its anisotropy ($\langle v^2 \rangle^{1/2} \approx 17$ km/s, and the proper motion dispersions $\sigma_{\alpha,\delta} \gtrsim \sigma_r$ the line of sight component – see Wright *et al.*, 2016). This is because it is not strongly sensitive to the initial

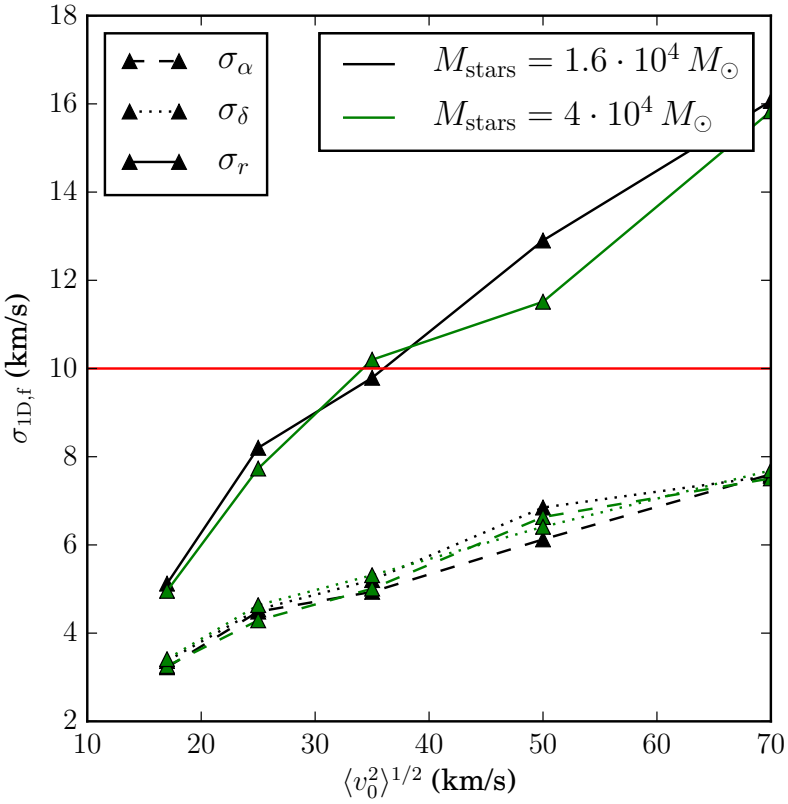

Fig. 6.4 The components of the velocity dispersion (σ_α, σ_δ and σ_r, where σ_r is the line of sight component) in our model using the Wright *et al.* (2016) field of view after 3 Myr of evolution versus the initial three-dimensional velocity dispersion over the entire cluster, $\langle v_0^2 \rangle^{1/2}$. The initial conditions are not sub-structured (`UNIF`) and have initial parameters $a_{\rm gas} =$ 10 pc, $a_{\rm stars} = 7$ pc, $\tau_{\rm exp} = 1.5$ Myr and two different stellar masses $M_{\rm stars} = 1.6 \cdot 10^4 M_\odot$, $4 \cdot 10^4 M_\odot$ (black and green lines respectively). The horizontal red line represents the mean observed 1D velocity dispersion $\langle v^2 \rangle^{1/2}/\sqrt{3} \approx 10$ km s^{-1}. The radial (line of sight) velocity dispersion $\sigma_r > \sigma_{\alpha,\delta}$ due to projection effects and velocity sorting. Observationally we require a model such that the 1D velocity dispersion components are of the same order (in fact observations indicate $\sigma_{\alpha,\delta} \gtrsim \sigma_r$). This is not reproduced by the `UNIF` model.

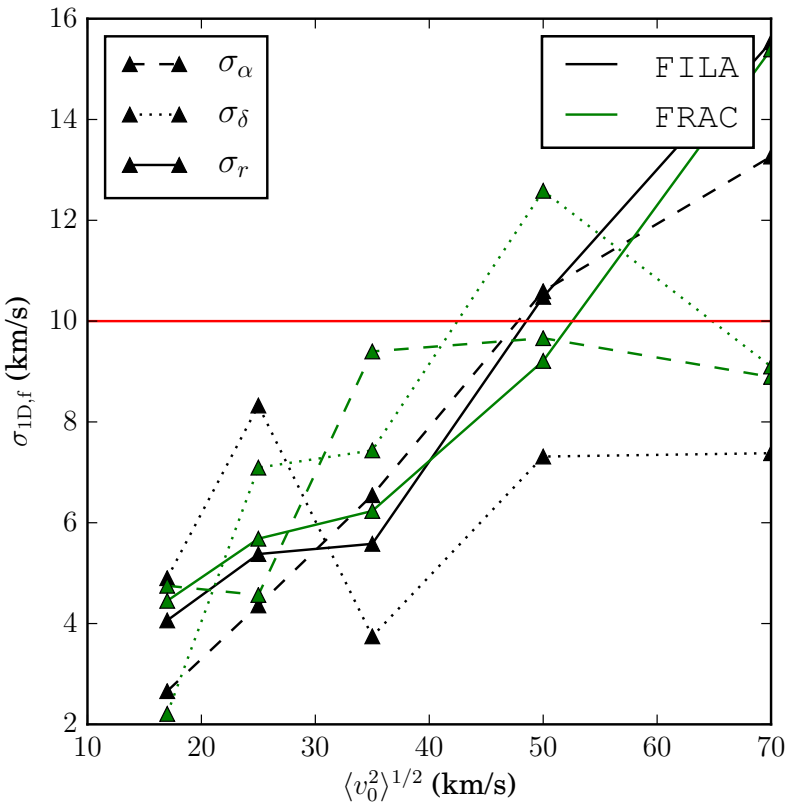

Fig. 6.5 The components of the velocity dispersion ($\sigma_{\alpha,\delta,r}$) as in figure 6.4 but for a fixed stellar mass $M_{\rm stars} = 1.6 \cdot 10^4 M_\odot$. Instead of the UNIF model in figure 6.4, the black lines represent the case for a FILA cluster model and the green lines are for a FRAC cluster model, both with $P_0 = 1$ and $D_0 = 2.5$. In this case the large scale sub-structure gives rise to much greater stochastic variations in the relative 1D velocity dispersions, and is consistent with observations.

stellar mass of the cluster. We demonstrate this by considering UNIF cluster models (where cluster conditions are relatively non-stochastic) for a range of initial 3D velocity dispersions and stellar masses; we plot the results in figure 6.4. As the potential is dominated by the gas in the cluster, and the stellar component is itself highly supervirial, the final central velocity dispersion is insensitive the total stellar mass.

Figure 6.4 demonstrates that UNIF models fail to reproduce the observed velocity dispersion. This is because in a non-sub-structured model we find suppressed proper motion velocity dispersions $\sigma_{\alpha,\delta}$ with respect to the radial component σ_r, since stars with high velocities in the plane of the sky preferentially leave the central field of view over time (velocity sorting). To remedy this, we need to incorporate sub-structure into our model.

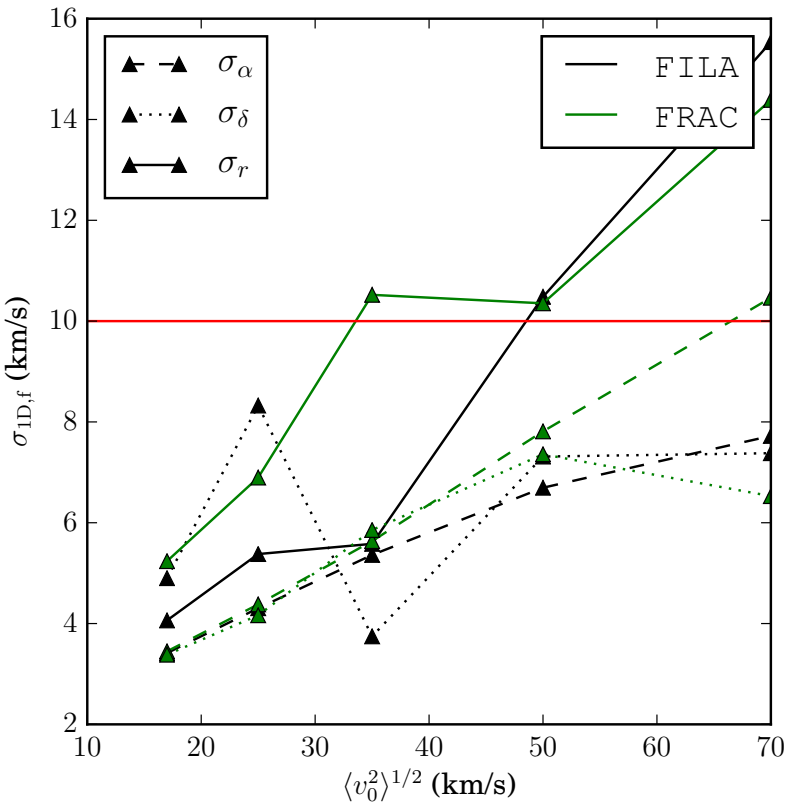

Fig. 6.6 The same as in figure 6.5 but with smaller scale sub-structure ($P_0 = 2$). In this case the scale of sub-structure is insufficient to result in proper motion velocity dispersions comparable to the radial dispersion (we have $\sigma_{\alpha,\delta} < \sigma_r$).

To demonstrate the influence of sub-structure on the components of the velocity dispersion within a finite field of view, we run `FILA` and `FRAC` models with large scale sub-structure ($P_0 = 1$), and rotate a snapshot at 3 Myr such that the radial velocity dispersion is approximately minimised. The results of this process are shown in figure 6.5, where the decomposed velocity components are again compared with the initial three-dimensional velocity dispersion. The anisotropies in the velocity dispersion are reproduced in both `FILA` and `FRAC` cluster models.

The degree of anisotropy in the velocity dispersion is dependent on the scale of sub-structure. Figure 6.6 shows the results for initially smaller filaments/clumps (using $P_0 = 2$). While there still exist stochastic fluctuations in the components of the velocity dispersion, the degree of anisotropy is not sufficient to yield proper motion velocity dispersions greater than the radial component. This suggests that the initial region consisted of large clumps or filaments of mass $\sim 10^4\ M_\odot$.

We estimate that the required initial velocity dispersion in Cyg OB2 is $\langle v_0^2 \rangle^{1/2} \sim 50$ km/s, although the stochasticity of the sub-structured models makes precise estimates impractical.

In future models we will assume this is the initial three-dimensional velocity dispersion. Other required parameters, such as the initial stellar mass, are chosen to be consistent with this property.

Central mass

We wish to alter the initial stellar mass such that the central density at the end of the simulation is consistent with observations. A cluster model with a central mass of $1.6 \times 10^4 M_\odot$ after 3 Myr of evolution is required, where $\langle v_0^2 \rangle^{1/2} = 50$ km/s as discussed in Section 6.4.3. To find the appropriate initial mass we run `UNIF`, `FRAC` and `FILA` models at stellar masses $M_{\rm stars} = 2 \times 10^4 M_\odot$, $4 \times 10^4 M_\odot$ and $8 \times 10^4 M_\odot$. The results are shown in figure 6.7. We find that $M_{\rm stars} = 8 \times 10^4 M_\odot$ (figure 6.7c) is sufficient to yield the required central mass after 3 Myr of evolution.

Neither the initial mass nor the sub-structure has a significant effect on the fraction of the stellar mass which remains within a 13 pc projected radius (approximately a quarter in each case). As in the case of our velocity investigation, this is because the stellar contribution to the potential energy is much smaller than the total kinetic energy.

The central mass in all of our models undergoes a similar temporal evolution. In figure 6.7 we see an initial rapid mass loss as stars with the highest energies escape the potential. This is because we do not truncate the velocity dispersion such that escapers are initially forbidden; it is not clear whether this is physically realistic, and the effect of choosing such initial conditions is discussed in Section 6.4.3 in the context of primordial gas mass. However, since stars which escape the central regions are not considered in our PPD models and the gravitational potential is dominated by the gas component, whether these early escapers are initially included in the model is of secondary importance. After this initial decline in mass, some high energy stars remain bound, and therefore return to the central regions, causing a modest oscillation in the mass. This is again a consequence of using a Boltzmann velocity distribution without truncating the high velocity end. The magnitude of this oscillation is more variable for sub-structured regions where velocities (and therefore kinetic energies) are correlated. Gas expulsion (starting at $\tau_{\rm delay} = 1$ Myr and continuing over $\tau_{\rm exp} = 1.5$ Myr) results in a decrease in gravitational potential, and as the number of stars with energies sufficient to escape increases, the central mass decreases.

Summary of best fitting model

By considering gas expulsion, stellar mass, velocity dispersion and initial sub-structure, we have found a model for the evolution of Cyg OB2, summarised by the parameters in

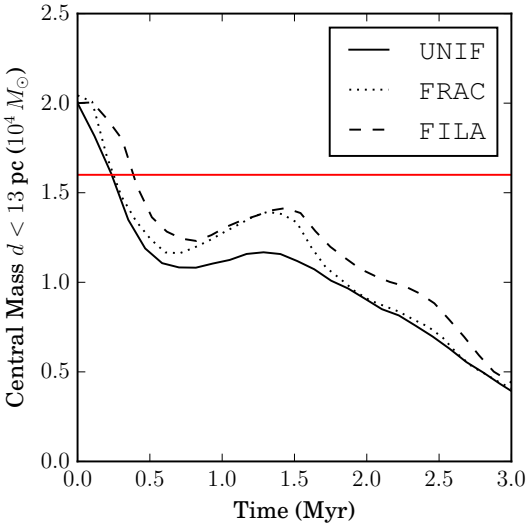

(a) $M_{\rm stars} = 2 \cdot 10^4\,M_\odot$

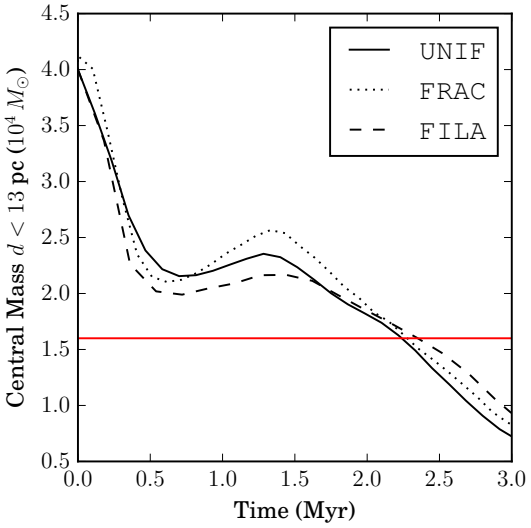

(b) $M_{\rm stars} = 4 \cdot 10^4\,M_\odot$

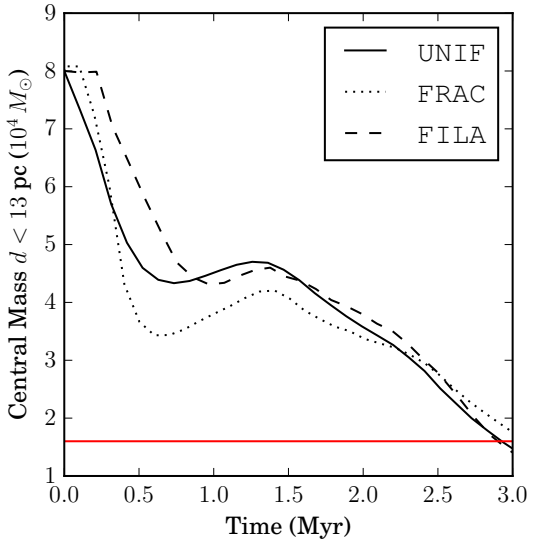

(c) $M_{\rm stars} = 8 \cdot 10^4\,M_\odot$

Fig. 6.7 Evolution of the stellar mass within a projected distance of 13 pc from the centre of the cluster. We show the results for `UNIF`, `FRAC` and `FILA` cluster models (solid, dotted and dashed respectively) over 3 Myr. All models have initial parameters $a_{\rm gas} = 10$ pc, $a_{\rm stars} = 7$ pc, $\tau_{\rm delay} = 1.5$ Myr, $\tau_{\rm exp} = 1.5$ Myr and varying stellar mass. The horizontal red line indicates the observed central mass $\sim 1.6 \times 10^4\,M_\odot$ (Wright *et al.*, 2015). We find that an initial mass of $\sim 8 \times 10^4\,M_\odot$ reproduces the observed central density.

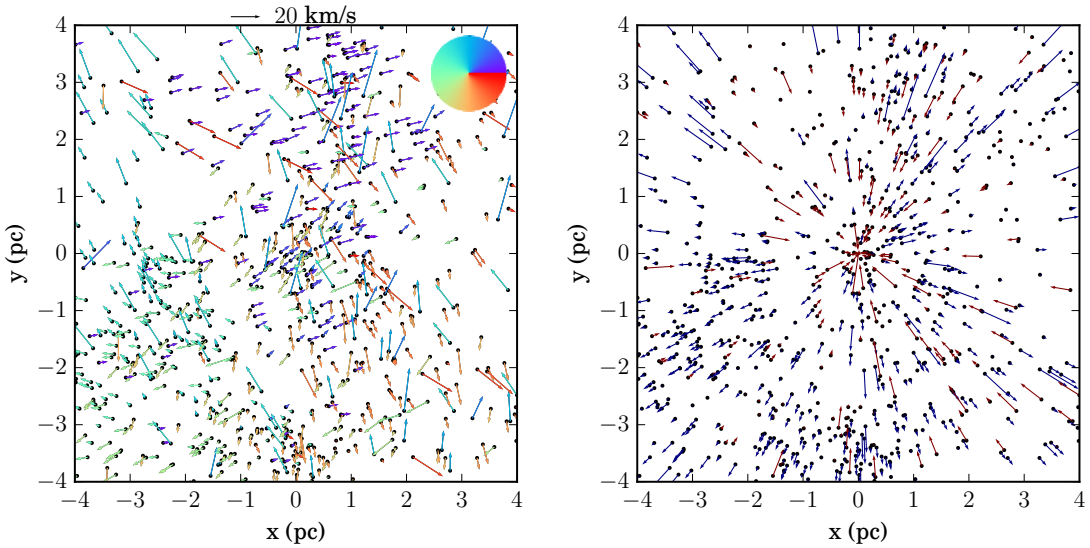

(a) (b)

Fig. 6.8 Velocity field of a subset of 800 stars in the central region of our chosen model (summarised by the parameters in Table 6.1) after 3 Myr of evolution. In figure 6.8a velocity vectors are colour coded by their direction to illustrate the underlying sub-structure; a correlation can be seen between position and velocity vectors. In figure 6.8b only the radial components in the plane of the sky are shown, coloured blue for stars moving outwards from the centre and red for infalling stars. There is no clear bias between infalling and outgoing velocities – see text for details. Similarly, Wright *et al.* (2016) found correlations between position and velocity vectors, and that Cyg OB2 shows no sign of expansion from the apparent centre.

Table 6.1, which fits observations of the stellar population. We refer to this as our 'best-fit' model, however it is the result of our deduction process, not the optimisation of a statistical metric or parameter space exploration. In our models we find gas expulsion was completed ~ 0.5 Myr ago (for a PPD viscous timescale of 0.5 Myr), the initial velocity dispersion was ~ 50 km/s and the initial cluster mass was $\sim 8 \times 10^4 M_\odot$. We further suggest that the largest scales of initial coherent clumps within the primordial Cyg OB2 had a mass of $\sim 10^4 M_\odot$. No significant dynamical differences can be found between `FRAC` and `FILA` type models at the present time, and we hereafter use a `FILA` model in our analysis of the disc population (Section 6.4.4).

The gas mass required for initial virial equilibrium is $M_{\rm gas} \sim 8 \cdot 10^6 M_\odot$ (with a scale parameter $a_{\rm gas} = 10$ pc). This would make the primordial GMC massive compared to known Milky Way molecular clouds, although the census is not complete (see Longmore *et al.*, 2014, for a review). It is also possible that the initial velocity dispersion is overestimated due to the

Type	$M_{\rm stars}$	$a_{\rm stars}$	γ	P_0	D_0	$M_{\rm gas,0}$	$a_{\rm gas}$	$\tau_{\rm delay}$	$\tau_{\rm exp}$
FILA	$8 \cdot 10^4\ M_\odot$	7 pc	5.8	1	2.5	$7.9 \cdot 10^6\ M_\odot$	10 pc	1 Myr	1.5 Myr

Table 6.1 Parameters of the 'best-fit' model, used to reproduce the properties of the observed stellar population of Cyg OB2.

truncation of equation 6.4 at high velocities (simulations suggest stars have a subvirial initial velocity dispersion with respect to the primordial gas – see Offner *et al.*, 2009; Kruijssen, 2012). While this would not influence the central velocity dispersion (high velocity stars leave the centre in any case) it would reduce the number of escapers early on in the cluster evolution and therefore the required initial stellar mass. It would also reduce the gas mass necessary for virial equilibrium as $M_{\rm gas} \propto \langle v^2 \rangle$ if $M_{\rm gas} \gg M_{\rm stars}$ (equation 6.3). If our gas mass estimate is accurate then this makes the star formation efficiency $\sim 1\%$, although this is probably a lower limit (an upper limit on $M_{\rm gas}$).

Sub-structure and expansion observables

Alternate kinematic constraints not considered in the previous analysis include the measures of sub-structure and the absence of expansion signatures in the stellar kinematics (Wright *et al.*, 2016). We find that determining these metrics is problematic for a given cluster model. This is because the values obtained differ stochastically depending on initial conditions, the time of 'observation' and the subset of stars used in taking a measurement. To obtain an accurate probability of finding the observed values for these metrics, a large number of models would need to be tested, which would be computationally expensive. However, for our chosen model the velocity field is illustrated in figure 6.8. We find that the correlation between positions and proper motions is clear (figure 6.8a), while figure 6.8b does not show clear evidence of expansion. However, the stellar components are in fact expanding globally since they are unbound.

To illustrate this point more fully, we define the expansion parameter:

$$\mathscr{E} = \frac{T^+}{T^- + T^+} \tag{6.8}$$

where $T^{+/-}$ is defined as the total kinetic energy of stars directed in the postive/negative projected radial direction (in the plane of the sky). Thus, $\mathscr{E} \to 1$ or 0 if the velocity dispersion indicates rapid expansion or contraction respectively. A value of $\mathscr{E} \approx 0.5$ would usually be taken as evidence that a stellar population is not expanding. In Figure 6.9 we show the cumulative distribution of the measured expansion parameter for random subsets of 800

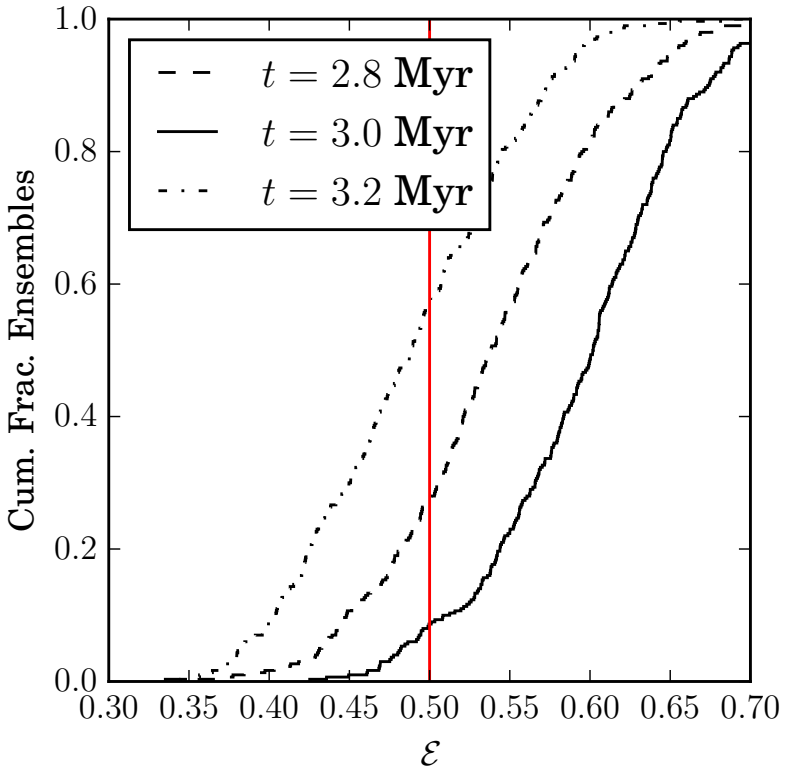

Fig. 6.9 The cumulative fraction of the number of ensembles (each defined to be a subset of 800 stars in the Wright *et al.* 2016 field of view) with expansion parameter $\mathscr{E}$ (equation 6.8) in our chosen model. A value of $\mathscr{E} \approx 0.5$, which was found by Wright *et al.* (2016) for Cyg OB2, would observationally be taken as an indication that no expansion is occuring.

stars in the Wright *et al.* (2016) field of view (the central 8 pc $\times$ 8 pc). We find that a wide range of values for $\mathscr{E}$ is possible at any given time. Depending on the time at which the velocities are observed and the chosen subsample, our model is found to be consistent with an observed value $\mathscr{E} \approx 0.5$. This is because the $\mathscr{E}$ distribution varies considerably and non-monotonically in time even for a single model. However, at any given time the stellar population is expanding (filaments are moving away from each other). Alternative geometrical signatures may be more successful at gauging such expansion. Due to the stochasticity and wide range of possible $\mathscr{E}$ values for our model, we conclude that $\mathscr{E}$ alone is not a sufficient metric to draw conclusions on the expansion of a sub-structured association. For further discussion on the kinematic indicators of expansion in OB associations, see Baumgardt and Kroupa (2007) and Ward and Kruijssen (2018).

In the remainder of this work we will first revisit the disc population in our model, checking that the population is consistent with the known disc fractions in the region.

Subsequently, we will explore predictions for the disc mass and radius distribution relevant for future observations in the region.

6.4.4 Disc properties

In what follows we will consider a `FILA` model with the properties described in Table 6.1. We fix the α-viscosity of the disc population with the value $\alpha = 10^{-2}$ (Section 6.4.2). As in Section 6.4.2 all discs are assumed to have an initial mass that is uniformly distributed between 1 – 10% of their host star mass (see Section 6.3.2), and scale radius as in equation 6.7. We consider the same range of stellar masses 0.5 – 2 $M_{\odot}$ and calculate the evolution of a subset of 5000 discs.

Disc fractions in best-fit model

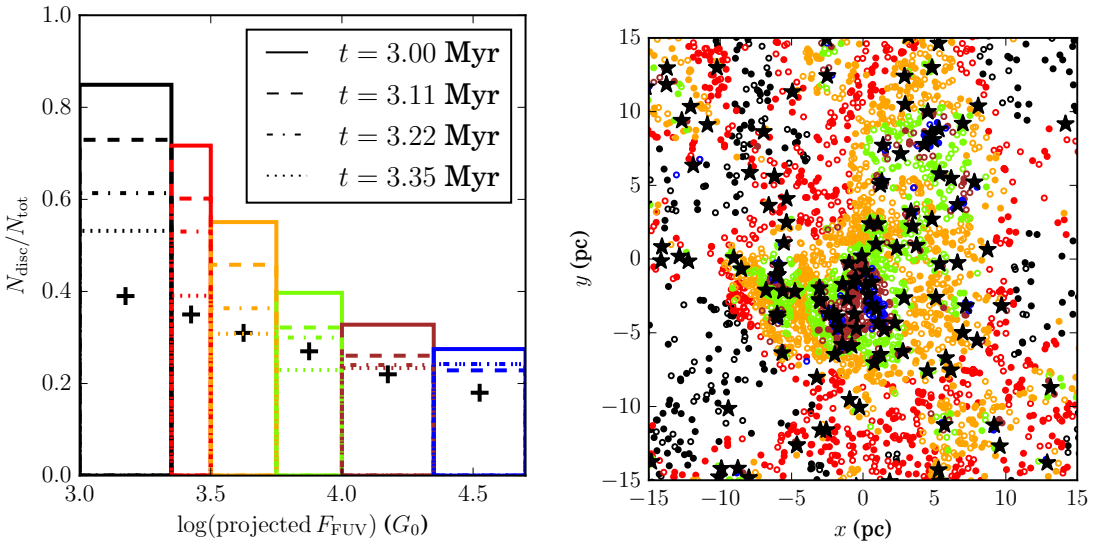

(a) (b)

Fig. 6.10 Model of the disc population in a model described by the parameters in Table 6.1. In figure 6.10a we show the disc fraction as a function of FUV flux, calculated by projected distance to massive stars, at varying times. These fractions are in good agreement with the observed disc fractions, indicated by black crosses. In figure 6.10b we show the physical distribution of the disc population after 3 Myr, colour coded by the projected FUV flux as in figure 6.10a. Star markers represent the positions of stars with a mass $> 10 M_{\odot}$. Empty circles represent a disc with a mass $< 10^{-5} M_{\odot}$, while filled circles are 'surviving' discs with a greater mass (c.f. fig. 3 in Guarcello *et al.*, 2016).

The disc fraction distribution in our best-fit model after ~ 3 Myr is summarised by figure 6.10, in which we show the surviving disc fraction as a function of projected FUV flux (figure

6.10a) with the spatial distribution and projected $F_{\rm FUV}$ in figure 6.10b. We find that after 3 Myr the number of surviving discs is slightly overestimated in our model, particularly at the lower FUV fluxes. There are two reasons why we expect this to be the case. Firstly, extinction in the FUV may decrease before gas is fully removed from the cluster. If gas is expelled due to the flux from massive stars, then the central, highly irradiated environments would become less dense and allow efficient photoevaporation at earlier times. Additionally, clumpy gas distributions may have a similar effect in reducing extinction during this period. Secondly, internal photoevaporation due to the stellar host depletes the gas content even when a PPD evolves in isolation. This speeds up destruction timescales, particularly in regions of lower $F_{\rm FUV}$, where the mass loss rates induced by internal and external photoevaporation become comparable.

The influence of the above considerations is uncertain and we therefore do not attempt to model them here. Our model does however reproduce the correct disc fractions within a reasonable period of time, particularly at $F_{\rm FUV} \gtrsim 3000\,G_0$. We conclude that the observations of Guarcello *et al.* (2016) can be explained by external photoevaporation of the PPD population in Cyg OB2.

Disc mass and FUV flux environment

To make predictions about the disc population in Cyg OB2 for comparison with future observations we consider PPD mass as a function of FUV flux (figure 6.11). We find that, if used in isolation, the local flux experienced by a given star is a poor predictor of the disc mass. Correlation with real or projected FUV flux only becomes clear when the host mass, to which the final PPD mass is closely correlated (as demonstrated by the colour gradient in figure 6.11 and discussed in Section 6.4.4), is also taken into account. In particular, we expect that low mass stars ($< 1\,M_\odot$) in the centre of Cyg OB2 host exclusively low mass discs ($\lesssim 10^{-3}\,M_\odot$, if any).

Without taking into account stellar mass, can we find differences in disc properties between PPDs in apparently high versus low FUV flux environments? To answer this, we must consider the sensitivity limit for future observations. Considering *ALMA* band 6 sensitivity, reasonable integration times ($\sim$ 30 minutes) for a survey sample suggest flux densities down to $F_\nu(850\,\mu{\rm m}) \sim 40$ μJy can be detected. At the distance of Cyg OB2 this means that dust masses can be established down to a few $M_\oplus$ (Andrews and Williams, 2005). The corresponding total disc masses are $M_{\rm disc} \sim 10^{-3}\,M_\odot$ if the gas to dust ratio is $\Sigma_{\rm gas}/\Sigma_{\rm dust} = 10^2$. Given that the PPDs are likely to be gas depleted by external photoevaporation, the latter assumption is probably not accurate for many discs (Ansdell *et al.*, 2016), and this complicates the interpretation of observations. Nonetheless, we show

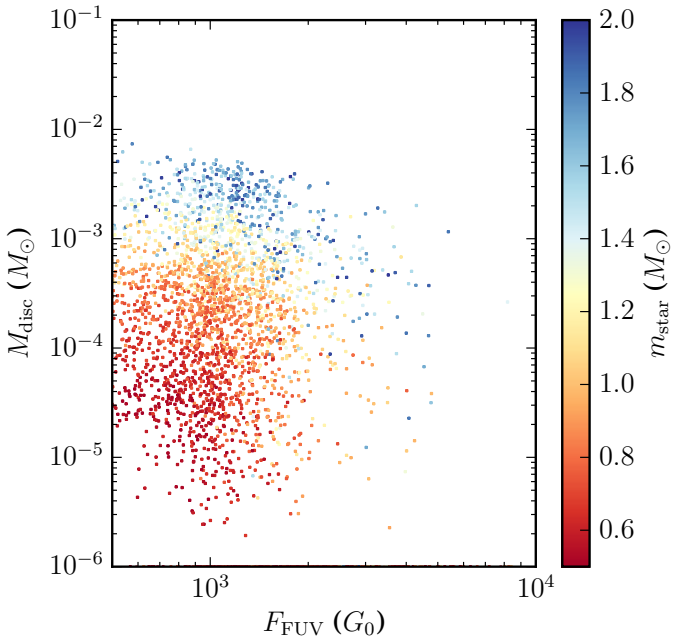

(a)

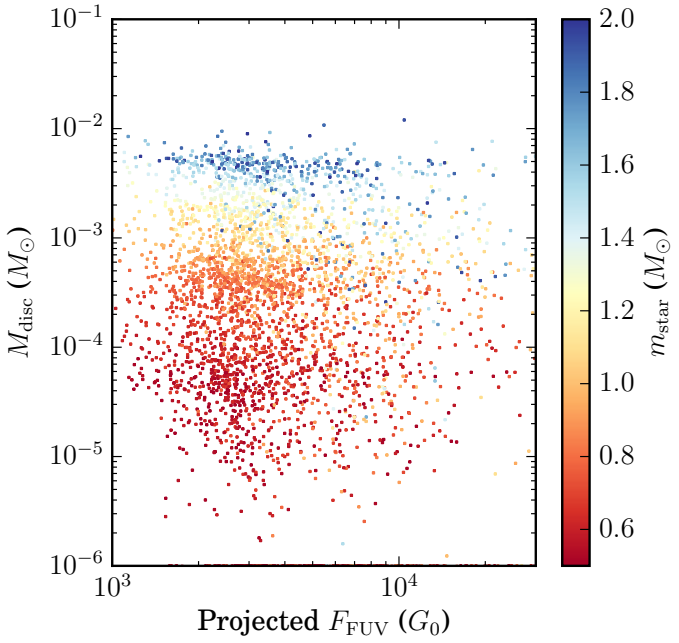

(b)

Fig. 6.11 PPD mass after 3 Myr in our chosen model (described by the parameters in Table 6.1) as a function of real and projected FUV flux (figures 6.11a and 6.11b respectively). Points are colour coded by the mass of the host star. Initial disc masses are drawn from a uniform distribution between 1% and 10% of the host mass. In the context of figure 6.10, discs with masses $< 10^{-5} M_\odot$ are considered 'destroyed'. We find that $F_{\rm FUV}$ is a poor indicator of disc mass.

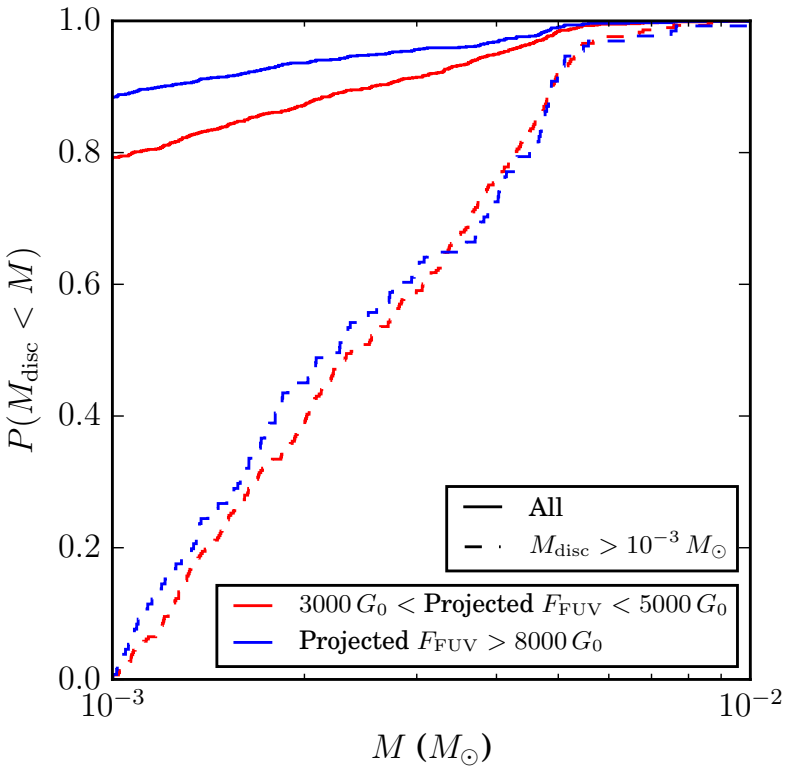

Fig. 6.12 Cumulative fraction of disc mass after 3 Myr in our chosen model. Solid lines are for the entire disc population, while the dashed lines include only discs which have $M_{\rm disc} > 10^{-3}\,M_\odot$. The disc population is divided up by projected (observed) FUV flux; the red lines are for stars experiencing an apparent $F_{\rm FUV}$ between 3–5 $\times\,10^3\,G_0$, while the blue lines correspond to stars with $F_{\rm FUV} > 8 \times 10^3$. A large sample of all discs would be required to detect differences between the masses in the two FUV flux bins.

the cumulative PPD mass fraction after 3 Myr for two FUV flux bins in figure 6.12. While disc masses are indeed suppressed at higher projected FUV flux, considering the sensitivity limit of *ALMA* makes finding differences between the two populations impractical. A sample of several 100s of PPDs would be required to find a difference between the total population in high and low FUV flux environments (including non-detections). We find that similar sample sizes would be required to find differences in disc outer radius distributions in the two environments.

Stellar mass independent disc initial conditions

In obtaining the results in Section 6.4.4 we have already assumed that the initial disc mass is dependent on the stellar mass of the host. We wish to confirm our results are not sensitive to this assumption. We therefore recalculate the PPD evolution in our model under the

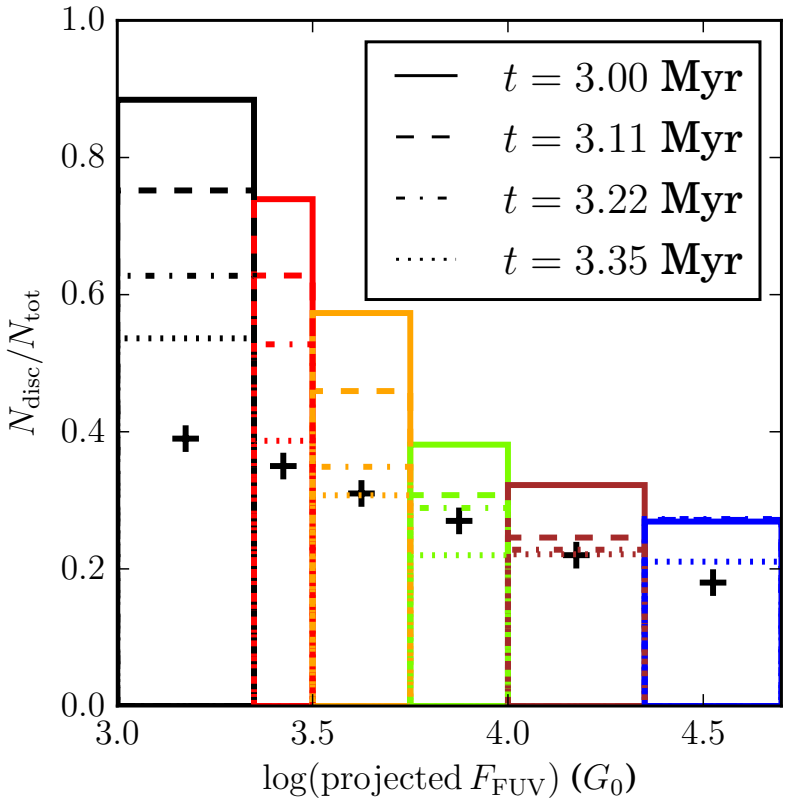

Fig. 6.13 As in figure 6.10a but for a distribution of initial disc masses independent of the stellar host mass (see text for details). This demonstrates that reproducing the observed disc fractions is not sensitive to the choice of PPD initial conditions.

assumption that the initial disc mass is uncorrelated to the stellar mass. To this end we draw the initial disc masses from a log-normal distribution:

$$M_{\rm disc,0}/M_\odot = e^{\mu+\sigma X}$$

where the random variable $X \sim \mathcal{N}(0,1)$ is drawn from a standard normal distribution, uncorrelated with $m_{\rm star}$. The values of $\mu = -3.25$ and $\sigma = 0.7$ are chosen such that the mean and dispersion of $M_{\rm disc,0}$ match those chosen for the stellar mass dependent initial conditions. The scale radius R_1 is again defined according to equation 6.7. This distribution of initial conditions recovers similar disc fractions as a function of projected $F_{\rm FUV}$ (figure 6.13). The resulting disc mass distribution is shown in figure 6.14. Our findings do not differ greatly from those in figure 6.11, except for a predictable weaker correlation between final disc mass and host mass.

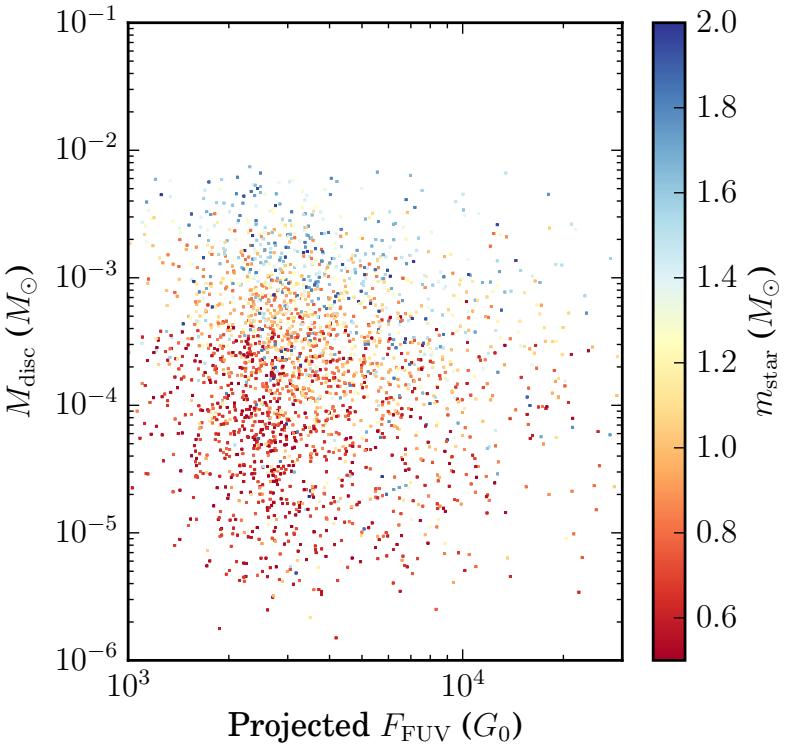

Fig. 6.14 As in figure 6.11b but for a distribution of initial disc masses independent of the stellar host mass (see text for details).

Disc mass dependence on host mass

The relationship between final disc mass and stellar mass is considered in figure 6.15a (figure 6.15b) for disc masses initially correlated (uncorrelated) with the host star mass. We obtain power law indices ($M_{\rm disc} \propto m_{\rm star}^{\beta}$) $\beta = 3.93 \pm 0.11$ and 2.75 ± 0.12 respectively. In both cases this is a substantially more superlinear relationship than in local PPD populations that have not been significantly photoevaporated ($1 < \beta < 1.9$ Andrews *et al.*, 2013; Pascucci *et al.*, 2016). Physically this is because $\dot{M}_{\rm wind}$ is strongly dependent on stellar mass such that discs around low mass stars are depleted much faster (due to a shallower potential) than those around high mass stars for a fixed flux and disc radius (Haworth *et al.*, 2018a). In regions where a disc population has undergone significant photoevaporation we then expect lower mass stars to host lower mass PPDs. Even if it proves impossible to obtain sufficiently large samples of mm-based mass determinations in Cyg OB2 to conduct the comparison made in figure 6.12, an alternative way to test the role of external photoevaporation would be to examine any evidence for steep disc mass–stellar mass relationship. Indeed, Ansdell *et al.* (2017) find a steepening of the relationship with age across different regions that could be due to external photoevaporation. To the contrary, Eisner *et al.* (2018) find a shallow disc

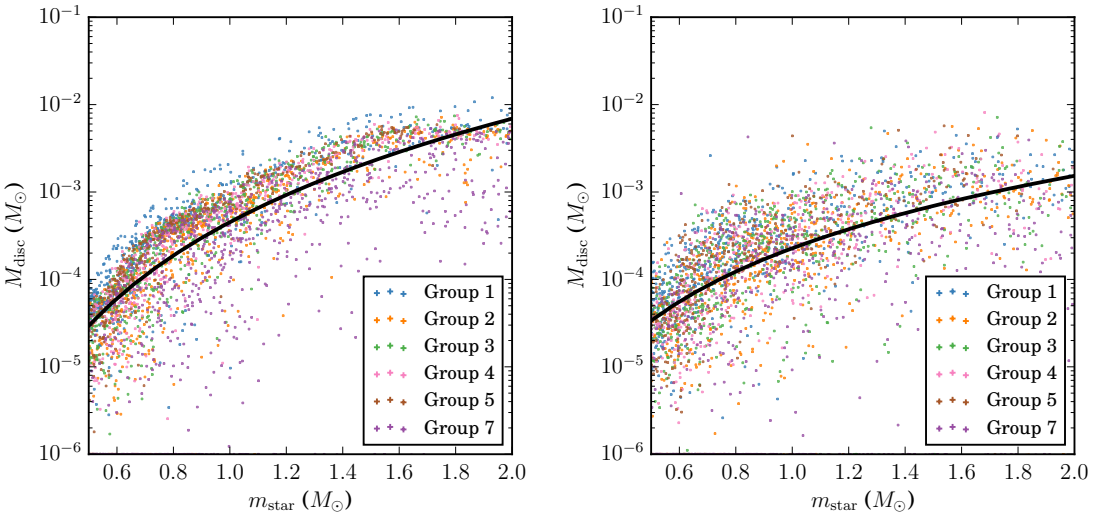

(a) (b)

Fig. 6.15 PPD mass distribution after 3 Myr of evolution in our chosen model (see text and Table 6.1 for details). In figures 6.15a and 6.15b initial disc masses are dependent on and independent of stellar host mass respectively. The black line follows $(M_{\rm disc}/M_\odot) = 4.5 \cdot 10^{-4} \, (m_{\rm star}/M_\odot)^{3.9}$ in figure 6.15a, and $(M_{\rm disc}/M_\odot) = 2.3 \cdot 10^{-4} \, (m_{\rm star}/M_\odot)^{2.8}$ in figure 6.15b. The points are colour coded by the largest scale fractal sub-group to which they belong.

mass–host mass relationship in the strongly irradiated discs of the ONC; this could be the result of the youth or complex formation history of the stellar population (Beccari *et al.*, 2017; Kroupa *et al.*, 2018). Disentangling these effects requires a detailed modelling of those regions, such as that presented in this chapter.

To estimate whether detecting large β values is possible in Cyg OB2, we extract a subset of 20 discs from our model, choosing them such that they lie in a region of projected FUV flux $3000\,G_0 < F_{\rm FUV} < 8000\,G_0$. A lower limit of $3000\,G_0$ is appropriate since below this figures 6.10a and 6.13 suggest that alternative processes to external photoevaporation have a comparable influence on disc evolution. We also select stellar masses to be approximately uniformly distributed between $0.5 - 2\,M_\odot$. We assume uncertainty of 30% in $M_{\rm disc}$, with $M_{\rm disc} < 10^{-3}\,M_\odot$ constituting a non-detection, and a 10% uncertainty in $M_{\rm star}$. We then attempt to fit a power law using the LINMIX package (Kelly, 2007) for a number of different PPD subsets. An illustrative example of such an exploration is shown in figure 6.16. In all cases we find that the fit effectively discounts power law relations with $\beta \leq 1.9$. Values of $\beta \leq 1.9$ are similarly discounted in the model with stellar host mass independent disc initial

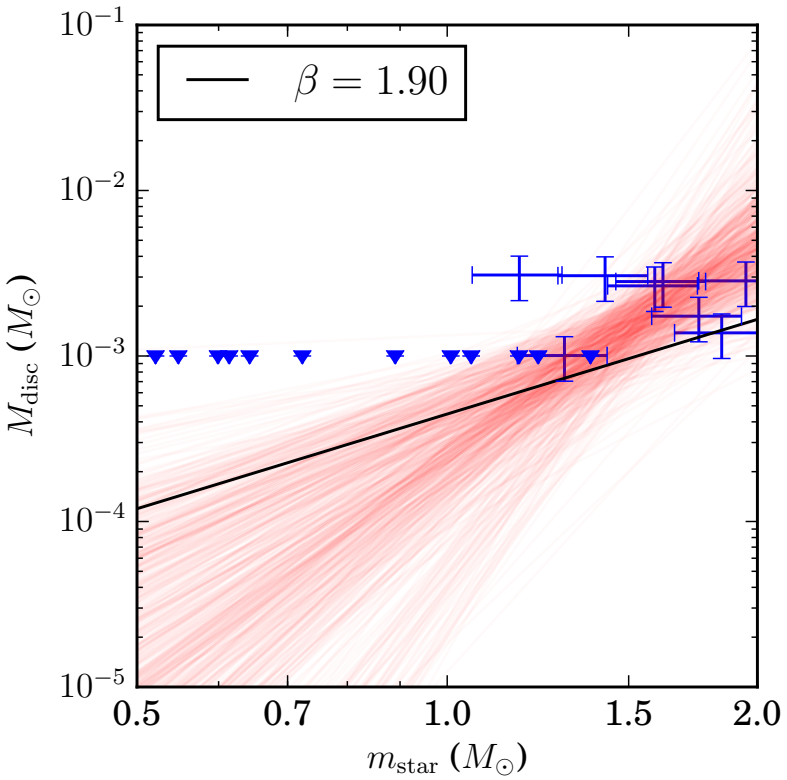

Fig. 6.16 A subset of 20 discs of those shown in figure 6.15a (after 3 Myr of evolution), chosen to be approximately uniformly distributed over a range of stellar masses $0.5-2\,M_\odot$. All discs are also selected such that they are in an environment where the projected flux has an instaneous value $3000\,G_0 < F_{\rm FUV} < 8000\,G_0$. Discs with $M_{\rm disc} < 10^{-3}\,M_\odot$ are considered upper limits (non-detections). The red lines are a subset of samples from the posterior distribution obtained from Markov chain Monte Carlo modelling (using the LINMIX package - Kelly, 2007). The black line is a model with $\beta = 1.9$ selected from the posterior distribution such that the true β is greater than this value with 2σ confidence.

conditions. Our findings suggest that, if a sample is carefully selected, evidence of external photoevaporation should be detectable in future observations of Cyg OB2.

One might ask whether it is possible to find signatures of underlying sub-structure within a population of PPDs. Given that the dynamical history is linked to the irradiation by FUV photons, it may be possible to detect distinct groups in the mass distribution of a disc sample. As discussed previously, in an externally photoevaporated population, disc properties are more strongly correlated with host mass than FUV flux. Therefore considering disc properties as a function of host mass is the best chance of finding distinct groups within a sample. This possibility is explored in figure 6.15, where the largest scale fractal membership is indicated for each PPD. We find that the mass distribution does not demonstrate a clear segregation

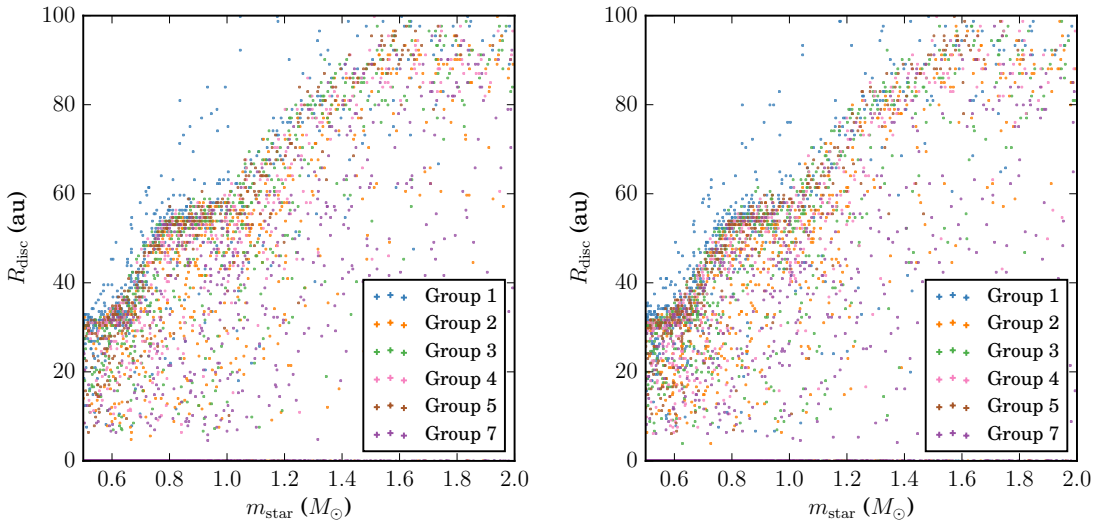

(a) (b)

Fig. 6.17 As in figure 6.15 but for disc outer radius distributions. In figure 6.17a initial disc masses are drawn from a distribution which scales linearly with stellar host mass, while in figure 6.17b the initial PPD mass is not correlated to host mass. Points are coloured by the largest scale fractal membership. We find that the outer radii are largely independent of disc initial conditions and are correlated with stellar host mass. A host mass dependent preference for certain outer radii is found, most obviously at outer radii between 30–60 au and host masses 0.5–1 $M_\odot$. These radii are set by the balance between viscous expansion and FUV induced mass loss, and correspond to the region of parameter space where mass loss rate increases rapidly with outer radius (see, for example, figure A3 in Haworth *et al.*, 2018a).

between groups. The subgroups are in themselves massive ($\sim 10^4\,M_\odot$) and the high mass end of the IMF is therefore well sampled in each filament. It is possible that for smaller scale sub-structure (with filaments of mass $< 10^3\,M_\odot$, see Chapter 5) a less well sampled IMF might mean that different filaments have quite different local $F_{\rm FUV}$. In this case we should expect to see a distinct PPD mass and outer radius distributions between filaments.

Disc radii

An alternative observable property, the outer disc radius $R_{\rm out}$, may prove to be a better probe of sub-structure in future observations. This is because, while $M_{\rm disc}$ is depleted over the entire lifetime of the disc, the outer radius in regions of strong FUV flux is likely to be set by a balance between photoevaporative mass loss and viscous expansion on short timescales. We have so far neglected discussion of disc radius simply because disc radii resolved down to $\sim$ 10s au are likely to be challenging in a region such as Cyg OB2; the highest resolution of

ALMA is $\sim 0.02''$, corresponding to ~ 30 au at 1.33 kpc distance. However, because it may be possible to resolve disc radii to sufficient accuracies in closer young stellar environments, we illustrate the distribution of disc radii in figure 6.17. There are some indications of different radius distributions between different fractal associations, but no clear segregation between them. The majority of discs have $R_{\rm disc} < 60$ au which would require $< 0.05''$ resolution at the distance of Cyg OB2. Further, outer disc radius measurements can be subject to large uncertainties and dust radius estimates are likely to underestimate the gas extent (e.g. Birnstiel *et al.*, 2010; Guilloteau *et al.*, 2011; de Gregorio-Monsalvo *et al.*, 2013). This discrepancy may be less problematic in regions where disc radii are externally suppressed (for example close stellar encounters may result in wavelength independent PPD outer radius measurements, as in the case of the disc around HV Tau C – Monin and Bouvier, 2000, and Chapter 2). This assumption requires further study into gas-dust physics in externally photoevaporating discs (see Cleeves *et al.* 2016 for discussion of gas and dust evolution in an FUV irradiated PPD). Overall we see the same trend as in disc masses that the outer radius is correlated with host mass. This is again because $\dot{M}_{\rm wind}$ decreases with $m_{\rm star}$, such that the radius at which viscous expansion is in equilibrium with FUV induced mass loss is more extended for more massive host stars.

6.5 Conclusions

Using *N*-body simulations and viscous disc evolution models we have successfully reproduced the properties of Cygnus OB2, including the stellar kinematics and the surviving PPD fractions as a function of projected FUV flux. Our modelling supports the following scenario:

- If the viscous evolution of PPDs is well described by a Shakura and Sunyaev α-parameter $\alpha = 10^{-2}$ ($\tau_{\rm visc} \approx 0.5$ Myr for a solar mass star), then expulsion of the primordial gas content in the region must have concluded ~ 0.5 Myr ago. Approximately 0.5 Myr of exposure to strong FUV fields is required to reproduce the current disc survival rates as a function of (projected) flux. This value of α will be an upper limit if FUV extinction due to the primordial gas was not efficient (because of a clumpy spatial distribution, for example).

- The initial three-dimensional stellar velocity dispersion must have been ~ 50 km/s to be consistent with the present day central velocity dispersion. This is large with respect to observed stellar populations, even for OB associations (e.g. Ward and Kruijssen 2018 and references therein). However, velocity gradients ~ 10 kms^{-1}pc^{-1} are found

across giant molecular clouds, particularly in the case of cloud-cloud collision (Wu *et al.*, 2015; Bisbas *et al.*, 2018; Pols *et al.*, 2018).

- Anisotropy in the present day velocity dispersion requires the presence of primordial subtructure. We find that Cyg OB2 must have been comprised of large scale filaments (or fractal clumps), with a mass $\sim 10^4\ M_\odot$.
- In such a model, a gas content of $\sim 8 \times 10^6 M_\odot$ is required to maintain initial virial equilibrium. This is massive compared to the known distribution of molecular cloud masses in the Milky Way (Longmore *et al.*, 2014).
- The total stellar mass required to sustain a sufficient central mass after 3 Myr is $\sim 8 \times 10^4\ M_\odot$. This suggests a star formation efficiency of $\sim 1\%$.
- The apparent lack of expansion measured by Wright *et al.* (2016) need not be interpreted as evidence of no physical expansion of the stellar population. We find that our (expanding) model is equally consistent with an expansion parameter $\mathscr{E} \approx 0.5$. Such a measurement can only be interpreted probabilistically for an association with large scale sub-structure.

The primary caveat of these conclusions is that the gas expulsion timescale derived by disc fractions is degenerate with α. Our choice ($\alpha = 10^{-2}$, although this is in turn dependent on choice of scale radius R_1 – see equation 1.6) yields a good fit to the disc fractions and also allows us to reproduce kinematic observations with gas expulsion timescale $\tau_{\rm gas} = 2.5$ Myr. In future, observations of PPD populations in regions with a strong FUV flux but with more modest velocity dispersions (and primordial gas density) might offer further constraints for α.

Finally, we make predictions for future observations of the disc mass and radius distribution in Cyg OB2. We find that samples of PPDs in highly FUV irradiated environment have significantly reduced masses and outer radii than in regions of more modest flux. However, taking into account sensitivity limits, statistically observing these differences requires sample sizes of $\gtrsim$ 100s of discs in both high and low FUV flux bins. This is similarly true for disc outer radii, and makes probing the difference between disc property distributions as a function of FUV environment directly impractical at present.

In Cygnus OB2 we expect a strong correlation between stellar mass and disc mass ($M_{\rm disc} \propto m_{\rm star}^{\beta}$, with $\beta > 2$) which is because, for a disc with given radius and in a given FUV environment, the mass loss rate is higher in the shallower potential of low mass stars. This effect should be clear in a sufficiently large sample of sufficiently irradiated discs in any environment. Taking into account the finite sensitivity of *ALMA*, we demonstrate that it

would be sufficient to target around 20 stars of known mass in Cygnus OB2 to demonstrate a value of β that is steeper than the canonical value ~ 1 – 1.9 which is seen in non-irradiated disc samples. We conclude that, pending empirical confirmation, discs around low mass stars born in environments of strong FUV flux are likely to have a significantly depleted mass budget for planet formation. Indeed, unless dust within PPDs can rapidly grow to size scales where it is immune to photoevaporative stripping (e.g. Youdin and Goodman, 2005), planet formation may be completely suppressed for such host stars (Haworth *et al.*, 2018b).

Chapter 7

Future prospects and context: links to galactic-scale environment

In this chapter, by way of conclusion, I perform an illustrative exercise in summarising some physical arguments that can be used to link the previous chapters to the broader context of star formation. New work in this chapter was led by myself and Dr. Diederik Kruijssen, and forms the basis of a paper that has yet to be submitted for publication. I have performed the theoretical analysis and I am the sole contributor to the text in the form presented here. I thank Dr. Sebastian Trujillo-Gomez for kindly sharing his results quantifying the minimum young stellar cluster mass prior to publication.

7.1 Introduction

In the previous chapters we have demonstrated how a PPD responds to the external influence of neighbouring stars in dense environments, and we have quantified the nature of some local environments to indicate dispersal rates in real young star forming regions. A natural next stage of this work is to understand the degree to which the mechanisms we have considered may influence discs born in other galactic environments. Clearly this goal is ambitious and many uncertainties regarding the dispersal of PPDs in diverse environments require further scrutiny (for example, the influence of metallicity – Ercolano and Clarke, 2010). However, we illustrate in this chapter the first stages in such an enterprise: characterising the distribution of stellar birth environments in a general sense.

The broad goal of this chapter is establishing probability density functions (PDFs) for stellar birth environment in stellar density–FUV flux space (ρ_*–F; we drop the subscript

for flux since we consider exclusively FUV photons). To this end, we apply the following method:

1. In Section 7.2 we evaluate the stellar density PDF, which is related to the degree of tidal truncation (Chapter 3 and 4) and the local FUV field strength in massive stellar clusters (Chapter 5). This involves estimating the primordial gas density distribution (Section 7.2.1), and then factoring in the local star formation efficiency (SFE; Section 7.2.2).

2. The FUV flux experienced by a star is dependent on the most massive neighbour, the expected value of which varies with the cluster mass. In Section 7.3 we quantify the initial cluster mass function (ICMF; Section 7.3.1) and relate this mass to the expected FUV luminosity of the most massive member (Section 7.3.2).

3. In Section 7.4 we use the ICMF to calculate how the distribution of stellar birth environments deviates from the relationship between ρ_* and F found in Chapter 5. This allows us to calculate the two-dimensional PDF for stellar birth environments in Section 7.4.4.

Having established this PDF, we are able to estimate the corresponding distribution of externally induced PPD dispersal timescales using the findings of the previous chapters. In this way we illustrate the importance of the themes presented in this work in the broader context of star formation over time and space. Overall conclusions and suggestions for future work are made in Section 7.7.

7.2 Stellar density distribution

Our aim in this section is to relate the distribution of primordial gas to the PDF of stellar densities. We define the gas overdensity, $x \equiv \rho_{\rm g}/\rho_0$, where $\rho_{\rm g}$ is the local and ρ_0 is the large-scale mean gas density. However, it will be convenient to express the final PDF in units of stellar density rather than gas density, since the former is the relevant quantity for evaluating the influence of tidal encounters. We define $y \equiv \rho_*/\rho_0 = x\varepsilon(x)$, for a given star formation efficiency (SFE), ε; y is the *stellar* overdensity with respect to the average gas density ρ_0. Hence, the stellar density PDF is:

$$\frac{\partial p}{\partial y} = \frac{\partial p}{\partial x}\left(\varepsilon + x\frac{\partial \varepsilon}{\partial x}\right)^{-1}. \tag{7.1}$$

However, we are in fact interested in the fraction of stars per infinitesimal region of overdensity space dy, which is $\partial p/\partial x$ weighted by stellar density:

$$\frac{\partial \mathscr{F}_*}{\partial y} = y\frac{\partial p}{\partial y} = \frac{\partial p}{\partial x}\left(x^{-1} + \frac{\partial \ln \varepsilon}{\partial x}\right)^{-1} \approx x\frac{\partial p}{\partial x}, \tag{7.2}$$

where the last approximation can be made since $\ln \varepsilon$ changes slowly with x (and for large x, $\varepsilon = \varepsilon_{\rm core}$ is constant – see Section 7.2.2). We now quantify $\partial p/\partial x$ and ε to evaluate equation 7.2.

7.2.1 ISM properties

Here we relate the ISM properties to the galactic scale observable quantities in the galactic disc (the mean surface density Σ_0 and angular speed Ω). We discuss the parameters appropriate for the solar neighbourhood and the central regions of the Milky Way, which we will use as illustrative comparisons throughout this chapter.

Gas density distribution

On sufficiently large scales, the PDF of the gas overdensity, x, with respect to the mean gas density in an isothermal, supersonically turbulent region is scale-free and follows a lognormal distribution (e.g. Vazquez-Semadeni, 1994; Padoan and Nordlund, 2002; Hill *et al.*, 2012). It can be written:

$$\frac{\partial p}{\partial x} = \frac{1}{\sqrt{2\pi\sigma_\rho^2 x}} \exp\left\{-\frac{(\ln x - \overline{\ln x})^2}{2\sigma_\rho^2}\right\}, \tag{7.3}$$

where the logarithmic mean is

$$\overline{\ln x} = -\sigma_\rho^2/2 \tag{7.4}$$

The logarithmic standard deviation of the density is related to the velocity of the turbulence, which can be expressed in terms of the one-dimensional Mach number $\mathscr{M}$:

$$\sigma_\rho^2 \approx \ln\left(1 + 3b^2\mathscr{M}^2\right), \tag{7.5}$$

where simulations indicate $b \approx 0.5$ (Padoan *et al.*, 1997; Federrath *et al.*, 2010). Hence, estimating $\mathscr{M}$ for a region defines the overdensity PDF, equation 7.3, and combined with the average density ρ_0 this defines the gas density distribution.

Throughout the course of this work, we will frequently refer to the properties of gas in the solar neighbourhood and in the CMZ, which we will use as regions for illustrative comparisons. We consider the values of $\mathscr{M}$ and ρ_0 in the galactic disc and the CMZ below.

Properties of the galactic disc

To estimate the conditions in the solar neighbourhood, we follow Krumholz and McKee (2005) in assuming the galactic disc can be modelled as a gas disc in hydrostatic equilibrium. Then we can write an expression for the Toomre (1964) Q parameter in terms of the mean surface density Σ_0 and angular velocity Ω of the galactic-scale primordial gas:

$$Q \equiv \frac{\kappa \sigma_v}{\pi G \Sigma_0} \approx \frac{\sqrt{2}\Omega\sigma_v}{\pi G \Sigma_0} \tag{7.6}$$

where the epicyclic frequency $\kappa \approx \sqrt{2}\Omega$ for a galaxy with a flat rotation curve, and σ_v is the one-dimensional velocity dispersion. Using equation 7.6, the mid-plane density for a disc in hydrostatic equilibrium and with scale height h_0 is:

$$\rho_0 = \frac{\Sigma_0}{2h_0} = \frac{\pi G l_P \Sigma_0^2}{2\sigma_v^2} = \frac{l_P \Omega^2}{\pi G Q^2}, \tag{7.7}$$

where $l_P \approx 3$ is a correction factor for the stellar contribution to the gravitational potential. Considering typical sound speeds in star forming clouds (~ 0.3 km/s), the corresponding Mach number is approximately:

$$\mathscr{M} \approx 0.028\, Q l_{\bar{P}}^{1/8} \left(\frac{\Omega}{\mathrm{Myr}^{-1}}\right)^{-1} \frac{\Sigma_0}{M_\odot\,\mathrm{pc}^{-2}} \tag{7.8}$$

where:

$$l_{\bar{P}} \approx 10 - 8 f_{\mathrm{GMC}} \tag{7.9}$$

is the ratio of the mean pressure in a GMC to the mid-plane pressure, and f_{GMC} is the fraction of the ISM mass in GMCs. The value of $l_{\bar{P}}$ increases with the fraction of dissociated/ionised gas, since this increases the mass surrounding a GMC without contributing to the star forming material. The approximation in equation 7.9 is made assuming that the majority of molecular gas is in GMCs and uses a simple interpolation between the completely molecular and completely atomic limits (see discussion in Appendix B of Krumholz and McKee, 2005). Empirically, the fraction of molecular gas f_{GMC} is related to the mean surface density (Wong

and Blitz, 2002; Rosolowsky and Blitz, 2005):

$$f_{\rm GMC} \approx \left\{ 1 + 250 \left(\frac{\Sigma_0}{M_\odot \, {\rm pc}^{-2}} \right)^{-2} \right\}^{-1}. \tag{7.10}$$

The angular velocity and the mean surface density are empirically related by the expression:

$$\Omega = 6.1 \times 10^{-3} \left(\frac{\Sigma_0}{M_\odot \, {\rm pc}^{-2}} \right)^{0.49} {\rm Myr}^{-1}, \tag{7.11}$$

with a scatter of ~ 0.5 dex. Finally, a range of values $0.5 < Q < 6$ are observed (Kennicutt, 1989; Martin and Kennicutt, 2001). For the solar neighbourhood we will choose a canonical value of $Q = 1.5$ and $\Sigma_0 = 12 M_\odot$ pc^{-2} in line with Kruijssen (2012).

Properties of the central molecular zone

The central molecular zone (CMZ) in the Milky Way occupies the central ~ 250 pc in galactocentric radius, and exhibits gas properties which vary significantly from those of the disc (see Molinari *et al.*, 2014, for a review). The mean volume density of gas clouds is $\rho_0 \sim 250 \, M_\odot$ pc^{-3}, with a corresponding surface density $\Sigma_0 \sim 1000 \, M_\odot$ pc^{-2} (Guesten and Henkel, 1983). Henshaw *et al.* (2016) find a 1D Mach number $\mathscr{M} \approx 16$, and we follow Kruijssen *et al.* (2014) in adopting the same Toomre parameter as in the disc, $Q = 1.5$. Molinari *et al.* (2011) find an angular speed for the molecular ring at a radius ~ 80 pc of $\Omega \sim 1$ Myr^{-1}.

7.2.2 Star formation efficiency

We now calculate the SFE $\varepsilon = \varepsilon(x)$, a function of the local gas overdensity, with the view to rewrite equation 7.3 in terms of the stellar overdensity.

Specific star formation rate per free-fall time

Assuming star formation proceeds on a free-fall time $\tau_{\rm ff}$, the SFE ε can be related to the specific star formation rate per free fall time, $\zeta_{\rm ff}$. There remains debate on the exact value of $\zeta_{\rm ff}$ (e.g. Elmegreen, 2002; Krumholz and McKee, 2005; Elmegreen, 2007; Padoan and Nordlund, 2011; Hirota *et al.*, 2018). While in some regions the value has been found to be up to a factor ~ 5 higher (Evans *et al.*, 2009; Hirota *et al.*, 2018), $\zeta_{\rm ff} \approx 0.012$ is found across a wide dynamic range, and we will use this fiducial value in this work.

Star formation timescale

The SFE at a given density is dependent on the time for which star formation is allowed to proceed, as a multiple of the free-fall timescale. The free-fall timescale at local density $\rho_{\rm g}$ is

$$\tau_{\rm ff} = \sqrt{\frac{3\pi}{32G\rho_{\rm g}}} \tag{7.12}$$

and the associated SFE is

$$\varepsilon_{\rm fb} = \frac{\zeta_{\rm ff}}{\tau_{\rm ff}}\tau_{\rm fb}, \tag{7.13}$$

where $\tau_{\rm fb}$ is the feedback timescale, the time it takes to halt star formation. The feedback timescale can be written as the sum of the time until the first supernova $\tau_{\rm sn} \sim 3$ Myr and the subsequent time until pressure equilibrium with the surrounding ISM is reached. We refer readers interested in the full derivation of $\tau_{\rm fb}$ to Kruijssen (2012) and simply quote the result of such a calculation here:

$$\tau_{\rm fb} = \frac{\tau_{\rm sn}}{2}\left(1+\sqrt{1+\frac{2\pi^2 G^2 \tau_{\rm ff} Q^2 \Sigma_0^2}{\Phi_{\rm fb}\zeta_{\rm ff}\tau_{\rm sn}^2\Omega^2 x}}\right). \tag{7.14}$$

where $\Phi_{\rm fb}$ is a constant which represents the rate at which feedback injects energy into the ISM per unit mass. Its exact value is uncertain (Silk, 1997; Mac Low and Ferrara, 1999; Efstathiou, 2000; Abadi *et al.*, 2003; Dib *et al.*, 2006), and we use an order of magnitude estimate $\Phi_{\rm fb} \approx 3.2\times10^{32}$ erg s^{-1} $M_\odot^{-1}$ (see Appendix B in Kruijssen, 2012, and references therein).

Where star formation timescales are long, we wish to limit our consideration to stars which host a disc, i.e. with ages $\lesssim 10$ Myr. In the case where the overdensity $x \to 0$, we have large $\tau_{\rm fb} \propto x^{-3/4}$ and $\varepsilon_{\rm fb} \propto x^{-1/4}$. We therefore limit our definition of SFE to those stars formed within $\tau_{\rm inc}$ of the onset of star formation; for such stars the 'incomplete' SFE is:

$$\varepsilon_{\rm inc} = \frac{\zeta_{\rm ff}}{\tau_{\rm ff}}\tau_{\rm inc}, \tag{7.15}$$

where $\tau_{\rm inc} = 10$ Myr.

In general, we can write the SFE as the minimum of the feedback limited, incomplete and core accretion limited efficiencies:

$$\varepsilon = \min\left\{\varepsilon_{\rm fb}, \varepsilon_{\rm inc}, \varepsilon_{\rm core}\right\}, \tag{7.16}$$

where the latter limit is obtained by factoring in mass-loss through outflows during core accretion. We choose $\varepsilon_{\rm core} = 0.5$, consistent with the range $0.25 < \varepsilon_{\rm core} < 0.7$ found by Matzner and McKee (2000).

Caveats for SFE

While the SFE given by equations 7.12–7.16 is convenient since it is a function of x only for a given environment, some discussion is necessary on the shortcomings of such a prescription. When we consider FUV flux throughout a star forming region we will be motivated to define the maximum star mass within the local environment, dependent on the cluster mass $M_{\rm c}$ (see Section 7.3.2). Ideally, $\tau_{\rm sn}$ would also be a function of $M_{\rm c}$, such that $\varepsilon = \varepsilon(x, M_{\rm c})$. However, when we define the overall PDF in ρ_*–F space this would considerably complicate our prescription. It would require a mapping from the gas overdensity distribution to both ρ_* and F, while the PDF for the latter is already a function of the former. This problem is mitigated somewhat for two reasons. Firstly, we impose a maximum SFE, such that $\varepsilon = \varepsilon_{\rm core}$ will be independent of $\tau_{\rm sn}$ beyond a certain value. For such dense environments the physical SFE will vary on the order unity, and our approximation is reasonable for establishing order of magnitude PDFs for stellar environment. Secondly, the innate dispersion of ε will in a practical sense be accounted for when we consider the empirical scatter of stellar environments in density–FUV flux space (Section 7.4.4). Hence, while our prescription for ε may not be accurate for all regions of parameter space, physical variations are a second order effect for the problem considered here.

7.3 Cluster properties

The mass of the most massive stellar neighbour (and local FUV flux), is consistent with with random drawing from the IMF, and is therefore a function of cluster mass. Throughout this chapter, we consider a Kroupa (2001) IMF:

$$\frac{\partial \mathscr{F}_*}{\partial m_*} = \xi_*(m_*) \propto \begin{cases} m_*^{-1.3} & \text{for} 0.08\,M_\odot \leq m_* < 0.5\,M_\odot \\ m_*^{-2.3} & \text{for} 0.5\,M_\odot \leq m_* < 100 M_\odot \\ 0 & \text{else} \end{cases} , \tag{7.17}$$

such that $\xi_*(m)$ is normalised and continuous. We choose an upper limit of $100\,M_\odot$ because this is the upper limit of the stellar atmosphere models we adopt in Section 7.3.2. This is not a problem since the clusters with mass $M_{\rm c} < 10^3\,M_\odot$ practically always have $m_{\rm max} \ll 100\,M_\odot$

(and for clusters of mass $\gtrsim 10^3\,M_\odot$, FUV field strength is no longer strongly variable with maximum stellar mass – Chapter 5). In the remainder of this section we will define the distribution of cluster masses, and the associated FUV luminosity of the most massive members.

7.3.1 Cluster mass spectrum

To estimate the deviation of the FUV flux experienced by stars from the relationship found in Chapter 5, we must estimate the initial cluster mass function (ICMF) in a given region. We follow Trujillo-Gomez, Reina-Campos and Kruijssen (in prep., hereafter TRK) in assuming that the ICMF follows a Schechter (1976) function, additionally truncated from below by a minimum mass:

$$\xi_{\rm c} \equiv \frac{{\rm d}\mathscr{F}_{\rm c}}{{\rm d}M_{\rm c}} \propto \phi^{-\beta} \exp\left(-\frac{\phi}{\phi_{\rm max}}\right) \exp\left(-\frac{\phi_{\rm min}}{\phi}\right) \tag{7.18}$$

where $\beta = 2$ due to hierarchical collapse of molecular clouds (Elmegreen and Falgarone, 1996). We have introduced:

$$\phi \equiv \frac{M_{\rm c}}{M_{\rm crit}} \tag{7.19}$$

the ratio of the cluster mass to the critical mass, $M_{\rm crit} = 10^3\,M_\odot$, which we use in our parameterisation of FUV luminosity in Section 7.3.2. The ICMF is truncated at a maximum $\phi_{\rm max}$ and minimum $\phi_{\rm min}$, which we discuss below.

Maximum cluster mass

We follow Reina-Campos and Kruijssen (2017) in calculating the maximum cluster mass $\phi_{\rm max}$, by considering the most massive molecular cloud that can survive disruption by feedback. The ISM is stable to perturbations with a wavelength longer than the Toomre (1964) length,

$$\lambda_{\rm T} = \frac{4\pi^2 G\Sigma_0}{\kappa^2} = \frac{2\pi^2 G\Sigma_0}{\Omega^2}, \tag{7.20}$$

where $\kappa \approx \sqrt{2}\Omega$ is the epicyclic frequency, and this is therefore the largest scale on which collapse can take place. The corresponding Toomre mass is:

$$M_{\rm T} = \frac{\pi\Sigma_0\lambda_{\rm T}^2}{4} = \frac{\pi^5 G^2\Sigma_0^3}{\Omega^4}. \tag{7.21}$$

Considering the galactic plane as an infinite sheet, the 2D free fall time (collapse within the plane) of a region with radius $\lambda_{\rm T}/2$ (Burkert and Hartmann, 2004):

$$\tau_{\rm ff,2D} = \sqrt{\frac{\lambda_{\rm T}}{2\pi G\Sigma_0}} = \frac{\sqrt{\pi}}{\Omega}. \tag{7.22}$$

If the feedback timescale $\tau_{\rm fb} < \tau_{\rm ff,2D}$ then the collapsing region will be destroyed by this feedback before the conclusion of collapse. Since $M_{\rm T} \propto \tau_{\rm ff,2D}^4$ in the absence of feedback, the maximum mass of the GMC is given by:

$$M_{\rm MC,max} = f_{\rm coll.} M_{\rm T} \tag{7.23}$$

where

$$f_{\rm coll.} = \min\left\{1, \frac{\langle\tau_{\rm fb}\rangle}{\tau_{\rm ff,2D}}\right\}^4 \tag{7.24}$$

is the fraction of mass which survives collapse. We have introduced the feedback time across the entire region, which is evaluated using equation 7.35:

$$\langle\tau_{\rm fb}\rangle \approx \tau_{\rm fb}(x=1). \tag{7.25}$$

To convert this into a maximum cluster mass, Reina-Campos and Kruijssen (2017) multiply this by the SFE and the cluster formation efficiency. However, we are not interested here in whether a cluster is bound, and hence we only consider the SFE. We have:

$$\phi_{\rm max} = \frac{\varepsilon_{\rm eff} f_{\rm coll.} M_{\rm T}}{M_{\rm crit}}, \tag{7.26}$$

where we have defined an effective SFE in the high mass GMC limit. In line with Reina-Campos and Kruijssen (2017), we choose an effective SFE $\varepsilon_{\rm eff} = 0.1$.

Minimum cluster mass

The minimum expected mass for a stellar cluster is more nuanced in this context, and depends on the definition we adopt for a 'cluster'. As we have already discussed, in the context of this work we are not interested in whether a group of stars is initially 'bound' in the sense that we aim to establish the conditions that a star experiences early in its evolution. However, we are interested in the bottom of the hierarchy for early mergers within molecular clouds, since this defines the lowest number of neighbours in a cluster. We follow TRK in deriving

this minimum mass by considering a molecular cloud mass dependent SFE:

$$\tilde{\varepsilon}(M_{\rm GMC}) = \frac{\zeta_{\rm ff}}{\tilde{\tau}_{\rm ff}}\tilde{\tau}_{\rm fb}. \tag{7.27}$$

We will find that $\tilde{\varepsilon}$ decreases with increasing $M_{\rm GMC}$ (in the limit of small $M_{\rm GMC}$), such that above a certain cloud mass:

$$\tilde{\varepsilon} \gtrsim \varepsilon_{\rm th} \approx 0.2, \tag{7.28}$$

where the threshold SFE $\varepsilon_{\rm th}$ is given by the efficiency required to produce a bound cluster after instaneous gas expulsion (Baumgardt and Kroupa, 2007). For cloud masses below this limit $M_{\rm th}$, the SFE is high enough to result in the hierarchical merging of single objects (which can be considered to be associated within our context), and hence we have:

$$\phi_{\rm min} = \frac{\varepsilon_{\rm th} M_{\rm th}}{M_{\rm crit}}. \tag{7.29}$$

We are now left with the problem of solving the equations for SFE with respect to the galactic scale primordial gas properties.

In the numerical derivation of $\phi_{\rm min}$ we consider the SFE across an entire molecular cloud, $\tilde{\varepsilon}$, as opposed to the local SFE considered in Section 7.2.2, ε, which is dependent on x and consistent with the calculation of Kruijssen (2012). The primary difference is that in the former case, we can estimate the supernova timescale $\tilde{\tau}_{\rm sn}$ based on the local stellar mass (but not the influence of density), while in the latter we can assess the influence of local density on feedback efficiency (but not the variation in supernova timescale). Ideally we would consider the SFE as a function of both cloud mass and local density, however as discussed in Section 7.2.2 this would greatly complicate our prescription. Instead, we are content to consider $\tilde{\varepsilon}$ for the purposes of assessing the minimum cluster mass, noting that these two different prescriptions are physically compatible; $\tilde{\varepsilon}$ being SFE on a molecular cloud scale, and ε being SFE on a local (stellar) scale.

We refer the reader interested in the derivation of the feedback timescale to TRK, and briefly review the fundamental concepts here. The SFE is calculated by considering the average cloud density $\rho_{\rm GMC}$, which can be approximated:

$$\rho_{\rm GMC} = \frac{3}{4}\left(\frac{\pi\Sigma_0^3 f_\Sigma^3}{M_{\rm GMC}}\right)^{1/2}, \tag{7.30}$$

where we define $f_\Sigma \equiv \Sigma_{\rm GMC}/\Sigma_0$, the ratio between the MC surface density and the mean gas surface density. Following Krumholz and McKee (2005) and Kruijssen (2015), for a virial parameter $\alpha_{\rm vir} = 1.3$ (an appropriate value for GMCs confined by the pressure of the

surrounding medium – Bertoldi and McKee, 1992) this ratio is:

$$f_\Sigma = 3.92\left(\frac{10-8f_{\rm GMC}}{2}\right)^{1/2}. \tag{7.31}$$

In the solar neighbourhood this yields $\Sigma_{\rm GMC} \approx 90 M_\odot$ pc^{-2} (consistent with the findings of Bolatto *et al.*, 2008). We also estimate the timescale for a supernova to occur by considering the progenitor formation timescale, such that we have:

$$\tilde{\tau}_{\rm sn} = \tau_{\rm sn} + \Delta\tau_{\rm sn}, \tag{7.32}$$

where we have defined $\Delta\tau_{\rm sn}$ as the time it takes for a stellar cluster to reach a sufficient mass to form an OB star. This mass is calculated by TRK to be $M_{\rm OB} \approx 139 M_\odot$, and the corresponding timescale:

$$\Delta\tau_{\rm sn} = \frac{M_{\rm OB}\tilde{\tau}_{\rm ff}}{M_{\rm GMC}\zeta_{\rm ff}}. \tag{7.33}$$

Finally, we can define the MC mass dependent free fall timescale:

$$\tilde{\tau}_{\rm ff} = \sqrt{\frac{1}{8G}}\left(\frac{\pi M_{\rm GMC}}{f_\Sigma^3\Sigma_0^3}\right)^{1/4}. \tag{7.34}$$

With these adjustments, an alternate version of equation 7.14 is:

$$\tilde{\tau}_{\rm fb} \approx \frac{\tilde{\tau}_{\rm sn}}{2}\left[1+\sqrt{1+\frac{8\pi^{1/4}\rho_0 M_{\rm GMC}^{5/4}}{15\sqrt{2G}\Phi_{\rm fb}\tilde{\tau}_{\rm sn}^2(f_\Sigma\Sigma_0)^{7/4}}}\right]. \tag{7.35}$$

We can solve the system of equations 7.27 to 7.35 for $M_{\rm th}$ such that

$$\tilde{\varepsilon}\big|^{M_{\rm th}} = \varepsilon_{\rm th}, \tag{7.36}$$

to give $\phi_{\rm min}$. From the above formulation there is no physical reason why we cannot have $\phi_{\rm min} > \phi_{\rm max}$. In this case, the bottom of the hierarchy exceeds the maximum mass that can be produced in such an environment, and the former is therefore set by the latter. This results in a narrow distribution of cluster masses, and $\phi_{\rm min} = \phi_{\rm max}$ (set by the maximum possible mass), such that our ICMF continues to be physically valid. For numerical reasons, it will also be convenient to set limits on the allowed values for $\phi_{\rm min}$ and $\phi_{\rm max}$. We define $\phi_{\rm max,min} = \phi_{\rm min,min} = 10^{-2}$ (i.e. $M_{\rm c} > 10 M_\odot$), $\phi_{\rm min,max} = 100$ and $\phi_{\rm max,max} = 10^6$. These are chosen to be extreme values, and our results are not sensitive to these choices since the

mean FUV flux experienced by PPDs in high mass ($\phi \gg 1$) and low mass ($\phi \ll 1$) clusters converge to respective limits (see Section 7.4).

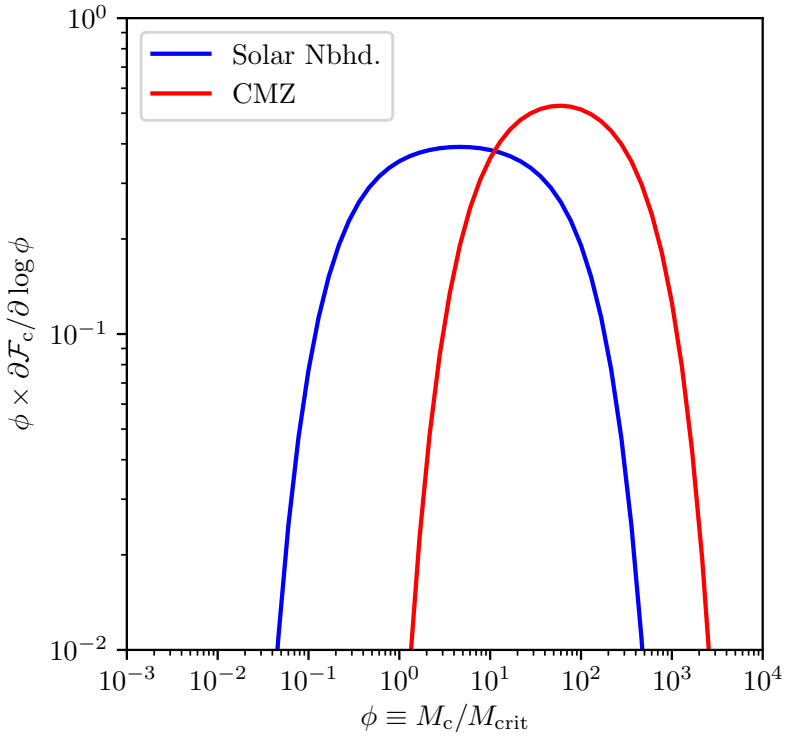

Fig. 7.1 The ICMF (equation 7.18) in terms of $\phi \equiv M_c/M_{crit}$, weighted by the stellar mass of the cluster, indicating the fraction of stars born in a cluster of a given mass. The lower limit ϕ_{min} is given by the bottom of the single-object merger hierarchy calculated by TRK. The maximum cluster mass ϕ_{max} is the stellar component of a MC with mass given by the feedback limited fraction of the Toomre mass (Reina-Campos and Kruijssen, 2017). The blue line is for the solar neighbourhood, while the red line relates to the CMZ.

Derived initial cluster mass function

The theoretical ICMFs of the solar neighbourhood and CMZ are shown in figure 7.1, weighted by mass to illustrate the fraction of stars initially found in a region of a given mass. Our upper mass estimates are somewhat larger than those of Reina-Campos and Kruijssen (2017) since we are not interested in the cluster formation efficiency. We find that clusters in the CMZ have initial masses below $\phi_{max} \approx 620$, while the solar neighbourhood has $\phi_{max} \approx 126$.

7.3.2 Maximum FUV luminosity of cluster members

We follow the method presented in Chapter 5 for obtaining the FUV and EUV luminosity of the most massive star in a given cluster. During this chapter, we will regularly refer to this FUV luminosity L, and it will be useful to have an analytic approximation for this parameter. This luminosity is shown in figure 7.2 for a given stellar cluster mass $M_{\rm c}$. We find that for the critical cluster mass $M_{\rm crit} = 10^3\,M_\odot$, we have $L_{\rm crit} \approx 8.3 \times 10^{38}$ erg s^{-1}. The results in figure 7.2 again justify our choice for $M_{\rm crit}$, since above this limit $L_{{\rm max},1/2}$ varies only weakly with $M_{\rm c}$. An analytic estimate for the median luminosity follows the form:

$$\Gamma(\phi) \equiv \frac{L_{{\rm max},1/2}(\phi)}{L_{\rm crit}} \approx \left\{1 - e^{-(\alpha_1\phi)^{\alpha_2}}\right\} \ln(1+\phi)\,. \tag{7.37}$$

Equation 7.37 actually has three fitting parameters: $\alpha_1 = 8.0$, $\alpha_2 = 2.55$, and $M_{\rm crit} = 10^3\,M_\odot$ (the latter of which defines ϕ). The analytic approximation in equation 7.37 is shown as the dotted line in figure 7.2. We further define the logarithmic deviation in the maximum luminosity:

$$\sigma_L \approx \frac{8}{(3+\log\phi)^2} \tag{7.38}$$

indicated by the dotted line in the bottom panel of figure 7.2 (compared to the direct calculation shown as a solid line).

We emphasise that equation 7.37 does not have a physical basis. It is chosen as a functional form that permits an intuition for the physical quantities and simplify our calculations in the following sections. It is appropriate in the range of cluster masses discussed here under the assumption that the maximum star mass in a region is $\lesssim 100\,M_\odot$.

7.4 FUV flux distribution

To build a distribution of FUV flux F as a function of local density, we are motivated to first find limits on the expected (mean) flux $F_0(x,\phi)$. These limits are high mass environments, where F_0 is well approximated by the relationship between flux and density found in Chapter 5, and the low cluster mass limit where F_0 is dominated by the contribution of the background FUV field rather than neighbouring stars. We address these limits as follows.

7.4.1 High mass clusters

The upper limit for FUV flux at a given stellar density ρ_* is defined by the limit of a high mass stellar environment wherein the local region has a well-sampled IMF. In this regime we

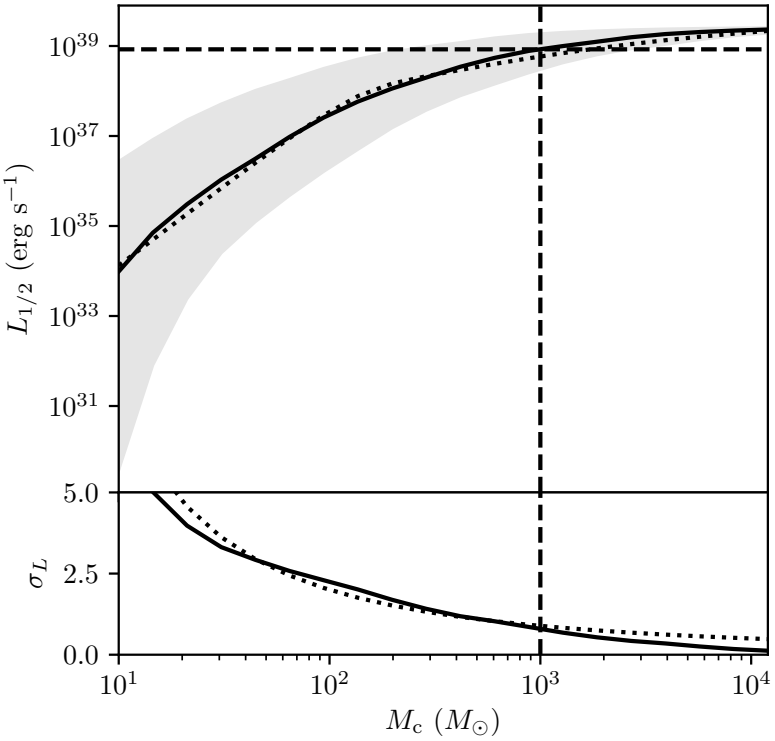

Fig. 7.2 Top: The median luminosity $L_{1/2}$ of the most massive star in a cluster with stellar mass M_c with the IMF described by equation 4.7. The dotted line follows the analytic approximation, equation 7.37. The vertical dashed line is at the critical mass $M_{crit} \approx 10^3\ M_\odot$ beyond which the local FUV flux is well determined by equation 7.39. The associated critical luminosity $L_{crit} \approx 8.4 \times 10^{38}$ erg s^{-1} cm^{-2} is shown as a horizontal dashed line. The shaded region represents the logarithmic standard deviation in $L_{1/2}$. Bottom: The solid line is the value logarithmic standard deviation σ_L of the luminosity, with equation 7.38 indicated by the dotted line.

base the expected flux at fixed local stellar density $\rho_* = \varepsilon(x)\rho_g$ on our findings in Chapter 5. Empirically, the mean FUV flux in high mass environments is

$$F_0^{HM} \approx 1300 \left(\frac{\rho_*}{M_\odot\,\mathrm{pc}^{-3}} \right)^{1/2} G_0. \tag{7.39}$$

We will assume that as the mass of the local environment increases, the flux distribution converges to this average.

7.4.2 Flux in the field

To define the full PDF of FUV flux for a given density, it will be further necessary to define a minimum value for which the FUV exposure is set by the field strength across the entire region. Below a certain density $\rho_{\rm f}$, the FUV flux experienced by a given star is set by the global distribution of stars throughout the region, rather than the contribution of individual neighbouring stars. This happens when the distance between stars approaches the distances between clusters, which is on the order of the Jeans length:

$$\left(\frac{\langle m_*\rangle}{\rho_{\rm f}}\right)^{1/3} \sim \lambda_{\rm J} = \sqrt{\frac{\pi}{G\rho_0}}c_{\rm s} \tag{7.40}$$

where $c_{\rm s}$ is the sound speed and

$$\langle m_*\rangle = \int m_*\xi_*(m_*)\,{\rm d}m_* \approx 0.5\,M_\odot \tag{7.41}$$

is the average stellar mass (established from the IMF, equation 7.17). Estimating $c_{\rm s} \sim 0.3$ km/s as before, we can rewrite equation 7.40:

$$x_{\rm f} \sim 9.4\times10^{-4}\left(\frac{\rho_0}{M_\odot\,{\rm pc}^{-3}}\right)^{1/2}, \tag{7.42}$$

where $x_{\rm f} \equiv \rho_{\rm f}/\rho_0$. For $x < x_{\rm f}$ we consider the contributions of the entire stellar population to the flux, not just neighbouring stars.

While we have described such cases as 'the field', this delineation between clusters and field stars is not physical. Whether stars in an environment of density ρ_* are attributed to a cluster is not of interest here, we simply argue that in such low densities, the flux contribution of the local environment approaches the flux contribution from the global environment. Therefore we have a minimum flux

$$F_0^{\rm f} = F_0^{\rm HM}(\varepsilon_{\rm eff}\rho_{\rm f}), \tag{7.43}$$

where $\varepsilon_{\rm eff} = 0.1$ is the effective SFE across the entire region and $F_0^{\rm HM}$ is defined in equation 7.39. I.e. the mean flux is independent of the local density for $x < x_{\rm f}$. Using the parameters for the solar neighbourhood $\Sigma_0 = 12\,M_\odot$ pc^{-2} and $Q = 1.5$, we find $F_0^{\rm f} \sim 1.1\,G_0$. This is a reasonable estimate of the FUV flux found in the solar neighbourhood (Habing, 1968).

7.4.3 Low mass clusters

Low mass environments do not have a well sampled IMF, but may still represent regions of high density. For this reason, we model deviations from the flux–density relationship:

$$\psi_0 \approx \begin{cases} 1 - e^{-\Gamma} + \psi_0^{\rm f} & \psi_0^{\rm f} < 1 \\ \psi_0^{\rm f} & \psi_0^{\rm f} \geq 1 \end{cases} \tag{7.44}$$

where we define the ratio of the average local flux to the high mass limit $\psi_0 \equiv F_0/F_0^{\rm HM}$, with $\psi_0^{\rm f} = F_0^{\rm f}/F_0^{\rm HM}$. Two limits of equation 7.44 need to be addressed. In the limit where x is small, we have $\psi_0^{\rm f} \geq 1$, then it follows that $\psi_0 = \psi_0^{\rm f}$. In this case the stellar PDF for ψ_0 is:

$$\left.\frac{\partial \mathscr{F}_*}{\partial \psi_0}\right|^{\psi_0^{\rm f} \geq 1} = \delta(\psi_0 - \psi_0^{\rm f}) \tag{7.45}$$

where δ is a Dirac delta function (for fixed x). In the upper and lower limits ($\psi_0 \geq 1 + \psi_0^{\rm f}$, $\psi_0 \leq \psi_0^{\rm f}$ respectively), no corresponding Γ exists, and we have:

$$\left.\frac{\partial \mathscr{F}_*}{\partial \psi_0}\right|^{\psi_0 \geq 1+\psi_0^{\rm f}} = 0 \qquad \left.\frac{\partial \mathscr{F}_*}{\partial \psi_0}\right|^{\psi_0 < \psi_0^{\rm f}} = 0 \tag{7.46}$$

Between these two limits, we can evaluate Γ for a given value ψ_0 and write the PDF:

$$\frac{\partial \mathscr{F}_*}{\partial \psi_0} = \frac{\partial \mathscr{F}_*}{\partial \phi}\frac{\partial \phi}{\partial \psi_0} = \frac{\partial \mathscr{F}_*}{\partial \phi}\frac{\partial \Gamma}{\partial \psi_0}\frac{\partial \phi}{\partial \Gamma}. \tag{7.47}$$

To evaluate the PDF with respect to ϕ, we consider the (normalised) ICMF defined in Section 7.3.1:

$$\frac{\partial \mathscr{F}_*}{\partial \phi} \propto \phi \xi_{\rm c}(\phi) \tag{7.48}$$

We have multiplied the ICMF by a factor ϕ since the number of stars within a cluster scales with cluster mass. Hence the PDF for FUV flux, equation 7.47, can be expressed analytically at a fixed overdensity x.

We are additionally interested in the influence of extinction of FUV photons due to the primordial gas present in the nascent cluster. The calculation of an equivalent normalised mean flux $\psi_0^{\rm ext}$ including extinction requires further assumptions regarding the initial distribution of stars and gas. These are reviewed in Appendix D.1 where we calculate the quantities relevant in producing an upper limit on the influence of primordial gas extinction.

7.4.4 Dispersion from mean FUV flux

Equation 7.47 defines a PDF for the mean flux distribution for fixed density, but in deriving it we have assumed that all clusters of a fixed mass exhibit the same flux distribution. This is clearly not the case, as the most massive star and the internal density profile can yield variations in the flux experienced by the stellar population. To model these variations, we consider deviations from the average flux ratio ψ_0 which we assume follow a lognormal distribution:

$$\frac{\partial \mathscr{F}_*}{\partial \delta\psi} = \frac{1}{\sqrt{2\pi\sigma_F^2}\delta\psi} \exp\left\{-\frac{(\ln\delta\psi)^2}{2\sigma_F^2}\right\} \tag{7.49}$$

where $\delta\psi \equiv \psi/\psi_0$ and $\psi = F/F_0^{\rm HM}$. The logarithmic flux dispersion σ_F is the contribution of the dispersion $\sigma_F^{\rm f}$ in flux arising from varying spatial separations from ionising sources, and the dispersion σ_L in the luminosity of the most massive cluster member. The former dominates the dispersion in the limit where FUV flux is determined by the field value, and in the limit of massive clusters where σ_L is small. In the intermediate regime, the dispersion is dominated by σ_L. Hence we estimate

$$\sigma_F \approx \sigma_F^{\rm f} + \sigma_L(\phi)\cdot\mathscr{W}_1(\psi_0)\cdot\mathscr{W}_2(\psi_0) \tag{7.50}$$

where we estimate $\sigma_F^{\rm f} = 0.5$ (approximated from the results presented in Chapter 5). The two weighting functions are defined:

$$\mathscr{W}_1 = \max\left\{\mathrm{erf}\left(\ln\psi_0 - \ln\psi_0^{\rm f}\right), 0\right\} \tag{7.51}$$

and

$$\mathscr{W}_2 = \max\left\{\mathrm{erf}\left[\ln\left(1+\psi_0^{\rm f}\right) - \ln\psi_0\right], 0\right\}, \tag{7.52}$$

such that equation 7.50 is a continuous function and satisfies our requirements.

Since ψ is the product of ψ_0 and $\delta\psi$, we can evaluate its PDF using equations 7.47 and 7.49:

$$\frac{\partial \mathscr{F}_*}{\partial \psi} = \int \mathrm{d}\psi_0 \frac{\partial \mathscr{F}_*}{\partial \psi_0}\frac{\partial \mathscr{F}_*}{\partial \delta\psi}\frac{1}{\psi_0}. \tag{7.53}$$

Hence we have a PDF for the FUV flux experienced by a stellar population at a fixed overdensity x.

In Section 7.5.2 we will consider how extinction due to primordial gas alters the flux PDF. In this case, the prescription above cannot be applied since we marginalise over the PDF for ϕ in the calculation of the PDF for the extincted flux $\psi_0^{\rm ext}$ (Appendix D.1). To simplify, we assume $\sigma_F = \sigma_F^{\rm f}$ as a first order estimate in this case. While this underestimates the

dispersion in flux for intermediate ϕ values, we perform these calculations to give a sense of the severity of FUV extinction for the most extreme regions. For these regions, the flux dispersion is $\sigma_F \sim \sigma_F^{\mathrm{f}}$ anyway. As discussed in Appendix D.1, more detailed estimates of the true influence of extinction are required, and we leave this for future work.

7.5 Stellar density–FUV flux distribution

7.5.1 No extinction

To illustrate the consequences of the formulation we have presented in this section, we now apply our results to the solar neighbourhood and the CMZ with parameters indicated in Section 7.2.1. The PDF for stars in terms of the local stellar density and FUV flux is given by:

$$\frac{\partial^2 \mathscr{F}_*}{\partial \rho_* \partial F} = \frac{\partial \mathscr{F}_*}{\partial \rho_*} \cdot \frac{\partial \mathscr{F}_*}{\partial F}. \tag{7.54}$$

The results of this calculation are shown in figure 7.3 in the case of no interstellar extinction. We have indicated contours of equal dispersal timescale for $\tau_{\mathrm{disp.}} = 1$, 2 and 3 Myr for a star of mass $m_* = 0.5\,M_\odot$ hosting a PPD with $\alpha = 5.4 \times 10^{-3}$:

$$\tau_{\mathrm{disp.}} \approx \left(\tau_{\mathrm{FUV}}^{-1} + \tau_{\mathrm{tidal}}^{-1}\right)^{-1}, \tag{7.55}$$

for the dispersal timescale due to FUV photons, τ_{FUV}, and the tidal dispersal timescale, τ_{tidal}. The former we calculate in the same way as in Chapter 6 with scale radius $R_1 = 40$ au and the initial disc mass $M_{\mathrm{d},0} = 0.1\,m_*$. We assume τ_{tidal} is the timescale on which a star undergoes an encounter within 50 au, with the theoretical encounter rate described in Chapter 1. This is reasonable since Chapter 3 and Chapter 4 indicate distant encounters are not important for disc evolution, and we are free to consider the timescale for a single, highly destructive encounter. Additionally, the findings in Chapter 4 show that the differential effect of encounters on discs with varying stellar host masses over time is small; we will therefore assume all stars have mass $m_* = \langle m_* \rangle = 0.5\,M_\odot$ in calculating the encounter rate.

Although the sample of young star forming regions compiled in Chapter 5 is not complete, we qualitatively compare our results in figure 7.3, where we overplot contours for some observed young cluster environments. As previously, we find that practically no stars exist at stellar densities sufficient to cause significant PPD truncation that are not also subject to high FUV field strengths. In the solar neighbourhood the most extreme values are $F \sim 10^5\ G_0$ and $\rho_* \sim 10^4\,M_\odot\ \mathrm{pc}^{-3}$. This reflects conditions within the core of the ONC; the most extreme observed environment in the solar neighbourhood. The lower limit in FUV flux is $\sim 1\,G_0$,

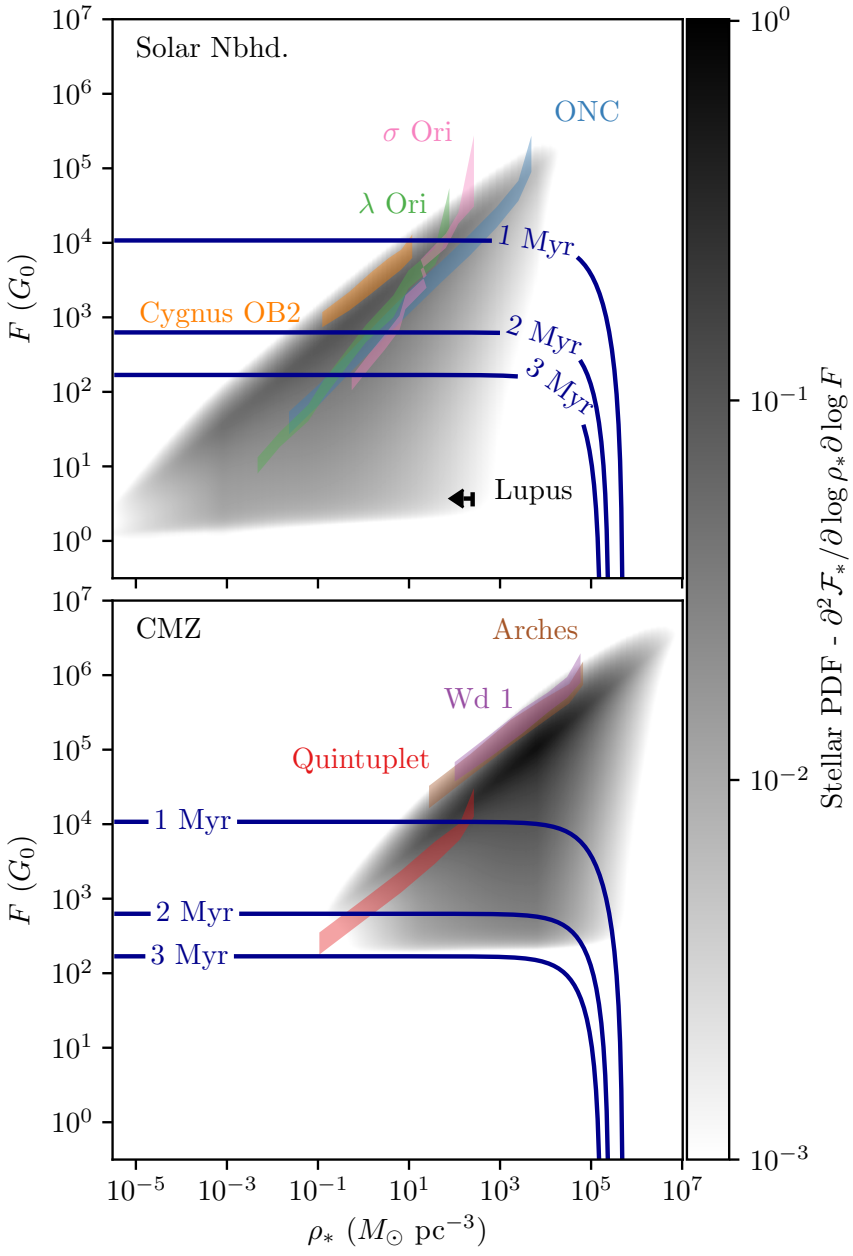

Fig. 7.3 Two dimensional PDF for stars in F–ρ_* (FUV flux–stellar density) space. The top panel is for the solar neighbourhood, described by mean surface density $\Sigma_0 = 12 M_\odot$ pc^{-2}, Toomre $Q = 1.5$, and mean volume density $\rho_0 \approx 0.06 M_\odot$ pc^{-3}. The bottom panel reflects conditions in the central molecular zone (CMZ), with $\Sigma_0 = 1000 M_\odot$, $Q = 1.5$ and $\rho_0 \approx 250 M_\odot$ pc^{-3}. We have marked contours in the PPD dispersal timescale based on the findings of previous chapters for a star of mass $m_* = 0.5\ M_\odot$ (approximately the mean mass stellar mass from our IMF) with a viscosity parameter $\alpha = 5.4 \times 10^{-3}$. We have additionally indicated some empirically derived contours calculated in Chapter 5 for a number of young stellar environments, truncated at a radius such that 90% of stars for each region are included.

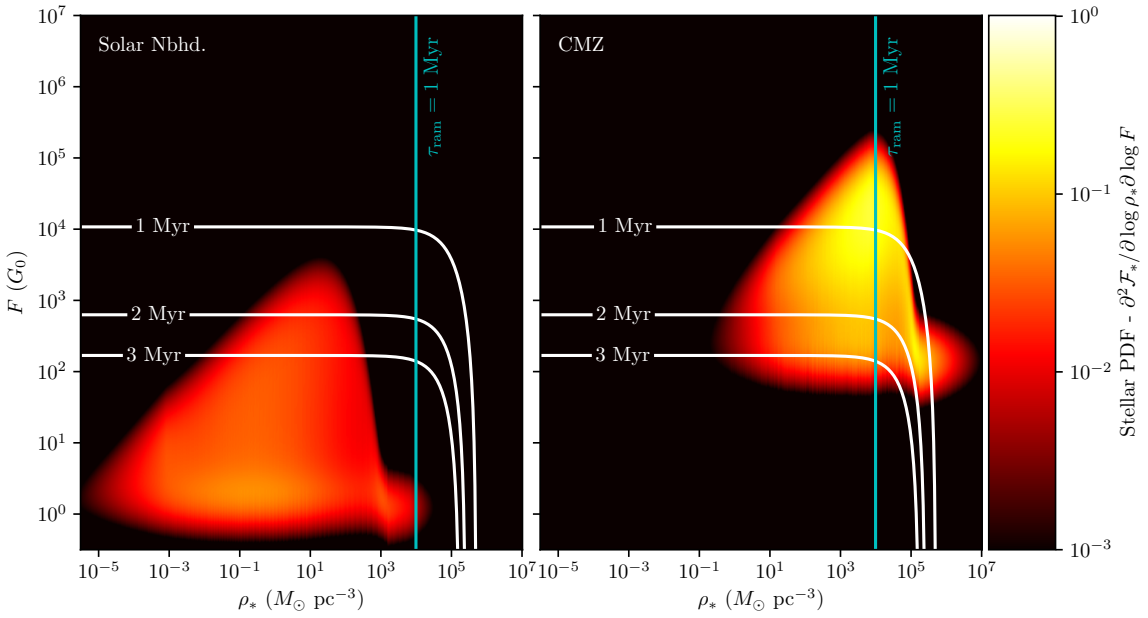

Fig. 7.4 As in figure 7.3 but including a prescription for the FUV extinction by primordial gas. The vertical cyan line marks the stellar density threshold above which ram pressure due to primordial gas will alter disc evolution on timescales $\lesssim 1$ Myr for a star with $m_* = 0.5\,M_\odot$. See text for details.

which is the observed field value in the solar neighbourhood (Habing, 1968). Additionally, we predict a number of regions with low $F \sim 1$–$10\,G_0$, but $\rho_* \sim 10^2\,M_\odot$ pc^{-3}. Lupus is a local example of such a young region (Nakajima *et al.*, 2000; Merín *et al.*, 2008; Cleeves *et al.*, 2016; Haworth *et al.*, 2017). In summary, the distribution of stellar environments is in good agreement with what we would expect from observations of local regions.

In the case of the CMZ we find much higher typical FUV field strengths and densities. The minimum expected FUV flux in the region is $\sim 150\,G_0$, and the most extreme regions lie at $\rho_* \sim 10^6\,M_\odot$ pc^{-3} and $F \sim 10^6\,G_0$. This is comparable to the conditions found in core of Arches and Westerlund 1 (see Chapter 5 and Figer *et al.*, 1999; Mengel and Tacconi-Garman, 2007). The distribution of stellar birth environments in the CMZ suggest that both FUV photons and tidal encounters play a role in PPD evolution (although for the majority of discs, external photoevaporation remains the dominant dispersal mechanism), and that discs cannot survive for long in such environments.

7.5.2 Maximal extinction

In Appendix D.1, we estimate the effect of extinction on the FUV flux distribution by assuming Plummer sphere geometry of the gas within a nascent cluster. We then integrate

over a radial coordinate defined to be consistent with the total cluster mass to calculate the resulting surface density if the most massive star is at the centre of the cluster. The gas surface density is then used to calculate the reduction in FUV flux a star experiences.

The result of this process is shown in figure 7.4. Our results indicate very high degrees of extinction at high local gas densities $\rho_{\rm g}$, and hence we find that many regions where PPDs that would otherwise be dispersed quickly by FUV photons are efficiently shielded during the embedded phase. Apart from the contours for $\tau_{\rm disp.}$ due to tidal encounters and external photoevaporation, we have further indicated a canonical limit above which gas density rapidly alters disc evolution through ram pressure, based on the findings of Wijnen *et al.* (2017a):

$$\tau_{\rm ram} \sim \frac{\Sigma_{\rm d}}{5\rho_{\rm g} v_{\rm g}}. \tag{7.56}$$

We assume that the relative speed of the star with respect to the gas $v_{\rm g} = |\vec{v}_{\rm g}| \approx \sigma_v = 1$ km/s, choose the initial disc surface density $\Sigma_{\rm d}$ close to $R_1 = 40$ au with a surface density as defined by equation 1.5, and assume that $M_{\rm d,0} = 0.1\, m_*$. In the case of the CMZ, the majority of stars which experience large FUV extinction have $\tau_{\rm ram} < 1$ Myr, and hence we would expect the ISM to play an important role in PPD evolution prior to gas expulsion.

As we discussed in Appendix D.1, the prescription we have implemented for FUV extinction underestimates the apparent FUV flux experienced by a given star since we have assumed that the local gas density distribution follows a Plummer density profile. This is not the case for a realistic, clumpy gas distributions. In the latter case, extinction efficiency is reduced. Hence the results of our calculations summarised in this section, rather than offering conclusive answers to the nature of disc evolution during the embedded phase, highlight the importance of the following issues for disc evolution:

1. The timescale of the embedded phase.
2. The efficiency of extinction during the embedded phase.
3. The (statistical) influence of ram pressure stripping on a PPD population as a function of local gas density.

To fully understand how PPD properties evolve early during the cluster history, these three questions must be addressed. Despite these uncertainties, in the case of the CMZ even our calculation for the minimum FUV flux experienced by stars is sufficient to significantly reduce PPD lifetimes. However, we have assumed this floor is unaffected by local FUV extinction. We justify this assertion by arguing that, since the field flux $F^{\rm f}$ is the sum of contributions from all directions, the clumpiness of the gas distribution makes it likely that it

is only reduced by a factor of order unity when averaged over time (dependent on the solid angle subtended by the gas). This assertion requires validation with a realistic treatment of extinction (point 2). In what follows we will focus on the lifetimes of discs post-gas expulsion.

7.6 Environment and PPD dispersal timescale

7.6.1 Dispersal timescale distribution

When answering the question of planet formation efficiency within a given environment, it is instructive to understand the expected distribution of PPD lifetimes. In environments where a large fraction of stars have discs that are quickly dispersed by stellar feedback, then we might expect a low planet formation efficiency. For this purpose, we consider the fraction of PPDs with a given lifetime $\tau_{\rm disp.}$ for fixed $\tau_{\rm visc.}$:

$$\frac{\partial \mathscr{F}_*}{\partial \tau_{\rm disp.}} = \int {\rm d}F \int {\rm d}m_* \frac{\partial \mathscr{F}_*}{\partial F} \frac{\partial \mathscr{F}_*}{\partial m_*} \frac{\partial \mathscr{F}_*}{\partial \rho_*} \left| \frac{\partial \tau_{\rm disp.}}{\partial \rho_*} \right|^{-1} \tag{7.57}$$

where $\partial \mathscr{F}_*/\partial m_* = \xi_*$ is the stellar IMF and

$$\left| \frac{\partial \tau_{\rm disp.}}{\partial \rho_*} \right| = \left| \frac{\partial \tau_{\rm tidal}}{\partial \rho_*} \frac{\partial \tau_{\rm disp.}}{\partial \tau_{\rm tidal}} \right| = 2 \left\{ \frac{1\,{\rm Myr}}{\tau_{\rm disp.}} + \frac{\rho_*}{5\times10^5\,M_\odot\,{\rm pc}^{-3}} \right\}^{-2} \frac{\rm yr}{M_\odot\,{\rm pc}^{-3}} \tag{7.58}$$

at fixed F, m_*.

The results of this calculation are presented as cumulative distribution of $\tau_{\rm disp.}$ for the stellar population in figure 7.5. We find that if we consider PPDs around all stars down to $0.08\,M_\odot$ with our chosen IMF, then we obtain median dispersal timescales of 2.3 Myr in the solar neighbourhood and 0.6 Myr in the CMZ. In both cases these medians are below the characteristic PPD lifetimes for non-photoevaporated populations ($\sim$ 3–10 Myr). However, if we instead consider only PPDs with host stars above $1\,M_\odot$, then the median dispersal timescales increase to 9.2 Myr in the solar neighbourhood, and 2.2 Myr in the CMZ. This highlights the large discrepancy between the expected lifetimes of discs around low- and high-mass stars under the influence of external photoevaporation. For all stars, disc lifetimes are suppressed by a factor $\gtrsim 3$ in the CMZ with respect to the solar neighbourhood. This finding has significant consequences for PPD evolution in the central $\sim$ 250 pc of the Milky Way, where the time and material available for planet formation is severely reduced by dispersal mechanisms (primarily external photoevaporation). Indeed, for the whole stellar

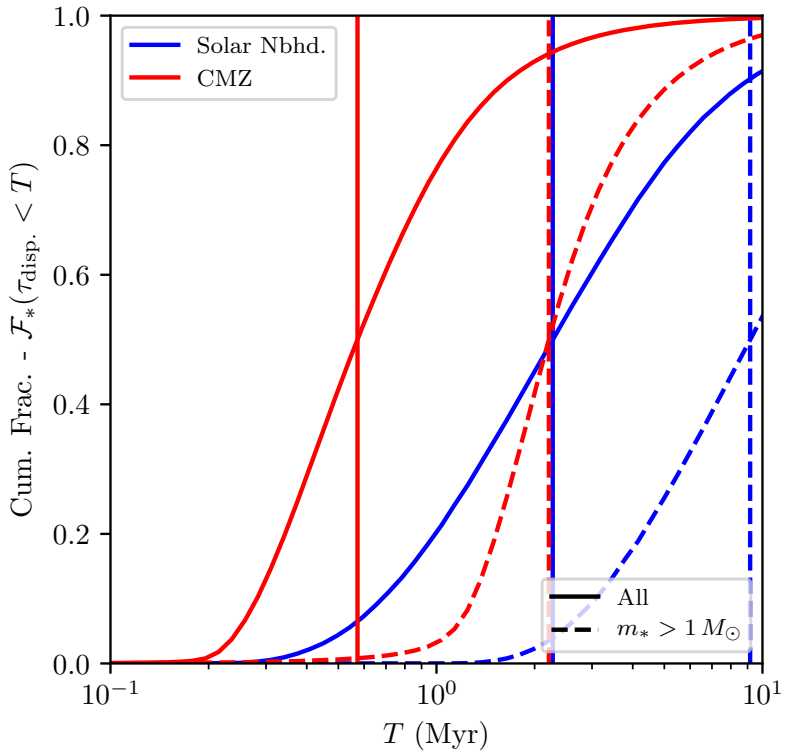

Fig. 7.5 Cumulative fraction of discs with $\tau_{\rm disp.} < T$ in the solar neighbourhood (blue lines) and CMZ (red lines). We have further shown the distributions for all discs (solid lines) and discs for which the host star has a mass $> 1\,M_\odot$ (dashed lines). The vertical lines of corresponding colour and style mark the median disc lifetimes for each PPD sample. We have assumed a viscosity parameter $\alpha = 5.4 \times 10^{-3}$.

population $\sim 70\%$ of PPDs are dispersed within 1 Myr of primordial gas expulsion due to external dispersal mechanisms alone.

7.6.2 Gas properties & PPD dispersal

To explore the parameter space for primordial gas properties and host stellar mass, we rewrite equation 7.57 for a fixed stellar mass:

$$0.5 = \int_0^{\tau_{\rm disp.,1/2}} {\rm d}\tau_{\rm disp.} \int {\rm d}F \frac{\partial \mathscr{F}_*}{\partial F} \frac{\partial \mathscr{F}_*}{\partial \rho_*} \left| \frac{\partial \tau_{\rm disp.}}{\partial \rho_*} \right|^{-1} \tag{7.59}$$

and solve numerically for the median dispersal timescale $\tau_{\rm disp.,1/2}$. In figure 7.6 we show $\tau_{\rm disp.,1/2}$ as a function of gas surface density Σ_0, and angular speed Ω within a galactic disc for varying Toomre Q, and stellar host mass m_*. Most obviously, the timescale for

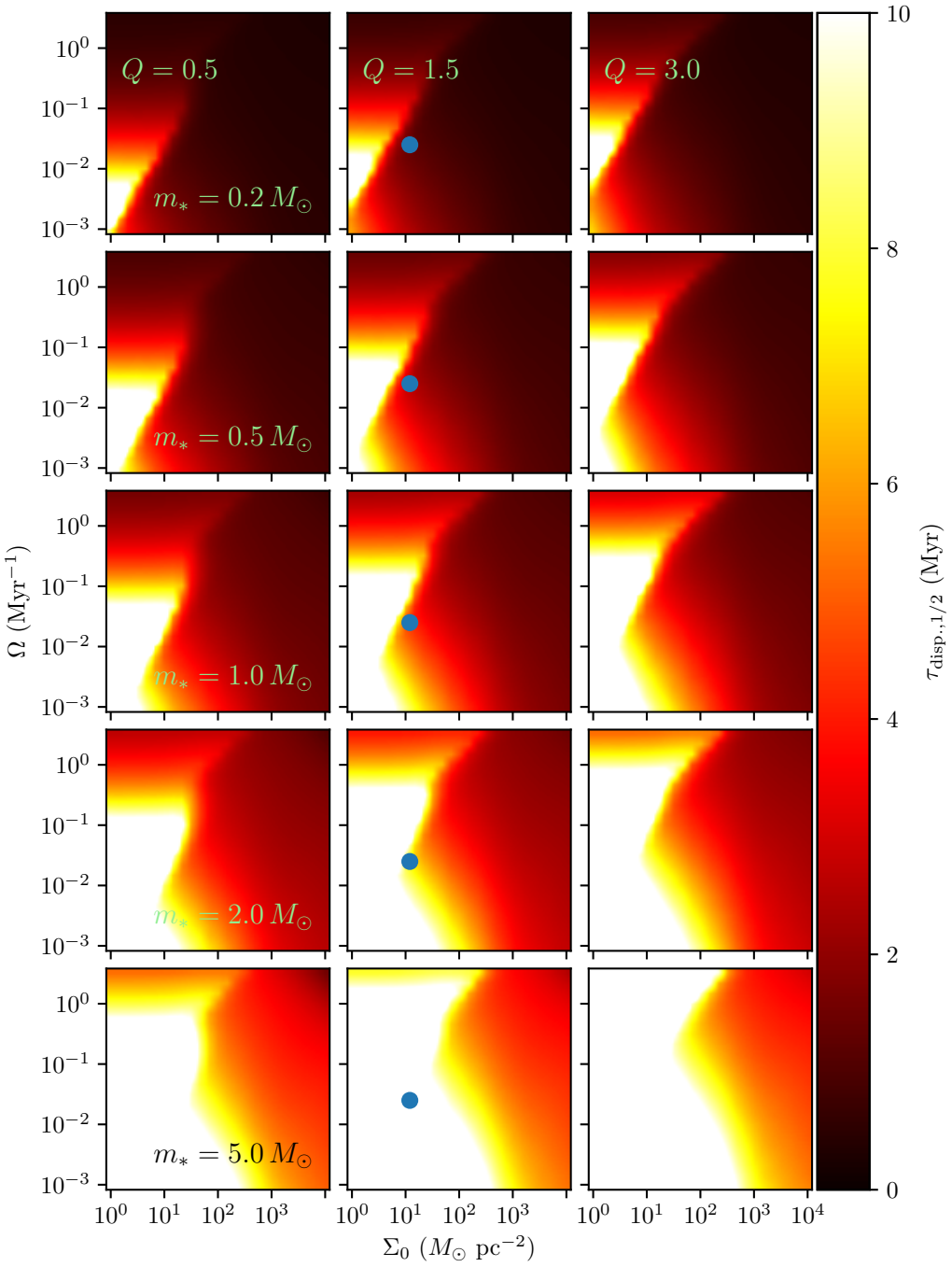

Fig. 7.6 The median dispersal timescales $\tau_{\mathrm{disp.},1/2}$ induced by external photoevaporation and tidal encounters for PPDs around a star of mass m_* as a function of primordial gas surface density Σ_0 and angular speed Ω for Toomre $Q = 0.5$, 1, 3. The blue circle marks the position of the solar neighbourhood. Regions of parameter space for which $\tau_{\mathrm{disp.},1/2} < 10$ Myr exhibit disc lifetimes that are significantly reduced with respect to a PPD evolving in isolation.

PPD destruction decreases with increasing Σ_0, and deceasing m_*. The former relationship is simply due to increasing stellar density and maximum cluster mass with Σ_0, leading to greater FUV flux. The opposite is true for Q, and therefore $\tau_{\text{disp.}}$ increases with increasing Q. The host mass dependence is due to the greater efficiency of external photoevaporation acting upon lower mass stellar hosts, since they have a reduced gravitational potential and therefore greater critical radius within the disc (see Haworth *et al.*, 2018a,b).

The dependence of $\tau_{\text{disp.}}$ on Ω is more complicated, and two competing factors dictate the relationship. Firstly, larger Ω means larger ρ_0 (equation 7.7), and hence higher densities. However, a high angular speed also restricts the maximum cluster mass (equation 7.21) and therefore reduces the local maximum FUV luminosity, unless Ω is sufficiently small such that $\langle \tau_{\text{fb}} \rangle < \tau_{\text{ff,2D}}$ (equations 7.22 and 7.24). Whether the latter factor is important depends on ρ_{f} (equation 7.42), and whether the resulting field flux F_{f} is sufficient to significantly influence disc evolution. If F_{f} is large, then the influence of the cluster mass function is negligible, and $\tau_{\text{disp.}}$ decreases with increasing Ω (and vice versa). These competing factors result in three regimes for dispersal timescale, with the variation in field flux dominating for high and low Ω and the rapid decrease in maximum cluster mass dominating for intermediate values.

Finally, we find that the position of the solar neighbourhood in the parameter space (marked by a blue dot in figure 7.6) is approximately at the maximum surface density where the majority of the disc population around stars with $m_* \sim 1 M_\odot$ do not get significantly depleted by external influences. Dependent on the exact Σ_0–Ω relationship within a galaxy (e.g. the approximate relationship equation 7.11 for local galaxies), regions of much higher or lower Ω for the same surface density may be unlikely. This is intriguing because it suggests that the position of the solar system within the galaxy is such that a maximal *number* (not fraction) of stars have PPDs which disperse largely by internal processes (including planet formation). We therefore tentatively suggest that the solar neighbourhood is a special region for the evolution of PPDs.

7.7 Overall conclusions

In this chapter we have used the results from the previous chapters to illustrate how star formation parameters can be linked to PPD dispersal timescales due to FUV induced photoevaporation and tidal encounters. This has numerous applications for assessing the planet formation potential of star forming regions, and establishing the typical influences on PPD evolution for future investigation. It also highlights the significance of the primary conclusions drawn from this dissertation, which we summarise as follows:

1. The solar neighbourhood lies close to the largest ISM surface density for which the majority of the PPD population are not influenced by external dispersal mechanisms. For surface densities much larger, the PPDs have lifetimes which are significantly shortened by (predominantly) FUV flux.

2. Due to the higher gas densities in the central molecular zone, much of the stellar population initially experiences high FUV flux. This results in dispersal timescales that are a factor $\gtrsim 3$ shorter than those in the solar neighbourhood. Across the entire IMF, we predict that $\sim 70\%$ of PPDs are destroyed within 1 Myr in the CMZ. Therefore we expect that planet formation in this region is severely limited in time and mass.

3. As found in Chapter 5, external photoevaporation is the dominant mechanism for disc dispersal in the solar neighbourhood, and we find that no stars exist in regions where type II tidal encounters can truncate PPDs. Extending this to the CMZ in this chapter, we find that the timescale for FUV induced disc destruction remains shorter than the tidal timescale after gas expulsion ($\tau_{\rm FUV} < \tau_{\rm tidal}$).

4. While type II encounters may be insignificant as a dispersal mechanism for PPDs, we have highlighted that this does not preclude encounters within multiple systems (type I), particularly during the earlier stages of disc evolution. In Chapter 2 we present evidence that HV and DO Tau is the first example of a presently unbound or marginally bound system that underwent a past close disc-disc encounter during the ejection of one of its members.

5. In this chapter we estimate an upper limit on the influence of extinction on the FUV flux. Our calculations suggest that PPDs in high density regions can be efficiently shielded by primordial gas. In this case tidal encounters remain insignificant as a depletion mechanism since the ram pressure imposed on a disc population operates on a much shorter timescale $\tau_{\rm ram} \ll \tau_{\rm tidal}$ (in agreement with Wijnen *et al.*, 2017b). We therefore conclusively rule out tidal encounters as a dispersal mechanism in any environment. For CMZ-like regions, the ram pressure influences PPDs on a short timescale in all regions where FUV flux is severely reduced by extinction.

6. Strong evidence for the FUV induced depletion of the PPD sample in Cygnus OB2 is discussed in Chapter 6, where we find that the disc fractions can be successfully explained by external photoevaporation. Through our modelling procedure, we also find that disc dispersal timescales are strongly correlated with host mass in regions where external photoevaporation is significant. This is because a shallower gravitational potential allows more efficient mass loss driven by FUV photons. We predict that

the signature of rapidly depleted discs around low mass stars should be evident in sufficiently photoevaporated samples such as in Cygnus OB2. This may also, for example, explain the low disc fraction around M-stars found by Hernández *et al.* (2010) in λ Ori if the hypothesised past supernova scenario is accurate (Dolan and Mathieu, 2001).

As well as providing insights into the link between star formation physics and planet formation, our findings also highlight particular questions for future work to answer. For each of the above findings we summarise some such issues:

1. Is the solar neighbourhood special? Future studies may, for example, compare our calculations to simulations and observations of star formation over time and space. In this way, statistical conclusions may be drawn regarding the significance of the position of the solar neighbourhood in Σ_0–Ω space.

2. What is the observed fraction of stars that have discs in the CMZ as a function of age? Early investigations on this topic suggest low disc fractions of a few percent in Arches (Stolte *et al.*, 2010, 2015).

3. How long is the typical viscous timescale for PPDs? In this chapter, we have assumed a viscous timescale of $\tau_{\rm visc.} = 1$ Myr for a star of mass $1\,M_{\odot}$. The dispersal timescale is a moderate function of this choice. In the case that MHD winds are instead responsible for the majority of accretion onto the central star such that the disc does not spread, how rapidly does the outside-in clearing due to external photoevaporation disperse a PPD?

4. Since type I encounters do occur, even in low density regions such as Taurus, the influence of multiplicity on disc evolution and the resultant exoplanet population remains an important issue. Any population synthesis for PPD samples and their resulting exoplanet population will be incomplete without considering realistic multiplicity in the early stages of cluster evolution.

5. What is the influence of primordial gas on disc evolution? This broad topic includes a number of questions regarding both star formation physics and the response of the disc to the ISM. Some of these include: How long is the embedded phase as a function of environment? How efficient is extinction in regions of high primordial gas density? What is the statistical influence of the motion of the dense ISM with respect to a population of PPDs?

6. Can we find evidence of a steep disc mass–host mass relationship in regions of strong FUV flux? Our modelling of Cygnus OB2 in Chapter 6 suggests that finding such observational signatures of photoevaporation should indeed be possible with relatively small sample sizes *if* PPDs in a region have been sufficiently depleted.

Overall we conclude that building a picture of planet formation predominantly based on PPDs in the solar neighbourhood, or ignoring external influences, will result in a biased understanding of the time and mass available for planet formation over galactic and cosmological scales. The prescription we have presented in this chapter is a tool for future studies wishing to estimate the variation of PPD properties in diverse environments. Our findings also highlight the key issues that need to be addressed to further quantify the importance of star formation conditions for planet formation.

References

Aarseth, S.J. (2003). *Gravitational N-Body Simulations*.

Abadi, M.G. et al (2003). Simulations of Galaxy Formation in a Λ Cold Dark Matter Universe. I. Dynamical and Photometric Properties of a Simulated Disk Galaxy. ApJ, **591**, 499–514.

Adamo, A. et al (2015). Probing the role of the galactic environment in the formation of stellar clusters, using M83 as a test bench. MNRAS, **452**, 246–260.

Adams, F.C. (2010). The Birth Environment of the Solar System. ARA&A, **48**, 47–85.

Adams, F.C. et al (2004). Photoevaporation of Circumstellar Disks Due to External Far-Ultraviolet Radiation in Stellar Aggregates. ApJ, **611**, 360–379.

Adams, F.C. et al (2006). Early Evolution of Stellar Groups and Clusters: Environmental Effects on Forming Planetary Systems. ApJ, **641**, 504–525.

Agnew, M.T., Maddison, S.T. and Horner, J. (2018). Prospecting for exo-Earths in multiple planet systems with a gas giant. MNRAS, **481**, 4680–4697.

Alexander, R.D., Clarke, C.J. and Pringle, J.E. (2005). Constraints on the ionizing flux emitted by T Tauri stars. MNRAS, **358**, 283–290.

Alexander, R.D., Clarke, C.J. and Pringle, J.E. (2006a). Photoevaporation of protoplanetary discs - I. Hydrodynamic models. MNRAS, **369**, 216–228.

Alexander, R.D., Clarke, C.J. and Pringle, J.E. (2006b). Photoevaporation of protoplanetary discs - II. Evolutionary models and observable properties. MNRAS, **369**, 229–239.

Ali, A., Harries, T.J. and Douglas, T.A. (2018). Modelling massive star feedback with Monte Carlo radiation hydrodynamics: photoionization and radiation pressure in a turbulent cloud. MNRAS, **477**, 5422–5436.

Allison, R.J. et al (2009). Dynamical Mass Segregation on a Very Short Timescale. ApJ, **700**, L99–L103.

ALMA Partnership et al (2015). The 2014 ALMA Long Baseline Campaign: First Results from High Angular Resolution Observations toward the HL Tau Region. ApJ, **808**, L3.

Alves de Oliveira, C. et al (2013). Herschel survey of brown dwarf disks in ρ Ophiuchi. A&A, **559**, A126.

Anderson, K.R., Adams, F.C. and Calvet, N. (2013). Viscous Evolution and Photoevaporation of Circumstellar Disks Due to External Far Ultraviolet Radiation Fields. ApJ, **774**, 9.

André, P. et al (2014). From Filamentary Networks to Dense Cores in Molecular Clouds: Toward a New Paradigm for Star Formation. *Protostars and Planets VI*, pages 27–51.

Andrews, S.M. and Williams, J.P. (2005). Circumstellar Dust Disks in Taurus-Auriga: The Submillimeter Perspective. ApJ, **631**, 1134–1160.

Andrews, S.M. and Williams, J.P. (2007). A Submillimeter View of Circumstellar Dust Disks in ρ Ophiuchi. ApJ, **671**, 1800–1812.

Andrews, S.M. et al (2013). The Mass Dependence between Protoplanetary Disks and their Stellar Hosts. ApJ, **771**, 129.

Ansdell, M. et al (2016). ALMA Survey of Lupus Protoplanetary Disks. I. Dust and Gas Masses. ApJ, **828**, 46.

Ansdell, M. et al (2017). An ALMA Survey of Protoplanetary Disks in the σ Orionis Cluster. AJ, **153**, 240.

Anthony-Twarog, B.J. (1982). The H-beta distance scale for B stars - The Orion association. AJ, **87**, 1213–1222.

Armitage, P.J. (2000). Suppression of giant planet formation in stellar clusters. A&A, **362**, 968–972.

Armitage, P.J. (2011). Dynamics of Protoplanetary Disks. ARA&A, **49**, 195–236.

Armitage, P.J., Clarke, C.J. and Tout, C.A. (1999). Accretion disc evolution in single and binary T Tauri stars. *MNRAS*, **304**, 425–433.

Armitage, P.J., Clarke, C.J. and Palla, F. (2003). Dispersion in the lifetime and accretion rate of T Tauri discs. MNRAS, **342**, 1139–1146.

Armitage, P.J., Simon, J.B. and Martin, R.G. (2013). Two Timescale Dispersal of Magnetized Protoplanetary Disks. ApJ, **778**, L14.

Bae, J., Zhu, Z. and Hartmann, L. (2017). On the Formation of Multiple Concentric Rings and Gaps in Protoplanetary Disks. ApJ, **850**, 201.

Bai, X.N. (2016). Towards a Global Evolutionary Model of Protoplanetary Disks. ApJ, **821**, 80.

Bai, X.N. and Stone, J.M. (2011). Effect of Ambipolar Diffusion on the Nonlinear Evolution of Magnetorotational Instability in Weakly Ionized Disks. ApJ, **736**, 144.

Bai, X.N. and Stone, J.M. (2013). Wind-driven Accretion in Protoplanetary Disks. I. Suppression of the Magnetorotational Instability and Launching of the Magnetocentrifugal Wind. ApJ, **769**, 76.

Bai, X.N. and Stone, J.M. (2017). Hall Effect-Mediated Magnetic Flux Transport in Protoplanetary Disks. ApJ, **836**, 46.

Bai, X.N. et al (2016). Magneto-thermal Disk Winds from Protoplanetary Disks. ApJ, **818**, 152.

Balbus, S.A. (2011). *Magnetohydrodynamics of Protostellar Disks*, pages 237–282. University of Chicago Press.

Balbus, S.A. and Hawley, J.F. (1991). A powerful local shear instability in weakly magnetized disks. I - Linear analysis. II - Nonlinear evolution. ApJ, **376**, 214–233.

Balbus, S.A. and Hawley, J.F. (1998). Instability, turbulence, and enhanced transport in accretion disks. *Rev. Mod. Phys.*, **70**, 1–53.

Balbus, S.A. and Papaloizou, J.C.B. (1999). On the Dynamical Foundations of α Disks. ApJ, **521**, 650–658.

Balbus, S.A. and Terquem, C. (2001). Linear Analysis of the Hall Effect in Protostellar Disks. ApJ, **552**, 235–247.

Ballesteros-Paredes, J., Hartmann, L. and Vázquez-Semadeni, E. (1999). Turbulent Flow-driven Molecular Cloud Formation: A Solution to the Post-T Tauri Problem? *ApJ*, **527**, 285–297.

Baraffe, I., Chabrier, G. and Gallardo, J. (2009). Episodic Accretion at Early Stages of Evolution of Low-Mass Stars and Brown Dwarfs: A Solution for the Observed Luminosity Spread in H-R Diagrams? ApJ, **702**, L27–L31.

Baruteau, C. and Papaloizou, J.C.B. (2013). Disk-Planets Interactions and the Diversity of Period Ratios in Kepler's Multi-planetary Systems. ApJ, **778**, 7.

Bastian, N. (2008). On the star formation rate - brightest cluster relation: estimating the peak star formation rate in post-merger galaxies. MNRAS, **390**, 759–768.

Bate, M.R. (2012). Stellar, brown dwarf and multiple star properties from a radiation hydrodynamical simulation of star cluster formation. MNRAS, **419**, 3115–3146.

Bate, M.R. (2018). On the diversity and statistical properties of protostellar discs. MNRAS, **475**, 5618–5658.

Baumgardt, H. and Kroupa, P. (2007). A comprehensive set of simulations studying the influence of gas expulsion on star cluster evolution. MNRAS, **380**, 1589–1598.

Bean, J.L. et al (2018). The Transiting Exoplanet Community Early Release Science Program for JWST. PASP, **130**(11), 114402.

Beccari, G. et al (2017). A tale of three cities. OmegaCAM discovers multiple sequences in the color-magnitude diagram of the Orion Nebula Cluster. A&A, **604**, A22.

Beckwith, S.V.W. et al (1990). A survey for circumstellar disks around young stellar objects. *AJ*, **99**, 924–945.

Beichman, C. et al (2014). Observations of Transiting Exoplanets with the James Webb Space Telescope (JWST). PASP, **126**, 1134.

Bertoldi, F. and McKee, C.F. (1992). Pressure-confined clumps in magnetized molecular clouds. ApJ, **395**, 140–157.

Bertout, C. and Genova, F. (2006). A kinematic study of the Taurus-Auriga T association. A&A, **460**, 499–518.

Bhandare, A., Breslau, A. and Pfalzner, S. (2016). Effects of inclined star-disk encounter on protoplanetary disk size. A&A, **594**, A53.

Bica, E., Bonatto, C. and Dutra, C.M. (2003). Does Cyg OB2 harbour any open cluster? A&A, **405**, 991–998.

Biddle, L.I. et al (2018). K2 Reveals Pulsed Accretion Driven by the 2 Myr Old Hot Jupiter CI Tau b. ApJ, **853**, L34.

Bik, A. et al (2003). Identification of the ionizing source of NGC 2024. A&A, **404**, 249–254.

Binney, J. and Tremaine, S. (1987). *Galactic dynamics*. Princeton University Press.

Birnstiel, T. et al (2010). Testing the theory of grain growth and fragmentation by millimeter observations of protoplanetary disks. A&A, **516**, L14.

Bisbas, T.G. et al (2012). 3D-PDR: a new three-dimensional astrochemistry code for treating photodissociation regions. MNRAS, **427**, 2100–2118.

Bisbas, T.G. et al (2015). STARBENCH: the D-type expansion of an H II region. MNRAS, **453**, 1324–1343.

Bisbas, T.G. et al (2018). The inception of star cluster formation revealed by [C II] emission around an Infrared Dark Cloud. MNRAS, **478**, L54–L59.

Blaes, O.M. and Balbus, S.A. (1994). Local shear instabilities in weakly ionized, weakly magnetized disks. ApJ, **421**, 163–177.

Blandford, R.D. and Payne, D.G. (1982). Hydromagnetic flows from accretion discs and the production of radio jets. MNRAS, **199**, 883–903.

Boffin, H.M.J. et al (1998). Numerical simulations of protostellar encounters - I. Star-disc encounters. MNRAS, **300**, 1189–1204.

Bolatto, A.D. et al (2008). The Resolved Properties of Extragalactic Giant Molecular Clouds. ApJ, **686**, 948–965.

Bonnell, I.A. and Davies, M.B. (1998). Mass segregation in young stellar clusters. MNRAS, **295**, 691.

Bonnell, I.A., Clark, P. and Bate, M.R. (2008). Gravitational fragmentation and the formation of brown dwarfs in stellar clusters. MNRAS, **389**, 1556–1562.

Booth, R.A., Sijacki, D. and Clarke, C.J. (2015). Smoothed particle hydrodynamics simulations of gas and dust mixtures. MNRAS, **452**, 3932–3947.

Boss, A.P. (1997). Giant planet formation by gravitational instability. *Science*, **276**, 1836–1839.

Boss, A.P. (2002). Evolution of the Solar Nebula. V. Disk Instabilities with Varied Thermodynamics. ApJ, **576**, 462–472.

Brauer, F. et al (2007). Survival of the mm-cm size grain population observed in protoplanetary disks. A&A, **469**, 1169–1182.

Breslau, A. et al (2014). Sizes of protoplanetary discs after star-disc encounters. A&A, **565**, A130.

Bressert, E. et al (2010). The spatial distribution of star formation in the solar neighbourhood: do all stars form in dense clusters? MNRAS, **409**, L54–L58.

Brogi, M. et al (2012). The signature of orbital motion from the dayside of the planet τ Boötis b. Nature, **486**, 502–504.

Burkert, A. and Hartmann, L. (2004). Collapse and Fragmentation in Finite Sheets. ApJ, **616**, 288–300.

Busso, M. (2018). Short-lived radioactivities in the early solar system: A fossil record of our origins in stars. *European Physical Journal Plus*, **133**, 274.

Butt, Y. et al (2003). Cosmic Ray Acceleration by Stellar Associations? The Case of Cygnus OB2. *ArXiv Astrophysics e-prints*.

Caballero, J.A. (2008a). Spatial distribution of stars and brown dwarfs in σ Orionis. MNRAS, **383**, 375–382.

Caballero, J.A. (2008b). Stars and brown dwarfs in the σ Orionis cluster: the Mayrit catalogue. A&A, **478**, 667–674.

Cabrit, S. et al (2006). Tidal stripping and disk kinematics in the RW Aurigae system. A&A, **452**, 897–906.

Cameron, A.G.W. (1978). Physics of the primitive solar accretion disk. *Moon and Planets*, **18**, 5–40.

Cameron, A.G.W. et al (1995). Massive Supernovae, Orion Gamma Rays, and the Formation of the Solar System. ApJ, **447**, L53.

Cardelli, J.A., Clayton, G.C. and Mathis, J.S. (1989). The relationship between infrared, optical, and ultraviolet extinction. ApJ, **345**, 245–256.

Carrasco-González, C. et al (2010). A Magnetized Jet from a Massive Protostar. *Science*, **330**, 1209.

Castelli, F. and Kurucz, R.L. (2004). New Grids of ATLAS9 Model Atmospheres. *ArXiv Astrophysics e-prints*.

Chambers, J.E. (1999). A hybrid symplectic integrator that permits close encounters between massive bodies. MNRAS, **304**, 793–799.

Chambers, J.E. and Wetherill, G.W. (2001). Planets in the asteroid belt. *Meteoritics and Planetary Science*, **36**, 381–399.

Chandrasekhar, S. (1960). The Stability of Non-Dissipative Couette Flow in Hydromagnetics. *Proceedings of the National Academy of Science*, **46**, 253–257.

Charbonneau, D. et al (2002). Detection of an Extrasolar Planet Atmosphere. ApJ, **568**, 377–384.

Chiang, E. and Youdin, A.N. (2010). Forming Planetesimals in Solar and Extrasolar Nebulae. *Annual Review of Earth and Planetary Sciences*, **38**, 493–522.

Cieza, L.A. et al (2008). The Masses of Transition Circumstellar Disks: Observational Support for Photoevaporation Models. ApJ, **686**, L115.

Cieza, L.A. et al (2010). The Nature of Transition Circumstellar Disks. I. The Ophiuchus Molecular Cloud. ApJ, **712**, 925–941.

Cieza, L.A. et al (2018). The ALMA early science view of FUor/EXor objects - V. Continuum disc masses and sizes. MNRAS, **474**, 4347–4357.

Clark, J.S. et al (2005). On the massive stellar population of the super star cluster Westerlund 1. A&A, **434**, 949–969.

Clarke, C.J. (2007). The photoevaporation of discs around young stars in massive clusters. MNRAS, **376**, 1350–1356.

Clarke, C.J. and Pringle, J.E. (1993). Accretion disc response to a stellar fly-by. MNRAS, **261**, 190–202.

Clarke, C.J., Gendrin, A. and Sotomayor, M. (2001). The dispersal of circumstellar discs: the role of the ultraviolet switch. MNRAS, **328**, 485–491.

Clarke, C.J. et al (2018). High-resolution Millimeter Imaging of the CI Tau Protoplanetary Disk: A Massive Ensemble of Protoplanets from 0.1 to 100 au. ApJ, **866**, L6.

Clarkson, W.I. et al (2012). Proper Motions of the Arches Cluster with Keck Laser Guide Star Adaptive Optics: The First Kinematic Mass Measurement of the Arches. ApJ, **751**, 132.

Cleeves, L.I. et al (2016). The Coupled Physical Structure of Gas and Dust in the IM Lup Protoplanetary Disk. ApJ, **832**, 110.

Colín, P., Vázquez-Semadeni, E. and Gómez, G.C. (2013). Molecular cloud evolution - V. Cloud destruction by stellar feedback. MNRAS, **435**, 1701–1714.

Comerón, F. (2008). *The Lupus Clouds*, page 295. The Southern Sky ASP Monograph Publications.

Comerón, F. and Pasquali, A. (2012). New members of the massive stellar population in Cygnus. A&A, **543**, A101.

Contopoulos, J. and Lovelace, R.V.E. (1994). Magnetically driven jets and winds: Exact solutions. ApJ, **429**, 139–152.

Correia, S. et al (2013). Stellar and circumstellar properties of visual binaries in the Orion Nebula Cluster. A&A, **557**, A63.

Craig, J. and Krumholz, M.R. (2013). Close Stellar Encounters in Young, Substructured, Dissolving Star Clusters: Statistics and Effects on Planetary Systems. ApJ, **769**, 150.

Cuello, N. et al (2019). Flybys in protoplanetary discs: I. Gas and dust dynamics. MNRAS, **483**, 4114–4139.

Daemgen, S., Correia, S. and Petr-Gotzens, M.G. (2012). Protoplanetary disks of T Tauri binary systems in the Orion nebula cluster. A&A, **540**, A46.

Daemgen, S. et al (2013). Protoplanetary disk evolution and stellar parameters of T Tauri binaries in Chamaeleon I. A&A, **554**, A43.

Dai, F. et al (2015). A tidal encounter caught in the act: modelling a star-disc fly-by in the young RW Aurigae system. *MNRAS*, **449**, 1996–2009.

Dale, J.E. and Bonnell, I. (2011). Ionizing feedback from massive stars in massive clusters: fake bubbles and untriggered star formation. MNRAS, **414**, 321–328.

Dale, J.E. et al (2005). Photoionizing feedback in star cluster formation. MNRAS, **358**, 291–304.

Dale, J.E. et al (2014). Before the first supernova: combined effects of H II regions and winds on molecular clouds. MNRAS, **442**, 694–712.

de Gregorio-Monsalvo, I. et al (2013). Unveiling the gas-and-dust disk structure in HD 163296 using ALMA observations. A&A, **557**, A133.

de Juan Ovelar, M. et al (2012). Can habitable planets form in clustered environments? A&A, **546**, L1.

Dib, S., Bell, E. and Burkert, A. (2006). The Supernova Rate-Velocity Dispersion Relation in the Interstellar Medium. ApJ, **638**, 797–810.

Dolan, C.J. and Mathieu, R.D. (2001). The Spatial Distribution of the λ Orionis Pre-Main-Sequence Population. AJ, **121**, 2124–2147.

Draine, B.T., Roberge, W.G. and Dalgarno, A. (1983). Magnetohydrodynamic shock waves in molecular clouds. ApJ, **264**, 485–507.

Drążkowska, J. and Dullemond, C.P. (2014). Can dust coagulation trigger streaming instability? A&A, **572**, A78.

Drew, J.E. et al (2008). Early-A stars from IPHAS, and their distribution in and around the Cyg OB2 association. MNRAS, **386**, 1761–1773.

Duchêne, G. and Kraus, A. (2013). Stellar Multiplicity. *Annual Review of Astronomy and Astrophysics*, **51**, 269–310.

Duchêne, G. et al (2010). Panchromatic Observations and Modeling of the HV Tau C Edge-on Disk. *ApJ*, **712**, 112–129.

Durisen, R.H. et al (1986). Dynamic fission instabilities in rapidly rotating N = 3/2 polytropes - A comparison of results from finite-difference and smoothed particle hydrodynamics codes. ApJ, **305**, 281–308.

Duvert, G. et al (2000). A search for extended disks around weak-lined T Tauri stars. A&A, **355**, 165–170.

Dzyurkevich, N. et al (2013). Magnetized Accretion and Dead Zones in Protostellar Disks. ApJ, **765**, 114.

Efstathiou, G. (2000). A model of supernova feedback in galaxy formation. MNRAS, **317**, 697–719.

Eisner, J.A. et al (2018). Protoplanetary Disk Properties in the Orion Nebula Cluster: Initial Results from Deep, High-resolution ALMA Observations. ApJ, **860**, 77.

Elmegreen, B.G. (2002). Star Formation from Galaxies to Globules. ApJ, **577**, 206–220.

Elmegreen, B.G. (2007). On the Rapid Collapse and Evolution of Molecular Clouds. ApJ, **668**, 1064–1082.

Elmegreen, B.G. and Falgarone, E. (1996). A Fractal Origin for the Mass Spectrum of Interstellar Clouds. ApJ, **471**, 816.

Elson, R.A.W., Fall, S.M. and Freeman, K.C. (1987). The structure of young star clusters in the Large Magellanic Cloud. ApJ, **323**, 54–78.

Ercolano, B. and Clarke, C.J. (2010). Metallicity, planet formation and disc lifetimes. MNRAS, **402**, 2735–2743.

Ercolano, B. et al (2008). X-Ray-Irradiated Protoplanetary Disk Atmospheres. I. Predicted Emission-Line Spectrum and Photoevaporation. ApJ, **688**, 398–407.

Ercolano, B., Clarke, C.J. and Drake, J.J. (2009). X-Ray Irradiated Protoplanetary Disk Atmospheres. II. Predictions from Models in Hydrostatic Equilibrium. ApJ, **699**, 1639–1649.

Ercolano, B., Clarke, C.J. and Hall, A.C. (2011). The clearing of discs around late-type T Tauri stars: constraints from the infrared two-colour plane. MNRAS, **410**, 671–678.

Erickson, K.L. et al (2015). An Optical Spectroscopic Survey of the Serpens Main Cluster: Evidence for Two Populations? AJ, **149**, 103.

Evans, II, N.J. et al (2009). The Spitzer c2d Legacy Results: Star-Formation Rates and Efficiencies; Evolution and Lifetimes. ApJS, **181**, 321–350.

Facchini, S., Clarke, C.J. and Bisbas, T.G. (2016). External photoevaporation of protoplanetary discs in sparse stellar groups: the impact of dust growth. MNRAS, **457**, 3593–3610.

Fang, M. et al (2018). A New Look at T Tauri Star Forbidden Lines: MHD-driven Winds from the Inner Disk. ApJ, **868**, 28.

Fatuzzo, M. and Adams, F.C. (2008). UV Radiation Fields Produced by Young Embedded Star Clusters. ApJ, **675**, 1361–1374.

Fedele, D. et al (2018). ALMA continuum observations of the protoplanetary disk AS 209. Evidence of multiple gaps opened by a single planet. A&A, **610**, A24.

Federrath, C. et al (2010). Comparing the statistics of interstellar turbulence in simulations and observations. Solenoidal versus compressive turbulence forcing. A&A, **512**, A81.

Figer, D.F., McLean, I.S. and Morris, M. (1999). Massive Stars in the Quintuplet Cluster. ApJ, **514**, 202–220.

Flock, M. et al (2015). Gaps, rings, and non-axisymmetric structures in protoplanetary disks. From simulations to ALMA observations. A&A, **574**, A68.

Font, A.S. et al (2004). Photoevaporation of Circumstellar Disks around Young Stars. ApJ, **607**, 890–903.

Forgan, D. et al (2011). The nature of angular momentum transport in radiative self-gravitating protostellar discs. MNRAS, **410**, 994–1006.

Gaia Collaboration et al (2016). The Gaia mission. A&A, **595**, A1.

Gaia Collaboration et al (2018). Gaia Data Release 2. Summary of the contents and survey properties. *ArXiv e-prints*.

Gammie, C.F. (1996). Layered Accretion in T Tauri Disks. ApJ, **457**, 355.

Gammie, C.F. (2001). Nonlinear Outcome of Gravitational Instability in Cooling, Gaseous Disks. ApJ, **553**, 174–183.

Gandolfi, D. et al (2018). TESS's first planet. A super-Earth transiting the naked-eye star π Mensae. A&A, **619**, L10.

Getman, K.V., Feigelson, E.D. and Kuhn, M.A. (2014). Core-Halo Age Gradients and Star Formation in the Orion Nebula and NGC 2024 Young Stellar Clusters. ApJ, **787**, 109.

Gieles, M. et al (2006). Observational evidence for a truncation of the star cluster initial mass function at the high mass end. A&A, **446**, L9–L12.

Gieles, M., Sana, H. and Portegies Zwart, S.F. (2010). On the velocity dispersion of young star clusters: super-virial or binaries? MNRAS, **402**, 1750–1757.

Gillon, M. et al (2017). Seven temperate terrestrial planets around the nearby ultracool dwarf star TRAPPIST-1. Nature, **542**, 456–460.

Ginsburg, A. et al (2018). Distributed Star Formation throughout the Galactic Center Cloud Sgr B2. ApJ, **853**, 171.

Goldreich, P. and Tremaine, S. (1978). The excitation and evolution of density waves. ApJ, **222**, 850–858.

Goldreich, P. and Tremaine, S. (1979). The excitation of density waves at the Lindblad and corotation resonances by an external potential. ApJ, **233**, 857–871.

Goldreich, P. and Ward, W.R. (1973). The Formation of Planetesimals. ApJ, **183**, 1051–1062.

Gonzalez, J.F., Laibe, G. and Maddison, S.T. (2017). Self-induced dust traps: overcoming planet formation barriers. MNRAS, **467**, 1984–1996.

Goodwin, S.P. (2009). The effect of the dynamical state of clusters on gas expulsion and infant mortality. Ap&SS, **324**, 259–263.

Goodwin, S.P. and Whitworth, A.P. (2004). The dynamical evolution of fractal star clusters: The survival of substructure. A&A, **413**, 929–937.

Gorti, U. and Hollenbach, D. (2009). Photoevaporation of Circumstellar Disks By Far-Ultraviolet, Extreme-Ultraviolet and X-Ray Radiation from the Central Star. ApJ, **690**, 1539–1552.

Gorti, U., Dullemond, C.P. and Hollenbach, D. (2009). Time Evolution of Viscous Circumstellar Disks due to Photoevaporation by Far-Ultraviolet, Extreme-Ultraviolet, and X-ray Radiation from the Central Star. ApJ, **705**, 1237–1251.

Gorti, U., Hollenbach, D. and Dullemond, C.P. (2015). The Impact of Dust Evolution and Photoevaporation on Disk Dispersal. ApJ, **804**, 29.

Grazier, K.R. (2016). Jupiter: Cosmic Jekyll and Hyde. *Astrobiology*, **16**, 23–38.

Gressel, O. et al (2015). Global Simulations of Protoplanetary Disks With Ohmic Resistivity and Ambipolar Diffusion. ApJ, **801**, 84.

Guarcello, M.G. et al (2007). Correlation between the spatial distribution of circumstellar disks and massive stars in the open cluster NGC 6611. Compiled catalog and cluster parameters. A&A, **462**, 245–255.

Guarcello, M.G. et al (2012). Optical Photometric GTC/OSIRIS Observations of the Young Massive Association Cygnus OB2. ApJS, **202**, 19.

Guarcello, M.G. et al (2013). The Protoplanetary Disks in the Nearby Massive Star-forming Region Cygnus OB2. ApJ, **773**, 135.

Guarcello, M.G. et al (2016). Photoevaporation and close encounters: how the environment around Cygnus OB2 affects the evolution of protoplanetary disks. *ArXiv e-prints*.

Guesten, R. and Henkel, C. (1983). H2 densities and masses of the molecular clouds close to the galactic center. A&A, **125**, 136–145.

Guilloteau, S. et al (2011). A dual-frequency sub-arcsecond study of proto-planetary disks at mm wavelengths: first evidence for radial variations of the dust properties. A&A, **529**, A105.

Guszejnov, D., Hopkins, P.F. and Grudić, M.Y. (2018). Universal scaling relations in scale-free structure formation. MNRAS, **477**, 5139–5149.

Habing, H.J. (1968). The interstellar radiation density between 912 A and 2400 A. Bull. Astron. Inst. Netherlands, **19**, 421.

Haisch, Jr., K.E., Lada, E.A. and Lada, C.J. (2000). A Near-Infrared L-Band Survey of the Young Embedded Cluster NGC 2024. AJ, **120**, 1396–1409.

Haisch, Jr., K.E. et al (2001a). A Mid-Infrared Study of the Young Stellar Population in the NGC 2024 Cluster. AJ, **121**, 1512–1521.

Haisch, Jr., K.E., Lada, E.A. and Lada, C.J. (2001b). Disk Frequencies and Lifetimes in Young Clusters. ApJ, **553**, L153–L156.

Hall, S.M., Clarke, C.J. and Pringle, J.E. (1996). Energetics of star-disc encounters in the non-linear regime. MNRAS, **278**, 303–320.

Hanson, M.M. (2003). A Study of Cygnus OB2: Pointing the Way toward Finding Our Galaxy's Super-Star Clusters. ApJ, **597**, 957–969.

Hartigan, P., Edwards, S. and Ghandour, L. (1995). Disk Accretion and Mass Loss from Young Stars. *ApJ*, **452**, 736.

Hartmann, L. et al (1998). Accretion and the Evolution of T Tauri Disks. ApJ, **495**, 385–400.

Harvey, P. et al (2007). The Spitzer c2d Survey of Large, Nearby, Interstellar Clouds. IX. The Serpens YSO Population as Observed with IRAC and MIPS. ApJ, **663**, 1149–1173.

Hasegawa, Y. et al (2017). Magnetically Induced Disk Winds and Transport in the HL Tau Disk. ApJ, **845**, 31.

Haworth, T.J. et al (2017). First evidence of external disc photoevaporation in a low mass star forming region: the case of IM Lup. MNRAS, **468**, L108–L112.

Haworth, T.J. et al (2018a). The FRIED grid of mass-loss rates for externally irradiated protoplanetary discs. MNRAS, **481**, 452–466.

Haworth, T.J. et al (2018b). Where can a Trappist-1 planetary system be produced? MNRAS.

Heggie, D.C. and Hut, P. (1993). Binary-single-star scattering. IV - Analytic approximations and fitting formulae for cross sections and reaction rates. ApJS, **85**, 347–409.

Heggie, D.C. and Rasio, F.A. (1996). The Effect of Encounters on the Eccentricity of Binaries in Clusters. MNRAS, **282**, 1064–1084.

Henshaw, J.D. et al (2016). Molecular gas kinematics within the central 250 pc of the Milky Way. MNRAS, **457**, 2675–2702.

Herbig, G.H. (1977). Eruptive phenomena in early stellar evolution. ApJ, **217**, 693–715.

Herbst, W. et al (1994). Catalogue of UBVRI photometry of T Tauri stars and analysis of the causes of their variability. AJ, **108**, 1906–1923.

Hernández, J. et al (2010). Spitzer Observations of the λ Orionis Cluster. II. Disks Around Solar-type and Low-mass Stars. ApJ, **722**, 1226–1239.

Hildebrand, R.H. (1983). The Determination of Cloud Masses and Dust Characteristics from Submillimetre Thermal Emission. *QJRAS*, **24**, 267.

Hill, T. et al (2012). The M 16 molecular complex under the influence of NGC 6611. Herschel's perspective of the heating effect on the Eagle Nebula. A&A, **542**, A114.

Hillenbrand, L.A. and Hartmann, L.W. (1998). A Preliminary Study of the Orion Nebula Cluster Structure and Dynamics. ApJ, **492**, 540–553.

Hirota, A. et al (2018). ALMA ^{12}CO (J = 1-0) imaging of the nearby galaxy M 83: Variations in the efficiency of star formation in giant molecular clouds. PASJ, **70**, 73.

Hollenbach, D. et al (1994). Photoevaporation of disks around massive stars and application to ultracompact H II regions. ApJ, **428**, 654–669.

Hollenbach, D.J. and Tielens, A.G.G.M. (1997). Dense Photodissociation Regions (PDRs). ARA&A, **35**, 179–216.

Horner, J. and Jones, B.W. (2012). Jupiter - friend or foe? IV: the influence of orbital eccentricity and inclination. *International Journal of Astrobiology*, **11**, 147–156.

Howard, C.D. et al (2013). Herschel/PACS Survey of Protoplanetary Disks in Taurus/Auriga - Observations of [O I] and [C II], and Far-infrared Continuum. *ApJ*, **776**, 21.

Hubber, D.A., Rosotti, G.P. and Booth, R.A. (2018). GANDALF - Graphical Astrophysics code for N-body Dynamics And Lagrangian Fluids. MNRAS, **473**, 1603–1632.

Jackson, J.D. (1975). *Classical electrodynamics*. Wiley.

Ji, H. et al (2006). Hydrodynamic turbulence cannot transport angular momentum effectively in astrophysical disks. Nature, **444**, 343–346.

Johansen, A. and Lacerda, P. (2010). Prograde rotation of protoplanets by accretion of pebbles in a gaseous environment. MNRAS, **404**, 475–485.

Johns-Krull, C.M. et al (2016). A Candidate Young Massive Planet in Orbit around the Classical T Tauri Star CI Tau. ApJ, **826**, 206.

Johnstone, D., Hollenbach, D. and Bally, J. (1998). Photoevaporation of Disks and Clumps by Nearby Massive Stars: Application to Disk Destruction in the Orion Nebula. ApJ, **499**, 758–776.

Jones, M.G., Pringle, J.E. and Alexander, R.D. (2012). The relationship between accretion disc age and stellar age and its consequences for protostellar discs. MNRAS, **419**, 925–935.

Kanagawa, K.D., Tanaka, H. and Szuszkiewicz, E. (2018). Radial Migration of Gap-opening Planets in Protoplanetary Disks. I. The Case of a Single Planet. ApJ, **861**, 140.

Kaufman, M.J. et al (1999). Far-Infrared and Submillimeter Emission from Galactic and Extragalactic Photodissociation Regions. ApJ, **527**, 795–813.

Kelly, B.C. (2007). Some Aspects of Measurement Error in Linear Regression of Astronomical Data. ApJ, **665**, 1489–1506.

Kennicutt, Jr., R.C. (1989). The star formation law in galactic disks. ApJ, **344**, 685–703.

Kenyon, S.J. and Hartmann, L. (1987). Spectral energy distributions of T Tauri stars - Disk flaring and limits on accretion. ApJ, **323**, 714–733.

Kenyon, S.J. and Hartmann, L. (1995). Pre-Main-Sequence Evolution in the Taurus-Auriga Molecular Cloud. ApJS, **101**, 117.

Kim, J.S. et al (2016). Proplyds Around a B1 Star: 42 Orionis in NGC 1977. ApJ, **826**, L15.

Kiminki, D.C. et al (2007). A Radial Velocity Survey of the Cyg OB2 Association. ApJ, **664**, 1102–1120.

Kiminki, D.C. et al (2008). Erratum: "A Radial Velocity Survey of the Cygnus OB2 Association" (ApJ, 664, 1102 [2007]). ApJ, **681**, 735.

Kiminki, D.C. et al (2015). Predicting GAIA's Parallax Distance to the Cygnus OB2 Association with Eclipsing Binaries. ApJ, **811**, 85.

Klessen, R.S. (2000). One-Point Probability Distribution Functions of Supersonic Turbulent Flows in Self-gravitating Media. ApJ, **535**, 869–886.

Knödlseder, J. (2000). Cygnus OB2 - a young globular cluster in the Milky Way. A&A, **360**, 539–548.

Koepferl, C.M. et al (2013). Disc clearing of young stellar objects: evidence for fast inside-out dispersal. MNRAS, **428**, 3327–3354.

Konigl, A. (1982). On the nature of bipolar sources in dense molecular clouds. ApJ, **261**, 115–134.

Krall, N.A. and Trivelpiece, A.W. (1973). *Principles of plasma physics*.

Kraus, A.L. and Hillenbrand, L.A. (2008). Spatial Distributions of Young Stars. *ApJL*, **686**, L111.

Kraus, S. et al (2009). Tracing the young massive high-eccentricity binary system θ^1Orionis C through periastron passage. A&A, **497**, 195–207.

Kroupa, P. (2001). On the variation of the initial mass function. MNRAS, **322**, 231–246.

Kroupa, P., Tout, C.A. and Gilmore, G. (1993). The distribution of low-mass stars in the Galactic disc. MNRAS, **262**, 545–587.

Kroupa, P. et al (2018). Evidence for feedback and stellar-dynamically regulated bursty star cluster formation: the case of the Orion Nebula Cluster. A&A, **612**, A74.

Kruijssen, J.M.D. (2012). On the fraction of star formation occurring in bound stellar clusters. MNRAS, **426**, 3008–3040.

Kruijssen, J.M.D. (2015). Globular clusters as the relics of regular star formation in 'normal' high-redshift galaxies. MNRAS, **454**, 1658–1686.

Kruijssen, J.M.D. et al (2014). What controls star formation in the central 500 pc of the Galaxy? MNRAS, **440**, 3370–3391.

Krumholz, M.R. (2014). The big problems in star formation: The star formation rate, stellar clustering, and the initial mass function. Phys. Rep., **539**, 49–134.

Krumholz, M.R. and McKee, C.F. (2005). A General Theory of Turbulence-regulated Star Formation, from Spirals to Ultraluminous Infrared Galaxies. ApJ, **630**, 250–268.

Kudoh, T. and Shibata, K. (1997). Magnetically Driven Jets from Accretion Disks. I. Steady Solutions and Application to Jets/Winds in Young Stellar Objects. ApJ, **474**, 362–377.

Kuiper, G.P. (1951). On the Origin of the Solar System. *Proceedings of the National Academy of Science*, **37**, 1–14.

Kurtovic, N.T. et al (2018). The Disk Substructures at High Angular Resolution Project (DSHARP). IV. Characterizing Substructures and Interactions in Disks around Multiple Star Systems. ApJ, **869**, L44.

Kutner, M.L., Evans, II, N.J. and Tucker, K.D. (1976). A dense molecular cloud in the OMC-1/OMC-2 region. ApJ, **209**, 452–457.

Kuznetsova, A., Hartmann, L. and Ballesteros-Paredes, J. (2018). Kinematics and structure of star-forming regions: insights from cold collapse models. MNRAS, **473**, 2372–2377.

Kwon, W. et al (2015). Resolving Protoplanetary Disks at Millimeter Wavelengths with CARMA. *ApJ*, **808**, 102.

Lada, C.J. and Kylafis, N.D., editors (1999). *The Origin of Stars and Planetary Systems*, volume 540 of *NATO Advanced Science Institutes (ASI) Series C*.

Lada, C.J. and Lada, E.A. (2003). Embedded Clusters in Molecular Clouds. ARA&A, **41**, 57–115.

Larson, R.B. (1995). Star formation in groups. *MNRAS*, **272**, 213–220.

Law, C.J. et al (2017). An SMA Continuum Survey of Circumstellar Disks in the Serpens Star-forming Region. AJ, **154**, 255.

Lee, D., Seon, K.I. and Jo, Y.S. (2015). Is The Dust Cloud around Lambda Orionis a Ring or a Shell, or Both? ApJ, **806**, 274.

Lenorzer, A. et al (2004). The peculiar circumstellar environment of NGC 2024 IRS2. A&A, **414**, 245–259.

Lepp, S. and McCray, R. (1983). X-ray sources in molecular clouds. ApJ, **269**, 560–567.

Lestrade, J.F. et al (2011). Stripping a debris disk by close stellar encounters in an open stellar cluster. A&A, **532**, A120.

Levine, J.L. et al (2006). Low-Mass Stars and Brown Dwarfs in NGC 2024: Constraints on the Substellar Mass Function. ApJ, **646**, 1215–1229.

Levison, H.F., Thommes, E. and Duncan, M.J. (2010). Modeling the Formation of Giant Planet Cores. I. Evaluating Key Processes. AJ, **139**, 1297–1314.

Li, Z.Y. and Nakamura, F. (2004). Magnetically Regulated Star Formation in Turbulent Clouds. ApJ, **609**, L83–L86.

Li, Z.Y., Chiueh, T. and Begelman, M.C. (1992). Electromagnetically driven relativistic jets - A class of self-similar solutions. ApJ, **394**, 459–471.

Liffman, K. (2003). The Gravitational Radius of an Irradiated Disk. PASA, **20**, 337–339.

Lin, D.N.C. and Papaloizou, J. (1979). On the structure of circumbinary accretion disks and the tidal evolution of commensurable satellites. MNRAS, **188**, 191–201.

Lindegren, L. et al (2018). Gaia Data Release 2: The astrometric solution. *ArXiv e-prints*.

Lissauer, J.J. (1987). Timescales for planetary accretion and the structure of the protoplanetary disk. Icarus, **69**, 249–265.

Longmore, S.N. et al (2013). Variations in the Galactic star formation rate and density thresholds for star formation. MNRAS, **429**, 987–1000.

Longmore, S.N. et al (2014). The Formation and Early Evolution of Young Massive Clusters. *Protostars and Planets VI*, pages 291–314.

Lovelace, R.V.E. et al (1999). Rossby Wave Instability of Keplerian Accretion Disks. ApJ, **513**, 805–810.

Lubow, S.H. (1981). Vertically driven resonances in accretion disks. ApJ, **245**, 274–285.

Lynden-Bell, D. and Kalnajs, A.J. (1972). On the generating mechanism of spiral structure. MNRAS, **157**, 1.

Lynden-Bell, D. and Pringle, J.E. (1974). The evolution of viscous discs and the origin of the nebular variables. MNRAS, **168**, 603–637.

Mac Low, M.M. and Ferrara, A. (1999). Starburst-driven Mass Loss from Dwarf Galaxies: Efficiency and Metal Ejection. ApJ, **513**, 142–155.

Maddalena, R.J. and Morris, M. (1987). An expanding system of molecular clouds surrounding Lambda Orionis. ApJ, **323**, 179–192.

Makino, J. and Aarseth, S.J. (1992). On a Hermite integrator with Ahmad-Cohen scheme for gravitational many-body problems. *PASJ*, **44**, 141–151.

Manara, C.F. et al (2016). Evidence for a correlation between mass accretion rates onto young stars and the mass of their protoplanetary disks. A&A, **591**, L3.

Mann, R.K. et al (2015). Protoplanetary Disk Masses in the Young NGC 2024 Cluster. ApJ, **802**, 77.

Martin, C.L. and Kennicutt, Jr., R.C. (2001). Star Formation Thresholds in Galactic Disks. ApJ, **555**, 301–321.

Maschberger, T. and Clarke, C.J. (2008). Maximum stellar mass versus cluster membership number revisited. MNRAS, **391**, 711–717.

Massey, P. and Thompson, A.B. (1991). Massive stars in CYG OB2. AJ, **101**, 1408–1428.

Massey, P., Johnson, K.E. and Degioia-Eastwood, K. (1995). The Initial Mass Function and Massive Star Evolution in the OB Associations of the Northern Milky Way. ApJ, **454**, 151.

Matzner, C.D. (2002). On the Role of Massive Stars in the Support and Destruction of Giant Molecular Clouds. ApJ, **566**, 302–314.

Matzner, C.D. and McKee, C.F. (2000). Efficiencies of Low-Mass Star and Star Cluster Formation. ApJ, **545**, 364–378.

Maucó, K. et al (2016). A Herschel View of Protoplanetary Disks in the σ Ori Cluster. ApJ, **829**, 38.

Mayne, N.J. and Naylor, T. (2008). Fitting the young main-sequence: distances, ages and age spreads. MNRAS, **386**, 261–277.

McCullough, P.R. et al (1995). Photoevaporating stellar envelopes observed with Rayleigh beacon adaptive optics. ApJ, **438**, 394–403.

McKee, C.F. and Ostriker, E.C. (2007). Theory of Star Formation. ARA&A, **45**, 565–687.

Mengel, S. and Tacconi-Garman, L.E. (2007). Medium resolution 2.3 μm spectroscopy of the massive Galactic open cluster Westerlund 1. A&A, **466**, 151–155.

Merín, B. et al (2008). The Spitzer c2d Survey of Large, Nearby, Interstellar Clouds. XI. Lupus Observed with IRAC and MIPS. ApJS, **177**, 551–583.

Meru, F. et al (2017). On the Origin of the Spiral Morphology in the Elias 2-27 Circumstellar Disk. ApJ, **839**, L24.

Meyer, M.R. (1996). *Stellar Populations of Deeply Embedded Young Clusters: Near–Infrared Spectroscopy and Emergent Mass Distributions*. Ph.D. thesis.

Mohanty, S., Ercolano, B. and Turner, N.J. (2013). Dead, Undead, and Zombie Zones in Protostellar Disks as a Function of Stellar Mass. ApJ, **764**, 65.

Molinari, S. et al (2010). Clouds, filaments, and protostars: The Herschel Hi-GAL Milky Way. A&A, **518**, L100.

Molinari, S. et al (2011). A 100 pc Elliptical and Twisted Ring of Cold and Dense Molecular Clouds Revealed by Herschel Around the Galactic Center. ApJ, **735**, L33.

Molinari, S. et al (2014). The Milky Way as a Star Formation Engine. *Protostars and Planets VI*, pages 125–148.

Monaghan, J.J. (1997). SPH and Riemann Solvers. *Journal of Computational Physics*, **136**, 298–307.

Monin, J.L. and Bouvier, J. (2000). Disks in multiple systems: direct imaging of a nearly edge-on circumstellar disk in the young triple system HV Tau. *AAP*, **356**, L75–L78.

Moran, P.A.P. (1950). Notes on continuous stochastic phenomena. *Biometrika*, **37**(1/2), 17–23.

Morris, J.P. and Monaghan, J.J. (1997). A Switch to Reduce SPH Viscosity. *Journal of Computational Physics*, **136**, 41–50.

Muñoz, D.J. et al (2015). Stellar orbit evolution in close circumstellar disc encounters. *MNRAS*, **446**, 2010–2029.

Nakajima, Y. et al (2000). A Near-Infrared Imaging Survey of the Lupus 3 Dark Cloud: A Modest Cluster of Low-Mass, Pre-Main-Sequence Stars. AJ, **119**, 873–881.

Nakatani, R. et al (2018a). Radiation Hydrodynamics Simulations of Photoevaporation of Protoplanetary Disks by Ultraviolet Radiation: Metallicity Dependence. ApJ, **857**, 57.

Nakatani, R. et al (2018b). Radiation Hydrodynamics Simulations of Photoevaporation of Protoplanetary Disks. II. Metallicity Dependence of UV and X-Ray Photoevaporation. ApJ, **865**, 75.

Nguyen, D.C. et al (2012). Close Companions to Young Stars. I. A Large Spectroscopic Survey in Chamaeleon I and Taurus-Auriga. ApJ, **745**, 119.

Nordlund, Å.K. and Padoan, P. (1999). The Density PDFs of Supersonic Random Flows. In J. Franco and A. Carraminana, editors, *Interstellar Turbulence*, page 218.

Nortmann, L. et al (2018). Ground-based detection of an extended helium atmosphere in the Saturn-mass exoplanet WASP-69b. *Science*, **362**, 1388–1391.

O'Brien, D.P. et al (2018). The Delivery of Water During Terrestrial Planet Formation. Space Sci. Rev., **214**, 47.

O'Dell, C.R. and Wen, Z. (1994). Postrefurbishment mission Hubble Space Telescope images of the core of the Orion Nebula: Proplyds, Herbig-Haro objects, and measurements of a circumstellar disk. ApJ, **436**, 194–202.

O'Dell, C.R., Wen, Z. and Hu, X. (1993). Discovery of new objects in the Orion nebula on HST images - Shocks, compact sources, and protoplanetary disks. ApJ, **410**, 696–700.

Offner, S.S.R., Hansen, C.E. and Krumholz, M.R. (2009). Stellar Kinematics of Young Clusters in Turbulent Hydrodynamic Simulations. ApJ, **704**, L124–L128.

Ogilvie, G.I. (2002). A non-linear theory of vertical resonances in accretion discs. MNRAS, **331**, 1053–1064.

Olczak, C., Pfalzner, S. and Spurzem, R. (2006). Encounter-triggered Disk Mass Loss in the Orion Nebula Cluster. ApJ, **642**, 1140–1151.

Ormel, C.W. and Klahr, H.H. (2010). The effect of gas drag on the growth of protoplanets. Analytical expressions for the accretion of small bodies in laminar disks. A&A, **520**, A43.

Osterbrock, D.E. (1961). On Ambipolar Diffusion in H I Regions. ApJ, **134**, 270–272.

Osterbrock, D.E. (1989). *Astrophysics of gaseous nebulae and active galactic nuclei*.

Ostriker, E.C. (1994). Capture and induced disk accretion in young star encounters. ApJ, **424**, 292–318.

Ostriker, E.C., Shu, F.H. and Adams, F.C. (1992). Near-resonant excitation and propagation of eccentric density waves by external forcing. ApJ, **399**, 192–212.

Ostriker, E.C., Stone, J.M. and Gammie, C.F. (2001). Density, Velocity, and Magnetic Field Structure in Turbulent Molecular Cloud Models. ApJ, **546**, 980–1005.

Owen, J.E. et al (2010). Radiation-hydrodynamic models of X-ray and EUV photoevaporating protoplanetary discs. MNRAS, **401**, 1415–1428.

Paczynski, B. (1977). A model of accretion disks in close binaries. ApJ, **216**, 822–826.

Padoan, P. and Nordlund, Å. (2002). The Stellar Initial Mass Function from Turbulent Fragmentation. ApJ, **576**, 870–879.

Padoan, P. and Nordlund, Å. (2011). The Star Formation Rate of Supersonic Magnetohydrodynamic Turbulence. ApJ, **730**, 40.

Padoan, P., Nordlund, A. and Jones, B.J.T. (1997). The universality of the stellar initial mass function. MNRAS, **288**, 145–152.

Papaloizou, J. and Pringle, J.E. (1977). Tidal torques on accretion discs in close binary systems. MNRAS, **181**, 441–454.

Pascucci, I. et al (2016). A Steeper than Linear Disk Mass-Stellar Mass Scaling Relation. ApJ, **831**, 125.

Pascucci, I. et al (2018). Disk Winds and the Evolution of Planet-Forming Disks. In E. Murphy, editor, *Science with a Next Generation Very Large Array*, volume 517 of *Astronomical Society of the Pacific Conference Series*, page 155.

Passot, T. and Vázquez-Semadeni, E. (1998). Density probability distribution in one-dimensional polytropic gas dynamics. Phys. Rev. E, **58**, 4501–4510.

Pelupessy, F.I. and Portegies Zwart, S. (2012). The evolution of embedded star clusters. MNRAS, **420**, 1503–1517.

Pérez, L.M. et al (2018). The Disk Substructures at High Angular Resolution Project (DSHARP). X. Multiple Rings, a Misaligned Inner Disk, and a Bright Arc in the Disk around the T Tauri star HD 143006. ApJ, **869**, L50.

Peterson, D.E. and Megeath, S.T. (2008). *The Orion Molecular Cloud 2/3 and NGC 1977 Regions*, page 590.

Pfalzner, S. and Kaczmarek, T. (2013). The expansion of massive young star clusters - observation meets theory. A&A, **559**, A38.

Pfalzner, S., Umbreit, S. and Henning, T. (2005a). Disk-Disk Encounters between Low-Mass Protoplanetary Accretion Disks. ApJ, **629**, 526–534.

Pfalzner, S. et al (2005b). Parameter study of star-disc encounters. A&A, **437**, 967–976.

Pfalzner, S., Olczak, C. and Eckart, A. (2006). The fate of discs around massive stars in young clusters. A&A, **454**, 811–814.

Piétu, V., Dutrey, A. and Guilloteau, S. (2007). Probing the structure of protoplanetary disks: a comparative study of DM Tau, LkCa 15, and MWC 480. *A&A*, **467**, 163–178.

Pollack, J.B. et al (1996). Formation of the Giant Planets by Concurrent Accretion of Solids and Gas. Icarus, **124**, 62–85.

Pols, S. et al (2018). The physical and chemical structure of Sagittarius B2. III. Radiative transfer simulations of the hot core Sgr B2(M) for methyl cyanide. A&A, **614**, A123.

Portegies Zwart, S.F., McMillan, S.L.W. and Gieles, M. (2010). Young Massive Star Clusters. ARA&A, **48**, 431–493.

Predehl, P. and Schmitt, J.H.M.M. (1995). X-raying the interstellar medium: ROSAT observations of dust scattering halos. A&A, **293**, 889–905.

Preibisch, T. and Zinnecker, H. (1999). The History of Low-Mass Star Formation in the Upper Scorpius OB Association. AJ, **117**, 2381–2397.

Preibisch, T. et al (2002). Exploring the Full Stellar Population of the Upper Scorpius OB Association. AJ, **124**, 404–416.

Press, W.H. and Teukolsky, S.A. (1977). On formation of close binaries by two-body tidal capture. ApJ, **213**, 183–192.

Pringle, J.E. (1981). Accretion discs in astrophysics. ARA&A, **19**, 137–162.

Pudritz, R.E. and Norman, C.A. (1983). Centrifugally driven winds from contracting molecular disks. ApJ, **274**, 677–697.

Raghavan, D. et al (2010). A Survey of Stellar Families: Multiplicity of Solar-type Stars. *The Astrophysical Journal Supplement Series*, **190**, 1–42.

Reina-Campos, M. and Kruijssen, J.M.D. (2017). A unified model for the maximum mass scales of molecular clouds, stellar clusters and high-redshift clumps. MNRAS, **469**, 1282–1298.

Ribas, Á. et al (2014). Disk evolution in the solar neighborhood. I. Disk frequencies from 1 to 100 Myr. A&A, **561**, A54.

Ricker, G.R. et al (2015). Transiting Exoplanet Survey Satellite (TESS). *Journal of Astronomical Telescopes, Instruments, and Systems*, **1**(1), 014003.

Rivera, J.L. et al (2015). Internal and Relative Motions of the Taurus and Ophiuchus Star-forming Regions. ApJ, **807**, 119.

Rochau, B. et al (2010). Internal Dynamics and Membership of the NGC 3603 Young Cluster from Microarcsecond Astrometry. ApJ, **716**, L90–L94.

Rosolowsky, E. and Blitz, L. (2005). Giant Molecular Clouds in M64. ApJ, **623**, 826–845.

Rosotti, G.P. et al (2014). Protoplanetary disc evolution affected by star-disc interactions in young stellar clusters. MNRAS, **441**, 2094–2110.

Rosotti, G.P. et al (2017). Constraining protoplanetary disc evolution using accretion rate and disc mass measurements: the usefulness of the dimensionless accretion parameter. MNRAS, **468**, 1631–1638.

Rosotti, G.P. et al (2018). Erratum: Protoplanetary disc evolution affected by star-disc interactions in young stellar clusters. MNRAS, **473**, 3223–3225.

Rosswog, S. (2015). Boosting the accuracy of SPH techniques: Newtonian and special-relativistic tests. MNRAS, **448**, 3628–3664.

Ruden, S.P. (2004). Evolution of Photoevaporating Protoplanetary Disks. ApJ, **605**, 880–891.

Safronov, V.S. (1960). On the gravitational instability in flattened systems with axial symmetry and non-uniform rotation. *Annales d'Astrophysique*, **23**, 979.

Safronov, V.S. and Zvjagina, E.V. (1969). Relative Sizes of the Largest Bodies during the Accumulation of Planets. Icarus, **10**, 109–115.

Salpeter, E.E. (1955). The Luminosity Function and Stellar Evolution. ApJ, **121**, 161.

Sauty, C. and Tsinganos, K. (1994). Nonradial and nonpolytropic astrophysical outflows III. A criterion for the transition from jets to winds. A&A, **287**, 893–926.

Scally, A. and Clarke, C. (2001). Destruction of protoplanetary discs in the Orion Nebula Cluster. MNRAS, **325**, 449–456.

Scally, A. and Clarke, C. (2002). Primordial substructure in the Orion Nebula Cluster. MNRAS, **334**, 156–166.

Schaefer, G.H. et al (2016). Orbits, Distance, and Stellar Masses of the Massive Triple Star σ Orionis. AJ, **152**, 213.

Schaller, G. et al (1992). New grids of stellar models from 0.8 to 120 solar masses at Z = 0.020 and Z = 0.001. A&AS, **96**, 269–331.

Schechter, P. (1976). An analytic expression for the luminosity function for galaxies. ApJ, **203**, 297–306.

Schlafly, E.F. et al (2014). A Large Catalog of Accurate Distances to Molecular Clouds from PS1 Photometry. ApJ, **786**, 29.

Schneider, N. et al (2006). A new view of the Cygnus X region. KOSMA ^{13}CO 2 to 1, 3 to 2, and ^{12}CO 3 to 2 imaging. A&A, **458**, 855–871.

Sedaghati, E. et al (2017). Detection of titanium oxide in the atmosphere of a hot Jupiter. Nature, **549**, 238–241.

Shakura, N.I. and Sunyaev, R.A. (1973). Black holes in binary systems. Observational appearance. A&A, **24**, 337–355.

Sherry, W.H. et al (2008). Main-Sequence Fitting Distance to the σ Ori Cluster. AJ, **135**, 1616–1623.

Shu, F. et al (1994). Magnetocentrifugally driven flows from young stars and disks. 1: A generalized model. ApJ, **429**, 781–796.

Shu, F.H., Adams, F.C. and Lizano, S. (1987). Star formation in molecular clouds - Observation and theory. ARA&A, **25**, 23–81.

Silk, J. (1997). Feedback, Disk Self-Regulation, and Galaxy Formation. ApJ, **481**, 703–709.

Simon, M., Holfeltz, S.T. and Taff, L.G. (1996). Measurement of T Tauri Binaries Using the Hubble Space Telescope Fine Guidance Sensors. *ApJ*, **469**, 890.

Skrutskie, M.F. et al (1990). A sensitive 10-micron search for emission arising from circumstellar dust associated with solar-type pre-main-sequence stars. AJ, **99**, 1187–1195.

Snellen, I.A.G. et al (2010). The orbital motion, absolute mass and high-altitude winds of exoplanet HD209458b. Nature, **465**, 1049–1051.

Solomon, P.M. et al (1987). Mass, luminosity, and line width relations of Galactic molecular clouds. ApJ, **319**, 730–741.

Spitzer, L. (1962). *Physics of Fully Ionized Gases*.

Spurzem, R. (1999). Direct N-body Simulations. *Journal of Computational and Applied Mathematics*, **109**, 407–432.

Squire, J. and Hopkins, P.F. (2018). Resonant drag instabilities in protoplanetary discs: the streaming instability and new, faster growing instabilities. MNRAS, **477**, 5011–5040.

Stamatellos, D., Whitworth, A.P. and Hubber, D.A. (2011). The Importance of Episodic Accretion for Low-mass Star Formation. ApJ, **730**, 32.

Stamatellos, D., Whitworth, A.P. and Hubber, D.A. (2012). Episodic accretion, protostellar radiative feedback, and their role in low-mass star formation. MNRAS, **427**, 1182–1193.

Stapelfeldt, K.R. et al (2003). Hubble Space Telescope WFPC2 Imaging of the Disk and Jet of HV Tauri C. *ApJ*, **589**, 410–418.

Stolte, A. et al (2010). Disks in the Arches Cluster–Survival in a Starburst Environment. ApJ, **718**, 810–831.

Stolte, A. et al (2015). Circumstellar discs in Galactic centre clusters: Disc-bearing B-type stars in the Quintuplet and Arches clusters. A&A, **578**, A4.

Störzer, H. and Hollenbach, D. (1999). Photodissociation Region Models of Photoevaporating Circumstellar Disks and Application to the Proplyds in Orion. ApJ, **515**, 669–684.

Strömgren, B. (1939). The Physical State of Interstellar Hydrogen. ApJ, **89**, 526.

Takeuchi, T., Clarke, C.J. and Lin, D.N.C. (2005). The Differential Lifetimes of Protostellar Gas and Dust Disks. ApJ, **627**, 286–292.

Tazzari, M. et al (2017). Physical properties of dusty protoplanetary disks in Lupus: evidence for viscous evolution? A&A, **606**, A88.

Testi, L. et al (2003). Large grains in the disk of CQ Tau. A&A, **403**, 323–328.

Testi, L. et al (2014). Dust Evolution in Protoplanetary Disks. *Protostars and Planets VI*, pages 339–361.

Testi, L. et al (2016). Brown dwarf disks with ALMA: Evidence for truncated dust disks in Ophiuchus. A&A, **593**, A111.

Tielens, A.G.G.M. and Hollenbach, D. (1985). Photodissociation regions. I - Basic model. II - A model for the Orion photodissociation region. ApJ, **291**, 722–754.

Tobin, J.J. et al (2009). Kinematics of the Orion Nebula Cluster: Velocity Substructure and Spectroscopic Binaries. ApJ, **697**, 1103–1118.

Toomre, A. (1964). On the gravitational stability of a disk of stars. ApJ, **139**, 1217–1238.

Toomre, A. and Toomre, J. (1972). Galactic Bridges and Tails. *ApJ*, **178**, 623–666.

Tripathi, A. et al (2017). A millimeter Continuum Size-Luminosity Relationship for Protoplanetary Disks. ApJ, **845**, 44.

Turner, N.J. et al (2014). Transport and Accretion in Planet-Forming Disks. *Protostars and Planets VI*, pages 411–432.

Urpin, V. and Brandenburg, A. (1998). Magnetic and vertical shear instabilities in accretion discs. MNRAS, **294**, 399.

van der Marel, N., Williams, J.P. and Bruderer, S. (2018). Rings and Gaps in Protoplanetary Disks: Planets or Snowlines? ApJ, **867**, L14.

Vazquez-Semadeni, E. (1994). Hierarchical Structure in Nearly Pressureless Flows as a Consequence of Self-similar Statistics. ApJ, **423**, 681.

Velikhov, E.P. (1959). Stability of an Ideally Conducting Liquid Flowing between Cylinders Rotating in a Magnetic Field. *"JETP"*, **36**, 1398.

Vincke, K. and Pfalzner, S. (2016). Cluster Dynamics Largely Shapes Protoplanetary Disk Sizes. ApJ, **828**, 48.

Vorobyov, E.I. and Basu, S. (2010). The Burst Mode of Accretion and Disk Fragmentation in the Early Embedded Stages of Star Formation. ApJ, **719**, 1896–1911.

Walch, S. and Naab, T. (2015). The energy and momentum input of supernova explosions in structured and ionized molecular clouds. MNRAS, **451**, 2757–2771.

Walch, S.K. et al (2012). Dispersal of molecular clouds by ionizing radiation. MNRAS, **427**, 625–636.

Wang, L. et al (2015). NBODY6++GPU: ready for the gravitational million-body problem. MNRAS, **450**, 4070–4080.

Ward, J.L. and Kruijssen, J.M.D. (2018). Not all stars form in clusters - measuring the kinematics of OB associations with Gaia. MNRAS, **475**, 5659–5676.

Watkins, S.J. et al (1998a). Numerical simulations of protostellar encounters - II. Coplanar disc-disc encounters. MNRAS, **300**, 1205–1213.

Watkins, S.J. et al (1998b). Numerical simulations of protostellar encounters - III. Non-coplanar disc-disc encounters. MNRAS, **300**, 1214–1224.

Weber, E.J. and Davis, Jr., L. (1967). The Angular Momentum of the Solar Wind. ApJ, **148**, 217–227.

White, R.J. and Ghez, A.M. (2001). Observational Constraints on the Formation and Evolution of Binary Stars. *ApJ*, **556**, 265–295.

Wijnen, T.P.G. et al (2017a). Characterising face-on accretion onto and the subsequent contraction of protoplanetary discs. A&A, **602**, A52.

Wijnen, T.P.G. et al (2017b). Disc truncation in embedded star clusters: Dynamical encounters versus face-on accretion. A&A, **604**, A91.

Williams, J.P. and Cieza, L.A. (2011). Protoplanetary Disks and Their Evolution. ARA&A, **49**, 67–117.

Williams, J.P. and Gaidos, E. (2007). On the Likelihood of Supernova Enrichment of Protoplanetary Disks. ApJ, **663**, L33–L36.

Winn, J.N. and Fabrycky, D.C. (2015). The Occurrence and Architecture of Exoplanetary Systems. ARA&A, **53**, 409–447.

Winter, A.J., Booth, R.A. and Clarke, C.J. (2018a). Evidence of a past disc-disc encounter: HV and DO Tau. MNRAS, **479**, 5522–5531.

Winter, A.J. et al (2018b). Protoplanetary disc response to distant tidal encounters in stellar clusters. MNRAS, **475**, 2314–2325.

Winter, A.J. et al (2018c). Protoplanetary disc truncation mechanisms in stellar clusters: comparing external photoevaporation and tidal encounters. MNRAS, **478**, 2700–2722.

Winter, A.J., Clarke, C.J. and Rosotti, G.P. (2019). External photoevaporation of protoplanetary discs in Cygnus OB2: linking discs to star formation dynamical history. MNRAS, **485**, 1489–1507.

Woitas, J. and Leinert, C. (1998). HV Tauri C - Herbig-Haro flow or stellar companion with strong forbidden emission lines? *AAP*, **338**, 122–126.

Wong, T. and Blitz, L. (2002). The Relationship between Gas Content and Star Formation in Molecule-rich Spiral Galaxies. ApJ, **569**, 157–183.

Wright, N.J. et al (2010). The Massive Star-Forming Region Cygnus OB2. II. Integrated Stellar Properties and the Star Formation History. ApJ, **713**, 871–882.

Wright, N.J. et al (2014a). Constraints on massive star formation: Cygnus OB2 was always an association. MNRAS, **438**, 639–646.

Wright, N.J. et al (2014b). The Chandra Cygnus OB2 Legacy Survey: Design and X-ray Point Source Catalog. *ArXiv e-prints*.

Wright, N.J., Drew, J.E. and Mohr-Smith, M. (2015). The massive star population of Cygnus OB2. MNRAS, **449**, 741–760.

Wright, N.J. et al (2016). Cygnus OB2 DANCe: A high-precision proper motion study of the Cygnus OB2 association. MNRAS, **460**, 2593–2610.

Wu, B. et al (2015). GMC Collisions as Triggers of Star Formation. I. Parameter Space Exploration with 2D Simulations. ApJ, **811**, 56.

Youdin, A.N. and Goodman, J. (2005). Streaming Instabilities in Protoplanetary Disks. ApJ, **620**, 459–469.

Zhang, K., Blake, G.A. and Bergin, E.A. (2015). Evidence of Fast Pebble Growth Near Condensation Fronts in the HL Tau Protoplanetary Disk. ApJ, **806**, L7.

Zhu, Z. et al (2009). Two-dimensional Simulations of FU Orionis Disk Outbursts. ApJ, **701**, 620–634.

Zhu, Z. et al (2010). Long-term Evolution of Protostellar and Protoplanetary Disks. I. Outbursts. ApJ, **713**, 1134–1142.

Zsom, A. et al (2010). The outcome of protoplanetary dust growth: pebbles, boulders, or planetesimals? II. Introducing the bouncing barrier. A&A, **513**, A57.

Appendix A

Appendix to Chapter 3

A.1 Linearised angular momentum transport equations

In order to derive results for a given ring at radius r within a disc, we adapt the results of Ostriker (1994), and henceforth equation numbers in brackets are in reference to that paper. Before we discuss the individual contributions, some consideration is given to particular equations and notation within that extensive study. We first briefly review the relevant vectors. The vector between the star with a disc and a given fluid element is defined to be

$$\boldsymbol{r} = \boldsymbol{r}_0(t) + \boldsymbol{r}_1$$

where $\boldsymbol{r}_0$ is the unperturbed position vector and $\boldsymbol{r}_1$ is the perturbation from this vector induced by the force from the secondary star. This can be expanded into the form

$$\boldsymbol{r}_1 \equiv r_1\hat{\boldsymbol{r}}^0 + \phi_1 r_0 \hat{\boldsymbol{\phi}}^0 + z_1\hat{\boldsymbol{z}}$$

where subscript (superscript) 0 denotes an unperturbed co-ordinate value (unit vector), and 1 the corresponding perturbed value. Note that $z_0 = 0$ in the chosen coordinate system. The external force per disc fluid element mass exerted by the perturbing star with mass M_2, separated by vector $\boldsymbol{x}$ from the host star, can be expanded in terms of spherical harmonics:

$$\boldsymbol{f}_{\rm ext} = GM_2 \sum_{l=2}^{\infty} \sum_{m=-l}^{l} \frac{4\pi}{2l+1} \boldsymbol{\nabla} \left[|\boldsymbol{r}'|^l Y_l^{m*}(\boldsymbol{r}') \right] \frac{Y_l^m(\boldsymbol{x})}{|\boldsymbol{x}|^{l+1}} \tag{A.1}$$

where $\boldsymbol{r}'$ is the distance between the perturbed fluid particle and the center of mass of the system

$$\boldsymbol{r}' = \boldsymbol{r} - \frac{M_{\rm disc}}{M_1 + M_{\rm disc}} \boldsymbol{r}_{\rm disc} \approx \boldsymbol{r}$$

assuming that the mass of this disc $M_{\rm disc}$ is negligible. The sum in equation A.1 starts at $l = 2$ since the $l = 0$ term is independent of $\boldsymbol{r}'$ and the $l = 1$ term vanishes in the frame that is accelerating due to the force exerted on the host star.

While working with spherical harmonics in this context it becomes necessary to define a quantity denoted in Ostriker (1994) as $Y_l^m(0)$. This quantity is used to represent the polar part of the spherical harmonic evaluated at $\boldsymbol{r}_0$, which is $Y_l^m(\pi/2, 0)$ given that the disc is fixed in the equatorial plane. For equation [2.15] and [2.16] the azimuthal component is cancelled when the Laplace transformation is applied to equations [2.10] and [2.11]. The integral over ϕ_0 is then simply a factor 2π.

To calculate the angular momentum change in the disc, we note that $\mathrm{d}\boldsymbol{L} \approx \mathrm{d}m\, \boldsymbol{r} \times \mathrm{d}\boldsymbol{v} = \mathrm{d}m\, \boldsymbol{r} \times \boldsymbol{f}_{\rm ext}\, \mathrm{d}t$ so that:

$$\Delta \boldsymbol{L} = G M_2 \int_{R_{\rm in}}^{R_{\rm out}} \mathrm{d}r_0\, r_0 \Sigma_0(r_0) \int_0^{2\pi} \mathrm{d}\phi_0 \int_{-\infty}^{\infty} \mathrm{d}t\, \boldsymbol{r} \times \boldsymbol{f}_{\rm ext}. \tag{A.2}$$

From equation 3.1, we can approximate the total change in angular momentum by the z-component of equation A.2. Although Ostriker (1994) finds a component proportional to $Y_l^{m+1}(0)$ and the Laplace-transformed z-coordinate, we show briefly that this term is not present in the vertical projection of the angular momentum transfer. This is important because it is the term which eventually leads to a vertical resonance contribution which dominates at large $x_{\rm min}/r$ in the calculations of Ostriker (1994). Substituting equation A.1 into equation A.2 and expanding by the product rule, it is immediately clear that any Y_l^{m+1} terms must come from the expression $\boldsymbol{r} \times \boldsymbol{\nabla} Y_l^{m*}(\boldsymbol{r})$. This is easier to evaluate in spherical coordinates ρ, θ, ϕ, in which case $\boldsymbol{\nabla} Y_l^{m*}(\boldsymbol{r})$ has $\hat{\boldsymbol{\theta}}$ and $\hat{\boldsymbol{\phi}}$ components only, which we denote $\nabla_\theta Y_l^{m*}(\boldsymbol{r})$ and $\nabla_\phi Y_l^{m*}(\boldsymbol{r})$. Now taking the cross product with r, we find

$$\boldsymbol{r} \times \boldsymbol{\nabla} Y_l^{m*}(\boldsymbol{r}) = \left[\theta \nabla_\phi Y_l^{m*}(\boldsymbol{r}) - \phi \nabla_\theta Y_l^{m*}(\boldsymbol{r})\right] \hat{\boldsymbol{\rho}} - \rho \nabla_\phi Y_l^{m*}(\boldsymbol{r}) \hat{\boldsymbol{\theta}} + \rho \nabla_\theta Y_l^{m*}(\boldsymbol{r}) \hat{\boldsymbol{\phi}}$$

Changing to cylindrical unit vectors, the z-component of this product is

$$\hat{\boldsymbol{z}} \cdot \left[\boldsymbol{r} \times \boldsymbol{\nabla} Y_l^{m*}(\boldsymbol{r})\right] = \left[\theta \nabla_\phi Y_l^{m*}(\boldsymbol{r}) - \phi \nabla_\theta Y_l^{m*}(\boldsymbol{r})\right] \cos\theta + \rho \nabla_\phi Y_l^{m*}(\boldsymbol{r}) \sin\theta.$$

Since $\cos\theta/\sin\theta = z_1/(r_0+r_1) \ll 1$, we have

$$\hat{\boldsymbol{z}}\cdot[\boldsymbol{r}\times\boldsymbol{\nabla}Y_l^{m*}(\boldsymbol{r})] \approx -imY_l^{m*}(\boldsymbol{r}).$$

Hence, the contribution of the vertical resonance is not dominant at large closest approach distances, and we find instead an ILR dominates angular momentum transfer in all regimes.

We now jump to the derived expression for the Lindblad resonances, which turn out to be the dominant contributions to the angular momentum loss in the disc. Equation [2.43] for angular momentum is

$$\Delta L^{\mathrm{ILR/OLR}} = \pm\sum_{m=0}^{\infty}\frac{1}{1+\delta_{m0}}\int_{\omega_{\min}}^{\omega_{\max}}\mathrm{d}\omega\,\frac{m\pi\Sigma_0(r_{\mathrm{L}})}{r_{\mathrm{L}}\kappa(r_{\mathrm{L}})\partial(m\Omega\mp\kappa)/\partial r_{\mathrm{L}}}\times \left|GM_2\sum_{l\geq|m|,2}^{\infty}\frac{4\pi}{2l+1}r_{\mathrm{L}}^l\left(l\pm\frac{2m\Omega(r_{\mathrm{L}})}{\kappa(r_{\mathrm{L}})}\right)Y_l^m(0)\int_{-\infty}^{\infty}\mathrm{d}t\,\frac{Y_l^m(\boldsymbol{x})}{|\boldsymbol{x}|^{l+1}}e^{-i\omega t}\right|^2 \quad \text{(A.3)}$$

where r_L is the radius defined such that $\omega = m\Omega(r_L)\mp\kappa(r_L)$ are satisfied for ILR/OLR respectively, where κ is the epicyclic frequency. The limits $\omega_{\min/\max}$ are defined similarly for the maximum and minimum disc radii. As discussed in Section 3.2.1, the epicyclic and Keplerian frequencies coincide when the disc mass is negligible. In this case, ω apparently vanishes for the $m=1$ contribution; the forcing frequency is small enough such that, although the radius of exact resonance is not well defined, a large range of radii are in a state of near resonance (and exact resonances do not exist). Formally the outer radius for which this is true is described in terms of a fiducial 'wave radius' r_w (Ostriker *et al.*, 1992). However, for a low-mass disc, the effect of the near resonance are nearly the same as the $m=1$ contribution to the exact resonance in equation A.3 and setting $\omega = 0$. This is physically equivalent to a secular perturbation, wherein the external trajectory is replaced by a ring of mass per unit length proportional to the inverse of the velocity at each point. We then have $\mathrm{d}\omega\cdot[\partial(\Omega-\kappa)/\partial r_{\mathrm{L}}]^{-1} \approx \mathrm{d}r$, from which comes equation [2.50]. The integration limits are swapped, and the value of m is negated. The secular resonance acts as an OLR since it propagates outwards. We are interested in the angular momentum transferred to a ring within the disc. This is obtained by treating the surface density distribution as a delta function $\Sigma_0(r)\to\delta(r-r_{\mathrm{r}})$, where the subscript 'r' denotes the ring quantity. Dividing through by the total angular momentum

$$L = 2\pi\int_{R_{\mathrm{in}}}^{R_{\mathrm{out}}} r^3\Sigma_0(r)\Omega(r)\,\mathrm{d}r$$

where $\Sigma_0(r)$ is again treated as a delta function gives $\Delta L_{\mathrm{r}}/L_{\mathrm{r}}$.

The final stage is to parameterise the trajectory of the perturbing star $\boldsymbol{x}$ relative to the central star, and the time t in terms of an angular coordinate ψ, phase with respect to pericentre. The appropriate transformation for $\tau = \tan(\psi/2)$ is

$$x(\tau) = x_{\rm min}(1+\tau^2); \quad t = \left(\frac{2x_{\rm min}^3}{GM_{\rm tot}}\right)^{1/2}\left(\tau+\tau^3\right)$$

so that the time integral is over ψ between $-\pi$ and π. Hence for the $m=1$, $\omega=0$ case the contribution of the ILR to angular momentum loss from a ring at radius r within the disc is

$$\left.\frac{\Delta L_{\rm r}}{L_{\rm r}}\right|^{\rm ILR}_{m=1,\,\omega=0} = -\frac{M_2^2}{4M_1M_{\rm tot}}\frac{x_{\rm min}}{r}\left|\sum_{l\geq 2}^{\infty}\frac{4\pi(l+2)}{2l+1}\left(\frac{x_{\rm min}}{r}\right)^{-l}Y_l^1(0)\int_{-\pi}^{\pi}{\rm d}\psi\,\cos^{2l-2}(\psi/2)Y_l^1(\boldsymbol{x})\right|^2 \tag{A.4}$$

where it is understood that the spherical harmonic as a function of the separation can be rotated in the axes described in Section 3.2.2 such that

$$Y_l^m(\boldsymbol{x}) = \sum_{m'=-l}^{l} Y_l^{m'}(\pi/2,\psi)d^l_{m'm}(\beta)e^{-im\alpha}$$

where $d^l_{m'm}$ is a Wigner-d matrix.

The contributions of the exact resonances can be found in a similar way to be

$$\left.\frac{\Delta L_{\rm r}}{L_{\rm r}}\right|^{\rm ILR} = -\sum_{m=2}^{\infty}\frac{mM_2^2}{2M_1M_{\rm tot}}\frac{x_{\rm min}}{r}\times$$
$$\left|\sum_{l=m}^{\infty}\frac{4\pi(l-2m)}{2l+1}\left(\frac{x_{\rm min}}{r}\right)^{-l}Y_l^m(0)\int_{-\pi}^{\pi}{\rm d}\psi\,\cos^{2l-2}(\psi/2)Y_l^m(\boldsymbol{x})\exp\left[-i2^{3/2}y\frac{\tan(\psi/2)}{\cos^2(\psi/2)}\right]\right|^2 \tag{A.5}$$

where

$$y = (m-1)\left(\frac{M_1}{M_{\rm tot}}\right)^{1/2}\left(\frac{x_{\rm min}}{r}\right)^{3/2}.$$

Equation A.4 has the clear properties that it scales as $(x_{\rm min}/r)^{1-2l}$, and is therefore dominated by the non-zero components with lowest values of l. As $Y_2^1(0)=0$, this is the $l=3$ term. While equation A.5 can simply be calculated numerically, in order to write the exact resonance contributions in a helpful form an approximation for the integral over ψ (for $\omega\neq 0$) is needed.

The approach for this is provided by Ostriker (1994), and we obtain

$$\left.\frac{\Delta L_{\rm r}}{L_{\rm r}}\right|^{\rm ILR} = -\sum_{m=2}^{\infty} \frac{m\pi M_2^2}{2M_1 M_{\rm tot}} \frac{x_{\rm min}}{r} \exp\left[-\frac{2^{5/2}}{3}y\right] \times \left|\sum_{l=m}^{\infty} \frac{4\pi(l-2m)}{2l+1} \frac{2^{3l/2+1/4}}{(2l-1)!!} y^{(2l-1)/2} \left(\frac{x_{\rm min}}{r}\right)^{-l} Y_l^m(0) Y_l^l(\boldsymbol{x}_{\rm min})\right|^2 . \quad \text{(A.6)}$$

This term is dominated by lower m values, and is thus referred to as the $m = 2$ ILR component. The total angular momentum lost in a close encounter can be approximated by the sum of equations A.4 and A.6.

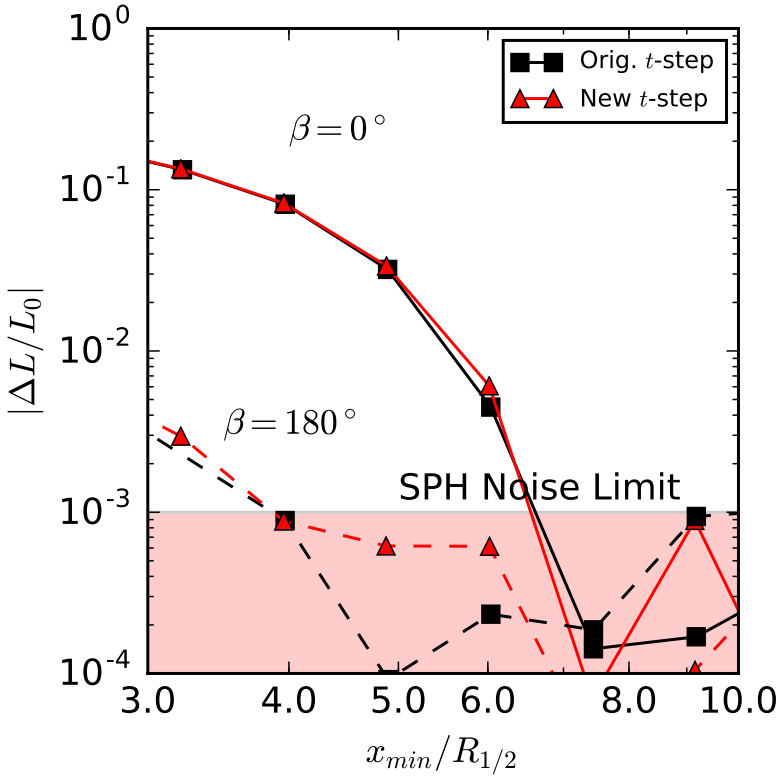

Fig. A.1 Time-step test for 2D SPH calculation results. The new results (red) use a smaller a time-step which is reduced by a factor three. This is compared to our original results (black) in the case where the encounter is prograde (solid) and retrograde (dashed). No significant difference is found between the two sets of results above the $|\Delta L/L| \sim 10^{-3}$ noise limit.

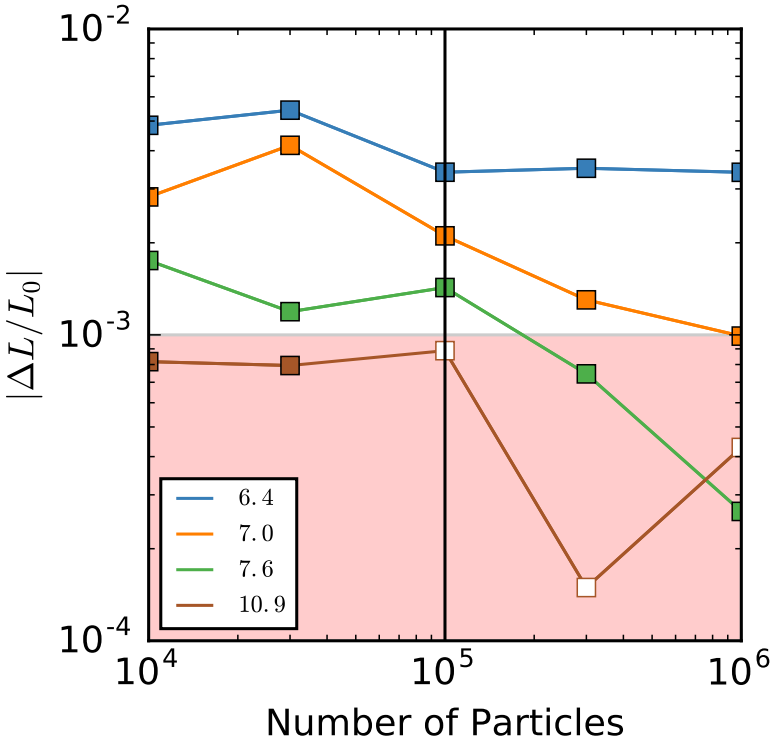

Fig. A.2 Change in angular momentum during an encounter for the prograde case in 2D SPH simulations and varying particle numbers. Numbers in the legend represent the value of $x_{\rm min}/R_{1/2}$. Results for which $\Delta L/L > 0$ are shown as empty squares, while filled squared represent angular momentum loss. The vertical line is placed at 10^5 particles, which is the resolution of the 2D SPH results presented in Section 3.3.2. The noise limit found for 10^5 particles is shaded. We find no significant change in the results with particle number for $x_{\rm min}/R_{1/2} \leq 6.4$.

A.2 Numerical convergence tests

To ensure that the results of our SPH calculations using GANDALF are numerically converged, we show the equivalent results in the 2D disc case for different particle resolutions and alternate time-step criteria. In our discussion of SPH results, we compare simulations performed with a Leapfrog time integration method to those of MERCURY's built in BS integrator. While the latter technically has much greater accuracy, we show that the Leapfrog integrator is accurate enough for the range of parameter space we are interested in by reducing the timestep (see figure A.1). We similarly confirm that the 2D results for close encounters are not limited by the number of particles in figure A.2. This is further explored in figure A.3, where the higher resolution (10^6 particle) 2D simulations are compared with the test particle case, to marginal improved agreement close to the noise threshold for angular momentum

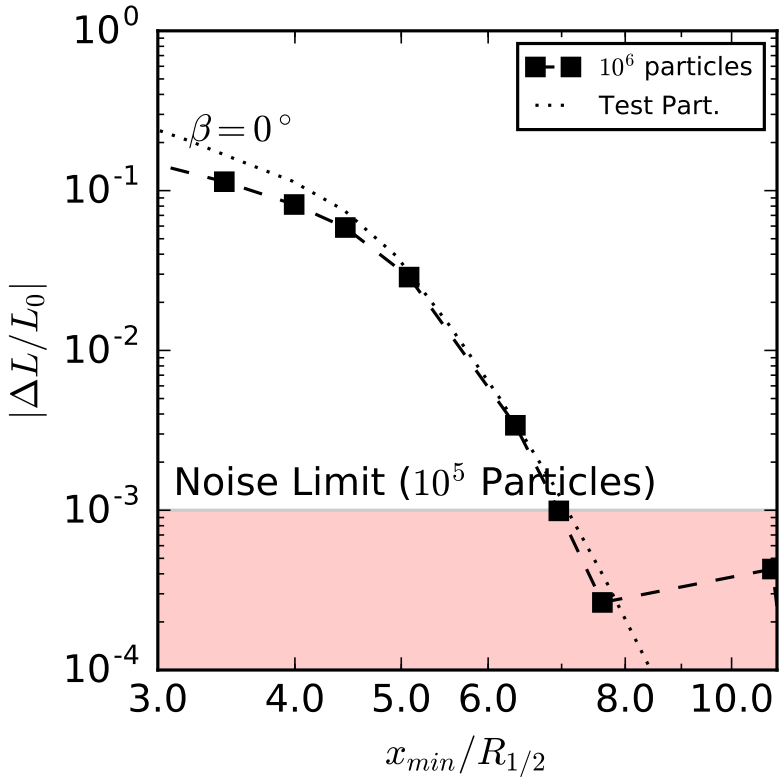

Fig. A.3 Angular momentum change calculations using SPH in 2D for a prograde encounter with 10^6 particles. The test particle reconstructed disc case is plotted for comparison, as in figure 3.6. The shaded region represents the assumed noise limit in the 10^5 particle case. Good agreement is found over the the same range as in the 10^5 particle case, with some marginal improvement at $x_{\rm min}/R_{\rm out} \sim 8$.

loss. We note that given our choice of a cubic kernel it is possible that noise limit might be improved by applying, for example, a higher order kernel (Booth *et al.*, 2015; Rosswog, 2015). However, given that the required accuracy has been achieved in the region of interest, we do not pursue this possibility further here. We conclude that the SPH results that we present in Section 3.3.2 are not resolution dependent in the high $|\Delta L/L| > 10^{-3}$ regime, and are not altered by improving the time-step criteria.

Appendix B

Appendix to Chapter 4

B.1 Particle number convergence

In Chapter 4 we use test particle ring simulations to calculate the angle-averaged change of disc outer radius due to an arbitrary encounter. To confirm that the choice of the number of particles in our simulations ($N = 200$) is sufficient, we run a convergence test by varying number of particles (see figure B.1). We find no significant change in angular momentum loss for $N > 50$ and conclude that our results are not particle number limited.

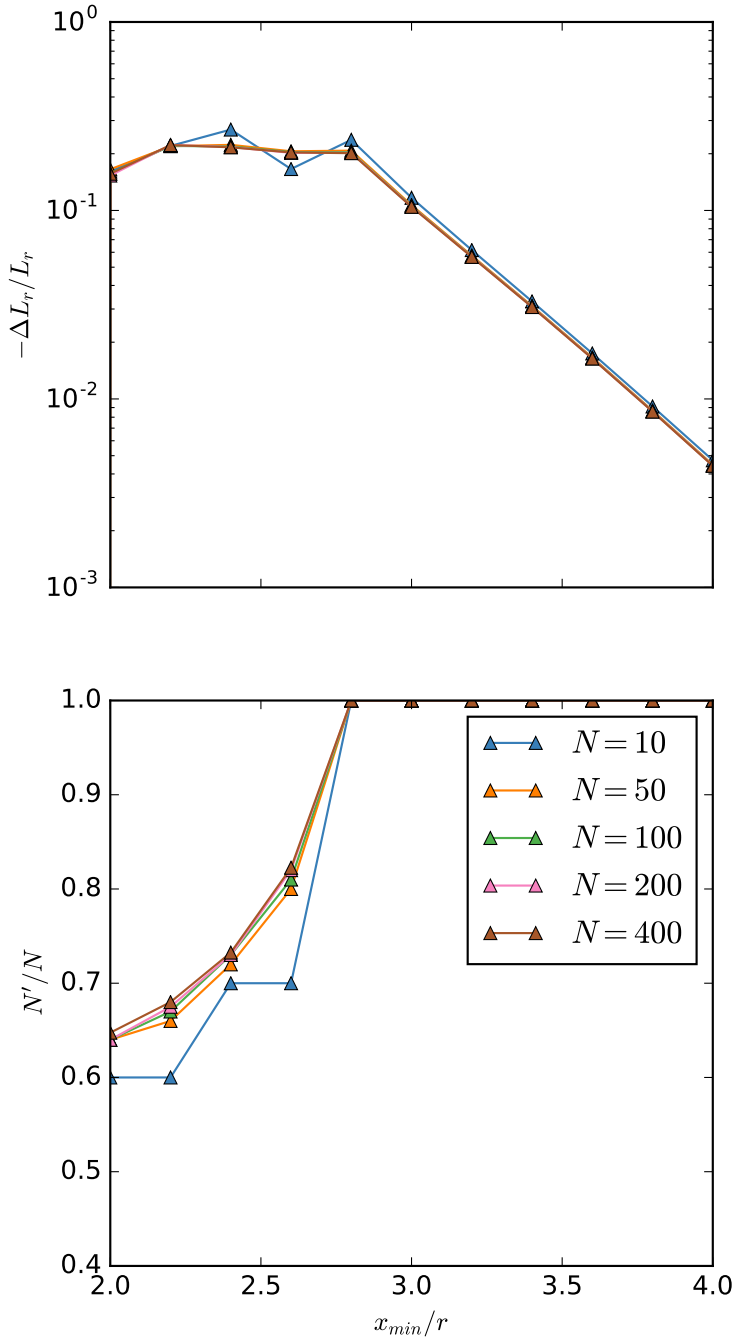

Fig. B.1 Results of the perturbation of an orbiting ring of test particles by an equal mass host in a coplanar, prograde, parabolic encounter. Top: mean fractional angular momentum loss of those particles that remain bound to the original host star. Bottom: fraction of particles which remain bound to the host N'/N. Results are shown for varying numbers of test particles, $N = 10$, 50, 100, 200 and 400. There is no significant change in the angular momentum loss until $N < 50$. Further, the particle rings only contribute to the outer radius calculation if the surviving particle fraction $N'/N > 0.9$ (see Section 4.3) which limits concerns about convergence to more distant encounters.

Appendix C

Appendix to Chapter 5

C.1 Cluster modelling

Below we review the assumptions made in the cases of specific clusters in order to model the FUV flux in the region, the results of which are shown in Section 5.2.3.

C.1.1 Cygnus OB2

The properties of Cygnus OB2 are discussed in detail in Chapter 6. For our simplified static model in Chapter 5 we make some corrections to our calculations to take into account the modest sub-structure and a slightly different IMF to our canonical choice. The IMF is found to be marginally shallower ($\xi \propto m^{-2.39\pm0.19}$) in the high-mass end. An increased population of massive stars will alter the $F_{\rm FUV}$ estimates and we therefore adopt this shallower IMF for $m > 1\,M_{\odot}$. To estimate the density enhancement, we apply the results of (Guarcello *et al.*, 2016) who used minimum spanning trees to simulate sub-clustering. We introduce a multiplicative factor to our number density profile such that the fraction of stars with number densities > 200 pc^{-3} agrees with the results shown in figure 12 of that paper. This results in an enhancement in the number densities by a factor ~ 12. Similarly the FUV flux is enhanced by the reduced distance to neighbouring stars, and Guarcello *et al.* (2016) find the $F_{\rm FUV} \sim 10^4\,G_0$ in the core. This only increases our $F_{\rm FUV}$ estimates by a small factor. We present both the enhanced and non-enhanced cases.

C.1.2 Serpens

The recent study of Law *et al.* (2017) found no significant differences in the PPD masses in the Serpens star forming region when compared to the low-density Taurus region which

is of a similar age ($1-3$ Myr). This suggests that neither tidal truncation nor external photoevaporation has had a significant influence on the disc evolution in this region.

At least two main sub-clusters are present in the Serpens region, Serpens A and B. Harvey *et al.* (2007) find the radius of sub-cluster A(B) to be $\sim 0.25(0.21)$ pc. They contain 44 and 17 stars respectively, while the the rest of the region contains an additional 174, at an average number density of ~ 2.5 pc^{-3}, and this sample is complete down to masses $\sim 0.08\,M_{\odot}$. Erickson *et al.* (2015) find the most massive star in Serpens to be 5.1 $M_{\odot}$ located at R.A. 18 h 29 m 56.1 s and Dec. 01° 00' 21.7" which places it close to the centre of Serpens A as projected onto the sky.

We model Serpens A and B as two Plummer spheres (with $\gamma = 4$ in Equation 5.2) with a maximum stellar mass of $5.1\,M_{\odot}$ placed at the centre of cluster A. The projected separations of the two sub-clusters is ~ 3 pc, which we use as our physical separation. The scale factors $a = 0.25$, 0.21 pc are taken for A and B respectively. The mass, $M_{\rm clust}$, of each A and B is fixed so that the correct number of stars are found within a from the centre when drawn from the IMF truncated above $5.1\,M_{\odot}$. We remove all stars outside of the radius a from the centre of the two Plummer spheres. Serpens has an elongated, filamentary shape, and therefore we arrange the remaining stars isotropically over a rectangular box centred on Serpens B such that the total number of stars is 235. We assume that the box has dimensions such that the two shortest sides have equal length of 2 pc and the third has length 7 pc. Because the number of stars in Serpens is relatively small, the approximate FUV flux experienced by those stars is dependent on the stochastic ICs. We therefore produce 100 versions of this model and perform statistics on the full sample in Serpens A, B and the remaining population. Thus we produce a reasonable range of $F_{\rm FUV}$ in the two cores.

We find that all versions of these initial conditions produce a local FUV flux which is $F_{\rm FUV} \ll 1\,G_0$ in all regions of Serpens. As the interstellar value is unity, we adopt this as the floor in our FUV flux estimates (i.e. the irradiation of discs due to member stars is insignificant). We choose the extremal number densities in all of our model generations as the range of $n_{\rm c}$.

C.1.3 IM Lup in Lupus 2

The Lupus clouds are a low-mass star forming complex located $\sim 140-200$ pc from the Sun. It is composed of multiple physically separated associations (e.g. Comerón, 2008). They are projected along the sky against the Scorpius-Centaurus OB association (Sco OB2), which is a distance of ~ 140 pc from the Sun and comprised of several spatially separated groups with varying ages. The stellar components of Sco OB2 are $\sim 5-16$ Myr old, with masses up to $\sim 20\,M_{\odot}$ and an approximate IMF with $\xi \propto m^{-2.6}$ at the high-mass end (Preibisch *et al.*,

2002). The number of OB members in close proximity to Lupus suggests a larger ambient field of UV radiation than other comparable low-mass star forming regions.

Cleeves *et al.* (2016, see also Haworth *et al.* 2017) studied the gas and dust structure of the disc around IM Lup, a $1\,M_{\odot}$ young ($\lesssim 1$ Myr) M0 type star associated with the Lupus 2 cloud, ~ 160 pc from the Sun. They make an estimate of the local $G_0 \sim 2.9-4.5$ depending on assumptions made about extinction, sufficient to alter the gas phase CO profile within the disc.

Clearly the diffuse and clumpy Lupus region is not well suited to modelling using the same density profile as in other cases. We do not estimate the local stellar number density in the region around IM Lup directly, but instead argue that the most dense region in Lupus is Lupus 3, which is thought to have a stellar number density up to ~ 500 pc^{-3} in the cores (Nakajima *et al.*, 2000; Merín *et al.*, 2008). This serves as an upper limit on the local number density around IM Lup.

C.1.4 NGC 1977

Kim *et al.* (2016) reported the discovery of seven proplyds in NGC 1977, a region which experiences much weaker FUV fields than the core of the location of the classic proplyds in the core of the ONC, with a G_0 value $10-30$ times lower. NGC 1977 is located at the interface between the Orion molecular cloud and the H II region S279 (Kutner *et al.*, 1976). The ionising source in this region is a B1 V star, HD 37018 (42 Ori), which is estimated to have a mass of $10\,M_{\odot}$. Thus the FUV flux at the distance of the proplyds (at separations of ~ 0.2 pc from 42 Ori) is estimated to be $\sim 3000G_0$ by Kim *et al.* (2016).

In total the region contains ~ 170 young stellar objects and 3 young B stars within a region of radius ~ 10', or ~ 1 pc (Peterson and Megeath, 2008). We therefore estimate the stellar density in the region to be ~ 40 pc^{-3}.

C.1.5 σ Orionis

The disc population of σ Orionis (σ Ori), a ~ 3 Myr old cluster at a distance of 350-440 pc (Mayne and Naylor, 2008; Sherry *et al.*, 2008), has been surveyed using both Herschel/PACS (Maucó *et al.*, 2016) and ALMA (Ansdell *et al.*, 2017). Maucó *et al.* (2016) report that 23% of the 142 T-Tauri stars in the dense core of radius $\sim 20'$ (or ~ 2 pc) are disc-hosting candidates, while the disc fraction outside this core out to $\sim 30'$ is 42%. Ansdell *et al.* (2017) also conclude that the dust mass within discs decreases with stars with closer proximity to the central massive star.

Observed stellar masses in σ Ori range from the O9 V star σ Ori A with mass $\sim 17 M_{\odot}$ down to brown dwarves with a minimum mass $\sim 0.033 M_{\odot}$ (Caballero, 2008b). In fact σ Ori A is part of a triple system, a spectroscopic binary previously considered to be a single star with components of mass 17 and $12.8 M_{\odot}$, and a B0.5 V star σ Ori B at a separation of $0.25''$ and mass ~ 11.5 (Schaefer *et al.*, 2016). For modelling purposes, as these components have similar masses, we place all of these stars in the centre of the cluster with a separation of 100 au for the wide binary (period ~ 150 yrs) and a distance of 8 au for the tight binary (period ~ 150 days).

The density profile in σ Ori was modelled by Caballero (2008a), where the surface density distribution is found to be well fit by a power law $\propto r_{\rm c}^{-1}$ in the core, with a steeper slope of $\propto r_{\rm c}^{-1.3}$ between $21'$ and $30'$ from the centre of the cluster. However, we find that by allowing small values of a and γ we can also fit this profile sufficiently with our assumed density profile in Equation 5.2. Small values of $\gamma \leq 2$ are acceptable because, although we don't have a value for $r_{\rm eff}$, we truncate the cluster outside $30'$ ($r_{\rm t} \approx 3$ pc). We fit the mass of the cluster using the average mass obtained from Equation 4.7 between 0.08 and $17 M_{\odot}$ and the total number of members in the Mayrit catalogue, 338 (Caballero, 2008b). Our density profile is such that the same number of sources can be found within 3 pc. A number of these candidates might be falsely associated with the cluster, and that the catalogue includes a number of brown dwarves. However for our purposes of number density and FUV flux calculations this approximation is sufficient.

C.1.6 λ Orionis

The λ Orionis (λ Ori) star forming region is an OB association at a distance of around 420 pc from the Sun (Schlafly *et al.*, 2014). It began forming stars ~ 5 Myr ago, and is located inside a shell-like structure of dust and gas which is thought to be the result of a supernova explosion ~ 1 Myr ago (Dolan and Mathieu, 2001; Lee *et al.*, 2015) . Its proximity makes it a good candidate for studying disc populations, and previously Hernández *et al.* (2010) have used data from the *Spitzer Space Telescope* to observe disc fractions of $\sim 20\%$ around M-type stars. However, at present there are no studies which establish the dependence of disc properties on location within the association.

Dolan and Mathieu (2001) report the masses of the 20 OB stars associated with λ Ori, of which the most massive HD 36861 (also known as λ Ori, with spectral type O8 III) has a mass of $26.8 M_{\odot}$, and lies in the centre of the region.

With regards to the spatial distribution of the stars, it is possible that the region formed in a flattened molecular cloud, and therefore does not have 3D symmetry (Maddalena and Morris, 1987). Also, the presence of the actively star forming clouds B30 and B35 at a

distance $\sim 2^\circ$ from the central star means that the projected surface density is not isotropic. In order to model the region close to λ Ori, we truncate our stellar distribution outside 15 pc. We then fit our surface density profile, Equation 5.1, to that obtained by Dolan and Mathieu in that range. Applying our IMF truncated at $26.8 M_\odot$, we find that the total mass up to $r_\mathrm{t} = 15$ pc is $214 M_\odot$, which is approximately consistent with the $450 - 600 M_\odot$ estimate of Dolan and Mathieu for the whole region. As in the case of σ Ori, we allow small values of a and γ, and obtain a similar density profile.

C.1.7 NGC 2024

NGC 2024 (also known as Orion B) is an HII region in the Orion star forming complex around 415 pc away (Anthony-Twarog, 1982). It is thought to be $\sim 0.5 - 1$ Myr old (Levine *et al.*, 2006; Getman *et al.*, 2014), although there is considerable extinction of $\gtrsim 27$ magnitudes due to dust in the region (Lenorzer *et al.*, 2004).

The region is known to contain ~ 300 sources (e.g. Meyer, 1996), of which around 85% show evidence of hosting a disc (Haisch *et al.*, 2000, 2001a). Mann *et al.* (2015) studied this PPD population and found no evidence of disc mass dependence on the projected distance from the massive star IRS 2b, which they attribute either to the youth of the cluster or the insufficient flux from the ionising source. The spectral type of IRS 2b itself is not well constrained, with Bik *et al.* (2003) concluding it has spectral type O8 V-B2 V ($15 - 25 M_\odot$). Similarly, the region has a clumpy dust distribution and the extent of the extinction is not well characterised.

Lada and Kylafis (1999) estimated the radius of the region in which there are 300 stars to be 0.9 pc, and the average stellar surface density in the area to be 179 pc^{-2}. The central 0.1 pc (projected from the centre) encompasses 50 stars, and therefore the association has a central surface density of 1600 pc^{-2}. While this is not sufficient to fit a full density profile, we assume the latter number density represents the central value, and fit associated values of γ and a.

We model two versions of NGC 2024, with $m_\mathrm{max} = 15 M_\odot$, $25 M_\odot$. Although IRS 2b does not lie directly in the centre of the cluster, we place it there for simplicity. Given that dynamical mass segregation can occur on short time-scales (e.g. Allison *et al.*, 2009) this is a reasonable assumption for the long-term properties of the environment.

C.2 Notes on specific flux-density contours

The results for certain clusters presented in Figure 5.3 require discussion where particular simplifying assumptions have been made. These cases are discussed below.

C.2.1 Wd 1

In all of the six examples for which density profiles are taken directly from the review of Portegies Zwart *et al.* (2010), with the exception of the ONC and Westerlund 1 (Wd 1), the maximum stellar masses are taken to be such that 84% of clusters of equal mass are expected to contain a higher mass star ($m_{\rm max} = m_{\rm max}^{-\sigma}$). In the case of the ONC we use the observed maximum stellar mass which coincides with this value. For Wd 1 we find $m_{\rm max}^{-\sigma} \approx 114 M_{\odot}$, which is the only case which is greater than the upper mass limit for our stellar atmosphere models. We have therefore used this upper limit, $m_{\rm max} = 100$. This is a further underestimate of the flux in the region. However we find that for massive clusters where the upper limit of the IMF is relatively well sampled, the FUV flux in the cluster is less sensitive to $m_{\rm max}$. In figure 5.3, all the massive clusters follow contours in the parameter space within an order of magnitude of each other, particularly in the most dense regions. Thus our decision for Wd 1 is justified.

C.2.2 Cygnus OB2

For the Cygnus OB2 association, we show two contours in figure 5.3 (both in brown, enhanced density marked by triangles), for the first of which we simply use the results as implied by our density profile without any sub-structure. The second takes the same results normalised to reflect the maximum densities and fluxes obtained by Guarcello *et al.* (2016), wherein the considerable sub-structure observed in the association is accounted for. While this is a crude approximation, we find that the factors ~ 12 and ~ 1.2 for number density and flux respectively. This suggests that the effect of sub-structure enhances number density more than the local $F_{\rm FUV}$ values. We would expect this as on large scales given that most stars will not have any significant reduction in the distance to the most massive stellar components of the cluster which make up the dominant contribution to the FUV flux.

C.2.3 NGC 2024

The association NGC 2024 is also represented by two contours. Because of the observational complications in that region, the stellar masses are not well constrained and hence we have

produced two models for $m_{\max} = 15\,M_{\odot}, 25\,M_{\odot}$. This represents a range of likely fluxes in the region, although the ionization in the region is consistent with a source closer to $\sim 25 M_{\odot}$ (Bik *et al.*, 2003). Given the difficulty modelling the clumpy dust distribution, we do not account for extinction in the region, which may somewhat reduce flux estimates. However, as NGC 2024 is contained within a small region ~ 0.9 pc in radius, we expect the range of fluxes suggested by the two contours without extinction to be reasonable.

Appendix D

Appendix to Chapter 7

D.1 FUV extinction

D.1.1 Modified flux distribution

At early times, the presence of primordial gas causes intra-cluster extinction in the FUV; we wish to evaluate its influence on the flux PDF at fixed x. This is the dependent on the effective local gas surface density $\Sigma_{\rm eff}$ between a given star and FUV source. We define the corresponding surface overdensity $\chi \equiv \Sigma_{\rm eff}/\Sigma_0$. In order to proceed we assume that the local extinction does not influence the flux in the field, which remains the floor of the distribution of F. Then the ratio of the extincted flux to the local mean flux is $\psi_0^{\rm ext} \equiv F_0^{\rm ext}/F_0^{\rm HM}$ is

$$\psi_0^{\rm ext} = \begin{cases} e^{-C_{\rm ext}\chi}\left(1-e^{-\Gamma}\right)+\psi_0^{\rm f} & \psi_0^{\rm f} < 1 \\ \psi_0^{\rm f} & \psi_0^{\rm f} \geq 1 \end{cases} \tag{D.1}$$

where the extinction properties of the ISM are contained within the constant

$$C_{\rm ext} = \frac{\Sigma_0}{13.36 M_\odot\,{\rm pc}^{-2}} \tag{D.2}$$

based on the ratio of extinction in FUV to the visible $A_{\rm FUV}/A_{\rm V} \approx 2.7$ (Cardelli *et al.*, 1989) and the column density of hydrogen required for 1^m of extinction in the visible $N_{\rm H}/A_{\rm V} = 1.8\times10^{21}$ cm^{-2} mag^{-1} (Predehl and Schmitt, 1995). As before we can immediately evaluate the PDF for $\psi_0^{\rm ext}$ at certain limits. Equation 7.45 applies here as before, as does equation 7.46 except the upper limit for $\psi_0^{\rm ext}$ is now set by χ. Physically, χ varies for a given Γ (or equivalently ϕ), and therefore establishing the probablity of obtaining a given $\psi_0^{\rm ext}$ requires evaluating the PDF for χ.

D.1.2 Effective surface density

Gas density profile

To evaluate the appropriate surface density, we are required to make assumptions about the geometry of the system. This involves introducing an additional parameter, describing the relative position in a local environment such that we can link $\rho_{\rm g}$ to $\Sigma_{\rm eff}$. We define a radial coordinate r within a cluster of scale radius a, and the relative radius $\gamma \equiv r/a$, and assume a Plummer density profile:

$$\rho_{\rm g} = \frac{\rho_{\rm c}}{(1+\gamma^2)^{5/2}}. \tag{D.3}$$

The local overdensity in the centre $x_{\rm c} \equiv \rho_{\rm c}/\rho_0$ is a monotonic function of $\gamma > 0$, which we assume has the same PDF as defined for x, truncated such that $x_{\rm c} > x$. The corresponding PDF for γ at fixed x is

$$\frac{\partial \mathscr{F}_*}{\partial \gamma} = \frac{\partial \mathscr{F}_*}{\partial x_{\rm c}} \frac{\partial x_{\rm c}}{\partial \gamma} \propto \gamma\left(1+\gamma^2\right)^4 \frac{\partial p}{\partial x_{\rm c}}. \tag{D.4}$$

For a given γ, we can also calculate the corresponding a such that the total cluster gas mass is $\phi M_{\rm crit}/\varepsilon$:

$$a = \left(\frac{3M_{\rm crit}}{4\pi\varepsilon\rho_0 x_{\rm c}}\right)^{1/3} = \left(\frac{3M_{\rm crit}}{4\pi\varepsilon\rho_0}\right)^{1/3} x^{-1/3}\phi^{1/3}(1+\gamma^2)^{-5/6}. \tag{D.5}$$

Ionisation

Having defined our local density profile, we integrate over the relevant range to establish the effective surface density. When a massive star occupies the central region of a cluster, then we would expect material within a certain radius to be ionised (and therefore optically thin to FUV photons). This size scale is initially given by the Strömgren (1939) radius:

$$R_{\rm S} \approx \left(\frac{3\dot{\mathscr{N}}_{\rm LyC} m_{\rm p}^2}{4\pi\alpha_{\rm B}\rho_{\rm c}^2}\right)^{1/3} = \left(\frac{3\dot{\mathscr{N}}_{\rm LyC} m_{\rm p}^2}{4\pi\alpha_{\rm B}\rho_0^2}\right)^{1/3} x^{-2/3}(1+\gamma^2)^{-5/3} \tag{D.6}$$

where $\dot{\mathscr{N}}_{\rm LyC}$ is the number of ionising (Lyman continuum) photons emmitted by the central source per unit time, $\alpha_{\rm B} \approx 2.7 \times 10^{-13}$ cm^3 s^{-1} is the recombination coefficient assuming a temperature $\sim 10^4$ K for the ionised gas (Osterbrock, 1989) , assuming constant local density for $r < R_{\rm S}$.

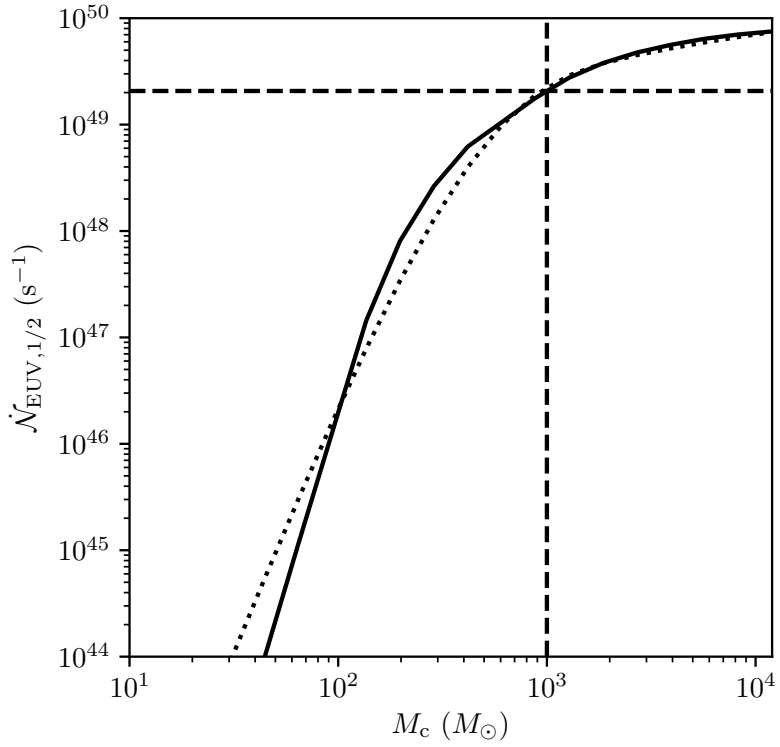

Fig. D.1 As in figure 7.2 but for the number of EUV counts $\dot{\mathcal{N}}_{\rm EUV,1/2}$ of the most massive cluster member as a function of cluster mass $M_{\rm c}$. The solid line is calculated directly from random drawing and the stellar atmosphere models, while the dotted line follows our analytic approximation, equation D.7. The vertical dashed line is at $M_{\rm crit}$ and the corresponding number of counts $\dot{\mathcal{N}}_{\rm EUV,crit} = 2.07 \times 10^{49}$ s^{-1} is shown as a horizontal dashed line.

We assume EUV photons dominate ionisation and define the median number of EUV counts from the most massive star $\dot{\mathcal{N}}_{\rm EUV,1/2}(\phi)$. For this we define a fitting formula:

$$\Theta(\phi) \equiv \frac{\dot{\mathcal{N}}_{\rm EUV,1/2}}{\dot{\mathcal{N}}_{\rm EUV,crit}} \approx \left\{1 - e^{-\delta_1 \phi}\right\}^{\delta_2} \ln\left(1 + \delta_1 \phi\right) \tag{D.7}$$

where $\dot{\mathcal{N}}_{\rm EUV,crit} = 2.07 \times 10^{49}$ s^{-1}, and we find $\delta_1 = 2.9$, $\delta_2 = 4.0$. This expression is compared to the direct calculation from the stellar atmosphere models in figure D.1.

Combining equations D.6 and D.7, we have:

$$\gamma_{\rm S} \equiv \frac{R_{\rm S}}{a} = \left(\frac{\dot{\mathcal{N}}_{\rm EUV,crit} m_{\rm p}^2}{\alpha_{\rm B} M_{\rm crit} \rho_0}\right)^{1/3} \varepsilon^{1/3} x^{-1/3} \phi^{-1/3} \left(1 + \gamma^2\right)^{-5/6} \Theta^{1/3}, \tag{D.8}$$

in dimensionless quantities. Evaluating the prefactor:

$$\left(\frac{\dot{\mathscr{N}}_{\rm EUV,crit} m_{\rm p}^2}{\alpha_{\rm B} M_{\rm crit} \rho_0}\right)^{1/3} \approx \left(\frac{\rho_0}{1.6 M_\odot \,{\rm pc}^{-3}}\right)^{-1/3}. \tag{D.9}$$

Effective surface density PDF outside Strömgren radius

We assume that F is dominated by sources at the center of the density profile, then we have:

$$\Sigma_{\rm eff} = a \int_{\gamma_{\rm S}}^{\gamma} \frac{(1-\varepsilon)\rho_{\rm c}}{(1+\tilde{\gamma}^2)^{5/2}} \,{\rm d}\tilde{\gamma} \tag{D.10}$$

By making the simplifying assumption that the SFE is constant over the region such that $\varepsilon = \varepsilon(x) \neq \varepsilon(\gamma)$, equation D.10 becomes:

$$\chi_1 \approx \frac{(1-\varepsilon)}{3\varepsilon^{1/3}} \left(\frac{3 M_{\rm crit} \rho_0^2}{4\pi \Sigma_0^3}\right)^{1/3} x^{2/3} \phi^{1/3} (1+\gamma)^{5/3} \left[\frac{\gamma(2\gamma^2+3)}{(1+\gamma^2)^{3/2}} - \frac{\gamma_{\rm S}(2\gamma_{\rm S}^2+3)}{(1+\gamma_{\rm S}^2)^{3/2}}\right], \tag{D.11}$$

where we have defined $\chi_1 \equiv \chi(\gamma > \gamma_{\rm S})$, since $\chi(\gamma < \gamma_{\rm S}) = 0$.

Now we have a definition for χ, we use the PDF for γ (equation D.4) and ϕ (equation 7.48) to calculate the corresponding PDF for χ at a fixed x. Since there is a non-zero probability that $\chi = 0$, we must separately consider the regions inside and outside the Strömgren radius. The PDF of χ_1 (that is, assuming $\chi > 0$ – a star outside the Strömgren radius) is:

$$\frac{\partial \mathscr{F}_*}{\partial \chi_1} = \int_0^\infty {\rm d}\phi \frac{\partial \mathscr{F}_*}{\partial \phi} \frac{\partial \mathscr{F}_*}{\partial \gamma} \left|\frac{\partial \chi_1}{\partial \gamma}\right|^{-1}, \tag{D.12}$$

where $\gamma(\phi, \chi_1)$ is evaluated numerically. Figure D.2 shows the result for solar neighbourhood- and CMZ-like regions. The effective surface density experienced by a given star increases with local gas density x, as expected. Regions of high overdensity are therefore severely influenced by extinction. However, we must also consider the fact that stars at high density are more likely to be found towards the centre of the cluster, and therefore to occupy the Strömgren sphere (hence $\chi = 0$).

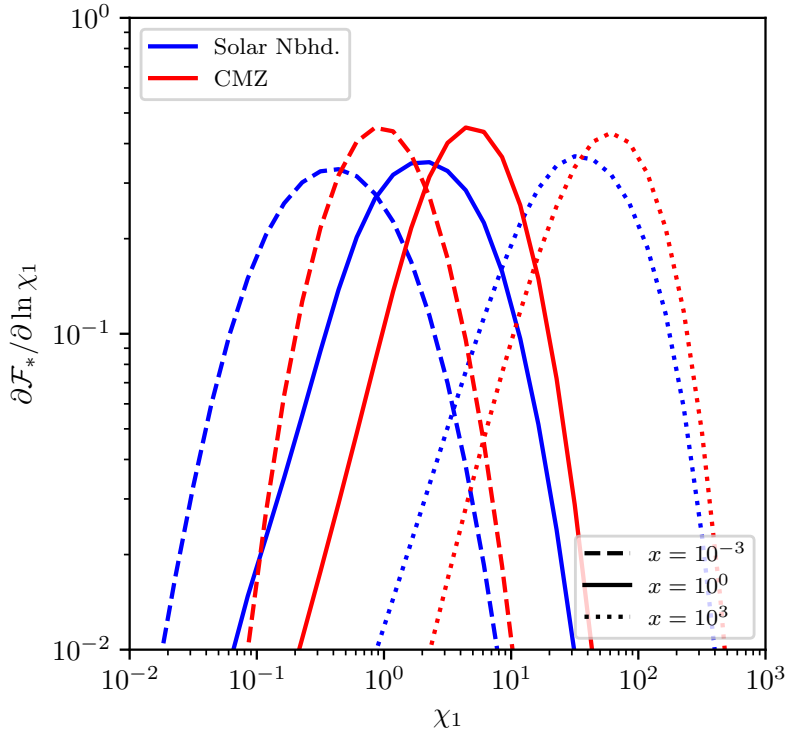

Fig. D.2 PDF of χ_1 (i.e. χ such that we assume $\chi > 0$) for varying overdensity x in the solar neighbourhood (blue lines) and CMZ (red lines). The value of χ_1 is the effective surface density experienced by a given star in the direction of the centre of the cluster during the embedded phase.

Fraction of stars within the Strömgren radius

The probability that $\chi = 0$ is equivalent to the probability that a star is found inside a radius γ_S. This can be written:

$$p_S(\phi, x) \equiv \mathcal{F}_*(\chi = 0; \phi, x) = \int_{\gamma < \gamma_S} \mathrm{d}\gamma \frac{\partial \mathcal{F}_*}{\partial \gamma}, \tag{D.13}$$

where the region $\gamma < \gamma_S$ is defined numerically for a fixed ϕ, x. Equation D.13 is evaluated using equation D.4 in figure D.3, from which we find that the probability of finding a star within a Strömgren radius is small ($\ll 10\%$) throughout the parameter space, especially for high ρ_0 environments. This is intuitively true from equation D.8; in the limit of large ρ_0, x, ϕ, we have small γ_S, and hence a small p_S. Since the contribution to the PDF from stars with $\gamma < \gamma_S$ is small, we have $\partial \mathcal{F}_* / \partial \chi_1 \approx \partial \mathcal{F}_* / \partial \chi$ and we limit our consideration to the distribution of $\chi_1 > 0$ in calculation of the PDF for ψ_0^{ext}.

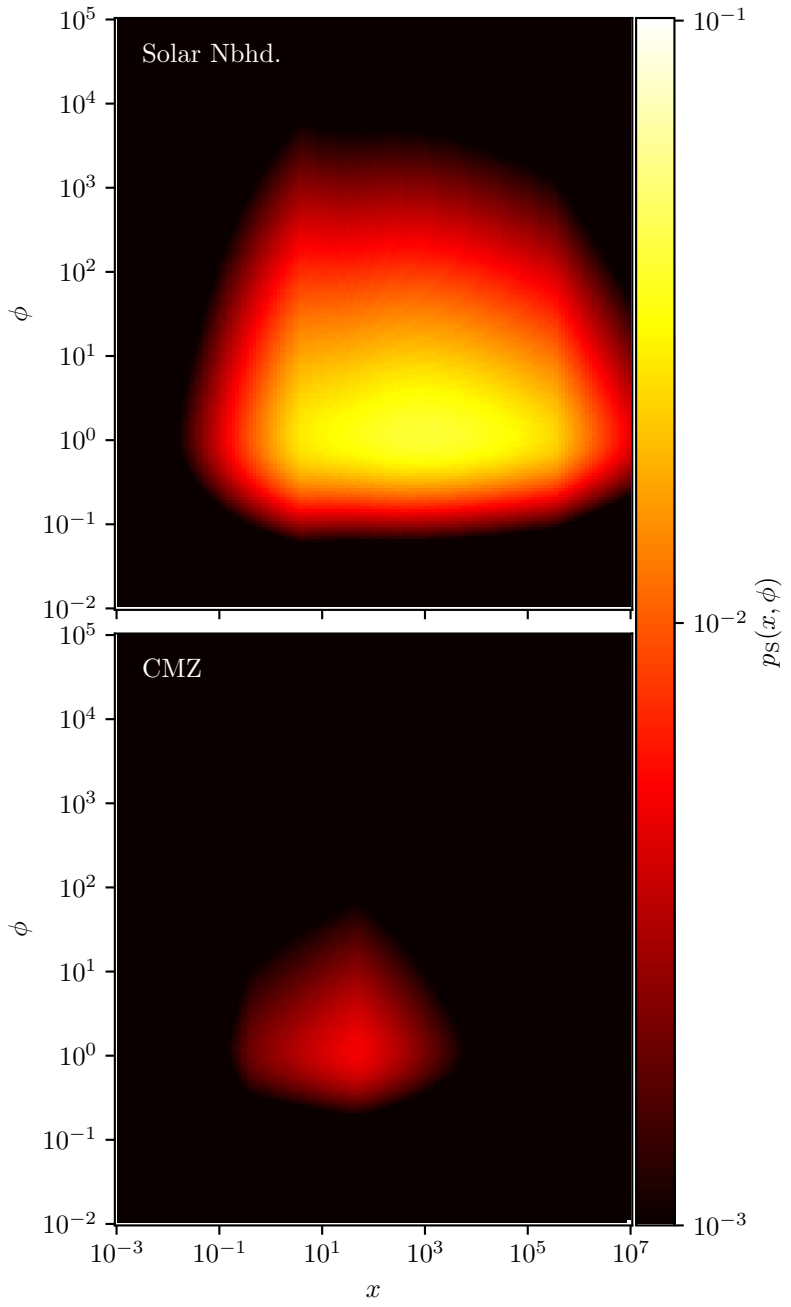

Fig. D.3 Probability p_S of finding a given star within the Strömgren radius ($\gamma < \gamma_S$) as a function of cluster mass ϕ and overdensity x for the solar neighbourhood (top panel) and CMZ (bottom panel). This is equivalent to the probability that a star has $\chi = 0$, and does not experience significant extinction of FUV photons from neighbouring stars.

D.1.3 PDF for extincted FUV flux

As a result of the above analysis, we can now write the PDF for $\psi_0^{\rm ext}$:

$$\frac{\partial \mathscr{F}_*}{\partial \psi_0^{\rm ext}} \approx \int_{\delta\chi}^{\infty} \mathrm{d}\chi_1 \, \frac{\partial \mathscr{F}_*}{\partial \chi_1} \frac{\partial \mathscr{F}_*}{\partial \phi} \left| \frac{\partial \psi_0^{\rm ext}}{\partial \phi} \right|^{-1} \tag{D.14}$$

for some sufficiently small $\delta\chi$. Equation D.14 is the PDF for the flux in the embedded phase of the cluster (at fixed x), and can be compared to the non-extincted PDF (equation 7.47) to estimate the role of gas with regards to stellar birth environment at early times.

This formulation gives an upper limit to the extinction experienced within a given environment. We have neglected the fact that realistically we would expect a clumpy density distribution, which considerably reduces the influence of extinction averaged over time. Additionally, we have established the Strömgren radius by assuming a constant central density, and the EUV luminosity of the single most massive star. In the case of a steep density profile, or multiple ionising sources, this will be an underestimate. Nor have we considered the rate of expansion of such an ionised region (Bisbas *et al.*, 2015). For these reasons, the true FUV flux experienced by a star is larger than the estimate we establish here.